UNIVERSITY OF SOUTHAMPTON
FACULTY OF ENGINEERING & THE ENVIRONMENT
SCHOOL OF ENGINEERING SCIENCES

DEVELOPMENT OF A ZINC-CERIUM REDOX FLOW BATTERY

By

Pui-ki Leung

Thesis for the degree of Doctor of Philosophy, 2011

Supervised by

Prof. Frank C. Walsh, Dr. Carlos Ponce-de-León

'*Development of a zinc-cerium redox flow battery*'

by Puiki Leung

Abstract

Redox flow batteries (RFBs) can be used to store energy on the large and medium scale (kW – MW), particularly in applications such as load levelling of electrical power supplies, power quality control application and facilitating renewable energy deployment. In this thesis, the development of a divided and undivided zinc-cerium redox flow battery from its fundamental chemistry in aqueous methanesulfonic acid has been described. This comprehensive investigation has focused on the selection of electrode materials, evaluation of zinc corrosion of the negative electrode, characterization of the redox flow battery and the cycling performance. Voltammetric studies of both the zinc and the cerium half-cell reactions have been carried out under various operating conditions and for electrolyte compositions. These studies suggested that the positive electrode reaction could limit the use of higher current densities. After testing a range of two- and three-dimensional positive electrode materials, only three-dimensional platinised titanium mesh and carbon felts were capable of discharge at 50 mA cm^{-2} with high charge (> 70 %) and voltage (> 60 %) efficiencies in an divided system based on the optimum electrolyte compositions obtained in the half-cell studies. In order to avoid the diffusion of protons across the membrane and to simplify the construction, an undivided, membraneless system was proposed. With specific design arrangement and carbon felt positive electrode, this system can operate at room temperature with a high energy efficiency (~ 75 %) instead of 60 ^{o}C as reported in the patented system in the literature. In order to facilitate zinc electrodeposition and prevent zinc corrosion, several electrolytic additives and corrosion inhibitors have been suggested. Further challenges and research directions are also discussed.

Declaration of authorship

I, PUI-KI LEUNG, declare that this thesis entitled '***Development of a zinc-cerium redox flow battery***' and the work presented in it are my own and have been generated by me as the result of my own original research.

I confirm that:

1. This work was done wholly or mainly while in candidature for a research degree at this University;
2. Where any part of this thesis has previously been submitted for a degree or any other qualification at this University or any other institution, this has been clearly stated;
3. Where I have consulted the published work of others, this is always clearly attributed;
4. Where I have quoted from the work of others, the source is always given. With the exception of such quotations, this thesis is entirely my own work;
5. I have acknowledged all main sources of help;
6. Where the thesis is based on work done by myself jointly with my supervisors (Prof. F.C. Walsh and Dr. C. Ponce de León), I have made clear exactly what was done by others and what I have contributed myself;
7. I am fully responsible for all sorts of ***ethnic and legal duties*** corresponding to the contents in this thesis;
8. The '***concept'*** or ***'idea''*** of an undivided zinc-cerium flow battery was solely introduced by me and my supervisor Dr. C. Ponce de León with no doubt;
9. The '***design'*** of an undivided flow battery was modified by me from the original divided flow cell provided by Dr. C.T.J. Low;
10. The flow battery used in this work was manufactured by the mechanical engineering work shop, University of Southampton;
11. ***Every single word of the literature review*** was solely written by me and has been edited/ modified by my supervisors (Prof. F.C. Walsh and Dr. C. Ponce de León) and my advisors (Dr. R.G.A. Wills), no other individual has been involved;
12. Part of this work have been submitted to journals for review and have been published, see 'List of papers and published papers'.

Signed: 

PUI-KI LEUNG

List of papers and published papers

Published papers:

1. P.K. Leung, C. Ponce de Leon*, C.T.J. Low, F.C. Walsh, 'Ce(III)/ Ce(IV) in methanesulfonic acid as the positive half cell of a redox flow battery', Electrochimica Acta, Vol 56 (5), 2011, 2145-2153.
2. P.K. Leung, C. Ponce de Leon*, C.T.J. Low, A.A. Shah, F.C. Walsh, 'Characterization of a zinc-cerium flow battery', Journal of Power Sources, Vol 196 (11), 2011, 5174-5185.
3. P.K. Leung, C. Ponce de Leon*, F.C. Walsh, 'An undivided zinc-cerium redox flow battery operating at room temperature', Electro-chemistry Communications, Vol 13 (8), 2011, 770 – 773.
4. P.K. Leung, C. Ponce de Leon*, C.T.J. Low, F.C. Walsh, 'Zinc deposition and dissolution in methanesulfonic acid onto a carbon composite electrode as the negative electrode reaction of a redox flow battery', Electrochimica Acta., Vol 56 (18), 2011, 6536-6546.

List of prepared papers:

1. P.K. Leung, X. Li, C. Ponce de Leon*, P. Herrasti, F.C. Walsh, 'Prevention of zinc corrosion in methanesulfonic acid for flow battery application', prepared for Corrosion Science.
2. P.K. Leung, C. Ponce de Leon*, F.C. Walsh, 'Importance of operating conditions on an undivided zinc-cerium redox flow battery', prepared for Journal of Power Sources.
3. P.K. Leung, X. Li, C. Ponce de Leon*, F.C. Walsh, 'Development and applications of redox flow battery', prepared for Journal of Power Sources.
4. P.K. Leung, C. Ponce de Leon*, F.C. Walsh, 'Electrodeposition of zinc and the importance of additives', prepared for Surface Coating and Technology.

Acknowledgements

First and foremost, I wish to express my sincerest gratitude to my project supervisors, Professor Frank Walsh, Dr Carlos Ponce-de-León and my advisor Dr Richard Wills. Without their patient teaching and guidance, this project would not have been possible. I highly appreciate their continuous encouragement and contributions of time, ideas and provision of laboratory facilities. Their trainings on electrochemical techniques and safety issues are highly valuable for an engineer graduate to conduct research in the area of electrochemistry. Under their supervision, I have improved my writing skills for scientific papers. Indeed, I am especially appreciative of their time and effort spent on training me. I also thank them for providing models of successful academic.

I gratefully acknowledge the financial support provided by the Research Institute for Industry (RIfI) at the University of Southampton. In Southampton, Drs XiaoHong Li, Dmitry Bavykin, Matthew Roberts, Akeel Shah, Alexander Kulak, Shuncai Wang and Suleiman Abu Sharkh have contributed immensely to my project by giving helpful comments and supports throughout the PhD programme. I am also particularly indebted to my most sincere and dearest friends in Southampton's lab, Dr Ignacio Sires (Universitat de Barcelona), Dr. Eduardo Terrazas (Universitat de Guanajuato), Miss Vianey Hernandez (Universitat de Guanajuato) and Mr. Ruslim Mohd Mohammad (Universiti Malaysia Pahang), for their patient and fabulous help/ teaching on fundamental electrochemical techniques and inspirational discussions for the key issues to obtain battery discharge in this project. Many thanks particularly go to Ignacio for his professional advice on the fabrication of the three-dimensional electrodes, analyzing the reaction kinetics and the structures of several research papers which have been submitted to science journals. From him, I have attempted to learn and write in 'nacho' style (characterized by his detailed and professional description

with no mistake all the time) for this thesis and all my scientific papers. Apart from the people in Southampton, I am also grateful for the insight discussion and the warm support from Dr Len Berlouis and my friend, Mr. George Nikiforidis (University of Strathclyde), which have been very useful for me to develop and improve my flow battery system.

In regards to the zinc corrosion chapter, I need to acknowledge the training skills and the insight comments provided by Professor Pilar Herrasti (Universidad Autonoma de Madrid), Dr Javier Recio (Universidad Autonoma de Madrid) and Mr Derek Egan. It is also important to acknowledge the time and training skill provided by Drs Mark Light and Xiaohong Li for the assistance of using the X-ray diffraction experiment. In the zinc electrodeposition chapter, I am graceful for the training skill and assistance of using the scanning electron microscopy provided by Miss Chao Ma and Dr Shuncai Wang. Also, I need to thank Mr ShaoPang Wang for further training of the scanning electron microscopy. My sincere thanks also go to the tools and flow battery manufactured by Mr James Chitty, Mr Chris Williams, Mr Rob Dalley and other colleagues in the mechanical workshop. I gratefully acknowledge the glass blowing skills provided by Mr Lee Mulholland and Mr Pezemyslaw Tryc for the glassware used throughout this programme. It is also worthwhile to mention Dr C.T. John Low, who modified the first draft of my cerium chapter, designed the ‘divided’ flow cell based on my design, assisted me superficially in the early parts of this work.

In these three years, surely the most unpleasant time of my life, I gratefully acknowledge and always remember for the time spent with Dr Carlos Ponce-de-León, Dr Ignacio Sires (Universitat de Barcelona), Dr Eduardo Terrazas (Universitat de Guanajuato), Miss Vianey Hernandez (Universitat de Guanajuato) and Mr Ruslim Mohd Mohammad (Universiti Malaysia Pahang) in the electrochemical laboratory, and my truest or dearest friends in Portsmouth and Southampton. I also especially thank my previous personal tutors

and project supervisors, Professors Yi-Feng Yang and Kai Luo for their teaching during my first degree study.

Finally, I am grateful for all the GOD's blessings to me, especially for rescuing me from the edge of failing this PhD and all sorts of sabotages. Several papers have been accepted by peer-reviewed journals therefore, it is important for me to thank the journal reviewers for their valuable suggestions. Through this PhD, it became important for me to learn that the ability to get this thesis done was not because of my own intelligence but also the mercy of GOD.
In GOD, I said all the truest word from the deepest part of my heart.

Contents

Contents

Table Contents

Figure Contents

List of symbol

Symbol	Meaning	Units
A	Electrode area	m^2
B	Proportionality constant obtained from β_c, and β_a	
c	Metal concentration in the electrolyte	mol cm^{-3}
$c_{(0)}$	Initial cerium ion concentration	mol dm^{-3}
$c_{(t)}$	Cerium ion concentration at time t	mol dm^{-3}
c_0	Cerium concentration in the bulk solution	mol cm^{-3}
D	Diffusion coefficient	cm^2 s^{-1}
$E^{\ominus}$	Standard electrode potential	V *vs.* SHE
E_{Ce}	Potential of positive electrode	V *vs.* Ag|AgCl
E_{cell}	Cell voltage	V
E_{cor}	Corrosion potential	V
E_{IR}	Voltage drop across the membrane and electrolyte	V
E_S	Specific electrochemical energy consumption	W h g^{-1}
E_{Zn}	Potential of negative electrode	V *vs.* Ag|AgCl
F	Faraday's constant	Dimensionless
$H_{2\ inhibitor}$	Volume of hydrogen evolution with the additions of corrosion inhibitor	cm^3
$H_{2\ without\ inhibitor}$	Volume of hydrogen evolution without the additions of corrosion inhibitor	cm^3
I	Current	A
j	Current density	mA cm^{-2}
j_{cor}	Corrosion current density	mA cm^{-2}
j_{lim}	Limiting current density	A cm^{-2}
j_p	peak current density	A cm^{-2}
k	Apparent first order first order rate constant	s^{-1}
k_m	Mass transport coefficient	m s^{-1}
$m_{experimental}$	Mass of the reactant obtained	g
$m_{theoretical}$	Theoretical mass of reactant calculated according to Faraday's Laws	g
P	Inhibitive efficiency	%

R	Ohmic resistance	Ω
R_p	Polarization resistance	Ω cm^{-2}
t	Electrolysis time	s
V	Volume of electrolyte within the reactor	dm^3
v	kinematic viscosity of the electrolyte	cm^2 s^{-1}
v	potential sweep rate	mV s^{-1}
z	Number of electrons involved in the electrode reaction	Dimensionless
β_a	Anodic Tafel gradients	mV decade^{-1}
β_c	Cathodic Tafel gradients	mV decade^{-1}
δ_N	Diffusion layer thickness	cm
η	Overpotetnials	V
η	Overpotetnials	V
Φ	Current efficiency	Dimensionless
ω	rotation rate of the disk	radians s^{-1}

Chapter 1
Introduction and research objectives

Chapter 1 Introduction and research objectives

1. Introduction

Large and medium scale energy storage technologies can be combined with conventional power generation sources such as fossil fuels and hydro-electricity [1, 2]. Insufficient energy storage can lead to problems, such as raised market volatility and increased burden on electricity distribution systems [3]. Since the 1970s, a number of redox flow batteries for energy storage, such as iron-chromium [4, 5], all vanadium [6-9], zinc-bromine [10], polysulfide-bromine [11, 12] and soluble lead acid [13] batteries have been proposed. A typical application of redox flow batteries is load-levelling, which consists on storing energy during off-peak hours from a power plant and release it when the demand rises [3]. This technology is often used with other renewable energy sources, such as photovoltaic cells [14-16] and wind turbines [15, 16]. Due to the rapid growth of renewable energy and more advanced power generating sources, increasing attention has been given to the development of a more advanced, reliable and safer redox flow batteries for energy storage.

1.1. Properties of redox flow cells

In a redox flow battery, soluble redox couples in the electrolyte are used to store energy during battery charge and release energy during discharge. In a typical cell, positive and negative electrodes are separated by an ion exchange membrane. The membrane allows ion exchange and helps to prevent the mixing of the two electrolytes, which are stored in separate tanks and re-circulated through the battery by the pumps during operation as shown in Figure 1.1a. As in a proton exchange membrane fuel cell (PEMFC), an ion exchange membrane is necessary for flow battery operation but there are membranless (undivided) systems currently at the early stages of development [17-20] (Figure 1.1b).

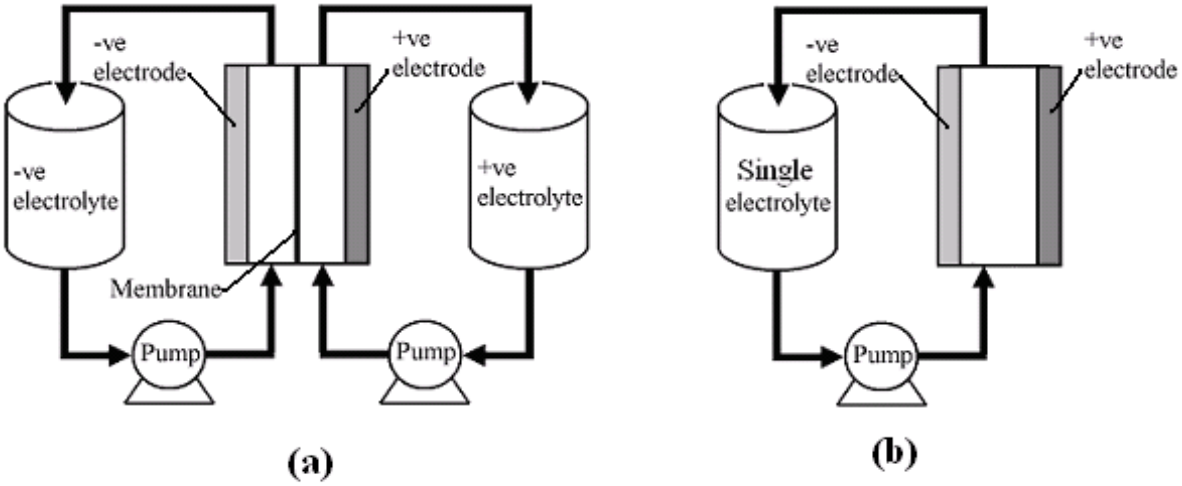

Figure1.1. Schematic of (a) divided and (b) a membraneless redox flow battery.

In practice, a flow battery is not just operating as an unit cell, there are a number of cells in a stack. In order to reduce weight, volume and cost, bipolar plates are often used in which only two external electrical contacts to the two end electrodes, while monopolar configuration requires electrical contact to each electrode. An example of a redox flow battery stack with four cells using bipolar electrodes is shown in Figure 1.2.

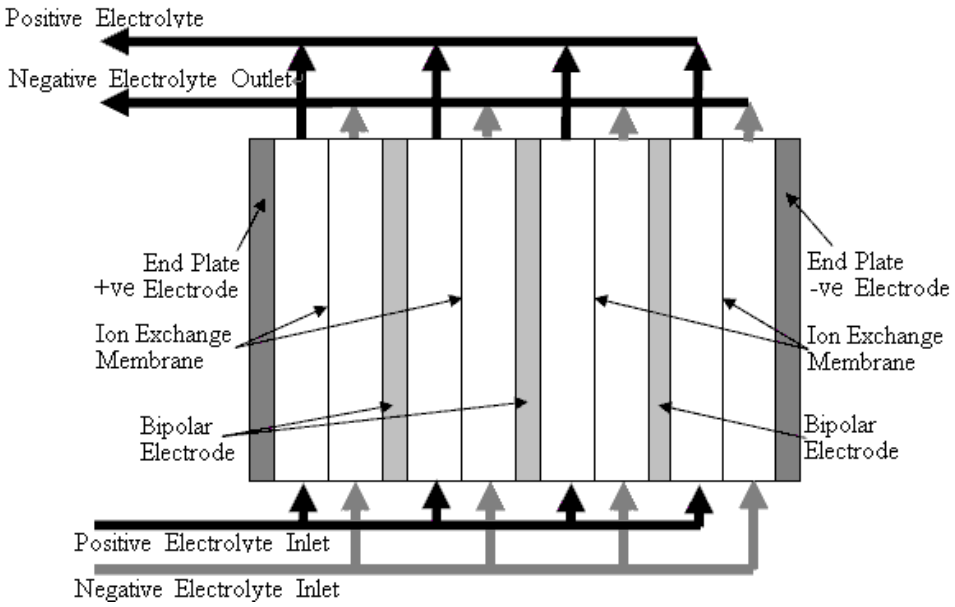

Figure 1.2. A stack design of a four cell stack with bipolar arrangement [14]

Unlike other electrochemical energy storage systems, such as conventional batteries, flow batteries store energy in the form of reduced and oxidized electroactive species in the electrolyte, while conventional static batteries store energy within the electrode structure. The chemical reactions involved in a flow battery should be reversible during charge and discharge. As a result, the electrolyte of the flow cell should always remain within the system, while in a fuel cell the reactants stored externally to the cell and are consumed to release energy. Table 1 shows the differences between static batteries, redox flow cells and fuel cells [6, 7, 14, 28].

Electrochemical Device	**Site of Reactants/products**	**Electrolyte Conditions**	**Separator**
Static battery	Active electrode material	Static and held within cell	Microporous Polymer Separator
Redox flow Battery	Aqueous electrolytes in reservoirs	Electrolyte recirculates through the cell	Ion exchange membrane (Cationic/ anionic) or not necessary
Fuel cell	Gaseous or liquid fuel (anode) plus air (cathode)	Solid polymer or ceramic acts as solid electrolyte within cell	Ion exchange membrane polymer or ceramic

Table 1. Comparisons between conventional static battery, redox flow battery and fuel cell. [29]

By comparing the conventional lead acid batteries which have been widely used for transportation, redox flow batteries have great advantages in cost, performance, mobility and flexibility. Due to the pre-fabricated modular design and long-life performance, the construction and maintenance of redox flow batteries would be the lowest among all other energy storage systems and the mobility and power output be

enhanced. In some cases, flow batteries can also be discharged completely, without any damage to the electrode or the electrolyte.

The power and energy capacity of redox flow cells can be varied easily; hence flexibility of energy storage is enhanced. Scale-up can be easily achieved by increasing the electrode size or by adding more electrodes in each stack in either monopolar or bipolar connection, Power can be just simply determined by the numbers of cell in the stack and the size of electrodes. The concentration and volume of the electrolyte determine the energy storage capacity.

1.2. The zinc-cerium redox system

The first zinc-cerium system was developed by Plurion Inc. (UK) in the 2000s [21, 22]. Both zinc and cerium are advantageous materials for energy storage due to their high standard electrode potential values in aqueous media, as shown in Figure 1.3. This results in the zinc-cerium system having a high open-circuit cell voltage of *c.a.* 2.43 V and thus a large energy density. Such a large potential difference implies challenges, such as material selection and secondary reactions, for example, gaseous evolution of hydrogen (0 V *vs.* SHE) and oxygen (1.23 V *vs.* SHE) depending on the overpotential at the electrode surface.

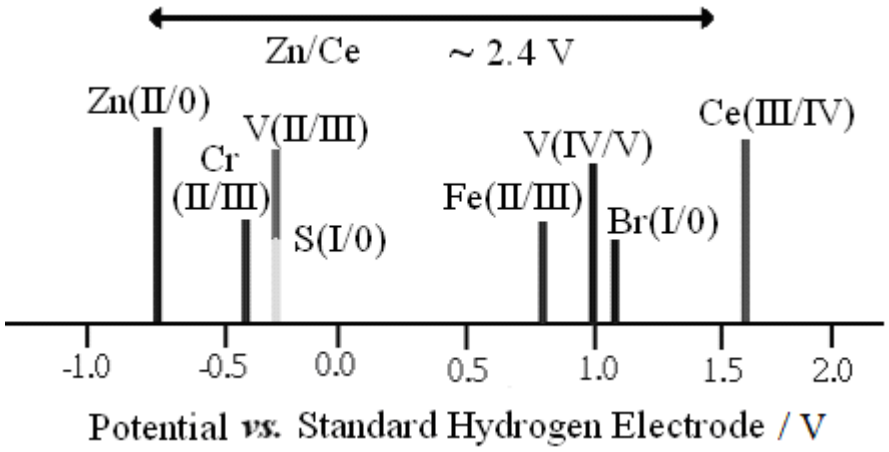

Figure 1.3. Half-cell potentials of various redox couples.

The main electrode reactions are as follows [23]: at the negative electrode, the primary reaction is the electrodeposition and dissolution of zinc:

$$Zn(CH_3SO_3)_2 + 2\,H^+ + 2e^- \underset{\text{Discharge}}{\overset{\text{Charge}}{\rightleftharpoons}} Zn + 2\,CH_3SO_3H \qquad E^{\ominus} = -0.76\ \text{V } \textit{vs.}\ \text{SHE} \qquad (1)$$

During battery charge, hydrogen evolution can also take place on this electrode as the secondary reaction:

$$2\,H^+ + 2e^- \xrightarrow{\text{Charge}} H_2 \qquad E^{\ominus} = 0\ \text{V } \textit{vs.}\ \text{SHE} \qquad (2)$$

At the positive electrode, the primary reaction is the oxidation process of Ce(III) and the reduction of Ce(IV) during charge and discharge, respectively. The positive standard electrode potential of this reaction lies within in the range between + 1.28 and + 1.72 V *vs.* Ag|AgCl depending on the background electrolytes. Assuming that the standard electrode potential of cerium reaction in methanesulfonate medium is similar to that in nitrate medium [24]

$$2\,Ce(CH_3SO_3)_3 + 2\,CH_3SO_3H \underset{\text{Discharge}}{\overset{\text{Charge}}{\rightleftharpoons}} 2\,Ce(CH_3SO_3)_4 + 2\,H^+ + 2e^- \qquad E^{\ominus} = +1.67\ \textit{vs.}\ \text{SHE} \qquad (3)$$

(Nitrate medium)

During charge, oxygen evolution is a secondary reaction on this electrode:

$$H_2O \xrightarrow{\text{Charge}} 0.5\,O_2 + 2H^+ + 2e^- \qquad E^{\ominus} = +1.23\ \text{V } \textit{vs.}\ \text{SHE} \qquad (4)$$

The overall cell reaction of the zinc-cerium redox flow battery:

$$Zn(CH_3SO_3)_2 + 2\,Ce(CH_3SO_3)_3 \underset{\text{Discharge}}{\overset{\text{Charge}}{\rightleftharpoons}} Zn + 2\,Ce(CH_3SO_3)_4 \qquad E_{CELL} \approx +2.4\,V \qquad (5)$$

[22]

Methanesulfonic acid is used as a solvent for both zinc and cerium ions, due to its comparable conductivity to that of hydrochloric acid and its lower corrosivity compared with other mineral acids, such as sulphuric acid. Cerium in methanesulfonic acid has the advantage of easy preparation and high solubility. The solubility limits of Ce(III) and Ce(IV) ions in methanesulfonic acid can be as high as 1 mol dm^{-3} compared to less than 0.5 mol dm^{-3} in sulphuric acid [23]. The solubility of zinc is also high (2.16 mol dm^{-3}) in this acid [25].

The concept of using zinc and cerium as the redox couples in energy storage application is not entirely new. Zinc is a common electrode option for modern energy storage systems. Previous studies involving zinc or cerium redox couples in flow batteries include zinc-chlorine [26-28], zinc-bromine [10, 29], zinc-ferricyanide [30], zinc-air [31], vanadium-cerium [32] and the zinc-cerium system of Plurion Inc. [21, 22]. Although previous work by Plurion Inc. has been described in several patents [21, 22], information on the experimental conditions and discharge performance are limited. Moreover, only few papers in the literature describe the electrochemical reactions of zinc and cerium in aqueous methanesulfonic acid [23]. An improved understanding of the flow battery performance under various operating conditions and electrolyte compositions are crucial.

1.3. Project objectives

The objective of this work is to describe the development of a zinc-cerium redox flow battery from its fundamental chemistry. Major challenges include material selection, solubility and chemical side reactions, such as the evolution of hydrogen and oxygen. The main objective is to develop an understanding of the electrochemisty of each half-cell reaction using a methanesulfonic acid bath as supporting electrolyte. The electrochemical study includes the electrodeposition and dissolution of zinc and the oxidation and reduction of cerium. Variables include the metal ion concentration, the acid concentration, the controlled flow conditions, electrolyte temperatures and the applied current density and voltage. The aim of this work is to determine the optimum conditions and the limiting factors of each half-cell reaction as well as for the redox flow battery. Different choices of electrolytic additives and electrode materials were also investigated. System efficiencies and life-cycle of a zinc-cerium redox flow battery were evaluated.

1.4. Thesis outline

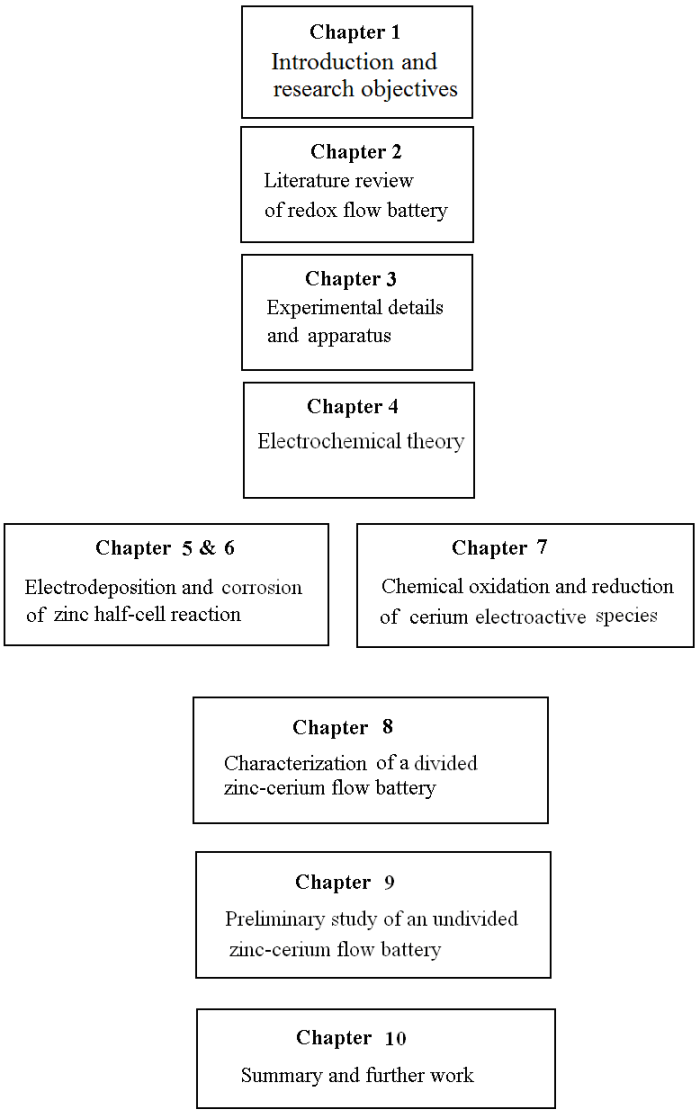

Figure 1.4. Thesis outline.

This thesis is organised into nine chapters. The first chapter gives an overview of the electrochemical principles used in flow battery technology, the zinc-cerium redox couple and the objectives of this project. Chapter 2 provides a comprehensive description on the background and recent development including applications of redox flow battery technology. Chapter 3 – 4 describes the electrochemical theory and the experimental

set-up as well as the procedures of the main experiments. Chapter 5 – 6 investigate the electrochemical behaviour of zinc half-cell reactions including electrodeposition and the corrosion study of zinc in aqueous methanesulfonate solution under various operating conditions. Chapter 7 studies the chemical oxidation and reduction of the cerium redox couple in two- and three-dimensional platinised titanium electrodes. The half-cell studies of zinc negative and cerium positive electrodes are useful in defining the suitable operating parameters and the electrolyte compositions. Chapter 8 focuses on the battery performance of a combined system of zinc-cerium couples, which include the characterization and the life-cycle of a redox flow battery. With the findings in chapter 8, a membraneless zinc-cerium redox flow battery has been proposed in chapter 9. At the end of this thesis, chapter 10 gives the summary of this project and suggestions for further work.

1.5. Research novelty

This work describes the development of a zinc-cerium redox flow battery from its fundamental chemistry to a novel membraneless system. The electrochemistry of zinc in methanesulfonic acid is a completely novel study, as no detailed information has been provided by previous papers in the literature. Although there are a few electrochemical studies of cerium reaction in methanesulfonic acid, the novelty of this work focus on increasing cerium ion concentration and the reversibility of this redox couple. Thus, the information of the cerium redox couple in methanesulfonic acid is enhanced.

Since there are limited details of experimental conditions and no charge-discharge performance is given by the previous patents, this work provides the first charge-discharge performance and characterization of a zinc-cerium redox flow battery at

various electrolyte compositions and operating conditions. The novelty of using carbon felt as a positive electrode in a zinc-cerium redox flow battery, shows a superior performance and is less expensive than the platinum based electrode. The high reversibility of the positive reaction using carbon felt was found to have a promising prospect for future battery applications. With the use of carbon felt, an undivided, membraneless system was proposed and was able to operate at room temperature with a high energy efficiency (76 %).

1.6. References

1. The Electricity Advisory Committee. Bottling Electricity: Storage as a Strategic Tool for Managing Variability and Capacity Concerns in the Modern grid - A report by The Electricity Advisory Committee, December 2008. http://www.oe.energy.gov/DocumentsandMedia/final-energy-storage_12-16-08.pdf accessed on 1 September 2010.
2. N. Tokuda, T. Kanno, T. Hara, T. Shigematsu, Y. Tsutsui, A. Ikeuchi, T. Itou, T. Kumamoto, SEI Tech. Rev. 50 (1998) 88-94.
3. J. Makansi, J. Abboud, Energy Storage Council White Paper (2002).
4. M. Yoshitake, M. Takabatake, O. Hamamoto, T. Hiramatu, S. Kondo, J. Proc. Electrochem. Soc. 266 (1988) 88-11.
5. M. Shimizu, M.S. N. Mori, Japan Patent - 63128560, 01/07/1988, (1988).
6. M. Skyllas-Kazacos, M. Rychcik, P.G. Robins, A.G. Fane, M.A. Green, J. Electrochem. Soc. 133 (1986) 1057-1058.
7. M. Rychcik, M. Skyllas-Kazacos, J. Power Sources 19 (1987) 45-54.
8. M. Skyllas-Kazacos, F. Grossmith, J. Electrochem. Soc. 134 (1987) 2950-2953.
9. M. Rychcik, M. Skyllas-Kazacos, J. Power Sources 22 (1988) 59-67.
10. R.F. Koontz, R.D. Lucero, Handbook of Batteries, Vol. 39, 39.1-39.22.
11. F.C. Walsh, J. Pure Appl. Chem. 73 (2001) 1819-1837.
12. DTI, Regenesys Utility Scale Energy Storage, Project Summary Pub URN 04/1048. http://www.dti.gov.uk/energy/renewables/publications/pubs_distributedgeneration.shtml accessed on 1 September 2010.
13. D. Pletcher, R. Wills, J. Power Sources 149 (2005) 96-102.

14. I. Tsuda, K. Kurokawa, K. Nozaki, Photovoltaic Energy Conversion, 1994., Conference Record of the Twenty Fourth IEEE Photovoltaic Specialists Conference - 1994, 1994 IEEE First World Conference 1 (1994) 946-949.
15. L. Joerissen, J. Garche, C. Fabjan, G. Tomazic, J. Power Sources 127 (2004) 98-104.
16. K.L. Huang, X.G. Lia, S.Q. Liu, N. Tan, L.Q. Chen, Renewable Energy 33 (2008) 186-192.
17. J.Q. Pan, Y.Z. Sun, J. Cheng, Y.H. Wen, Y.S. Yang, P.Y. Wan, Electrochem. Comm. 10 (2008) 1226-1229.
18. A. Hazza, D. Pletcher, R. Wills, J. Phys. Chem. Chem. Phys. 6 (2004) 1773 - 1778.
19. Y. Xu, Y.H. Wen, J. Cheng, G.P. Cao, Y.S. Yang, Electrochem. Comm. 11 (2009) 1422-1424.
20. P.K. Leung, C. Ponce de León, F.C. Walsh, Electrochemistry Communications (2011) Accepted.
21. R.L. Clarke, B.J. Dougherty, S. Harrison, P.J. Millington, S. Mohanta, US 2004/ 0202925 A1, (2004).
22. R.L. Clarke, B.J. Dougherty, S. Harrison, J.P. Millington, S. Mohanta, US 2006/0063065 A1, (2005).
23. R.P. Kreh, R.M. Spotnitz, J.T. Lundquist, J. Org. Chem. *54* (1989) 1526-1531.
24. J. Bard, L.R. Faulkner, Electrochemical Methods-Fundamentals and Applications, 2nd ed. Wiley, (2001).
25. M.D. Gernon, M. Wu, T. Buszta, P. Janney, Green Chem. 1 (1999) 127-140.
26. T.R. Crompton, Battery Reference Book, 3 ed. Elsevier Science & Technology Books, Boston : Newnes, Oxford, England, Vol. Chapter 14 (2000).
27. P.C. Symons, J. Electrochem. Soc. International Conference on electrolytes for power sources, Brighton (1973).
28. P.C. Butler, P.A. Eidler, P.G. Grimes, S.E. Klassen, R.C. Miles, Zinc bromine batteries, Handbook of batteries, 3rd ed. McGraw Hill, Vol. 39 (2001).
29. P.C. Butler, D.W. Miller, A.E. Verardo, 17th Intersoc. Energy Conversion Eng. Conf., Los Angeles (1982).
30. L.W. Hruska, R.F. Savinell, J. Electrochem. Soc. 128 (1981) 18-25.
31. Y.H. Wen, J. Cheng, S.Q. Ning, Y.S. Yang, J. Power Sources 188 (2009) 301-307.
32. B. Fang, S. Iwasa, Y. Wei, T. Arai, M. Kumagai, Electrochim. Acta 47 (2002) 3971-3976.

Chapter 2
Development and applications of redox flow batteries

Chapter 2 The development and applications of redox flow batteries

2.1. The development of redox flow batteries

Redox flow batteries were introduced in the 1970s. Early developments were carried out by the National Aeronautics and Space Administration (NASA), Energy Development Associates (EDA), Exxon Corp and Gould Ltd (USA). The first redox flow battery was the iron-chromium system developed by Thaller [10] in 1974. NASA early studies include redox couples such as: Fe(II) / Fe(III), Ti/ TiO(II), Cr(II)/ Cr(III), V(II)/ V(III), $Fe(O_3)^{3-}$/ $Fe(O)_3^{4-}$, V(IV)/ V(V), Br^-/ Br^{3-} and $Cu(NH_3)$ (II)/ $Cu(NH_3)_4$(II). The main focus of NASA was large-scale energy storage applications [11], while EDA and Exxon Corp. focused on zinc-halogen systems using acidic electrolytes, zinc-chlorine and zinc-bromine batteries, to compete with sealed lead acid battery for vehicle power system [12] and for large-scale energy storage [13], respectively. Zinc-ferricyanide is another early proposed system based on alkaline electrolyte developed by Adams [14] of Lockheed Missiles and Space Co. (USA) in 1979. Although the self-discharge of zinc electrode and hydrogen evolution are less significant due to the alkaline medium, this system has not been studied extensively in the past decades.

The iron-chromium redox flow battery was the most studied system in the 1970—1980s. This was built up to the kW scale in the United States. and Japan. The iron-chromium system suffers from many technical problems, such as cross contamination, poor reversibility of the chromium redox reactions and a high degree of hydrogen evolution on charge. Despite this, large scale iron chromium flow battery is currently under development by Deeya Energy (USA). Evaluation of V(II)/V(III) and V(IV)/V(V) redox couples were carried out by NASA in 1977. However, these couples were reported to have less reversibility than Fe(II)/Fe(III) in acidic chloride electrolytes

[11]. In 1978, the possibility of using V(IV)/V(V) redox couples in a redox flow battery has been mentioned in the patent of Pellegri and Spaziante [15]. During 1980 to 1985, Kummer and Oei [16, 17]of Ford Motor Company (USA) have demonstrated the use of V(II)/V(III), Mo(III)/Mo(IV) and $SiW_{12}O_{40}^{5-}$/S $W_{12}O_{40}^{4-}$ as the negative electrode reactions with V(IV)/V(V) positive electrode reaction. In 1985, the first halogen-polysulfide system was introduced in a patent of Remick and Ang [18]. Since 1985, successful demonstration and significant developments of all-vanadium redox flow battery has been attributed to Skyllas-Kazacos *et al.* [19-22] at University of New South Wales, Australia.

In 1986, the primary patent of all-vanadium redox flow battery (expired in 2006) was filled by Skyllas-Kazacos *et al.* [23] with Unisearch Ltd. (University of New South Wales) as the applicant, which was later sold to Pinnacle Ltd. (Australia) in 1998. The technology of all-vanadium redox flow battery has also been licensed to Sumitomo Electric Industries Ltd. (Japan) in 1992, while Pinnacle Ltd. was acquired by Vanteck Ltd. (Canada) and became VRB Power System Inc. (Canada) in 2002. In 2005, the vanadium flow battery technology and intellectual properties of Sumitomo Electric Industries were further acquired by VRB Power System Inc, which was sold to JD holdings Inc. (China) and renamed as Prudent Energy (China) in 2009.

Since 1993, all-vanadium redox flow batteries have been commercialized for various applications, such as load-levelling, power quality control and renewable coupling [24]. More than 20 large-scale plants have been installed globally by manufacturers, such as VRB Power System Inc., Sumitomo Electric Industries Ltd., Mitsubishi Chemicals and Pinnacle VRB [24]. The development of all-vanadium redox flow battery has been assisted by tremendous improvements in electrode [20, 21, 25] and

membrane [26, 27] materials. In order to have higher cell potential and energy density, vanadium-cerium [28] and vanadium-polyhalide [29] system were introduced in 2002 and 2008, respectively. In 2011, Li *et al.* [30] of Pacific Northwest National Laboratory, United States, reported that improved stability and solubility (2.5 mol dm^{-3}) of all vanadium active species at wider range of temperature (− 5 — 50 ^{o}C) were observed with the sulphate-chloride mixed electrolytes.

In Japan, a long term development of the zinc-bromine redox flow battery has been carried out under the Moonlight Project during the 1980s. In the 1980s, Exxon's patent of zinc-bromine flow battery was transferred to Johnson Control Inc. (USA) and licensed to Studiengesellschaft für Energiespeicher and Antriebssysteme, SEA (Austria), Toyota Motor (Japan), Meidensha (Japan) and Sherwood Industries (Australia). The technology of Johnson Control Inc. was further acquired by ZBB Energy (USA) in 1994. In the United States, zinc-bromine has been investigated by ZBB Energy, the Department of Energy (D.O.E.) and Sandia National Laboratories [31]. In 1990, a 1 MW/ 4 MW h zinc-bromine redox flow battery was installed at the Imajuku substation, Fukuoka, Japan [31].

During the 1990s, multi-MW bromine polysulfide systems have been developed by Innogy plc (Regenesys®) (UK) [24]. In the early 2000s, the construction of two 15 MW/ 120 MW h demonstration plants started. These were cancelled later however due to insufficient funding from the parent company Innogy plc, RWE AG. In 2004, Regenesys was taken over by VRB Power Systems Inc. [32], which was subsequently acquired by Prudent Energy (China) in 2009.

After 2004, several undivided flow batteries, such as soluble lead-acid [6], zinc-nickel [33], copper-lead dioxide [5], cadmium-chloranil [7], and zinc-cerium [8], have been

developed. These batteries can utilize a single electrolyte and do not require an ion-exchange membrane. They have advantages of lower costs and greater simplicity than typical flow battery systems [34]. Among these systems, some were reported to have excellent round-trip DC energy efficiency (regardless of energy loss by pump and temperature controlling devices) and cycle life of more than 80 % and 1000 cycles, respectively [33]. Since 2010, two types of lithium flow batteries storing energy on flowable electrode materials (patented by A123 Systems (USA))[35, 36] and aqueous positive electrolyte [37, 38] have been introduced. These batteries were reported to have discharge cell voltage up to 3.8 V and energy density per electrolyte volume as high as 397 Wh dm^{-3}, which are attractive for the application of electric vehicles.

Since the previous literature reviews [9, 39, 40] mainly focused on the early development [39], battery characteristics, including charge-discharge performance and experimental conditions, of the typical flow battery systems [9] and all-vanadium redox flow battery [40], this paper provides an updated review of the overall development and applications of the redox flow battery technology in the past 40 years (as summarized in Figure 2.1).

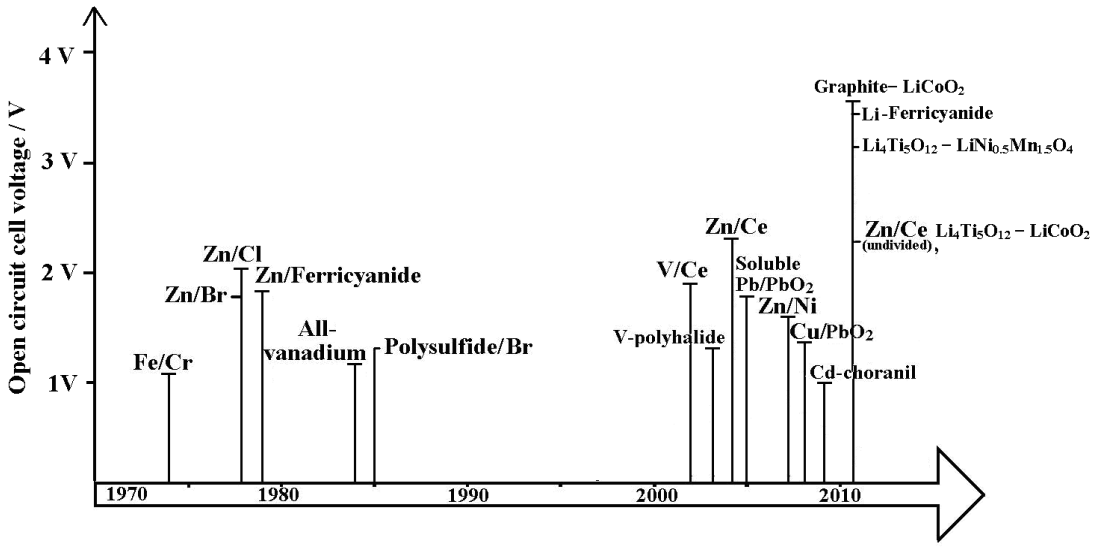

Figure 2.1 Schematic of (a) divided and (b) a membraneless redox flow battery.

2.2 Types of redox flow battery

Table 2.1 summarises the open circuit cell voltages and the electrochemical reactions of the main redox flow battery systems. A redox flow battery is a rechargeable battery that allows energy to be stored in the form of reduced and oxidized species. Therefore, energy capacity can be easily varied by changing the electrolyte concentration and volume. Due to different forms of chemical reactions, redox flow batteries can store energy in either a) electrolyte or b) electrode or c) both (hybrid) as shown in Figure 2.2.

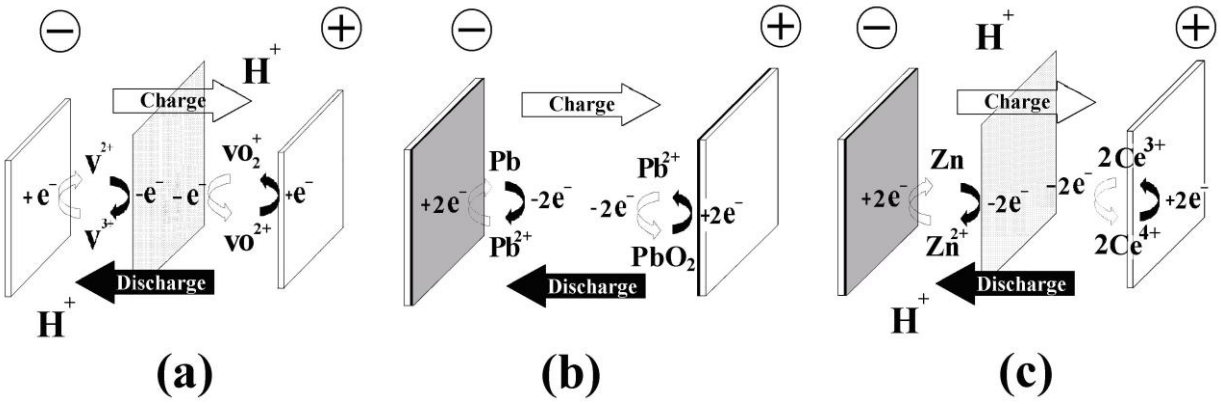

Figure 2.2 Types of redox flow batteries. Energy stored (a) in the electrolyte, (b) in the electrode plate and (c) hybrid (combined).

Electrochemical reactions of flow battery	**E *vs.* SHE / V**	**E_{cell} / V**	**Ref.**
Energy stored in electrolytes			
Iron-chromium couple			
Positive electrode $Fe^{2+} - e^- \underset{Discharge}{\overset{Charge}{\rightleftharpoons}} Fe^{3+}$	+0.77	1.18	[203,
Negative electrode $Cr^{3+} + e^- \underset{Discharge}{\overset{Charge}{\rightleftharpoons}} Cr^{2+}$	–0.41		204]
All uranium couple			
Positive electrode $UO_2^+ - e^- \underset{Discharge}{\overset{Charge}{\rightleftharpoons}} UO_2^{2+} UO_2^+$	+0.06	0.67	[59]
Negative electrode $U^{4+} + e^- \underset{Discharge}{\overset{Charge}{\rightleftharpoons}} U^{3+}$	–0.607		
All-vanadium couple			
Positive electrode $VO^{2+} + H_2O - e^- \underset{Discharge}{\overset{Charge}{\rightleftharpoons}} VO_2^+ + 2H^+$	+1.00	1.26	[107]
Negative electrode $V^{3+} + e^- \underset{Discharge}{\overset{Charge}{\rightleftharpoons}} V^{2+}$	–0.26		
Vanadium-cerium couple			
Positive electrode $2Ce^{3+} - 2e^- \underset{Discharge}{\overset{Charge}{\rightleftharpoons}} 2Ce^{4+}$	+1.61	1.87	[28]
Negative electrode $V^{3+} + e^- \underset{Discharge}{\overset{Charge}{\rightleftharpoons}} V^{2+}$	–0.26		
Vanadium-bromine couple			
Positive electrode $2Br^- + Cl^- - 2e^- \underset{Discharge}{\overset{Charge}{\rightleftharpoons}} ClBr_2^-$	NA	1.30	[50]
Negative electrode $VBr_3 + 2e^- \underset{Discharge}{\overset{Charge}{\rightleftharpoons}} VBr_2 + Br^-$	NA		
Bromine-polysulfide couple			
Positive electrode $3Br^- - 2e^- \underset{Discharge}{\overset{Charge}{\rightleftharpoons}} Br_3^-$	+1.09	1.36	[9][143]
Negative electrode $S_4^{2-} + 2e^- \underset{Discharge}{\overset{Charge}{\rightleftharpoons}} 2S_2^{2-}$	–0.27		
Hybrid flow batteries			
Zinc-bromine couple			
Positive electrode $2Br_3 - 2e^- \underset{Discharge}{\overset{Charge}{\rightleftharpoons}} 2Br_3^-$	+1.09	1.85	[143]
Negative electrode $Zn^{2+} + 2e^- \underset{Discharge}{\overset{Charge}{\rightleftharpoons}} Zn$	–0.76		
Zinc-cerium couple			
Positive electrode $2Ce^{3+} - 2e^- \underset{Discharge}{\overset{Charge}{\rightleftharpoons}} 2Ce^{4+}$	+1.44	2.20	[81, 82]
Negative electrode $Zn^{2+} + 2e^- \underset{Discharge}{\overset{Charge}{\rightleftharpoons}} Zn$	–0.76		
Cadmium– chloranil couple			
Positive electrode $QCl_4 + 2H^+ - 2e^- \underset{discharge}{\overset{charge}{\rightleftharpoons}} QH_2Cl_4$	+0.402	1.112	[7]
Negative electrode $Cd^{2+} + 2e^- \underset{discharge}{\overset{charge}{\rightleftharpoons}} Cd$	–0.71		
Energy stored in electrodes			
Zinc-nickel couple			
Positive electrode $2Ni(OH)_2 + 2OH^- - 2e^- \underset{Discharge}{\overset{Charge}{\rightleftharpoons}} 2NiOOH + 2H_2O$	+0.49	1.71	[81, 82]
Negative electrode $Zn(OH)_4^{2-} + 2e^- \underset{Discharge}{\overset{Charge}{\rightleftharpoons}} Zn + 4OH^-$	–1.22		
Soluble Lead-lead dioxide couple			
Positive electrode $Pb^{2+} + 2H_2O - 2e^- \underset{Discharge}{\overset{Charge}{\rightleftharpoons}} PbO_2 + 4H^+$	+1.49	1.62	[5]
Negative electrode $Pb^{2+} + 2e^- \underset{Discharge}{\overset{Charge}{\rightleftharpoons}} Pb$	–0.13		
Copper-lead dioxide couple			
Positive electrode $PbSO_4 + 2H_2O - 2e^- \underset{Discharge}{\overset{Charge}{\rightleftharpoons}} PbO_2 + 4H^+ + SO_4^-$	+1.69	1.35	[34]
Negative electrode $Cu^{2+} + 2e^- \underset{Discharge}{\overset{Charge}{\rightleftharpoons}} Cu$	+0.34		

Table 2.1 Electrochemical reactions of the main redox flow battery systems studied (*NA= Not available).

2.2.1. Chemical energy stored in the electrolyte

Liquid-phase redox flow batteries store and discharge energy in the soluble electroactive species through reduction and oxidation processes. Operating parameters of previous research on the liquid-phase systems are summarised in Table 2.2. Since energy is stored in the electrolyte, the energy storage capacity can be increased unlimitedly by using larger volume of electrolytes. As early as 1973, NASA Lewis Research Center investigated the feasibility of various possible couples, including Fe(II)/ Fe(III), Cr(II)/Cr(III) and Ti(II)/ Ti(III). In the 1970s, the most studied liquid-phased systems were iron-chromium and iron-titanium, these systems were not highly reversible on metallic electrodes. Porous three-dimensional electrodes, such as graphite felt, graphite cloth, graphite foam, reticulated vitreous carbon, carbon chips, silver screen and other metal screens etc., have been introduced by NASA [11].

Since iron-titanium has a relatively low open-circuit cell voltage and has the problem of TiO_2 passivation, iron-chromium redox flow battery was the most studied system in the early developments. Although no catalyst is required for the iron half-cell reaction, the reduction of chromium is slow on most electrode surfaces. This system suffers from cross-contamination of electrolytes and hydrogen evolution [41]. Recently, liquid electroactive species, such as Fe(III)/Fe(II) [42, 43], Ce(IV)/Ce(III) [44], Cr(III)/ Cr(II) and Cr(V)/ Cr(III) [45] were reported to have higher reaction rate constants by complexing with triethanolamine (TEA), diethylenetriaminepentaacetate (DPTA) and ethylenediaminetetra-acetate (EDTA) ligands, respectively. This enhances the possibility of some couple combinations in flow batteries, such as all chromium, vanadium-cerium and iron-bromine systems.

Systems	Electrode material	Negative electrolyte	Positive electrolyte	Back-ground Electro-lyte	Membrane	Charge voltage (app. Value)	Discharge Voltage	Current Density (mA cm^{-2})	Temp.	Round-trip DC Energy eff.	Ref.
Energy stored in electrolytes											
Cr-EDTA/ Cr-EDTA	Graphite felt & rod	0.05 M Cr(III)-EDTA	0.1 M Cr(III)-EDTA	1 M Sodium Acetate	Cation-ex Nafion® 450	1.4 V (H-cell)	NA	0.57 mA cm^{-2} (H-cell)	NA	NA	[45, 46]
Fe- Cr	Negative: carbon fibre Positive: Carbon felt + catalyst	1M $CrCl_3$	1M $FeCl_2$	2 M HCl	Cation-ex Nafion® 117	1.05 V	1.03 V	21.5 mA cm^{-2}	25 °C	NA	[203, 204]
Fe-TEA/ Br_2	graphite felts	2 M NaBr	0.2- 0.5 Fe(III)-TEA + 0.4 M NaCl	NaBr / NaOH	Cation-ex Nafion® 117	2.0 V	1.7 V	20 mA cm^{-2}	Room temp.	70 %	[42]
Fe-Ti	97% tungsten-3% rhenium electrodes	1 M Ti (III)/ Ti (II)	1 M Fe (III)/ Fe (II)	4 M HCl	Anion-ex membrane	NA	0.22 V	NA	NA	NA	[11]
Fe- Co	Platinum or graphite	Co (III)/ Co(II)-o-phenanthroline and related ligands	Fe (III)/ Fe (II)-o-phenanthroline and related ligands	H_2SO_4	NA	NA	NA	NA	NA	NA	[205] [206]
Fe- V	Graphite foam	1 M V(II)/ V(III)	1 M Fe (III)/ Fe (II)	1 M H_2SO_4	Anion-ex membrane	NA	0.26 V	NA	NA	NA	[11]
All-vanadium	Thick felt-heat bonded graphite impregnated polyethylene plate	2 M V(II)/ V(III)	2 M V(IV)/ V(V)	2M H_2SO_4	Cation-ex polystyrene sulphonic acid membrane	1.47 V	1.30 V	30 mA cm^{-2}	35 °C	83%	[107]
Vanadium chloride-polyhalide	Graphite felts compressed	1M VCl_3	1 M NaBr	1.5 M HCl	Cation-ex Nafion® 112 membrane	1.2 V	0.98 V	20 mA cm^{-2}	NA	66.4%	[50]
V-Ce	Carbon fibres	0.5 M V (III)/ V (II)	0.5 M Ce(III) /Ce(IV)	1 M H_2SO_4	Vycor glass membrane (Asahi Glass Co. Ltd.)	1.83 V	1.51 V	22 mA cm^{-2}	40 °C	67.8 %	[28]
V- Mn	Spectral pure graphite	0.3 M V (III)/ V (II)	0.3 M Mn(II) /M(III)	5 M H_2SO_4	Cation-ex Nafion® 117	1.83 V	1.66 V	20 mA cm^{-2}	Ambient temp.	62.7%	[29]
Br-Poly-sulfide	Negative: Nickel foam Positive: Polyacrylonitrile (PAN)-based carbon felt	1.3 M Na_2S_4	4 M NaBr	1 M NaOH	Cation-ex Nafion® 117	1.75 V	1.38 V	40 mA cm-2	26 °C	77.2 %	[143]
All-uranium	Glassy carbon	1 M U(III)/ U(IV)-acetylacetone	1 M U (V)/ U (VI) - acetylacetone	Aprotic solvents	NA	1.04 V (Est.)	1.04 V (Est.)	70 mA cm^{-2}	NA	98% (Est.)	[59]
Cr(V/IV/III/ II/I)-$(acac)_3$ (non-aqueous)	Graphite electrodes	0.05 M $Cr(acac)_3$	0.05 M $Cr(acac)_3$	0.5 M $TEABF_4$ + CH_3CN	Anion-ex Neosepta AHA	4.15 V	2.1 V – 1.2 V	Charge: 1 mA / $7cm^2$ Discharge: 1 mA / $7cm^2$	Room temp.	21 – 22 %	[67]

Table 2.2 The operating parameters of redox flow battey research using soluble electroactive species (* NA = Not available).

In 1985, an all-chromium redox system were proposed by Doria *et al.* [46]. Since the kinetics of the chromium reactions are very slow in chloride and sulphate media [47], the development of all-chromium flow battery was abandoned. In 1985, the all-vanadium redox flow battery began development by Skyllas-Kazacos *et al.* at the University of New South Wales [48]. This system does not have significant gas evolution and the cross-mixing of electrolytes across the membrane does not lead to any electrolyte contamination. Due to its high round-trip DC energy efficiency (> 80%) [49], this system has been used in various industrial applications and has been studied continuously. Accompany with the development of all-vanadium flow batteries, tremendous improvements in electrode and membrane materials for redox flow batteries have been achieved.

The major drawback of all-vanadium flow battery is its relatively low specific energy of 25 — 35 W h kg^{-1} (both electrolytes) and the self-discharge of vanadium ions, which limits its use in applications, such as electric vehicles. A vanadium-polyhalide flow battery has been proposed by Skyllas-Kazacos [50] in 2003 to increase its energy density up to 50 W h kg^{-1} [51]. This system uses VCl_2/VCl_3 and Br^- $Cl^-/ClBr_2^-$ as the electroactive species in the negative and positive half-cells respectively. Recently, Li *et al.* [30] reported that improved solubility (2.5 mol dm^{-3}) and stability of all vanadium species at wide temperature range (− 5 — 50 ^oC) were observed in the sulphate-chloride mixed electrolytes. Skyllas-Kazacos and Milne [52] have also proposed a low-cost titanium polyhalide system, which uses an electrolyte of $TiCl_4$ in HBr/HCl background electrolyte for both positive and negative electrolyte compartments. The open circuit cell voltage and coulombic efficiency were reported to be 0.9 V and *c.a.* 97 — 98 % but low voltage efficiency (~ 30 %) were observed associated with the large ohmic losses. Since the cost

of titanium is much lower than that of vanadium electrolyte, there are still possibilities for large scale operation if further improvement has been achieved.

In order to achieve higher cell voltage, Mn(II)/ Mn(III) [29] and Ce(III)/ Ce(IV) [28] have been used as the positive electroactive species in vanadium redox flow batteries. According to Fang *et al.* [28], vanadium-cerium flow battery has advantages of high coulombic efficiency (87%), high cell voltage (1.87 V) and low self-discharge rate, but the low solubility of cerium sulfate was the main technical issue of this system. Despite this, Kreh *et al.* [53] have reported that a high concentration of cerium ions can be achieved in methanesulfonic acid. In such media, the electrochemistry of cerium redox reactions has been recently studied [54]. Due to the low cathodic current density recorded in the cyclic voltammetry, a high surface area electrode, such as three-dimensional platinised titanium mesh and carbon felt, was reported to be crucial for the positive cerium reaction at reasonable current density [55].

Bromine-polysulphide is another prominent flow battery system, which has been scaled up by the former Rengenesys® Technologies company, Innogy plc. in the 1990s. Due to its low cost and high energy density, number of large-scaled bromine- polysulphide batteries have been installed [56]. In the 2000s, Shiokawa *et al.* of Tohoku University, Japan, reported that the two redox couples of uranium [57-59] and neptunium [60-62] have remarkable similarities with all-vanadium redox couples. In the positive electrolyte, both redox couples of vanadium and neptunium are in the form of VO^{2+}/VO_2^{+} and NpO_2^{+}/NpO_2^{2+}, respectively, while negative electrolytes contain metal ions of V^{2+}/V^{3+} and Np^{3+}/Np^{4+}, respectively. By complexing with acetylacetonate in aprotic solvents, higher

solubility can be obtained. A large amount of such elements can be collected from the nuclear power industry and can be used in flow battery for load-levelling application in a safe and radiation shield environment [62]. Although excellent round-trip DC energy efficiency (up to 99%) has been estimated by kinetics mathematical models, discharge performance of a real system is still not available [59].

In most chemistry, aqueous electrolytes are used in most of the redox flow battery systems. Due to the water content in the aqueous electrolyte, the operating temperature is limited to < 100 ^{o}C. The possibility of using organic non-aqueous electrolytes in redox flow battery have been recently evaluated as in theory they were believed to have wider potential window, larger temperature range and higher power density than their aqueous counterparts. As early as 1988, Matsuda *et al.* [63] have shown an open circuit cell voltage of 2.6 V with the use of the ruthenium complex, tris(2,2'-bipyridine) ruthenium(II) tetrafluoroborate, while ruthenium acetylacetonate [64, 65], uranium beta-diketonates [57], vanadium acetylacetone [66] and chromium acetrylacetonate [67] have been recently investigated. At this point in time, the round-trip DC energy efficiency of such chemistries were still too low (< 20 %) and much more development are needed before further practical application.

2.2.2. Chemical energy stored on the electrode plates

Energy can be stored as electrodeposits at the negative and positive electrodes and released by dissolving such electrodeposits during discharge. Several flow battery systems of this type have been developed (Table 2.3). In most of the systems proposed, a single electrolyte is circulated through the cell and no ion-exchange membrane is required, hence

the cost and the design complexity can be reduced significantly. The chemicals used in these systems are generally low cost. These features make them attractive for energy storage on a large scale [68].

Energy stored in electrodes									
Systems	**Electrode materials**	**Electrolyte**	**Background Electrolyte**	**Charge Voltage**	**Discharge Voltage**	**Current Density**	**Temp.**	**Round-trip DC Energy eff.**	**Ref.**
Pb- PbO_2	Negative: Reticulated nickel foam, Positive: Scraped reticulated vitreous carbon	1.5 M $Pb(CH_3SO_3)_2$	0.9 M CH_3SO_3H	2.07 V	1.45 V	20 mA cm^{-2}	25 ^oC	65 %	[6] [34]
Cu- PbO_2	Negative: High purity graphite, Positive: 98% lead dioxide, 1.2% graphite fiber	1 M $CuSO_4$	1.9 M H_2SO_4	1.45 V	1.29 V	20.8 mA cm^{-2}	Room temp.	83%	[5]
Zn-Ni	Negative: Cadmium plated copper, Positive: Sintered nickel hydroxide electrode	1 M ZnO	10 M KOH	1.85 V	1.72 V	10 mA cm^{-2}	Room temp.	86%	[33, 75]
Zn- MnO_2	Negative: Granular zinc, Positive: 30 wt % Manganese(IV) oxide	2 M KOH		NA	1.05 – 1.2 V	NA (through 550 Ω)	Room temp.	NA	[76]

Table 2.3. The operating parameters of undivided flow batteries storing energy on the electrodes (*NA= Not available).

A soluble lead-acid flow battery has been developed by Pletcher *et al*. [6, 34, 69-72] and has several advantages over the traditional lead acid battery. In the traditional lead acid battery, storage capacity is limited by the amount of paste material forming in the

electrode. Since methanesulfonic acid was used as the supporting electrolyte in the novel system, lead ions can be made soluble at high concentration (2.6 mol dm^{-3} [73]) and electrodeposition of lead and lead dioxide on the two electrodes are realized. Due to these characteristics, storage capacity in theory is just limited by the electrodeposit thickness and can be increased easily by using higher lead ion concentration and larger electrolyte volumes using the flow battery concept. Despite this, storage capacity in the real system is restricted mostly by the dendritic growth at the negative electrode, especially under prolonged charge or at high current density. Therefore, electrolytic additives for dendrite suppression have been evaluated and used [71]. The inefficiency of this system was attributed to the large overpotential at the lead dioxide electrode [6], which is higher than those of the liquid-phase positive reactions, such as V(IV)/V(V) [74] and Ce(III)/Ce(IV) [55], at large surface area electrodes. Since both lead and lead dioxide are electrodeposited on the electrode surface, mass transport did not have any significant effect on battery discharge as reported in the early investigation [69].

In order to avoid the dendritic issues as in the soluble lead-acid flow battery, a single flow Cu–H_2SO_4–PbO_2 battery was proposed by Pan *et al.* [5] in 2008, which used copper and lead dioxide pastes as the negative and positive electrode, respectively. This system was reported to have round-trip DC energy efficiency of up to 83 % compared to 65 % of the soluble lead acid system at *c.a.* 20 mA cm^{-2}. The drawback of using copper instead of lead as the negative electrode is the lower open circuit cell voltage (1.35 V). Since lead dioxide-lead sulphate paste is an electroactive material for discharge and has been ‘as-prepared’ at the positive electrode, lower overpotential and mass transport are therefore required compared to the electrodeposition approach used in the soluble lead acid system. Although up to 450 cycles have been obtained in this system, the actual

reversibility has not been reflected due to the 'as-prepared' lead dioxide-lead sulphate electroactive material in the positive electrode. Since the positive electrode reaction does not involve any electrodeposition, storage capacity is dependent on the electrode size but not on the electrolyte volume [5].

The zinc-nickel single flow battery was recently proposed by Li *et al.* [33, 75] in 2007. This system was developed from the fundamentals of the traditional zinc-nickel secondary battery and uses two layers of sintered nickel hydroxide with capacity of 25 mA h cm^{-2} each as the positive electroactive material. High concentration of zincate solution in potassium hydroxide was used as the supporting electrolyte. During battery charge, zinc is electrodeposited from the zincate ions and $Ni(OH)_2$ is oxidized to NiOOH at the negative and positive electrodes, respectively. The reverse process occurs when the battery discharges. Compared to the other two single-flow systems mentioned in this section, zinc-nickel system is reported to have a high round-trip DC energy efficiency of 88% at 10 mA cm^{-2} and 1000 cycles had been achieved. In terms of cost and performance, this system seems to be promising for load levelling and other large scale applications. Similar to the copper-lead dioxide system mentioned earlier, the storage capacity is also limited by the positive electrode size. Despite this, both copper-lead dioxide and zinc-nickel systems were able to discharge at more than 10 mA cm^{-2} for two hours with a capacity of > 20 mA h cm^{-2}.

More recently, a single flow zinc-manganese dioxide flow battery has been demonstrated by Sawyer *et al.* [76] using a flow-through packed-bed electrode design rather than the conventional 'flow-by' design (electrolyte flowing parallel to the

electrode). With this specific set-up, an ion-exchange resin is used as the ‘separator’ material and the distance between the two electrodes can be increased to avoid the short circuit induced by the dendritic growth at the negative electrode. The discharge cell voltage of this system was reported to be *c.a.* 1.2 V varying with the separator materials and the distances between the two electrodes.

2.2.3. Hybrid redox flow batteries

Unlike the aforementioned redox flow battery, hybrid flow battery stores energy as a form of electrodeposits and soluble electroactive species in its negative and positive electrode, respectively. Operating parameters of some hybrid systems are summarized in Table 2.4. Zinc is a typical negative electrode that has been used extensively in the batteries due to its large negative electrode potential in both acidic (− 0.76 V *vs.* SHE) and alkaline (− 1.22 V *vs.* SHE) aqueous media. Due to the negative electrode potential of zinc and the highly reversible ferro/ferricyanide couple in an alkaline medium, a zinc-ferricyanide redox flow battery was introduced by Adams [14] in 1979. The experimental open-circuit cell voltage was reported to be 1.86 V, which is higher than the theoretical value of calculated using thermodynamic principles. Although this system has the advantages of low self-discharge and hydrogen evolution rate, this system has not been studied extensively in the previous decades compared to their zinc-halogen counterparts.

Systems	Electrode materials	Negative electrolyte	Positive electrolyte	Back-ground Electrolyte	Membrane	Charge Voltage	Discharge Voltage	Current density	Temp.	Round-trip DC Energy eff.	Ref.
Hybrid batteries											
Zn-ferri-cyanide	Negative: Silver-plated iron Positive: Porous nickel	ZnO	$K_3Fe(CN)_6$ / $Na_3Fe(CN)_6$	5 – 7 M KOH/ NaOH	Nafion XR 475	2 V	1.5 V	20 mA cm^{-2} (charge) 35 mA cm^{-2} (discharge)	38 ºC	74 %	[14]
Zn-Cl	Negative: Dense graphite electrode Positive:Porous flow-through electrode	2 M $ZnCl_2$	2 M $ZnCl_2$	4 M KCl	Kynar separator	2.30 V	1.80 V	22 mA cm^{-2}	25 ºC	66%	[207]
Zn-Br	Carbon electrodes	$ZnBr_2$ in excess of Br_2	$ZnBr_2$ in excess of Br_2	$ZnBr_2$ in oil	Cation-ex Nafion® 125	1.92 V	1.64 V	15 mA cm^{-2}	25 ºC	> 80 %	[186]
Zn-Ce (Plurion)	Negative: Carbon Positive: Platinised Titanium	0.6 M $Ce(CH_3SO_3)_3$ + 1.3 M $Zn(CH_3SO_3)_2$	0.72 M $Ce(CH_3SO_3)_3$ + 0.9 M $Zn(CH_3SO_3)_2$	CH_3SO_3H	Cation-ex Nafion®	2.75 V –3.15 V	1.8 V (Const. discharge voltage)	50 – 100 mA cm^{-2} (charge) 5 –50 mA cm^{-2} (discharge)	60 ºC	NA	[9, 81, 82]
Zn-Ce (Un-Divided)	Negative: Carbon plastic Positive: Carbon felt	1.5 M $Zn(CH_3SO_3)_2$ + 0.2 M $Ce(CH_3SO_3)_3$		0.5 M CH_3SO_3H	Membran-less	2.5 V	2.1 V	20 mA cm^{-2}	23 ºC	75 %	[8]
Cd-chloranil	Negative: Copper foil Positive: 90 % w,t, chloranil film mixed with carbon black	0.5 M $CdSO_4$ + 1.5 M $(NH_4)_2SO_4$		0.5 M H_2SO_4	Membran-less	1.18 V	0.97 V	10 mA cm^{-2}	Room temp.	82 %	[7]
Pb-Tiron	Negative: solid lead Positive: Carbon felt	0.25 M Tiron	Pb^{2+}	3 M H_2SO_4	Cation-ex Nafion® 115	1.1 V	0.9 V	10 mA cm^{-2}	Room temp.	82 %	[87]

Table 2.4. The operating parameters of various hybrid flow battery systems (*NA = Not available).

Zinc-halogen redox flow batteries, including zinc-chlorine [77, 78] and zinc-bromine [13], were also introduced in 1970s. These systems have advantages in cell voltage, energy density and cost. Although the solubility of zinc bromine us up to 10 mol dm^{-3} of $ZnBr_2$, the actual solubility is practically lower than 5 mol dm^{-3} due to the quaternary ammonium complexes [79]. In addition, dendritic growth of the zinc electrode often does not allow a thick electrodeposit, which further limits the real energy density. In the early development, zinc-chlorine system was studied to compete with the conventional lead-acid batteries as a vehicle power system [12], while zinc-bromine redox flow batteries are now commercially available for load-levelling and other large scale applications [31, 80]. Due to the evolution of chlorine and bromine during charge, special reactor designs and electrolyte compositions are needed to dissolve the halogen gases, resulting in a more complicated system.

Zinc-cerium redox flow battery was introduced by Plurion Inc. (UK) in the 2000s [24, 81, 82]. This system has a high open circuit cell voltage of *c.a.* 2.4 V and has been claimed to be able to discharge at 400－500 mA cm^{-2}. Methanesulfonic acid is used as the supporting electrolyte, which is less corrosive than sulphuric acid and allows cerium ions to dissolve at higher concentration (> 1 mol dm^{-3} [53]). Recent work in the literature suggests that methanesulfonic acid can reduce the zinc dendritic growth significantly [83-85], which use to limit the cycle lives of the zinc-halogen systems [9]. Despite this, the experimental conditions and the charge-discharge performance provided by Plurion Inc.'s patents are very limited. Some investigations on the half-cell reactions and the characteristics of this system have been carried out [54, 55, 85, 86].

In the recent work (2011), an undivided zinc-cerium flow battery using a single

electrolyte at low acid concentration was proposed with the use of carbon felt positive electrode and a mixed electrolyte of both zinc and cerium electroactive species. In contrast to 50 — 60 ^{o}C reported in the earlier systems, the membraneless battery was reported to cycle at room temperature with an average round-trip DC energy efficiency of 75 %. Despite this, the cerium(III) concentration was limited to 0.2 mol dm^{-3} as higher acid concentration is necessary to dissolve more Ce(IV) species but leads to poor coulombic efficiency at the zinc negative electrode due to the hydrogen evolution. In order to achieve larger storage capacity, further investigations are important in an attempt to increase the solubility of cerium species by using mixed acid electrolyte to facilitate zinc electrodeposition at a highly acidic medium. The long term stability of carbon felt electrode in Ce(IV) species still need further investigations.

Another hybrid system requiring no membrane was also proposed recently by Xu *et al.* [7] using cadmium as the negative electrode due to its large hydrogen overpotential,. Within the positive electrode, a film of organic chloranil (90 % w.t.) was used as the positive electroactive material. In theory, such material can be synthesized from abundant sources [7]. Despite this, storage capacity is still limited by the solid phase chloranil material in the positive electrode. An aqueous organic species, tiron, was recently studied in a divided flow battery with lead negative reaction [87]. Similar to the cadmium-chloranil system, round-trip DC energy efficiency was relatively high (82 %) but low discharge cell voltage (< 1 V) was obtained at 10 mA cm^{-2}. The feasibility of using aqueous organic species for flow battery application is currently studied by General Electric (USA) under support of the Department of Energy, USA.

Different from the above mentioned system, all-iron redox flow battery has been proposed by Hruska and Savinell [88] in 1981. This system uses Fe(II)/Fe(0) and Fe(II)/Fe(III) as the negative and positive reactions, respectively. Instead of using acidic electrolyte, ammonium chloride was used as the supporting electrolyte. Due to its low energy density and poor round-trip DC energy efficiency (50%), this system has received little attention in the later years [88].

2.3 Design considerations and components of flow batteries

2.3.1 *Constructional materials*

A typical unit cell of a flow battery stack is illustrated in Figure 2.3, which is composed of a positive and a negative electrode with an ion exchange membrane separating them. Rubber gasket seal and steel tie-bolts were used to compress the stack and to avoid leakage. Metallic end-plates, such as aluminium and copper, were used as current conductors to provide electrical conductivity [96]. Turbulence promoters can be employed in the compartment to enhance the mass transport and the exchange of electroactive species [97].

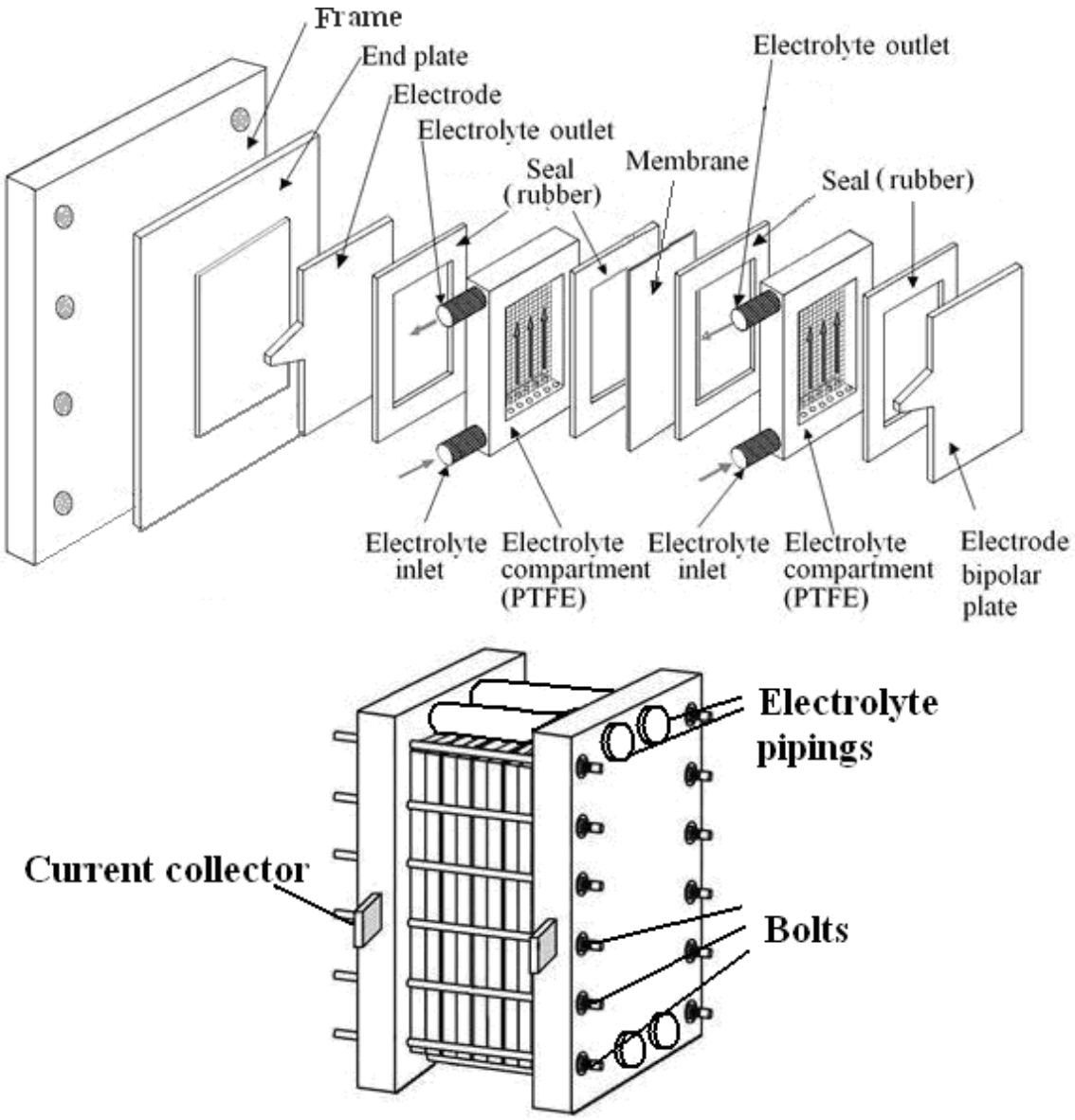

Figure 2.3 Components of a flow battery and a cell stack [97].

Since electrolytes used in redox flow batteries are often highly oxidizing, no metallic component should be in contact with the electrolytes. Chemically resistant polymers, such as polytetrafluoroethylene (PTFE), ethylene-polypropylene-diene (EPDM), polyvinylchloride (PVC), polyvinylidene (PVDF) and acrylics (Perspex®) are the typical materials for producing the battery components (excluding the metallic end-plate and the electrode). By connecting a number of unit cells in series in a bipolar

configuration to form a battery stack, a large cell voltage can be obtained. Easily folded rubber tanks can effectively utilize the available space, such as underground cisterns in the building [2].

2.3.2 *Electrode materials*

An ideal electrode material should provide a high electrical conductivity, good mechanical properties, a strong chemical resistance, be reasonable of cost and have a long cycle life in highly oxidizing media. Typical electrodes used in redox flow batteries are made of carbon-based or inert metallic materials. Carbon-based electrodes are more common than their metallic counterparts, as they do not undergo dissolution or formation of oxide during chemical oxidation. Metal ions of the metallic electrodes can dissolve into the electrolyte during discharge and corrosion, which could lead to unstable redox potentials and disturb the chemistry of the redox flow batteries. Metallic electrodes are generally based on noble metals, which have good electrochemical stability or catalytic property. Some other metallic electrode materials with high overpotentials for gaseous evolutions have been used to facilitate the desired reactions and avoid side reactions. Electrode materials used in various redox flow batteries are summarized in Table 2.5.

Material	Manufacturer	Flow type	Thickness	Electrode polarity	Flow battery system	Ref.
Carbon based electrodes						
Carbon polymer Binders: PVA, PVDF, HDPE	Engtegris Inc., USA [55]	Flow-by	6 mm (substrate)	− ve	Zinc-cerium	[55, 86]
Carbon felt GFA-type	SGL Group, Germany	Flow by	8 mm	+ ve	Zinc-cerium	[55]
Graphite felt	Le Carbonne, France	Flow-by	NA	+ ve & − ve	All-vanadium	[21]
PAN-based Graphite felt	XinXing Carbon Corp. China	Flow-by	5 mm	+ ve	Bromine-polysulfide	[103]
Cobalt coated PAN-based Graphite felt	XinXing Carbon Co. Ltd., China	Flow-by	5 mm	− ve	Bromine-polysulfide	[103]
70 ppi Reticulated Vitreous carbon	ERG Material and Aerospace Corp., USA	Flow-by	1.5 mm	+ ve	Soluble lead acid	[34]
Graphite felt bonded electrode assembly with nonconducting plastic substrate	FMI Graphite, USA	Flow-by	NA	+ ve & − ve	All-vanadium	[25]
Porous graphite	Union Carbide Corp., USA	Flow-through	2 mm	+ ve & − ve	Zinc-chlorine	[207]
Carbon felt CH type	Fiber Materials Inc., USA	Flow through	2.8 mm	+ ve & − ve	Zinc-bromine	[99]
Cylindrical bed of carbon particles	Sutcliffe Speakman Carbons Ltd, UK	Flow through	2.5 mm	+ ve & − ve	Bromine-polysulfide	[118]
Metallic electrodes						
Nickel foam	LuRun Material Co. Ltd., China	Flow-by	2.5 mm	− ve	Bromine-polysulfide	[75, 89]
Cadmium-plated Copper	NA	Flow-by	NA	− ve	Zinc-nickel & Zinc-air	[143]
Sintered nickel hydroxide	NA	Flow-by	NA	− ve	Zinc-nickel	[33, 75]
40 ppi Nickel foam	NA	Flow-by	1.5 mm	+ ve	Soluble lead acid	[34]
Three-dimensional platinised-titanium mesh stack (4 meshes, 70 g Pt m^{-2} loading, 3.5 μm thick)	Magneto GmbH, Netherlands	Flow-by	4 × 2.5 mm	+ ve	Zinc-cerium	[55]

Table 2.5 Electrode materials used in redox flow batteries (*NA = Not available).

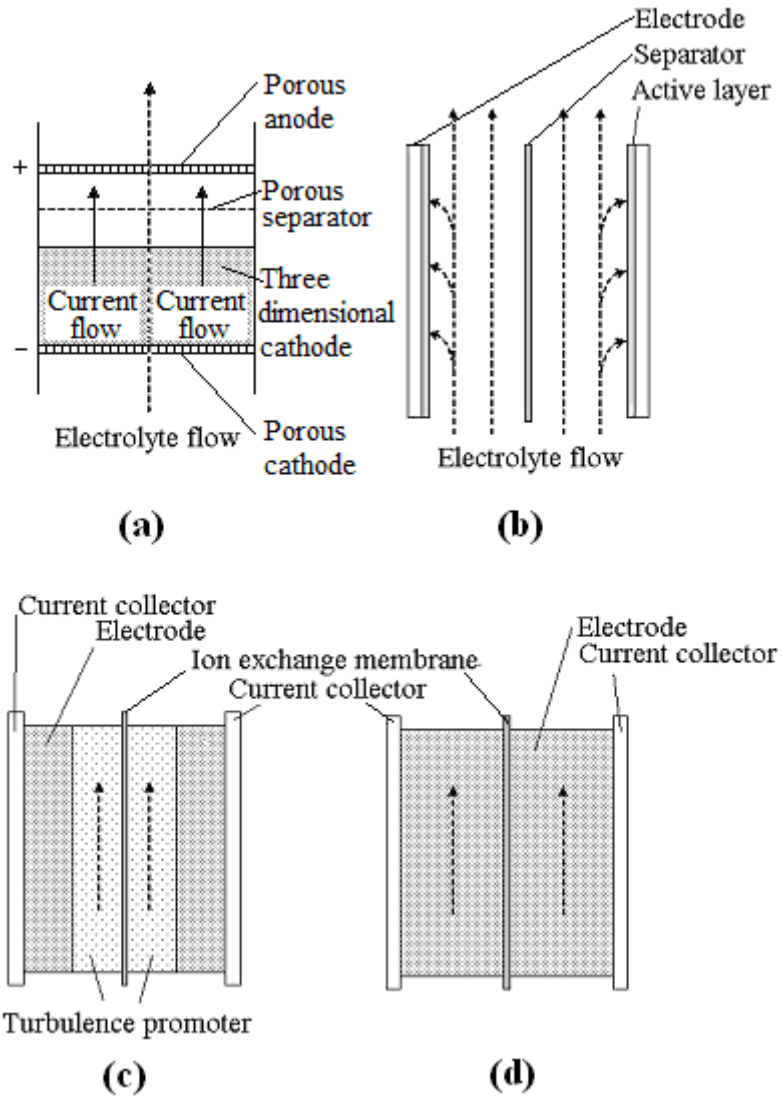

Figure 2.4 Schematics of (a) flow-through, (b) flow-by electrode, (c) two-dimensional and d) three-dimensional electrode configurations for redox flow battery [69 – 72].

Figures 2.4a and 2.4b show the two configurations for the electrolytes to flow through the electrode and to flow parallel to the electrode (flow-by configuration), respectively [98]. Although the flow-through configuration has a more uniform concentration of electroactive species and gives an enhanced mass transport [99], it is

often impractical due to the very low flow rate required [100] and the high scale-up cost [101, 102]. The flow bed depth of the flow-through configuration is limited by the potential drop occurred leading to non-uniform potential and current distribution. Therefore, most of the flow batteries in the literatures adapt the flow-by configuration. Within the flow-by configuration, electrodes are generally two or three-dimensional materials corresponding to different electrolyte flow modes as shown in Figures 2.4c and 4d [103]. Various three-dimensional electrodes have been used extensively in redox flow batteries due to their large surface area, results in faster electrochemical reactions and lower polarization at the electrodes.

2.3.2.1 *Carbon-based electrodes*

Carbon-based bipolar electrodes are the commonest materials used in redox flow batteries. In the past decades, various forms of carbon-based materials, including two- and three-dimensional electrodes have been studied. Typical two-dimensional carbon-based electrodes are carbon cloth [104], black carbon [105], activated carbon [69] and carbon-polymer composite [86]. Since pure carbon and graphite are brittle and often difficult to scale-up in stacks, composites of polymer binders and conductive particles, such as carbon polymer composites [106, 107] and polymer-impregnated graphite plates [108, 109] are often used, which have advantages in low cost, light weight and improved mechanical properties. Therefore, they have been used in various systems [110], such as zinc-bromine [111-114], all-vanadium [25], bromine-polysulfide [115], zinc-cerium [55, 86] and soluble lead acid [34, 96].

Carbon polymer composite material is held together by polymer binders, such as polyyvinylidene fluoride (PVDF), high-density polyethylene (HDPE) [86], polyvinyl acetate (PVA) [85, 96], polyvinyl-ester [8] and polyolefin [115] by injection moulding, which is a low-cost technique and has advantages in high volume processibility. Polymer-impregnated graphite plate is manufactured by compression moulding the expanded graphite with thermoplastic polymers. Since this moulding technique allows the use of a higher proportion of graphite than the injection moulding method, it has better electrical conductivity. Due to the thermoplastic polymer used in this technique, the mechanical properties, chemical resistance and thermal stability are superior to those produced by injection moulding. Since longer time is required to cool the mould before each half plate can be removed, the production cycle requires longer time (typically > 10 minutes). Therefore, the higher cost could hinder its use in redox flow battery for large-scale applications [116, 117]. Conductivity of the aforementioned composite materials can be provided by the addition of conductive filler material [25] or activated carbon particles [118, 119]. The high carbon content can lead to poor mechanical properties. Some investigations have reported that carbon black filler can cause undesirable reactions, such as gas evolutions and water decomposition, especially when the battery is overcharged. The oxidation of such carbon black-filler could also increase the electrical resistance [25].

Two-dimensional carbon electrodes were reported to be chemically unstable for the redox reactions of V(IV)/V(V) [20, 22, 120-122] and Ce(III)/Ce(IV) [28, 55, 123]. Since these reactions are highly positive and the local current density at the planar electrode surface can be very high, physical deterioration of the electrode surface can be observed. By mechanically compressing the carbon felt on the carbon-based current collector as the

positives electrodes, all-vanadium and the divided zinc-cerium systems are possible to operate at current density of > 50 mA cm^{-2} with more than 75 % voltage efficiencies [22, 55].

Due to the large specific area, typically 240 — 400 cm^2 cm^{-3} and 5 — 70 cm^2 cm^{-3} for the carbon felt [124] and reticulated vitreous carbon foam [125], respectively, three-dimensional carbon-based material has been used in various systems [103, 122, 126]. To date, polyarylonitrile (PAN) based carbon felt electrode is the commonest electrode material used in all-vanadium system. The PAN based graphite felt has advantages in wide potential range, good electrochemical activity, high chemical stability and low cost [122]. Novel modifications of graphite felt materials have been carried out [127-131]. For instance, the graphite felt can be modified by treating with sulphuric acid and heat treatment [121, 131]. During the acid treatment, surface functional group, such as –C=O and –COOH, were formed on the electrode surface, which was found to significantly increase the chemical activity in the highly acidic media.

Some researchers have further improved the catalytic property and the conductivity of the carbon felt by depositing metals on the electrode surface [132, 133]. For instance, Sun and Skyllas-Kazacos [133] have modified carbon felt electrodes through impregnation or ion-exchange with solutions containing ions, such as Pt^{4+}, Pd^{2+}, Te^{4+}, Mn^{2+}, In^{3+}, Au^{4+}, Ir^{3+}. In terms of electrocatalytic activity and stability, modified Ir^{3+} electrode was found to have the best performance to be used as the positive electrode in all-vanadium system, while large amount of hydrogen evolution was observed on those Pt, Pd and Au modified electrodes. In the other study, Fabjan *et al.* [134] reported that RuO_2 can improve the reaction rate and eliminate the side reactions of gaseous evolution.

Reticulated vitreous carbon electrodes have also been used in zinc-bromine [125] and soluble lead acid redox flow batteries [34]. The porosity of this material is beneficial to retain the solid complex of bromide during battery charge of a zinc-bromine system [135], while the rough surface of the scraped reticulated vitreous carbon in the soluble lead flow battery can allow adherent deposit to be formed within and supported by the compressed foam structure [34]. The use of nanostructured electrode materials in redox flow battery has also been introduced. Due to the excellent electrical conductivity and mechanical properties of carbon nanotube, Zhu *et al.* [136] suggested a graphite-carbon nanotube composite for all-vanadium redox flow battery. Despite the great advantages of carbon nanotubes, the sole use of carbon nanotube in vanadium reaction was found to give poor reversibility and activity compared to pure graphite. In order to benefit the advantages of both graphite and carbon nanotube, a composite of graphite with 5 wt. % CNT has been introduced and exhibited good reversibility and electrical conductivities. In the other work, grapheme oxide nanoplatelet electrode (GONP) was suggested for all-vanadium redox flow battery by Han *et al.* [137]. This material does not require tedious synthesis procedures and has good catalytic property for both V(II)/V(III) and V(IV)/V(V) redox reactions due to the functional groups of C–OH and COOH on the electrode surface. Polarization of the GONP can be further reduced after heat treatment at temperature of 120 ^{o}C.

2.3.2.2. *Metallic electrodes*

Metallic electrodes are less commonly used in redox flow batteries because of the corrosion and dissolution issues. Although precious metals, such as platinum and gold, have excellent chemical stability and electrical conductivity, the expensive cost makes

them impractical for large-scale energy storage. Moreover, precious metals do not necessarily have good electrochemical behaviour in some chemical reactions. For instance, vanadium reactions are not reversible at a gold electrode [22, 131] and platinum forms nonconductive oxide during the oxidation of cerium(III) [138]. Passivation can also occur at other metals, such as lead and titanium electrodes during vanadium(IV) oxidation [131]. However, some redox couples, including V(II)/V(III) [139] and V(IV)/V(V) [140], are more reversible at metallic electrodes than at carbon. For instance, redox reactions of Cr(II)/ Cr(III) and Ti(III)/TiO(II) are irreversible at carbon electrodes but showed better reversibility at amalgamated lead and tungsten-rhenium alloy, respectively [11]. Other reactions, such as $Fe(O)_3^{3-}$/ $Fe(O)_3^{4-}$ [11] and Ce(III)/Ce(IV) [54], are more reversible at a platinum electrode than at a carbon one. However, both V(IV)/V(V) [74] and Ce(III)/Ce(IV) [55] reactions were found to turn from irreversible at glassy carbon to reversible when carbon felts were used.

Due to the high cost of platinum, a dimensionally stable anode (DSA) has been used as the positive reactions in all-vanadium [20, 141, 142] and zinc-cerium flow batteries [54, 81]. In general, a DSA electrode is manufactured by coring a titanium substrate with a thin metal or alloy coating oxide selected from the group of Mn, Pt, Pd, Os, Rh, Ru and Ir. In the study of Rychcik and Skyllas-Kazacos [20], IrO_2 coated DSA electrode was reported to have good reversibility for the vanadium reactions. In order to discharge a zinc-cerium flow battery at higher current densities, such as 50 mA cm^{-2}, three-dimensional DSA mesh stack electrode by spot-welding three pieces of platinised titanium mesh, has been used due to the larger surface area than the two-dimensional one [54]. As shown in Figure 2.5, high surface area of such platinised titanium mesh stack and carbon felts allow high cerium positive half-cell potential at increased discharge

current densities, while a significant potential drop was observed with two-dimensional materials platinised titanium, graphite and carbon polymer positive electrode at current density larger than 25 mA cm^{-2}.

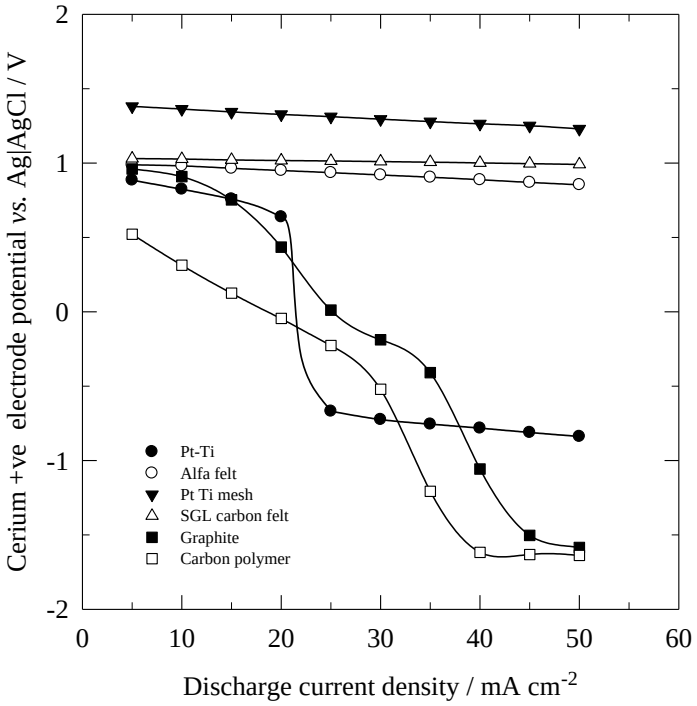

Figure 2.5 Effect of discharge current density on cerium positive electrode potentials of a zinc-cerium redox flow battery using different positive electrode materials. ● 2-d Pt-Ti, ○Alfa Aesar carbon felt, ▼ Pt-Ti mesh stack, Δ SGL carbon felt, ■ 2-d graphite and □ 3-d carbon polymer.

Apart from noble metals, some metals having a high overpotential for gaseous evolution have been used as the substrate electrodes in several flow batteries. The recent flow battery systems, such as zinc-nickel and zinc-air have used a high H_2-overpotential cadmium plated nickel sheet as the negative electrode to reduce the dendritic growth and to suppress hydrogen evolution effectively [75, 89]. Three-dimensional nickel foam is another metallic electrode, which has been used in bromine-polysulfide [143] and soluble

lead acid systems [34]. Like other three-dimensional materials, nickel foam provides a large surface area, hence further reduce the polarization. Zhao *et al*. [143] reported that this material is electrocatalytic active for both negative and positive reactions of a sodium polysulphide flow battery. The small pores (about 150 — 250 μm) of nickel foam electrodes can allow the electrolyte to flow smoothly within the electrode, which further improve the mass-transport at the reaction sites [144].

2.3.3. *Separators*

Ideal separator should prevent mixing and direct chemical reaction of active species or chemical products, such as electrodeposits, in the positive and negative electrolytes, which can result in losing energy. Hence, permeation of the active species and the selectivity of the charge-carrying ions are highly important [145]. Typical separators for redox flow battery are ion exchange membranes, which are produced from polymeric materials with pore diameter of 20 Å [146]. In aqueous electrolyte, ion-exchange are designed to conduct positively charged ion (cation, i.e. H^+) or negatively charged ion (anion, i.e. SO_4^{2-}) by mean of cation or anion exchange membrane, respectively. In the recent lithium-ferricyanide flow battery, solid electrolyte separator is used to conduct Li^+ ion and effectively prevent the aqueous positive electrolyte from reaching the negative electrode [37]. The ideal membrane for redox flow battery should be chemically resistant to aggressive species and pose low area resistivity to minimize the ohmic loss [147, 148]. Ion Exchange Capacity (IEC) is often used to measure the charge-carrying ions passing through the membrane. The conductivity of a membrane is determined by various factors, such as thickness, ionic group concentration, the degree of cross-linking, the size and valence of the counter ions [27].

According to Vafiadis and Kazacos [27], there is no direct correlation observed amongst IEC, resistivity, diffusivity and the membrane thickness for the vanadium electrolytes. Electrolyte concentration and ion exchange groups within the membrane can have great influence on water uptake and hence the degree of swelling. With higher degree of crosslinking, better selectivity was observed with less pronounced swelling or water transfer across the membrane [27]. Although the across of vanadium ions through the membrane was found to highly depend on the concentration difference between the positive and negative electrolytes [149], cation- and anion- exchange membranes tend to have net volumetric transfer towards the positive and negative compartment, respectively [150]. Compared to anion exchange membrane, its cation counterpart is more chemically stable [101] and exhibits higher conductivity and species permeability/ diffusivity. The lower resistivity of cation exchange membrane can be attributed to the higher mobility of H^+ ion, than that of anion, such as SO_4^{2-}. The cause of lower permeability of V(IV) ions across the anion exchange membranes can be mainly due to the Donnan exclusion effect [151], which is a electrostatic repulsion between the cation groups within the membrane and the electroactive species. The development of ion-exchange membranes for vanadium redox flow battery has been reviewed by Li *et al.* [152] in 2011.

2.3.3.1 *Commercially available membranes*

Typical commercial ion exchange membrane used in fuel cell, electrodialysis and other electrochemical applications are summarized in Table 2.6. Due to the high conductivity and good chemical stability in the oxidizing electrolyte, perfluorinated membranes are usually hydrocarbon backbone based tetrafluoroethylene co-polymers commonly used in redox flow batteries. Perfluorinated membrane has been commercially available as the following trademarks: Nafion® (DuPont, USA), Flemion® (Asahi Glass, Japan), Fumapem® (Fumatech, Germany), Aciplex® (Asahi Chemicals, Japan) and Dow® (Dow Chemical, USA) [153]. Compared to other hydrocarbon type cation exchange membranes, such as Selemion® CMV, DMV (Asahi Glass), Nafion® membrane has superior chemical resistance as these degrade in the vanadium electrolyte while Nafion® membrane does not [154-156]. Despite this, vanadium active species can permeate through the Nafion® membrane and decrease the coulombic efficiency. The diffusion coefficient of vanadium ions across the Nafion® membrane has been determined be in the order of $V^{2+} > VO^{2+} > VO_2^{+} > V^{3+}$ by Sun *et al.* [149].

Company	Product name	Cation / Anion	Thickness / mm	Water uptake / wt %	Dimensional swelling / wt %	% Elongation at break or burst strength / kg cm^{-2}	Tensile modulus / MPa	Tensile strength / MPa	Electrical resistance / Ω cm^{-2} or conductivity / mS cm^{-1}	Thermal stability / ^{o}C	Ref.
Dupont (USA)	Nafion® 115/ 117 / 1110	Cation	0.127/ 0.183/ 0.254	38 (at 100 ^{o}C)	~ 10 - 15	> 225 %	> 249	> 32	> 100 mS cm^{-1} (in water)	> 220	[208]
Asahi Glass (Japan)	Selemion® CMV / AMV	Cation / anion	0.11 - 0.15	NA	NA	2 - 5 kg cm^{-2}	NA	NA	2- 3.5 / 1.5 – 3 Ω cm^{-2} (at 0.5 M NaCl)	< 100	[209]
Asahi Kasei (Japan)	Aciplex® K101/ A101	Cation / anion	0.21 - 0.23	~ 24 - 38	NA	3 - 6 kg cm^{-2}	NA	NA	~ 1.8 - 4.1Ω cm^{-2} (at 0.5 M NaCl)	NA	[210]
Fumatech (Germany)	Fumapem® F-930/ F-1050	Cation	0.03/ 0.05	~ 30- 35	~ 15 - 18	> 200 - 230 %	> 180	> 22	> 90 mS cm^{-1} (in water)	270 - 300	[211]
Gore (USA)	Gore® select	Cation	0.02	32	NA	NA	NA	> 15 - 34	~ 50 S cm^{-1}	NA	
Dow Chemical (USA)	Dow®	Cation	0.125	54	NA	NA	NA	NA	~ 150 mS cm^{-1}	NA	
ASTOM (Japan)	Neosepta® CMX / AMX	Cation / anion	0.17 / 0.14	NA	NA	5 - 6 / 4.5 - 5.5 kg cm^{-2}	NA	NA	4.08/ 2.55Ω cm^{-2} (at 0.5 M NaCl)	< 100	[212]
GE Water (USA)	CR 67 HMR/ AR 204 UZRA	Cation / anion	0.6	NA	NA	10.5 kg cm^{-2}	NA	NA	10/ 7Ω cm^{-2} (at 0.01 M NaCl)	< 100	
Ralex (Czech)	CMH / AMH PAD PES	Cation / anion	< 0.45	NA	< 3 - 10 % (length & thickness)	NA	NA	NA	8.5 - 10 / 7.0 - 7.5 Ω cm^{-2} (at 0.1 M KCl)	< 100	[213, 214]
PCA (Germany)	PC SK / PC SA	Cation / anion	0.09 - 0.130	NA	NA	4 - 5 kg cm^{-2}	NA	NA	NA	60	[215]

Table 2.6. Typical commercial ion exchange membrane used in fuel cell, electrodialysis and other electrochemical applications (From company websites).

As reported by Chiang [151], most of the commercial membranes have good selectively and high conductivity, such as Nafion® 112, 117 and 324 (Dupont, USA), K142 (Asahi Chemical, Japan), Selemion® CMV, CMS, AMV, DMV, ASS, DSV, Flemion® CMF, New Selemion® (Asahi Glass, Japan) and RAI® R1010, R4010 (Pall RAI, USA). Despite this, excessive transfer of electrolyte from one compartment to another has been observed with all these membranes. Apart from the membranes mentioned, properties and cycling performance of the other 15 commercial membranes have been evaluated by Vafiais and Skyllas-Kazacos [27] for the vanadium-bromine redox flow battery. As summarized in Table 2.7, the properties of these membranes are compared with the data of Nafion® membrane from the other literature [26]. Although Nafion® 117 and Hipore® are thicker than the others, smaller area resistance and larger permeation of V(IV) ion have been observed. Also, higher area resistance was observed with the high IEC membranes, such as the ABT membranes, than those with a low IEC, such as Gore® and Hipore® membranes. These suggested that there is no direct correlation between thickness, IEC, resistivity and diffusivity. Among these membranes, only Nafion®, ABT3, L01854 and M04494 were reported to have acceptable performance in terms of round-trip DC energy efficiency and chemical stability. Since all other membranes degrade rapidly in the vanadium-bromine electrolyte, the cycle life has been limited to less than 40 cycles [27].

Commercial membranes	**Manufacturer**	**Type**	**Thickness / mm**	**Area resistance / Ω cm^2**	**V(IV) permeability / 10^{-7} cm^2 min^{-1}**	**IEC / mmol g^{-1}**
Nafion® 117 [26]	Dupont, USA	Cation ex	0.165	2.5	8.63	NA
Gore L01854	W.L. Gore & Associates, USA	Cation ex	0.03	0.38	0.36	0.69
Gore M04494	W.L. Gore & Associates, USA	Cation ex	0.04	0.41	0.96	1.00
ABT3	Australian Battery Tech. & Trading	Cation ex	0.02	3.24	0.11	6.01
ABT4	Australian Battery Tech. & Trading	Cation ex	0.04	9.97	1.44	3.77
ABT5	Australian Battery Tech. & Trading	Cation ex	0.06	5.39	1.44	3.92
SZ	Guangzhou Delong Technologies Pry Ltd. China	Cation ex	0.13	19.03	2.34	2.5
Hipore®	Asahi Kasei, Japan	Microporous separator	0.62	1.4	148	1.14

Table 2.7 Commercial available membranes used in all-vanadium redox flow battery systems [27] (*NA = Not available).

2.3.3.2. *Modified/composite membranes*

Although Nafion® membrane has a high ionic conductivity and good chemical stability in an oxidizing electrolyte, the high permeability of active species across the membranes has been a major technical problem for redox flow batteries. In order to improve the ion selectivity or chemical properties, Nafion® membranes have been modified as hybrid or composite membranes using organic and inorganic materials, such as poly(4-vinyl pyridine)[157], pyrroles [158], polyaniline [159], polyethylenimine (PEI) [160], poly(diallydimethyl-ammonium chloride-polyanion poly(sodium styrene sulfonate)

(PDDA-PSS) [161], silicate (SiO_2) [162], organically modified silicate (ORMOSIL) [163, 164], organic silica modified TiO_2 [165] and zirconium phosphates (ZrP) [166]. These membranes are generally synthesized by (1) electrolyte soaking, (2) oxidation polymerization, (3) electrodeposition, (4) in-situ sol-gel or (5) impregnating method.

Regarding to the expensive cost of Nafion® membranes, some developments have focused on the modified/composite membranes based on non-Nafion® or other non-perfluorinated separators for all-vanadium redox flow battery as summarized in Table 2.8. Early approaches include modification of low cost separators, such as Daramic [142, 167] and low-density polyethylene (LDPE) [150, 167, 168] by grafting and sulfonation processes. Although the resulting membranes have high IEC and conductivity, the permeability of active species across the membrane is still significant. Therefore, polyvinylidene fluoride (PVDF) has been suggested to be grafted onto the matrix membranes. One example is the the poly(vinylidene fluoride)-graft-poly(styrene sulfonic acid) (PVDF-*g*-PSSA-PMAn), where MAn is the maleic anhydride used to reduce the irradiation to the membrane. The PVDF-*g*-PSSA-PMAn was reported to have good chemical stability and low ion permeability in vanadium electrolyte. Further increasing the degree of grafting could lead to higher water uptake, IEC and conductivity as observed by Luo *et al.* [169] (Table 2.8). Similar to polyvinylidene fluoride, other matrix materials, such as sulfonated poly(arylene thioether ketone) (SPTK), sulfonated poly(tetrafluorotheylene) (SPTKK) [170] and poly(tetrafluorotheylene) (PTFE) [171], have been investigated.

Modified membrane	Suppliers	Type	Thickness / mm	Area resistance / Ω cm^2	V(IV) permeability / 10^{-7} cm^2 min^{-1}	IEC / mmol g^{-1}	Ref.
PVDF-*g*-PSSA-11	NA	NA	0.151	NA	2.20	0.82	[169]
PVDF-*g*-PSSA-22	NA	NA	0.115	NA	2.53	1.2	[169]
PVDF-*g*-PSSA-co-PMAn	Kureha Co., Japan	Cation-ex	0.07	NA	0.73	NA	[216]
ETFE-*g*-PDMAEMA	ETFE: Kureha Engineering Ltd, Japan DMAEMA, Acros Organic, USA	Anion-ex	0.070	2.3	0.36	NA	[26]
SPEEK	PEEK: Victrex, PEEK450PF	NA	0.100	1.27	2.432	1.80	[173]
Nafion/ SPEEK	Nafion: Nafion R-100 Resin PEEK: Victrex, PEEK450PF	Cation-ex	0.100	1.6	1.928	1.67	[173]
PSSS-composite (concentration 75 g dm^{-3})	Daramic: W.R. Grace & Co. PSSS solution: Aldrich Chemical Company Inc., USA	NA	NA	1.09	4.48	NA	[150]
PSSS-composite (concentration 75 g dm^{-3})	Daramic: W.R. Grace & Co. PSSS solution: Aldrich Chemical Company Inc., USA	NA	NA	1.36	3.31	NA	[150]

Table 2.8 Modified/composite membranes used in all-vanadium redox flow battery (*NA = Not available).

Due to the electrostatic repulsion between the cation groups of the membrane and the soluble species, anion exchange membranes tend to have lower permeability than their cation counterpart. Modified anion exchange membranes based on polysulfone(PSf) and polyphenylenesulfidesulfone (PPSS) have been suggested by Hwang and Ohya [172]. However, the IEC of this membrane is still less than that of Nafion® 117. Therefore, Qiu *et al.* [26] suggested to graft dimethylaminoethyl methacrylate (DMAEMA), an anion monomer, onto an ethylene–tetrafluoroethylene (ETFE) membrane by UV-induced grafting. At 40 % graft yield, the ETFE-*g*-PDMAEMA membrane exhibits higher IEC, lower area resistance and less pronounced permeability than those of the Nafion® 117 membrane (Table 2.8). Despite this, Hwang *et al.* [147] reported that the high degree of crosslinking in anion membranes obtained by accelerated electron radiation can lead to membrane failure due to the reduced tensile stress.

By hot-pressing or immersing the substrate membranes into an aqueous Nafion® solution, multilayered composite membranes can be prepared to increase the chemical resistance. Substrate membranes are often low-cost material with high thermal conductivity. Due to the low ion permeability, sulfonated polyether ether ketone (SPEEK) has been used as the substrate for the Nafion-SPEEK composite membrane (N/S). A thin layer of Nafion® was used to prevent degradation in the electrolyte, while diamine was used to crosslink the sulfonic groups of Nafion® ionomer with SPEEK ionomer [173]. Although this membrane was found to be low-cost and chemically stable in vanadium electrolyte, round-trip DC energy efficiency was still observed to be lower than a battery using a Nafion® membrane.

In order to enhance the battery performance, a novel sandwich-type sulfonated poly(ether ether ketone) (SPEEK)/tungstophosphoric acid (TPA)/polypropylene (PP) composite membrane has been introduced by Jia *et al.* [174], which consists of a layer of polypropylene (PP) membrane sandwiched by two layers of SPEEK/TPA (S/T) membranes. Due to the sandwich design, the battery can operate for longer cycle life even when the external layers are detached or out of function. With this membrane, improved round-trip DC energy efficiency and permeability have also been observed in an all-vanadium flow battery.

2.4 Flow distributor and turbulence promoter

Flow distributor and turbulence promoter are often employed to enhance the mass transport and promote the exchange of active species between the bulk electrolyte and the electrode surface. Turbulence promoter are usually in the form of insulating nets or ribs but mesh, foam or fibrous bed electrodes sometimes can also function as turbulence promoters (Figure 2.6) [101]. Frías-Ferrer *et al.* [153] have evaluated the mass transport of four types of polyvinylchloride (PVC) turbulence promoters within the rectangular channel of the filter-press reactors. The effect of such turbulence promoters was found to be more pronounced in large systems as indicated by a significant increase in the global mass transport coefficient, while contrary effects were observed in the small systems as the electrolyte flow may not be fully developed due to the entrance/exit manifold effect. At increased Reynolds number, the decrease in global mass transport rates was reported to have no correlation with the projected area of the open spaces or the surface blocked by the promoter strands in contact with the electrodes, but could be due to the geometry of the fibres (or filaments), such as shape and size etc. Other possibilities with the incorporation of turbulence promoters can be: (1) Turbulence promoters could block the

access of the electroactive species and hence decrease the current, (2) turbulence promoter could divert the flow forming the preferential channels and form a bypass of the fluid and (3) turbulence promoter could lead to localized flow recirculation and create stagnant zones, which diminish the mass transport rate [97].

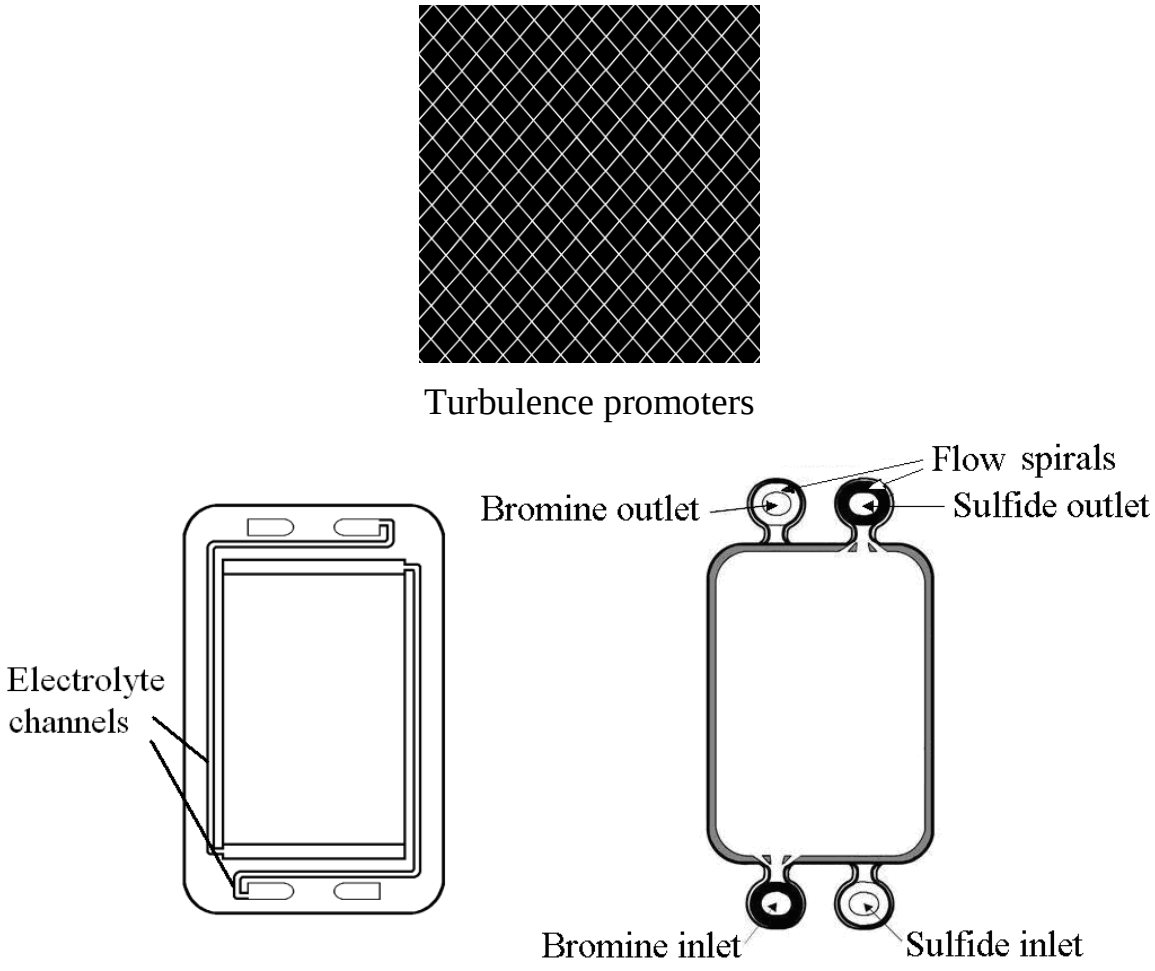

Figure 2.6 Schematics of turbulence promoter, flow frame and spiral-shaped paths [122-123].

The holes in the manifolds are often aligned to form the inlet and outlet of the battery. The change in geometry at the inlet and outlet can generate a high degree of turbulence

[176]. Since electrolyte in the manifold can lead to shunt (bypass or leakage) current in a battery stack, electrolyte channels in the flow frame are often designed to be long and narrow to increase the ionic resistance as shown in Figure 2.6 [177]. In the Regenesys® system, shunt current is reduced by creating a labyritnth in the spiral-shaped electrolyte paths as shown in Figure 2.6 [178]. Tsuda *et al.* [179] suggested that flushing the inert gas bubble through the piping can reduce the shunt current by increasing the resistance of the electrolyte stream.

The reaction environment in a filter-press bromine-polysulfide battery containing spiral-shaped paths in the manifolds has been investigated. The pressure drop across the bromine compartment was higher than those conventional filter-press reactors, such as the FM01-LC, as flow is restricted by the spiral in the manifold [180]. Figure 2.7 shows that both mast transport coefficient and pressure drop of the bromine compartment increases significantly with mean linear flow velocity. Although high pressure drop is often attributed to increased mass transport, it is not favourable as more powerful pumps are needed and leads to more expensive cost and power consumption [178].

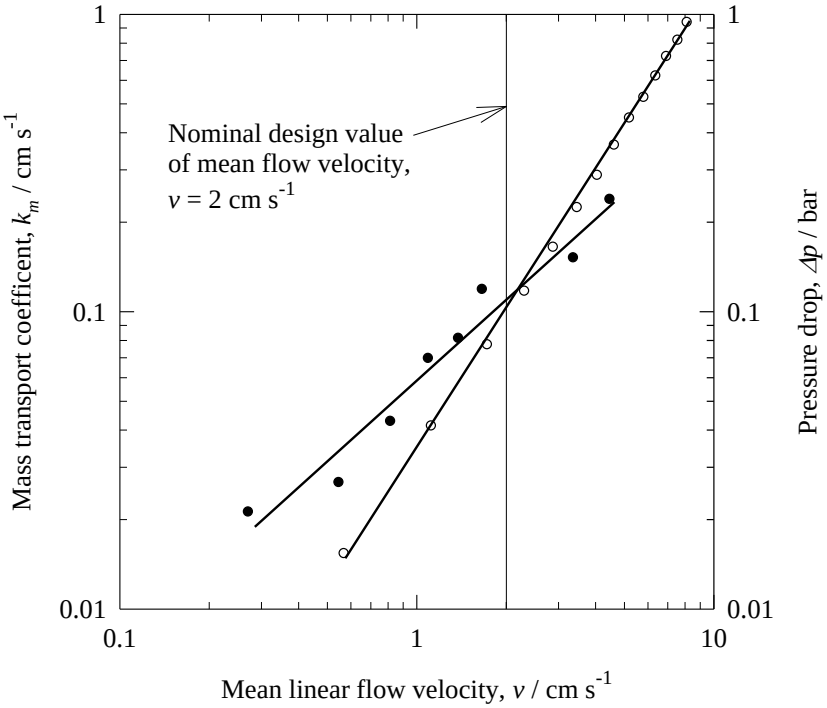

Figure 2.7 Log-log plots of (a) ● mass transport coefficient and (b) ○ pressure drop *vs.* mean linear electrolyte velocity for the bromine compartment of the polysulfide-bromine redox flow battery. Electrolyte: 1 mol dm^{-3} NaBr in 0.5 mol dm^{-3} Na_2SO_4 at pH 2. [178].

2.5 Electrolyte pumping system

Redox flow battery stores energy in the electroactive species, which are circulated during the operation. Storage tanks, pipes, pumps, control valves are the key components. Control valves are controlled by a controller and are used for switching the lines for conducting the electrolyte to and from the corresponding tanks. Alternatively, respective tappings for electrolyte flow are obscured by the diaphragm as pump electrolyte pumped will draw and return via the uncovered tappings, therefore valves are not necessary in this case [181].

For large-scaled redox flow batteries, centrifugal pumps are installed and are controlled by variable speed motors. In general, pump efficiency is about 50 % [179], which accounts to be about 2 – 3% of the overall energy efficiency [49]. At low concentration of electroactive species, a larger amount of electrolyte and a higher flow rate are required, which can result in larger pump losses [182]. Tsuda *et al.* suggested that the pump loss can be significant for redox flow battery under the low current condition, and can be reduced by adopting intermittent pump operation. Under the intermittent pump operation, energy efficiency evaluated including pump power increases significantly compared with the continuous flow operation [179].

The pump speed for the negative and positive electrolytes are highly dependent on the operating conditions. For instance, Hennessy [183] developed a control system that uses open-circuit electrode potentials and temperature measurement to determine the required pump speed. Due to the variation in electrolyte density and the viscosity at different state of charge, this method is not very accurate. The incorporation of flow meters or pressure transducers to measure the flow rates also make the system more complicated and costly [183]. Skyllas-Kazacos *et al.* have suggested to use the open-circuit potentials to adjust the pump speed as the open-circuit potential can monitor the state of charge in an all-vanadium system [184]. In order to minimize the energy consumption associated with the pumps, pumps are switched off when battery is idle and laminar electrolyte flow is used to minimize the pressure drops [185].

2.6. Applications

Since the 1970s, various redox flow batteries have been introduced but only all-vanadium, vanadium-polyhalide, zinc-bromine, zinc-cerium and bromine-polysulfide have been tested or commercialized at large scale. The commercial specifications of these redox flow batteries are summarized in Table 2.9. Among the four redox flow batteries, all-vanadium redox flow battery has the highest efficiency and the largest life cycle, while zinc-cerium and bromide-polysulfide systems have advantages in power density and cost, respectively. Figure 2.8 shows the plots of the cell voltage *vs.* time of the charge-discharge cycle of the four systems: all-vanadium (30 mA cm^{-2} for 2 hours) [107], zinc-bromine (15 mA cm^{-2} for 10 hours) [186], bromine-polysulfide (40 mA cm^{-2} for 30 mins) [115] and the undivided zinc-cerium system (20 mA cm^{-2} for 30 mins) [8]. Up to now, only all-vanadium and zinc-bromine systems have been commercialized and have been used in applications, such as load levelling, power quality control application, facilitating renewable energy deployment and energy storage for electric vehicles [3].

	All-vanadium	**Zinc-bromine**	**Bromine-polysulfide**	**Zinc-cerium**
Cell open circuit voltage (V) [217]	1.4	1.83	1.54	*c.a.* 2.43 [55]
Average power density (W m^{-2}) [217]	800	1000	800	1200 – 2500
Energy density (Wh/ liter) [218]	16 – 33	60 – 90	20 – 30	12 – 20 [217]
Cycle round-trip DC energy efficiency [Wh_{out}/ Wh_{in}] (%)[218, 219]	70 – 85	65 – 75	60 – 75	63 % (50 mA cm^{-2}, laboratory cell). [55]
Cycle life [218]	> 12, 000 cycles	> 2, 000 cycles	10-20 yrs [220, 221]	NA
Operation temp (^oC) [222]	30	50	35 [223]	60 [81]
Typical power range (M W_e) [219]	< 3	< 1	<15	< 1
Total system cost ($/k W) [224]	1828	1044	639	750
Cost attribution of storage module (%) [224]	80	80	60	50
Typical size range (M W h) [225]	0.5 – 5	0.01 – 5	0 – 120	NA
Life time (years) [218]	5 – 10	5 – 10	15	15 [223]
Stage of development [219]	Demonstration/ Commercial units	Demonstration/Commercial units	Demonstration	Demonstration
Major companies involved [224]	Prudent Energy (formerly Pinnacle, VRB), Sumitomo Electric, Cellstorm GmbH, Mitsubishi Chemical Corp, Cellenium, V-fuel Pty, Rongke Power, Ashlawn Energy and Re-fuel Tech.	ZBB, Premium Power, Moonlight Project by New Energy and Industrial Technology Develop Organization, Kyushu Electric Power Co., Meidensha Corp., Primus Power and Redflow Limited	VRB (using Regenesys technology), further acquired by Prudent Energy.	Plurion Inc.
Number of installations	> 20	> 10	2	1
Largest installation	4 MW/ 6 MW h in Subaru windfarm, Hokkaido by Sumitomo Electric	1 MW in Kyushu, by Kyushu Electric Power company	15 MW in Little Barford, UK, by Regenesys Technology	A 2 kW-1 MW testing facility in Glenrothes, Fife, Scotland by Plurion

Table 2.9. Commercial specifications and operating parameters of the most developed/ commercially available redox flow battery systems. (*NA = Not available).

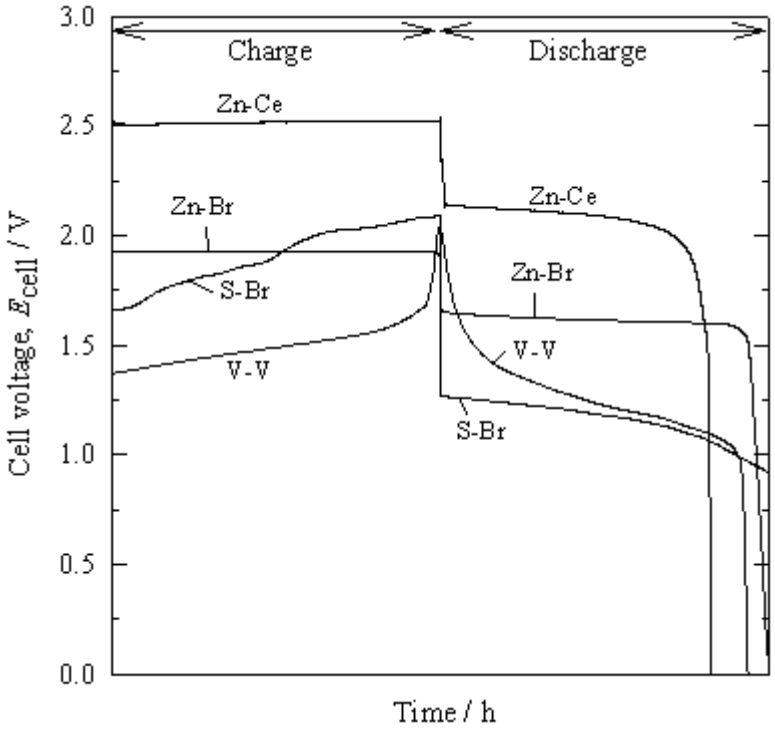

Figure 2.8 Cell voltage *vs.* time response during charge/discharge for all-vanadium (30 mA cm^{-2} for 2 hours) [107], zinc-bromine (15 mA cm^{-2} for 10 hours) [186], bromine-polysulfide (40 mA cm^{-2} for 0.5 hour) [115] and the undivided zinc-cerium (20 mA cm^{-2} for 0.5 hour) [8] redox flow batteries.

2.6.1. *Load levelling*

Large-scale energy storage systems allow the use of excess power and avoid high cost power plants to cycle on and off. By employing a redox flow battery, bottlenecks within the transmission system can be relieved; this can result in reduced power transmission losses and more reliable electric power [3]. The main installations of redox flow batteries used in load-levelling and uninterruptible power supply applications are summarized in Table 2.10.

Battery system	Company name	Customer	Basic specification	Application	Installation date
All-vanadium	VRB Power System Inc.	Stellenbosch University, South Africa	250 kW/ 500 kW h	Load levelling and UPS back-up power	2001
		Castle Valley, United States	250 kW/ 2M Wh	Load levelling	February 2004
	Sumitomo Electric Industries Ltd.	Tasumi Sub-station, Kansai Electric Power, Japan	450 kW/ 900 kW h	Load levelling	1996
		Urban Ace Awaza Building, Japan	100 kW/ 800 kW h	Office building load levelling	2000
		Kansai Electric Power, Japan	200 kW/ 1.6 MW	Load levelling	2000
		Tottori Sanyo Electric, Japan	AC 3 MW × 15 sec.	UPS	April 2001
		Kwansei Gakuin University, Japan	AC 500 kW × 10 h.	Load levelling	November 2001
		Cesi, Italy	42 kW × 2 h	Load levelling	November 2001
	Mitsubishi Chemicals	Kashima-Kita Electric Power Station	200 kW/ 800 kW h	Load levelling	1996
	Premium Power	Nairn substation, Scotland	150 kW h	Load leveling	2009
	Prudent Energy	Oxnard, Califonia	500 kW/ 3.6 MW h	Load leveling	After 2011
	Ashlawn Energy, V-fuel	Painesville Power Plant, Ohio	1 MW / 8 MW h	Smart-grid / load levelling	After 2011
Zinc-bromine	ZBB Energy Corp.	Detroit Edison, U.S.	400 kW h	Load levelling and voltage imbalance	June 2001
		United Energy, Melbourne, Australia	200 kW h	Demonstration unit for network storage applications	November 2001
		Nunawading Electrical Distribution Substation in Box Hill, Australia	400 kW h	Load levelling	2001
		Pacific Gas and Electric Co., U.S.	2 MW h	Peak power capacity (substation upgrade deferral)	October 2005
	Moonlight Project	Imajuku substation of Kyushu Electric, Japan	1 MW/ 4 MW h	Electric-utility applications	1990
Bromine-Polysulphide-	Regenesys Technologies Ltd.	Little Barforad Power Station, UK	15 MW/ 120 MW h	Load levelling	December 2000 (sold in 2003)
		Tennessee Valley Authority, U.S.	15 MW/ 120 MW h	Load levelling	2001 (sold in 2002)
Zinc-cerium	Plurion Ltd	Glenrothes, Fife, Scotland	2 kW – 1MW	Testing facility	2007

Table 2.10. Major installations of redox flow batteries for load-levelling and uninterruptible power supply application (from company websites [80, 197, 226, 227]).

Early installations of redox flow batteries started in Japan and Australia. In 1990, a 1 MW/ 4 MW h zinc-bromine battery has been installed in Imajuku, Fukuoka, Japan, which was under the 'Moonlight Project' sponsored by the Japanese government [187, 188]. Since 1994, more than 20 all-vanadium redox flow batteries have been installed. The first all-vanadium flow battery was a 15 kW h installed by the University of New South Wales in a demonstration solar house in Thailand [189]. In Japan, a number of vanadium redox flow batteries have been installed by Sumitomo and one has been installed by Mitsubishi Chemical in 1996 [24].

Innogy plc's bromine-polysulfide system (Regenesys®) focuses on multi-M W system. In early 2000s, two 15 MW/ 120 MW h Regenesys® flow batteries were under construction in Little Barford, Cambridgeshire, UK and Columbus, Mississippi, U.S. respectively. If completed, they would have been the largest energy storage in the world. As shown in Figure 2.9a, the 15 MW plant in Mississippi comprised of 120 100 kW filter-press cell stacks (Figure 2.9b), each having 200 bipolar electrodes. The electrolyte tanks of such system were in 30 feet tall and about 65 feet in diameter. The tank capacities for sodium bromide and sodium polysulfide were as high as 1,798, 000 and 2,1578,000 litres, respectively [190]. However, these two batteries were cancelled after one year of construction [191].

(a)

(b)

Figure 2.9 Photographs of (a) 15 MW bromine polysulfide (Regenesys®) under construction in Mississippi in 2001 (b) Three sizes of 1.4 kW, 8.1 kW and 100 kW modular cells developed by Regenesys technology.

2.6.2. *Power quality control applications*

Failure of an electrical power system during power generation often leads to the collapse of system, which can be costly and devastating, as a result fast stabilization is necessary. Redox flow batteries are favourable in these situations as their response time to power demand can be as quick as less than 1 minute and the maximum short-time overload output can be several times that of the rated capacity. This makes redox flow batteries attractive for both voltage and frequency control [24]. Redox flow batteries can be used as a battery-backed uninterruptible power supply (UPS) system for protection against faults on the power utility transmission and distribution system.

Energy storage for the UPS system is to provide electricity during power failure, which is generally used for orderly shutdown of computer systems or switch-on of the generator. Since diesel generators are often difficult to switch on, longer discharge time of energy storage is needed. Compared to sealed lead acid batteries, redox flow batteries have advantage of longer discharge time. Some of the redox flow batteries, such as those storing energy in the electrolytes, have a system capacity that can be increased easily by using more electrolyte volume and larger tanks. In addition, redox flow batteries can be restarted from idle within 1 minute by pumping electrolyte into the cell stacks [49].

Installations of redox flow batteries in UPS applications have been mainly vanadium redox flow batteries by Sumitomo Electric Industries in Japan. Since 2001, Sumitomo Electric Industries has installed a number of vanadium redox flow batteries in high-tech factories and office buildings. One prominent example is the 3 MW × 1.5 sec plus a 1.5 MW × 1 h system at the liquid crystal manufacturing plant of Tottori Sanyo

Electric in 2001. This system not only serves as an UPS, but also for load levelling. Other examples of load-levelling and UPS back-up include the early installation of a 250 kW/ 500 kW h VRB power by VRB in 2001 at Stellenbosch University for ESKOM Power Corporation, South Africa [24].

2.6.3. *Coupling with renewable energy sources*

Due to the large capacity and the long discharge time, flow batteries are attractive when coupling with renewable energy sources. As the energy production from renewable energy sources are usually intermittent and not be connected to the grid, energy storage is hence important. The rapid growing demand of energy generated by renewable energy sources has given rise to massive market opportunities.

2.6.3.1. *Coupling with solar cells*

Solar panels are traditionally connected to conventional lead acid batteries, which only use 25 – 75 % of their state of charge; hence only 50 % of the actual capacity is used. Redox flow batteries have advantages over conventional lead acid batteries in high efficiency, long cycle life and low cost [189]. Table 2.11 summarizes the main installations of redox flow batteries coupled with solar energy. The first use of redox flow battery with solar energy sources was a 5 kW/ 12 kW h all-vanadium flow battery system installed in Thailand by Thai Gypsum Products Co., Ltd., (TGP) in 1994, which was the first license based on the technology developed by Skyllas-Kazacos *et al.* [189]. In 2001, the second all-vanadium flow battery system coupling with solar panels was installed by VRB at a golf course in Japan [24]. Early installation of zinc-bromine system was a 50 kW/ 100 kW h by ZBB, which is in parallel with 50 kW rooftop solar cells at a

commercial customer facility in New York. Two further zinc-bromine batteries of ZBB have been installed in Australia (500 k W h) and the U.S. (2 × 50 kW h) in 2002 and 2003, respectively [192]. Department of Energy, United States, is currently building a 2.8 MW h zinc-bromine flow battery in Albuquerque, with 500 kW solar panels [193].

Battery system	Company name	Customer	Basic specification	Application	Start date
All-vanadium	University of South New Wales, Thai Gypsum Pcl	Solar Demonstration House, Thailand	5 kW/ 12 kW h	Coupling with solar cell	1994
	Sumitomo Electric Industries Ltd.	Obayashi Corp., Japan	DC 30 kW × 8 h.	Hybrid with photovoltaic cells	April 2001
	VRB Power System Inc.	University of Aalborg, Denmark	5 kW × 4 h	Coupling with wind turbines and solar cells	2006
		Risø TDU, Denmark	15 kW × 8 h	Hybrid with wind turbines and solar cells	May 2007
	Prudent Energy	Zhangbei, Heibei, China	1 MW h	Hybrid with wind turbines and solar cells	May 2011
		California Public Utilities Commission (CPUC)	100 kW / 300 kWh	Hybrid with solar cells	After 2011
Zinc-bromine	ZBB Energy Corp.	A commercial customer facility, New York, USA	50 kW/ 100 kW	Hybrid with solar cells for a demonstration project	NA
		Australian Inland Energy, Australia	500 kW h	Hybrid with solar cells	June 2002
		Power Light Corp., U.S.	2 × 50 kW h	Hybrid with solar cells	November 2003
		CSIRO research center, Newcastle, Australia	500 kW h	Hybrid with solar cells	End of 2009
	Redflow Limited	University of Queensland, Australia	12 × 120 kW h	Hybrid with solar cells	April 2011
	Department of Energy, US	Albuquerque, New Mexico, U.S.	2.8 MW h	Hybrid with 500 kW	After 2011

Table 2.11 Major installations of redox flow batteries coupling with solar energy (from company websites [80, 193, 197, 227]). (*NA = Not available)

2.6.3.2. *Coupling with wind turbines*

Coupling redox flow batteries with wind turbines is useful in removing fluctuation and maximizing the reliability of power. The demand of energy storage with wind-farms is going to increase dramatically in the coming decades. For instance, American Electric Power (AEP) has claimed to install 1,000 MW of energy storage by 2020 [194]. The main installations of redox flow batteries coupling with wind turbines are summarized in Table 2.12.

Battery system	Company name	Customer	Basic specification	Applications	Start date
All-vanadium	VRB Power System Inc.	Hydro Tasmania, Japan	200 kW × 4 h.	Hybrid with wind turbines	November 2003
		Tapbury Management (Letterkenny Co.), Ireland	2 MW × 6 h	Hybrid with wind turbines	August 2006
		University of Aalborg, Denmark	5 kW× 4 h	Coupling with wind turbines and solar cells	2006
		Risø TDU, Denmark	15 kW × 8 h	Hybrid with wind turbines and solar cells	May 2007
	Prudent Energy	Zhangbei, Heibei, China	1 MW h	Hybrid with wind turbines and solar cells	May 2011
	Sumitomo Electric Industries Ltd.	Hokkaido Electric Power Wind Farm, Japan	170 kW /1 M W	Wind turbine output power stabilization	2001
		Institute of Applied Energy, Japan	AC 170 kW × 6 h.	Stabilization of wind turbine output	March 2001
		J Power at Subaru Wind Farm, , Hokkaido, Japan	4 MW/ 6MW h	Wind energy storage and wind power stabilization	2005
	Pinnacle VRB	Hydro Tasmania, King island	250 kW/ 1M W h	Wind energy storage and diesel fuel replacement	2003
Zinc Bromine	ZBB Energy Corp.	Dundalk Institute of Technology, Ireland	125 kW, 500 kW h	Hybrid with wind turbines	December 2008

Table 2.12 Major installations of redox flow batteries coupling with wind energy (from company websites [80, 197, 226, 227]).

In Japan and Ireland, several redox flow batteries have been installed with wind turbines since 2000. The famous one includes the early installation of a 170 KW/ 1 MW vanadium redox flow batteries installed by Sumitomo Electric power in Hokkaido, Japan, while Sumitomo Electric Industries recently installed another 4 MW/ 6 MW h vanadium redox flow battery in Hokkaido for JPower at Subaru wind farm, which is the largest installation of all-vanadium redox flow battery so far [24]. Apart from Sumitomo Electric Industries, the largest redox flow batteries coupling with wind turbines are the 2 MW x 6 h vanadium redox flow batteries installed by VRB at the Sorne Hill, Ireland in 2006 [195]. Although most of the large-scale redox flow batteries coupling with wind power were installed by Sumitomo Electric Industries, smaller scales of vanadium and zinc-bromine flow batteries coupling with wind farm have been installed by manufacturers, such as Pinnacles [24] and ZBB [196] respectively. In 2011, Prudent Energy has installed a 1 MW h all-vanadium battery sized at a rated power 500 kW for the National Wind Power Integration Research and Test Center of China (NWIC) in Zhangbei, Hebei province [197].

2.6.4. *Electric vehicles*

As early as 1980, a 50 kW h zinc-chlorine redox flow battery was investigated by the Energy Development Associates (EDA) for vehicle power system to compete with the lead acid battery [12, 198]. Meanwhile, the Studiengesellschaft für Energiespeicher and Antriebssysteme (SEA, now PowerCell of Boston, GmbH) in Mürzzuschlag, Austria, has been developing zinc/bromine batteries for electric vehicles since 1983 and has produced batteries with capacities ranging between 5 and 45 kW h. A SEA 45 kW h 216 V battery

has been installed in a Volkswagen bus, which the Austrian Postal Service has been using. An electric vehicle with a 15 kW h/ 114 V battery was designed by Hotzenblitz (Germany) [31].

Electric vehicles with a 35 kW h zinc-bromine battery had been launched by the University of California in the 1990s [199, 200]. In Japan, a zinc-bromine battery was installed by Toyota Motor Corporation in an electric vehicle, namely EV-30 [31]. An electric golf-cart installed with a 36 V, 3.9 kW h vanadium battery prototype has been demonstrated at the University of South Wales, Australia in 1994. The golf cart was under road-testing for more than two years and was reported to have a maximum speed of 19 km h^{-1}. The total vehicle weight, including two passengers was in excess of 400 kg [50]. Since energy is stored in the electrolyte, 24 hour operation of an electric vehicle is possible if the electrolyte is refuelled every 4 to 5 hours [201]. However, the low energy density of all-vanadium redox flow battery remains the main challenge. Therefore, the recent larger specific energy density of vanadium-air [92] and lithium flow batteries [35-38] could be promising for longer mileage of electric vehicle but the safety conditions of using lithium flow battery still need to be identified. Previous progress and challenges of redox flow batteries in hybrid vehicle applications have been discussed in detailed by Mohammed *et al.* [202].

2.7 Conclusions

Redox flow batteries can have discharge time, ranging from minutes to many hours. Most of the flow batteries are capable of overload and total discharge without any risk of damage. Therefore, flow batteries have been used in applications, such as load levelling,

power quality control and the energy storage for electric vehicles. Due to the large energy capacity and long discharge time, flow batteries are attractive when coupled with renewable energy sources, as energy productions from renewable energy sources are usually intermittent and may not be connected to the grid. The rapid growing demand of energy generated from renewable energy sources has given rise to a massive market opportunity.

To date, only all-vanadium, vanadium-polyhalide, zinc-bromine, zinc-cerium and bromine-polysulfide systems have been tested or have been commercialized at large scale but other various redox flow battery systems with potential applications have been introduced in the past 40 years. The advantages and disadvantages of various systems have been critically reviewed. Recent advances of redox flow batteries, includes several undivided flow batteries, which utilize a single electrolyte and do not require an ion-exchange membrane. They have the advantages in low cost and design simplicity over the conventional flow battery systems. Recent attentions have been given to the use of organic and non-aqueous electrolytes but there are still some technical issues, such as limited solubility and low cell voltages, hindering them from practical applications. Recently, vanadium air and lithium flow batteries provide significantly larger specific energy density than conventional all-vanadium system. These batteries are attractive for electric vehicle application but technical issues regarding to safety and the use of higher current density still needs to be overcome.

An improved electrolyte composition and electrode/membrane materials could be implemented to the battery performance. For instance, the use of electrolytic additives to

reduce secondary reactions such as hydrogen and oxygen evolution as well as the use of catalysts incorporated into the electrode material to improve the reaction rate. It is also important to further increase the solubility of the electroactive species by modifying the ligand interactions in suitable solvents. Further investigation on the use of bipolar electrodes in a stack, is also necessary to scale-up the battery and to increase the power density and energy outputs.

2.8 References

1. The Electricity Advisory Committee. Bottling Electricity: Storage as a Strategic Tool for Managing Variability and Capacity Concerns in the Modern grid - A report by The Electricity Advisory Committee, December 2008. http://www.oe.energy.gov/DocumentsandMedia/final-energy-storage_12-16-08.pdf accessed on 1 September 2010.
2. N. Tokuda, T. Kanno, T. Hara, T. Shigematsu, Y. Tsutsui, A. Ikeuchi, T. Itou, T. Kumamoto, SEI Tech. Rev. 50 (1998) 88-94.
3. J. Makansi, J. Abboud, Energy Storage Council White Paper (2002).
4. J. Kondoh, I. Ishii, H. Yamaguchi, A. Murata, K. Otani, K. Sakuta, N. Higuchi, S. Sekine, M. Kamimoto, J. Energy Conversion and Management 41 (2000) 1863-1874.
5. J.Q. Pan, Y.Z. Sun, J. Cheng, Y.H. Wen, Y.S. Yang, P.Y. Wan, Electrochem. Comm. 10 (2008) 1226-1229.
6. A. Hazza, D. Pletcher, R. Wills, J. Phys. Chem. Chem. Phys. 6 (2004) 1773 - 1778.
7. Y. Xu, Y.H. Wen, J. Cheng, G.P. Cao, Y.S. Yang, Electrochem. Comm. 11 (2009) 1422-1424.

8. P.K. Leung, C. Ponce de León, F.C. Walsh, Electrochemistry Communications (2011) Accepted.
9. C. Ponce de León, A. Frías-Ferrer, J. González-García, D.A. Szánto, F.C. Walsh, J. Power Sources 160 (2006) 716-732.
10. L.H. Thaller, USP 3996064, Electrically Rechargeable Redox Flow Cells (1976).
11. U.S. Dept. of Energy, National Aeronautics and Space Administration, NASA TM-79067 (1979) 1-53.
12. T.R. Crompton, Battery Reference Book, 3 ed. Elsevier Science & Technology Books, Boston : Newnes, Oxford, England, Vol. Chapter 14 (2000).
13. P.C. Butler, D.W. Miller, A.E. Verardo, 17th Intersoc. Energy Conversion Eng. Conf., Los Angeles (1982).
14. G.B. Adams, USP 4180623, 25/12/1979, Electrically rechargeable battery.
15. A. Pelligri, P.M. Spaziante, GB Patent 2030349, *to Oronzio de Nori Impianti Elettrochimici S.p.A.* (1978).
16. J.T. Kummer, D. -G. Oei, J. Appl. Electrochem. 12 (1981) 87-100.
17. J.T. Kummer, D. -G. Oei, J. Appl. Electrochem. 15 (1985) 619-629.
18. R.J. Remick, P.G.P. Ang, US 1984/4485154, 27 Nov 1984, Electrically rechargeable anoionically active reduction-oxidation electrical storage-supply system (1984).
19. M. Skyllas-Kazacos, M. Rychcik, P.G. Robins, A.G. Fane, M.A. Green, J. Electrochem. Soc. 133 (1986) 1057-1058.
20. M. Rychcik, M. Skyllas-Kazacos, J. Power Sources 19 (1987) 45-54.
21. M. Skyllas-Kazacos, F. Grossmith, J. Electrochem. Soc. 134 (1987) 2950-2953.
22. M. Rychcik, M. Skyllas-Kazacos, J. Power Sources 22 (1988) 59-67.
23. M. Skyllas-Kazacos, R.G. Robins, US 4,786,567, All-vanadium redox battery (1986).

24. V-fuel Pty Ltd. Status of Energy Storage Technologies as Enabling Systems for Renewable Energy from the Sun, Wind, Waves and Tides. http://www.aph.gov.au/House/committee/Isr/renewables/submissions/sub21.pdf accessed on 1 September 2010.

25. C.M. Hagg, M. Skyllas-Kazacos, J. Appl. Electrochem. 32 (2002) 1063-1069.

26. J.Y. Qiu, M.Y. Li, J.F. Ni, M.L. Zhai, J. Peng, L. Xu, H.H. Zhou, J.Q. Li, G.S. Wei, J. Membr. Sci. 297 (2007) 174-180.

27. H. Vafiadis, M. Skyllas-Kazacos, J. Membr. Sci. 279 (2006) 394-402.

28. B. Fang, S. Iwasa, Y. Wei, T. Arai, M. Kumagai, Electrochim. Acta 47 (2002) 3971-3976.

29. F.Q. Xue, Y.L. Wang, W.H. Wang, X.D. Wang, Electrochim. Acta 53 (2008) 6636-6642.

30. L.Y. Li, S.W. Kim, W. Wang, M. Vijaayakumar, Z.M. Nie, B.W. Chen, J.L. Zhang, G.G. Xia, J.Z. Hu, G. Graff, J. Liu, Z.G. Yang, Adv. Energy Mater., Wiley Online Library, 1 (2011) 394-400 http://onlinelibrary.wiley.com/doi/10.1002/aenm.201100008/full Accessed on 20 June 2011.

31. R.F. Koontz, R.D. Lucero, Handbook of Batteries, Vol. 39, 39.1-39.22.

32. H. De Keulenaer, P. de Boer, J. Raadschelders, Leonardo Energy, EPQU Magazine 3 (2007).

33. J. Cheng, L. Zhang, Y.S. Yang, Y.H. Wen, G.P. Cao, X.D. Wang, Electrochem. Comm. 9 (2007) 2639-2642.

34. D. Pletcher, R. Wills, J. Phys. Chem. Chem. Phys. 6 (2004) 1779-1785.

35. Y.M. Chiang, W.C. Carter, B.Y. Ho, M. Duduta, US 2010/0047671 A1, High Energy Density Redox Flow Device (2010).

36. M. Duduta, B. Ho, V.C. Wood, P. Limthongkul, V.E. Brunini, W.C. Carter, Y.M. Chiang, Semi-Solid Lithium Rechargeable Flow Battery, Adv. Energy Mater., (2011) DOI: 10.1002/aenm.201100152.

37. Y.H. Lu, J.B. Goodenough, J. Mater. Chem. Advance Article (2011) doi:10.1039/c0jm04222f.

38. Y.H. Lu, J.B. Goodenough, Y.S. Kim, J. Am. Chem. Soc. 133 (2011) 5756 - 5759.

39. J. Bartolozzi, J. Power Sources 27 (1989) 219-234.

40. Z.G. Yang, J.L. Zhang, M.C.W. Kintner-Meyer, X.C. Lu, D.W. Choi, J.P. Lemmon, J. Liu, Chem. Rev., ACS (2011).

41. M. Futamata, S. Higuchi, O. Nakamura, I. Ogino, Y. Takeda, S. Okazaki, S. Ashimura, S. Takahashi, J. Power Sources 24 (1988) 137-155.

42. Y.H. Wen, H.M. Zhang, et al., Electrochim. Acta 51 (2006) 3769-3775.

43. Y.H. Wen, H.M. Zhang, et al., J. Electrochem. Soc. 153 (2006) A929-A934.

44. P. Modiba, A.M. Crouch, J. Appl. Electrochem. 38 (2008) 1293-1299.

45. C.H. Bae, E.P.L. Roberts, R.A.W. Dryfe, Electrochim. Acta 48 (2002) 279-287.

46. J. Doria, M.C. De Andres, C. Armenta, Proc. 9th Solar Energy Soc. 3 (1985) 1500.

47. C.-H. Bae, E.P.L. Roberts, R.A.W. Dryfe, J. Power Sources 48 (2002) 279-287.

48. M. Skyllas-Kazacos, M. Rychcik, R. Robins, AU Patent 575247, (1986).

49. M. Skyllas-Kazacos, C. Menictas, Telecommunications Energy Conference, 1997. INTELEC 97, 19th International (1997) 463-471.

50. M. Skyllas-Kazacos, J. Power Sources 124 (2003) 299-302.

51. M. Skyllas-Kazacos, A. Mousa, M. Kazakos, PCT Application PCT/GB2003/001757 (2003).

52. M. Skyllas-Kazacos, N. Milne, J. Appl. Electrochem. Article in press (2011) DOI 10.1007/s10800-011-0287-y.

53. R.P. Kreh, R.M. Spotnitz, J.T. Lundquist, J. Org. Chem. *54* (1989) 1526-1531.

54. P.K. Leung, C. Ponce-de-Leon, C.T.J. Low, F.C. Walsh, Electrochimica Acta 56 (2011) 2145-2153.

55. P.K. Leung, C. Ponce-de-Leon, C.T.J. Low, A.A. Shah, F.C. Walsh, J. Power Sources 196 (2011) 5174-5185.

56. F.C. Walsh, J. Pure Appl. Chem. 73 (2001) 1819-1837.

57. T. Yamamura, Y. Shiokawa, H. Yamana, H. Moriyama, Electrochim. Acta 48 (2002) 43-50.

58. K. Shirasaki, T. Yamamura, T. Herai, Y. Shiokawa, J. Alloys Compd. 418 (2006) 217-221.

59. Y. Shiokawa, T. Yamamura, K. Shirasaki, J. Phys. Soc. Jpn. 75 (2006) 137-142.

60. T. Yamamura, J. Electrochem. Soc. 152 (2005) A830-A836.

61. T. Yamamura, N. Watanabe, Y. Shiokawa, J. Alloys Compd. 408-412 (2006) 1260-1266.

62. K. Hasegawa, A. Kimura, T. Yamamura, Y. Shiokawa, J. Phys. Chem. Solids 66 (2005) 593-595.

63. Y. Matsuda, K. Tanaka, M. Okada, Y. Takasu, M. Morita, T. Matsumura-Inoue, J. Appl. Electrochem. 18 (1988) 909-914.

64. M.H. Chakrabarti, R.A.W. Dryfe, E.P.L. Roberts, Electrochimica Acta 52 (2006) 2189-2195.

65. M.H. Chakrabarti, E.P.L. Roberts, C. Bae, M. Saleem, Energy Conversion and Management 52 (2011) 2501-2508.

66. Q. Liu, A.E.S. Sleightholme, A.A. Shinkle, Y. Li, L.T. Thompson, Electrochemistry Communications 11 (2009) 2312-2315.

67. Q. Liu, A.A. Shinkle, Y. Li, C.W. Monroe, L.T. Thompson, A.E.S. Sleightholme, Electrochemistry Communications 12 (2010) 1634-1637.

68. C. Lotspeich, International Conference 2002 (EESAT2002), San Francisco (2002).

69. D. Pletcher, R. Wills, J. Power Sources 149 (2005) 96-102.

70. A. Hazza, D. Pletcher, R. Wills, J. Power Sources 149 (2005) 103-111.

71. D. Pletcher, H.T. Zhou, G. Kear, C.T.J. Low, F.C. Walsh, R.G.A. Wills, J. Power Sources 180 (2008) 621-629.

72. D. Pletcher, H.T. Zhou, G. Kear, C.T.J. Low, F.C. Walsh, R.G.A. Wills, J. Power Sources 180 (2008) 630-634.

73. M.D. Gernon, M. Wu, T. Buszta, P. Janney, Green Chem. 1 (1999) 127-140.

74. S. Zhong, M. Skyllas-Kazacos, J. Power Sources 39 (1992) 1-9.

75. L. Zhang, J. Cheng, Y.S. Yang, Y.H. Wen, X.D. Wang, G.P. Cao, J. Power Sources 179 (2008) 381-387.

76. B.D. Sawyer, G.J. Suppes, M.J. Gordon, M.G. Heidlage, J. Appl Electrochemistry (2010) DOI: 10.1007/s10800-011-0264-5.

77. P.C. Symons, J. Electrochem. Soc. International Conference on electrolytes for power sources, Brighton (1973).

78. P.C. Symons, USP 3713888, Process for electrical energy using solid halogen hydrates (1970).

79. D.J. Eustace, J. Electrochem. Soc. 127 (1980) 528-532.

80. ZBB http://www.zbbenergy.com/ accessed on 1 September 2010.

81. R.L. Clarke, B.J. Dougherty, S. Harrison, P.J. Millington, S. Mohanta, US 2004/ 0202925 A1, Cerium Batteries (2004).

82. R.L. Clarke, B.J. Dougherty, S. Harrison, J.P. Millington, S. Mohanta, US 2006/0063065 A1, Battery with bifunctional electrolyte (2005).

83. G. Brodt, J. Haas, W. Hesse, H.U. Jäqer, US 2003/0141195 Al, 31/07/2003, Method for electrolytic galvanizing using electrolytes containing alkane sulphonic acid (2003).

84. R. Clarke, USP 7582385 B2, 01/09/2009, Zinc air battery with acid electrolyte (2009).

85. P.K. Leung, C. Ponce de León, C.T.J. Low, F.C. Walsh, Electrochimica Acta (2011) Accepted.

86. G. Nikiforidis, L. Berlouis, D. Hall, D. Hodgson, J. Power Sources (2011) doi:10.1016/j.jpowsour.2011.01.036.

87. Y. Xu, Y.H. Wen, J. Cheng, G.P. Cao, Y.S. Yang, Electrochimica. Acta 55 (2010) 715-720.

88. L.W. Hruska, R.F. Savinell, J. Electrochem. Soc. 128 (1981) 18-25.

89. Y.H. Wen, J. Cheng, S.Q. Ning, Y.S. Yang, J. Power Sources 188 (2009) 301-307.

90. Y.H. Wen, J. Cheng, P.H. Ma, Y.S. Yang, Electrochimica. Acta 53 (2008) 3514-3522.

91. Y.H. Wen, J. Cheng, Y. Xun, P.H. Ma, Y. S.Yang, Electrochim. Acta 53 (2008) 6018-6023.

92. S.S. Hosseiny, M. Saakes, M. Wessling, Electrochem. Comm. (2010) Article in Press.

93. L.L. Swette, A.B. LaConti, S.A. McCatty, J. Power Sources 47 (1994) 343-351.

94. L. Jörissen, J. Power Sources 155 (2006) 23-32.

95. J. Pan, L. Ji, Y. Sun, P. Wan, J. Cheng, Y. Yang, M. Fan, Electrochemistry Communications 11 (2009) 2191-2194.

96. J. Collins, G. Kear, X. Li, C.T.J. Low, D. Pletcher, R. Tangirala, D. Stratton-Campbell, F.C. Walsh, C. Zhang, J. Power Sources 195 (2010) 1731-1738.

97. Á. Frías-Ferrer, J. González-García, V. Sáez, C. Ponce de León, F.C. Walsh, J. AIChE 54 (2008) 811-823.

98. L. Joerissen, J. Garche, C. Fabjan, G. Tomazic, J. Power Sources 127 (2004) 98-104.

99. K. Kinoshita, S.C. Leach, J. Electrochem. Soc. 129 (1982) 1993-1997.

100. N.A. Hampson, A.J.S. McNeil, Royal Society of Chemistry, SPR-Electrochemistry 9 (1984) 1-65 http://www.rsc.org/ accessed on 1 September 2010.

101. F.C. Walsh, A First Course in Electrochemical Engineering, Electrochemical Consultancy, Romsey, (1993).

102. J.A. Trainham, Electrochim. Acta 26 (1981) 455-469.

103. H.T. Zhou, H.M. Zhang, P. Zhao, B.L. Yi, Electrochim. Acta 51 (2006) 6304-6312.

104. N. Akira, K. Hiroko, N. Ken, Denki Kagaku oyobi Kogyo ButsuriKagaku 61 (1993) 1442.

105. J. Cathro, K. Cedzynska, J. Power Sources 19 (1987) 337.

106. S. Zhong, M. Kazacos, R.P. Burford, M. Skyllas-Kazacos, J. Power Sources 36 (1991) 29-43.

107. M. Kazacos, M. Skyllas-Kazacos, J. Electrochem. Soc. 136-9 (1989) 2759-2760.

108. P. Qian, H.M. Zhang, J. Chen, Y.H. Wen, Q.T. Luo, Z. Liu, D.J. You, B.L. Yi, J. Power Sources 175 (2008) 613-620.

109. M.S. Yazici, D. Krassowski, J. Prakash, J. Power Sources 141 (2005) 171-176.

110. G. Iemmi, D. Macerata, USP 4294893, Graphite-resin composite electrode structure, and a process for its manufacture (1981).

111. K. Fushimi, H. Tsunakaw, K. Yonahara, USP 4551267, Electrically conductive plastic complex material (1985).

112. G. Tomazic, USP 4615108, Process for the manufacture of bipolar electrodes and separators (1986).

113. C. Herscovici, USP 4920017, Porous and porous-nonporous composites for battery electrodes (1990).

114. C. Herscovici, A. Leo, A. Charkey, USP 4758473, Stable carbon-plastic electrodes and method of preparation thereof (1988).

115. D.A. Szánto, Characterization of Electrochemical Filter-Press Reactor, PhD Thesis, University of Portsmouth, UK (1989).

116. K. Roßberg, V. Trapp, Graphite–based bipolar plates. Handbook of Fuel Cells, John Wiley & Sons, Ltd., (2010).

117. E.H. Weber. Development and Modeling of Thermally Conductive Polymer/Carbon Composites, Michigan Technological University, 2001.

118. G.J.W. Radford, J. Cox, R.G.A. Wills, F.C. Walsh, Journal of Power Sources 185 (2008) 1499-1504.

119. Y. Shao, X. Wang, M. Engelhard, C. Wang, S. Dai, J. Liu, Z. Yang, Y. Lin, Journal of Power Sources 195 (2010) 4375-4379.

120. Y.M. Zhang, Q.M. Huang, W.S. Li, H.Y. Peng, S.J. Hu, J. Inorg. Mater. 22 (2007) 1051-1056.

121. B.T. Sun, M. Skyllas-Kazacos, Electrochim. Acta 37 (1992) 1253-1269.

122. H. Kaneko, K. Nozaki, A. Negishi, Y. Wada, T. Aoki, M. Kamimoto, Electrochim. Acta 36 (1991) 1191.

123. A. Paulenova, S.E. Creager, J.D. Navratil, Y. Wei, J. Power Sources 109 (2002) 431-438.

124. J. Gonza´lez-Garcıa, P. Bonete, E. Exposito, V. Montiel, A. Aldaz, R. Torregrosa-Macia, J. Mater. Chem. 9 (1999) 419-426.

125. J.M. Friedrich, C. Ponce-de-León, G.W. Reade, F.C. Walsh, J. Electroanal. Chem. 561 (2004) 203-217.

126. V. Haddadi-Asl, M. Kazacos, M. Skyllas-Kazacos, J. Appl. Electrochem. 25 (1995) 29.

127. X. Li, K. Horita, Carbon 38 (2000) 133-138.

128. M. Santiago, F. Stübera, A. Fortunyb, A. Fabregata, J. Fonta, Carbon 43 (2005) 2134-2145.

129. K. Jurewicz, K. Babe, A. Źió kowskic, H. Wachowska, Electrochim. Acta 48 (2003) 1491-1498.

130. N.S. Jacobson, D.M. Curry, Carbon 44 (2006) 1142-1150.

131. X.G. Li, K.L. Huang, S.Q. Liu, L.Q. Chen, J. Cent. South Univ. Technol. (English Edition) 14 (2007) 51-56.

132. W.H. Wang, X.D. Wang, Electrochim. Acta 52 (2007) 6755-6762.

133. B. Sun, M. Skyllas-Kazacos, Electrochim. Acta 36 (1991) 513-517.

134. C. Fabjan, J. Garche, B. Harrer, L. Jörissen, C. Kolbeck, F. Philippi, G. Tomazic, F. Wagner, Electrochim. Acta 47 (2001) 825-831.

135. M. Mastragostino, S. Valcher, Electrochim. Acta 28 (1983) 501-505.

136. H.Q. Zhu, Y.M. Zhang, L. Yue, W.S. Li, G.L. Li, D. Shu, H.Y. Chen, J. Power Sources 184 (2008) 637-640.

137. P. Han, H. Wang, Z. Liu, X. Chen, W. Ma, J. Yao, Y. Zhu, G. Cui, Carbon 49 (2011) 693-700.

138. Y. Liu, X. Xia, H. Liu, J. Power Sources 130 (2004) 299-305.

139. E. Sum, M. Skyllas-kazacos, J. Power Sources 15 (1985) 179-190.

140. E. Sum, M. Rychcik, M. Skyllas-kazacos, J. Power Sources 16 (1985) 85-95.

141. M. Skyllas-Kazacos, PCT Int. Appl. WO/1989/005526 (1989) 47.

142. B. Tian, C.W.Yan, F.H. Wang, J. Membr. Sci. 234 (2004) 51-54.

143. P. Zhao, H.M. Zhang, H.T. Zhou, B.L.Yi, Electrochim. Acta 51 (2005) 1091-1098.

144. S.H. Ge, B.L. Yi, H.M. Zhang, J. Appl. Electrochem. 34 (2004) 181-185.

145. S.C. Chieng, M. Kazacos, M. Skyllas-Kazacos, J. Power Sources 39 (1992) 11-19.

146. P. Arora, Z. Zhang, Chem. Rev. 104 (2004) 4419-4462.

147. G.J. Hwang, H. Ohya, J. Membr. Sci. 132 (1997) 55-61.

148. D.G. Oei, J. Appl. Electrochem. 15 (1985) 231-235.

149. C.X. Sun, J. Chen, H.M. Zhang, X. Han, Q.T. Luo, J. Power Sources 195 (2010) 890-897.

150. T. Mohammadi, M. Skyllas-Kazacos, J. Power Sources 56 (1995) 91-96.

151. S.C. Chieng, University of New South Wales, Sydney, Australia Ph.D. Thesis (1993).

152. X.F. Li, H.M. Zhang, Z.S. Mai, H.Z. Zhang, I. Vankelecom, Energy Environ. Sci. 4 (2011) 1147-1160.

153. W. Grot, Fluorinated ionomers, William Andrew Inc., Vol. 978 (2008) 10.

154. H. Tasai, T. Horigome, N. Nozaki, H. Kaneko, A. Negishi, Y. Wada, The 31th Denchi Touron Kouengai Yousisyu, Japan (1990) 301-302.

155. M. Skyllas-Kazacos, D. Kasherman, D.R. Hong, M. Kazacos, J. Power Sources 35 (1991) 399-404.

156. T. Mohammadi, M. Skyllas-Kazacos, J. Appl. Electrochem. 27 (1997) 153-160.

157. J.C. Woong, S. Venkataramani, S.C. Kim, Polymer International 55 (2006) 491-499.

158. J. Zeng, C.P. Jiang, Y.H. Wang, J.W. Chen, S.F. Zhu, B.J. Zhao, R.L. Wang, Electrochem. Commun. 10 (2008) 372-375.

159. S. Tan, D. Bélanger, J. Phys. Chem. B 109 (2005) 23480-23490.

160. Q.T. Luo, H.M. Zhang, J. Chen, P. Qian, Y.F. Zhai, J. Membr. Sci. 311 (2008) 98-103.

161. J.Y. Xi, Z.H. Wu, X.G. Teng, Y.T. Zhao, L.Q. Chen, X.P. Qiu, J. Mater. Chem. 18 (2008) 1232-1238.

162. J.Y. Xi, Z.H. Wu, X.P. Qiu, L.Q. Chen, J. Power Sources 166 (2007) 531-536.

163. D. Schulte, J. Drillkens, B. Schulte, D.U. Sauer, J. Electrochem. Soc. 157 (2010) A989-A992.

164. X.G. Teng, Y.T. Zhao, J.Y. Xi, Z.H. Wu, X.P. Qiu, L.Q. Chen, J. Power Sources 189 (2009) 1240-1246.

165. X.G. Teng, Y.T. Zhao, J.Y. Xi, Z.H. Wu, X.P. Qiu, L.Q. Chen, J. Membr. Sci. 341 (2009) 149-154.

166. S.B. Sang, Q.M. Wu, K.L. Huang, J. Membr. Sci. 305 (2007) 118-124.

167. T. Mohammadi, M. Skyllas-Kazacos, J. Membr. Sci. 107 (1995) 35-45.

168. G.J. Hwang, H. Ohya, J. Membr. Sci. 120 (1996) 55-67.

169. X.L. Luo, Z.Z. Lu, J.Y. Xi, Z.H. Wu, W.T. Zhu, L.Q. Chen, X.P. Qiu, J. Phys. Chem. B 109 (2005) 20310-20314.

170. D.Y. Chen, S.J. Wang, M. Xiao, Y.H. Meng, Energy Environ. Sci. 3 (2010) 622-628.

171. J.Y. Qiu, J.F. Ni, M.L. Zhai, J. Peng, H.H. Zhou, J.Q. Li, G.S. Wei, Radiat. Phys. Chem. 76 (2007) 1703-1707.

172. G.J. Hwang, H. Ohya, J. Membr. Sci. 140 (1998) 195-203.

173. Q.T. Luo, H.M. Zhang, J. Chen, D.J. You, C.X. Sun, Y. Zhang, J. Membr. Sci. 325 (2008) 553-558.

174. C. Jia, J. Liu, C. Yan, J. Power Sources 195 (2010) 4380-4383.

175. S.K. Karode, A. Kumar, J. Membr. Sci. 193 (2001) 69-84.

176. A. Frías-Ferrer, J. Gonzalez-Garcia, V.S.E. Expósito, C.M. Sánchez-Sánchez, V. Montiel, A. Aldaz, F.C. Walsh, J. Chem. Edu. 82 (2005) 1395-1398.

177. A. Leo, Energy Research Corporation, Energy Conversion Engineering Conference, 1989. IECEC-89., Proceedings of the 24th Intersociety 3 (1989) 1303-1309.

178. A. Ponce de León, G.W. Reade, I. Whyte, S.E. Male, F.C. Walsh, Electrochim. Acta 52 (2007) 5815-5823.

179. I. Tsuda, K. Kurokawa, K. Nozaki, Photovoltaic Energy Conversion, 1994., Conference Record of the Twenty Fourth IEEE Photovoltaic Specialists Conference - 1994, 1994 IEEE First World Conference 1 (1994) 946-949.

180. R.A. Scannell, F.C. Walsh, J. Inst. Chem. Engr. Symp. Ser. 112 (1989) 59-71.

181. J. Samuel, P. Ridley, WO/2003/069692 - Redox flow battery (2003).

182. I. Nagashima, J. Fukui, H. Gotoh, H. Kaneko, K. Nozaki, T. Ozawa, USP 4814241, 21 March 1989, Electrolytes for redox flow batteries.

183. T. Hennessy, WO/2006/076059 - System and method for optimizing efficiency and power output from a vanadium redox battery energy storage system (2006).

184. M. Skyllas-Kazacos, WO/2008/148148 - Efficient energy storage system using vanadium redox batteries for electricity trading fossil fuel reduction and electricity power cost savings for consumers, 11/12/2008.

185. A. Zocchi, B.M. Broman, WO0176000 - Redox flow battery and method of operating it, 11/10/2001.

186. H.S. Lim, A.M. Lackner, R.C. Knechtli, J. Electrochem. Soc. 124 (1977) 1154-1157.

187. S. Furuta, T. Hirabayashi, K. Satoh, H. Satoh, Proc. 3d Int. Conf. on Batteries for Utility Energy Storage, Kobe, Japan (1991) 49-63.

188. Y. Yamamoto, S. Kagata, T. Taneba, K. Satoh, S. Furuta, T. Hirabayashi, Proc. 3d Int. Conf. on Batteries for Utility Energy Storage, Kobe, Japan (1991) 107-125.

189. C. Menictas, D.R. Hong, D. Hong, Z. Yah, J. Wilson, M. Kazacos, M.Skyllas-Kazacos, The University of New South Wales, Australia http://www.arizonaenergy.org/Analysis/FuelCell/Vanadium%20Battery/vanadium_battery_solar%20DEMONSTRATION%20HOUSE.htm accessed on 1 September 2010.

190. Regenesys™ Energy Storage Facility Environmental Assessment, Appendix B, Description of the Proposed Facility. http://www.tva.gov/environment/reports/regenesys/appendix_b.pdf accessed on 1 September 2010.

191. J.D. Boyes, Sandia National Lab. (2002) http://www.sandia.gov/ess/Publications/Conferences/2002/BOYES%20-%20RegenAndNASMonitoring.pdf accessed on 1 September 2010.

192. B.J. Norris, P. Lex, G.J. Ball, V. Scaini, ZBB (2003) www. zbbenergy. com/papers/solar2002.pdf, accessed on 1 September 2010.

193. K.E. Waldrip, International Flow Battery Forum, Edinburgh, 4-5th May 2011 (2011) 11 - 13.

194. American Electric Power-news release 11 September 2007 Use of large-scale battery technology on its electricity grid.

http://www.aep.com/newsroom/newsreleases/?id=1397 accessed on 1 September 2010.

195. V.P. System Project and Installations, Sorne Hill. http://www.vrbpower.com/applications/projects-tapbury.html accessed on 1 September 2010.

196. B.L. Norris, R.J. Parry, R.M. Hudson, (ZBB), Windpower 2002 Conference (2003) http://www.zbbenergy.com/pdf/technicalpaper_evaluation.pdf accessed on 1 September 2010

197. Prudent Energy Corporation http://www.pdenergy.com/ accessed on 1 September 2010.

198. D.L. Douglas, J.R. Birk, Ann. Rev. Energy 5 (1980) 61-88.

199. D.H. Swan, B. Dickinson, M. Arikara, G.S. Tomazic, IEEE Systems magazine 9 (1994) 20-23.

200. A.H. Swan, B.E. Dickinson, M.P. Arikara, M.K. Prabhu, Publications of Institute of Transportation Studies, University of California, Davis.

201. M. Skyllas-Kazacos, University of New South Wales, Sydney http://www.arizonaenergy.org/Analysis/FuelCell/Vanadium%20Battery/recent_progress_with_the_unsw_va.htm accessed on 1 September 2010.

202. R. Mohammad, S.M. Sharkh, F.C. Walsh, Proceedings of the 5th IEEE Vehicle Power and Propulsion Conference (2009) 551-557.

203. G. Codina, J.R. Perez, M. Lopez-Atalaya, J.L. Vazquez, A. Aldaz, J. Power Sources 48 (1994) 293-302.

204. P. Garces, M.A. Climent, A. Aldaz, An. Quim. 83 (1987) 9-11.

205. Y.D. Chen, K.S.V. Santhanam, J.B. Allen, J. Electrochem. Soc. 128 (1981) 1460-1467.

206. Y.D. Chen, K.S.V. Santhanam, J.B. Allen, J. Electrochem. Soc. 129 (1982) 61-68.

207. J. Jorné, J.T. Kim, D. Kralik, J. Appl. Electrochem. 9 (1979) 573-579.

208. DuPont http://www.fuelcell.com/techsheets/Nafion%201135%20115%20117.pdf accessed on 11 May 2011.

209. SELEMION http://www.selemion.com/SEL3_4.pdf accessed on 11 May 2011.

210. Aciplex http://www.asahi-kasei.co.jp/chemicals/en/specialty/page02.html#aciplex accessed on 11 May 2011.

211. Fumapem http://www.fumatech.com/EN/Products/fumapem/ accessed on 11 May 2011.

212. ASTOM http://www.astom-corp.jp/en/en-main2-neosepta.html accessed on 11 May 2011.

213. Ralex http://www.eetcorp.com/lts/membraneproperties.pdf accessed on 11 May 2011.

214. Ralex. http://www.mega.cz/heterogenous-ion-exchange-membranes-ralex.html accessed on 11 May 2011.

215. PCA http://www.pca-gmbh.com/membrane/pcsa.pdf accessed on 11 May 2011.

216. J.Y. Qiu, L. Zhao, M.L. Zhai, J.F. Ni, H.H. Zhou, J. Peng, J.Q. Li, G.S. Wei, J. Power Sources 177 (2008) 617-623.

217. Plurion Inc. To be the dominant player in the multi billion dollar market for high capacity electricity storage. http://plurionsystems.com/media/Plurion%20Public%20Domain.ppt accessed on 1 September 2010.

218. EA technology Review of electrical energy storage technologies and system of their potential for the UK, DTI report contract no.: DG/DTI/00055/00/00, 2004. http://www.berr.gov.uk/files/file15185.pdf accessed on 1 September 2010.

219. A. Gonzalez, B.Ó. Gallachóir, E. McKeogh, Sustainable Energy Research Group, University College Cork Final Report (2004) http://www.sei.ie/uploadedfiles/FundedProgrammes/REHC03001FinalReport.pdf accessed on 1 September 2010.

220. S.M. Schoenung, W.V. Hassenzahi Long- vs. Short-Term Energy Storage Technologies Analysis. A Life-Cycle Cost Study: A Study for the DOE Energy Storage Systems Program. http://prod.sandia.gov/techlib/access-control.cgi/2003/032783.pdf accessed on 1 September 2010.

221. P. Denholm, G.L. Kulcinski, Energy Conversion and Management 45 (2004) 2153-2172.

222. K.L. Huang, X.G. Lia, S.Q. Liu, N. Tan, L.Q. Chen, Renewable Energy 33 (2008) 186-192.

223. A. Price, S. Male, M. Kleimaier, VDI Berichte 1734 (2002) 47-56.

224. R. Baxter, Energy Storage - A nontechnical guide, Electricity Storage Association, Penn Well Books, (2006).

225. Electricity Storage Association http://www.electricitystorage.org/tech/technologies_technologies.htm accessed on 1 September 2010.

226. Plurion Limited http://plurion.co.uk accessed on 1 September 2010.

227. Sumitomo Electric Industries Ltd. http://global-sei.com/ accessed on 1 September 2010.

Chapter 3

Theory

Chapter 3 Theory

3.1. Redox reactions at the electrodes

Electrochemical reactions occur via the transfer of charge across the interface between an electrode and an electrolyte. An electrochemical cell used to study a particular reactions, usually consists of three electrodes: a working electrode, a counter electrode and a reference electrode. The working electrode is the electrode at which the reaction of interest takes place, while the counter electrode is used to close the circuit with the electrolyte and the reference electrode is used to accurately measure the potential of the working electrode. The cell voltage of an electrochemical system is the potential across the working and counter electrodes.

A simple electron-transfer reaction in an aqueous solution may be represented as:

$$O + e^- \leftrightarrow R \qquad (1)$$

where O and R are the oxidized and reduced species, respectively.

Figure 3.1. shows the pathway of a general electrode reaction that involves several stages, (1) mass transport of reactant towards electrode (by diffusion or convection), (2) surface adsorption of reactant, (3) charge transfer, (4) surface desorption and (5) the removal of product.

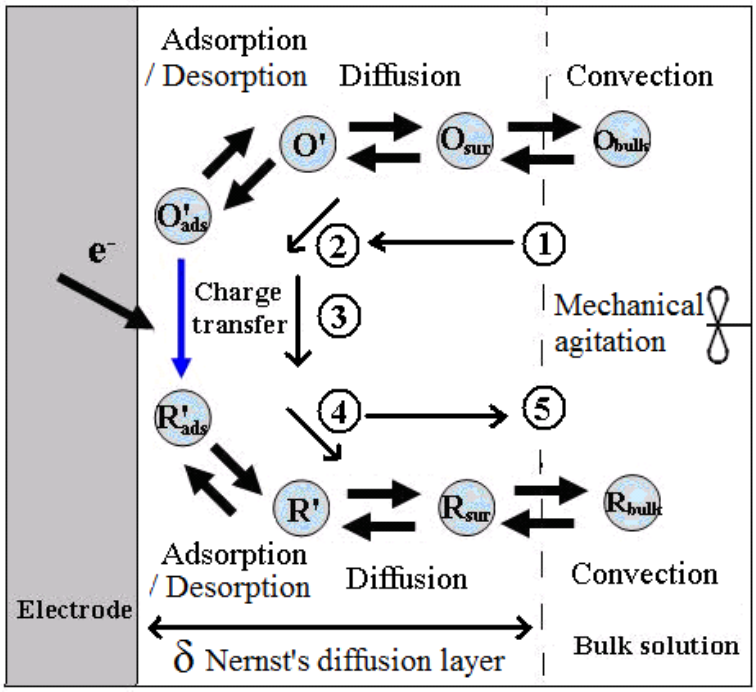

Figure 3.1. Process involved in an electrode reaction.

A typical electron transfer reaction requires the reactant species to be located within molecular distances of the electrode surface. At the electrode surface of a cathodic process, the reactant, species 'O' is reduced by gaining electron(s) to form a product, species 'R'. In addition to a charge-transfer process, the rates of reactant supply to the electrode surface and the removal of the product, can limit the rate of the overall reaction. This process is known as a mass-transport process, which mainly includes diffusion and convection. Diffusion dominates within the Nernst's diffusion layer, the effective thickness depends on the degree of mass transport from the bulk of solution, diffusion coefficient and solution viscosity. Forced convection, such as stirring or mechanical agitation, effectively enhances the transport of the material towards the electrode. In this chapter, the theoretical relationship between the current, the potential and the concentrations of the oxidant and the reduced species in the processes of charge-transfer and mass-transport are discussed.

3.1.1. *Faraday's law of electrolysis*

Faraday's law states that the electrical charge transferred through the electrode surface is proportional to the mass of the species generated or consumed at the electrode surface during electrolysis. Considering the volume of the electrolyte, the Faraday's law can be written as:

$$c = Q / (n\ F\ V) = I\ t / (n\ F\ V) \quad (2)$$

where c is the concentration [mol dm^{-3}] of a species generated or consumed over a period of time, t [s] at certain current, I [A], V is the electrolyte volume [m^3], F is the Faraday constant, [9,6485.3 C mol^{-1}] and n is the number of electrons involved in the reaction.

3.1.2. *Thermodynamics and the Nernst's equation*

From the thermodynamic point of view, the maximum amount of energy that can be extracted from a chemical reaction is the predicted available energy, known as the Gibbs free energy ΔG. In a redox flow battery, this chemical energy is transformed into electrical energy. When the reaction is at equilibrium, no net current flows and the cell shows the maximum cell voltage. With such cell voltage, the largest possible predicted work done can be evaluated and should be equal to the Gibbs free energy [J mol^{-1}] by definition as:

$$W_{max} = \Delta G = - n\ F\ E_{cell} \quad (3)$$

where E_{cell} is the *maximum cell voltage* [V], also known as the open-circuit potential (OCP) or the equilibrium potential. When the activity of each product and reactant is unity, equation (3) can be written as

$$\Delta G^0 = - n\ F\ E^0_{cell} \quad (4)$$

E^0_{cell} is known as the *standard electrode potential of the cell* (E^0 [V]) and relates to the *standard Gibbs free energy change* (G^0 [J mol^{-1}]). When $\Delta G^0 < 0$ the reaction is spontaneous and no energy is needed, while when $\Delta G^0 > 0$ an external energy source is required to drive the reaction forward. The law of mass action states that the rate of a chemical reaction is proportional to the product of the effective concentration of each participating molecule.

At chemical equilibrium of a system, the elements of the reaction mixture remain unchanged after the chemical reaction as the following:

$$aA + bB + ... \rightleftharpoons cC + dD + ... \tag{5}$$

where *a*, *b*, *c*, *d* …. are the stoichiometric factors and A, B, C, D are the elements of reactants and products.

The rate of forward reaction is equal to the rate of the reversion reaction, the activities of the reactants is hence proportional to the activities of the reaction products. The equilibrium constant *K* can be expressed as:

$$K = \frac{a_C^c \; a_D^d + ...}{a_A^a \; a_B^b + ...} \tag{6}$$

In equation (6), the activity of each substance is raised to a power equal to the number of moles of the corresponding substances in the reaction. In the case of a chemical equilibrium, Gibbs free energy ΔG can be expressed as the activity change in the electrolyte.

$$\Delta G = \Delta G^0 + RT \ln K \quad (7)$$

where R is the molar gas constant (8.3145 J mol^{-1} K^{-1}) and T [K] is the temperature. The activity is the thermodynamically effective concentration and can be expressed as:

$$a = \gamma \ c \quad (8)$$

where c is the species concentration and γ is the activity coefficient. The activity coefficient approaches unity at low concentration

$$\lim_{c \to 0} \gamma = 1 \quad (9)$$

For a simple half-cell reaction, as in equation (1), the Gibbs free energy can hence be expressed as:

$$\Delta G = \Delta G^0 + R \ T \ln [O] / [R] \quad (10)$$

The Gibbs free energy ΔG comprised the Gibbs free energy in its standard state, ΔG^0, at unity activity of each reactant and product and a variable term of a function of the temperature and the concentrations of the reduced and oxidized species. By combining equations (3), (4) and (10), the relationship between the cell potential and the concentrations of the electroactive species at the chemical equilibrium is obtained, which is also known as the *Nernst equation*:

$$E = E^0 + (R \ T / N f) \ln [O] / [R] \quad (11)$$

During battery discharge, the redox reactions in a zinc-cerium flow battery are as follows.

The negative electrode becomes anode due to the oxidation of metallic Zn into Zn(II) species,

$$\text{Oxidation: } Zn - 2e^- \rightarrow Zn^{2+} \qquad E^0 = -0.76 \text{ } vs. \text{ SHE} \quad (12)$$

The positive electrode becomes a cathode due to the reduction of Ce(IV) to Ce(III), assuming that the standard electrode potential of cerium reaction in methanesulfonate medium is similar to that in nitrate medium.

$$\text{Reduction: } 2Ce^{4+} + 2e^- \rightarrow 2Ce^{3+} \qquad E^0 = +1.67 \text{ } vs. \text{ SHE} \quad (13)$$

(Nitrate medium)

The calculation of the cell voltage of this system is the difference between the standard electrode potential values of the cathodic and the anodic half-cell reactions:

$$E^0_{cell} = E^0_{cathode} - E^0_{anode} \quad (14)$$

Assuming that the battery is operating under standard conditions, the cell voltage during battery discharge can be expressed as:

$$E^0_{cell} = E^0_{Ce\ cathode} - E^0_{Zn\ anode} = 1.67 \text{ V} - (-0.76) \text{ V} = 2.43 \text{ V} \quad (15)$$

During battery charge, the reactions occur in a different direction, the net cell reaction is reversed when the current through the cell is made to flow in the opposite direction. Hence, the negative electrode becomes a cathode and positive electrode becomes an anode.

$$E^0_{cell} = E^0_{Zn\ cathode} - E^0_{Ce\ anode} = -0.76 \text{ V} - (1.67) \text{ V} = -2.43 \text{ V} \quad (16)$$

By using equation 10, the predicted standard free energy change to charge and discharge a zinc-cerium battery can be estimated.

Battery charge: $\Delta G^0 = -(2)\,F\,(-2.43) = +468.9$ KJ (17)

Battery discharge: $\Delta G^0 = -(2)\,F\,(+2.43) = -468.9$ KJ (18)

The negative value indicates that discharge of a zinc-cerium battery is a spontaneous cell reaction and has high driving force, while during charging the battery requires an energy input to take place.

3.1.3. *Charge-transfer reaction*

Considering the simple electron-transfer reaction, equation (1), a flux of ions must take place in the electrolytic phase to balance the charge transfer interface at the electrode/ electrolytic interface at both zinc and cerium electrodes. The net current density of an electrochemical reaction, j [A m^{-2}], can be viewed as the difference between the partial cathodic (reduction) current density, $\overleftarrow{j}$ [A m^{-2}], and the partial anodic (oxidation) current, $\overrightarrow{j}$ [A m^{-2}]:

$$j = \overleftarrow{j} - \overrightarrow{j} \tag{19}$$

Each of these current densities is proportional to their corresponding heterogeneous rate constant, k_f [cm s^{-1}] and k_b [cm s^{-1}], for the forward reduction and backward oxidation electrode reactions, respectively. The partial cathodic current density of each electrode can be expressed as:

$$\overleftarrow{j} = \mathrm{n\,F}\,k_f\,C_O(0,t) \tag{20}$$

while the partial anode current density of each electrode can be expressed as:

$$\overrightarrow{j} = \mathrm{n\,F}\,k_b\,C_R(0,t) \tag{21}$$

where F is Faraday's constant and $C_u(x,t)$ [mol cm^{-3}] is the concentration of species u at the distance x [cm] from the electrode at the time t [s]. Considering the reactions at the electrode surface, x is equal to 0. The forward and reverse rate constants depend on the electrode potential with respect to a reference electrode and can be written as a function of the standard heterogeneous rate constant, k^0 [cm s^{-1}]:

$$k_f = k^0 e^{-\alpha f(E-Eeq')} \quad (22)$$

$$k_b = k^0 e^{(1-\alpha) f(E-Eeq')} \quad (23)$$

where the coefficient $f = F/(RT)$, E_{eq} is the equilibrium potential [V] and α is the transfer dimensionless coefficient with values between 0 and 1, and is often estimated to be 0.5 or determined by Tafel slope at charge transfer region (section 3.1.5). By dividing the expressions for the rate constants from equations (22) and (23), the equation governing the electrode kinetics is represented as the following:

$$k_b / k_f = e^{f(E-Eeq')} \quad (24)$$

Combining equations (18) – (23), the total current of the reaction under charge transfer controlled kinetics can be described by the *current vs. potential* relationship due to Butler and Volmer equation:

$$j = nF k^0 [C_O(0,t) e^{-\alpha f(E-Eeq')} - C_R(0,t) e^{(1-\alpha) f(E-Eeq')}] \quad (25)$$

3.1.4. *An electrode surface under equilibrium condition*

When an electrochemical reaction at an electrode is at equilibrium, there is no net current, because the system contains a cathodic current balanced by an equal magnitude opposite anodic current:

$$j_0 = \overleftarrow{j} = \overrightarrow{j} \tag{26}$$

where j_0 is the exchange current density, a kinetic parameter of a particular reaction on a particular electrode.

Since anodic and cathodic current densities are at equilibrium, the exchange current density can be written as the following according to equation (25):

$$j_0 = n\ F\ k^0\ C_O^*\ e^{-\alpha f(E-Eeq')} \quad (\text{or } j_0 = n\ F\ k^0\ C_R^*\ e^{(1-\alpha)\ f(E-Eeq')}) \tag{27}$$

By substituting equations (20) and (21) into equation (24),

$$e^{f(E-Eeq')} = C_O^*\ /\ C_R^* \tag{28}$$

If both sides of equation (28) are raised to the – α power and substitute into equation (27), the exchange current density can be arranged as:

$$j_0 = F\ k^0\ C_O{}^{*(1-\alpha)}\ C_R{}^{*\alpha} \tag{29}$$

where C* [mol cm^{-3}] is the bulk concentration for the species of a reactant or an oxidant. The exchange current density is the rate at which oxidized and reduced species transfer electrons with the electrode at the equilibrium. It is a measure of the electrocatalytic properties of the electrode material for a given reaction.

3.1.5. *An electrode surface under non-equilibrium condition*

For a non-spontaneous cell reaction to occur, an overpotential, η [V], must be applied over and above the equilibrium potential, E_{eq} [V] to drive the reaction forward. The overpotential can be written as:

$$\eta = E - E_{eq} \tag{30}$$

Figure 3.2. shows three cases: (1) net cathodic, (2) no net current and (3) net anodic current. The anodic and cathodic currents can be driven by the sign and the magnitude of an overpotential. The resulting current density is the algebraic sum of the partial cathodic and anodic current densities.

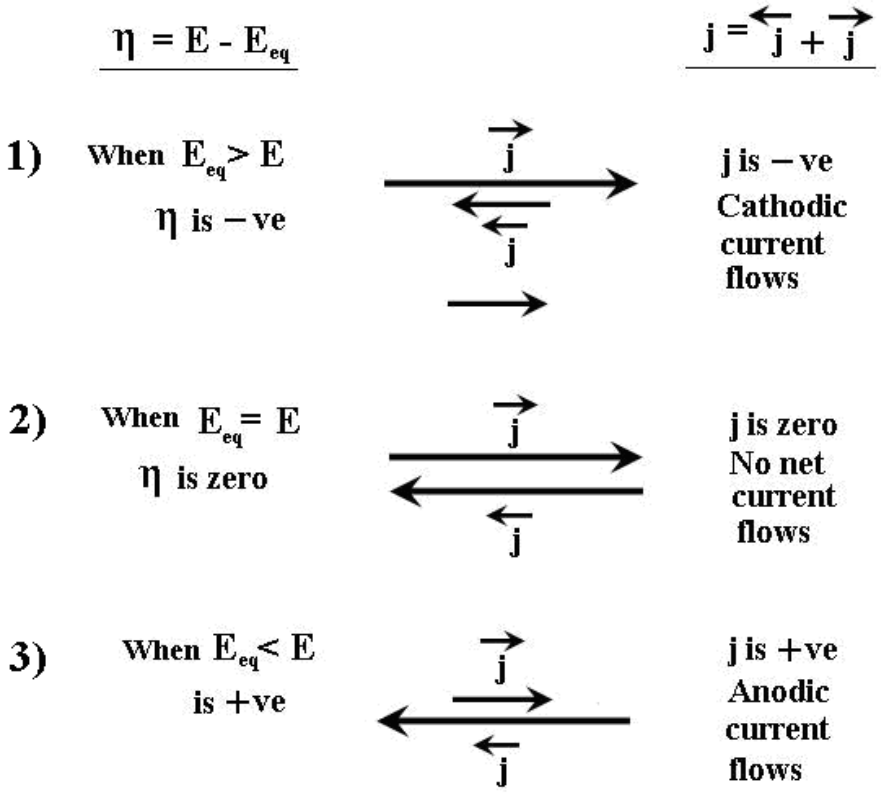

Figure 3.2. Three cases of different magnitude and size of an overpotential.

In order to calculate the current at certain value of the overpotential, the *current–overpotential equation* relationship can be obtained from equations (25) and (29):

$$j = j_0 [(C_o(0,t) / C_o^*) e^{-\alpha f \eta} - (C_R(0,t) / C_R^*) e^{(1-\alpha) f \eta}] \quad (31)$$

With efficient mass transport, the concentrations in the bulk solution and at the electrode surface ($x = 0$) are equal and equation (31) can be simplified to the following expression:

$$j = j_0 [e^{-\alpha f \eta} - e^{(1-\alpha) f \eta}] \quad (32)$$

This equation is known as the Butler-Volmer equation and can be used to predict the current when the mass-transport effect is eliminated. This approximation is useful when j is less than 10 % of the limiting current density, j_{lim} and in a well-stirred solution where diffusion of the electroactive species to the electrode surface is not a limiting factor in the experiment.

The exchange current density can be estimated experimentally from the plot of $\log|j|$ *vs.* η, also known as the Tafel plot. By using the set of data when overpotential is small (< 118 mV) under charge-transfer control, Tafel plot is useful for estimating kinetics parameters such as α and $j_{0.}$ When the overpotential is lower than 10 mV, Butler-Volmer equation (equation 32) is used to evaluate the current–overpotential relationship.

For large value of η (either positive or negative values), $e^{(1-\alpha) f \eta}$ becomes negligible and equation (32) becomes:

$$j = j_0 e^{-\alpha f \eta} \quad (33)$$

$$\eta = RT/\alpha F (\ln j_0 - \ln j) \quad (34)$$

By converting to decimal logarithms, equation (29) becomes:

$$\eta = 2.3RT/\alpha F \ (\log j_0 - \log j) \qquad (35)$$

As shown in Figure 3.3, there is an anodic branch with a gradient of $\alpha F / 2.3RT$ and a cathodic branch of a gradient $(1-\alpha) F / 2.3RT$. At 298 K, for a one electron transfer reaction and $\alpha_c = 0.5$, Tafel slope is 118 mV decade^{-1} by substituting in equation 35. Both linear segments extrapolate to an intercept of log j_0. Hence, the exchange current density that estimates the reaction rate at zero overpotential, can be calculated. At large overpotential (>118 mV), the reaction is probably under mixed or mass transport control, the gradient obtained experimentally will be lower than the Tafel slope due to the mass-transport limitation.

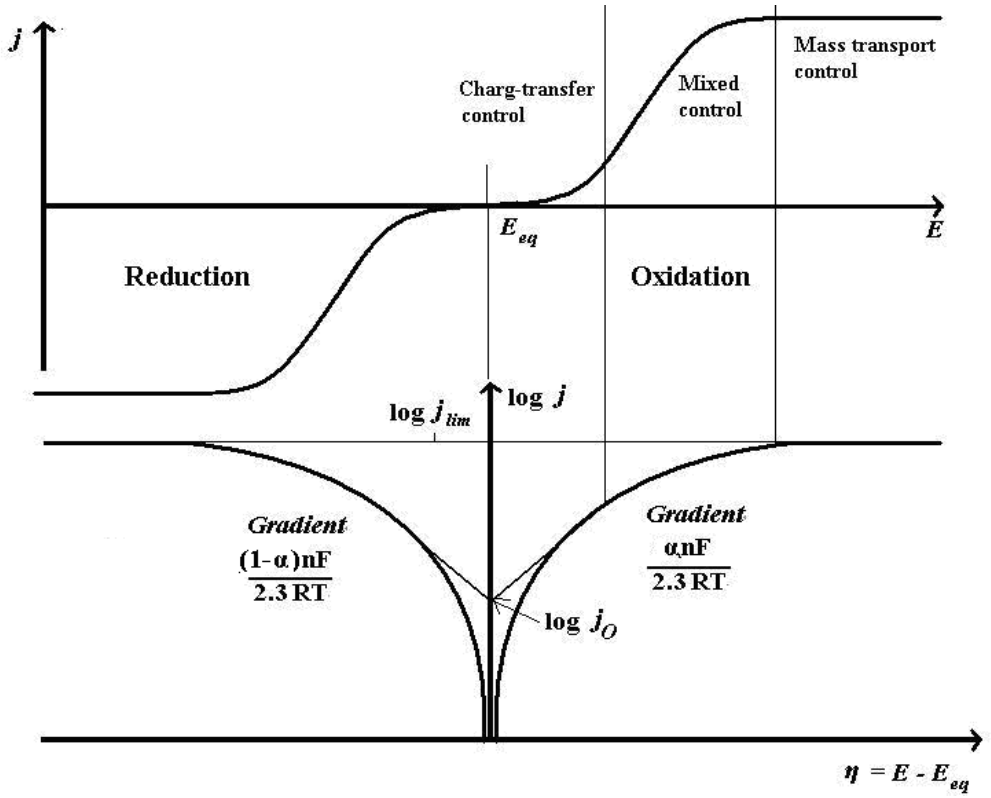

Figure 3.3. Semilogarithmic plot of current density *vs.* overpotential under charge-transfer, mixed and mass transport control.

3.2. Mass transport reaction

Mass transport involves the supply of reactants to the electrode surface and the removal of the products. The rate of mass transport is usually important when the reactant concentration is low or a high rate of reaction is required. In general, the contribution to mass transport includes: (1) Migration, (2) Diffusion and (3) Convection. The driving and nature of these three transport modes is indicated in Table 3.1.

Contribution to mass transport	**Driving force**	**Comment**
MIGRATION	Potential gradient	Ions move due to the potential difference between electrodes. Migration is not specific to electroactive species.
DIFFUSION	Concentration gradient	Always occurs close to electrode when current passes and chemical change occurs.
CONVECTION	External mechanical forces	Flow of solution, movement of electrode, gas sparking, natural convection due to thermal or density differences.

Table 3.1 The driving and the nature forces of the three mass transport modes.

3.2.1. *Migration*

Migration is the movement of ions due to the electrostatic attraction between the electrodes and the electrolytic ions at the presence of an electric field. In general, the rate at which the ions migrate to or away from an electrode surface increases with the applied

current or electrode potential. From the following equation, it can be seen that a charged particle at an electric field accelerates until reaching the constant drift velocity V_d [m s^{-1}]:

$$V_d = u\,E \tag{36}$$

where u is the electric mobility [m^2 V^{-1} s^{-1}] and E is the electric field gradient [V m^{-1}]. In general, the current due to migration is negligible for the oxidized or reduced electroactive species which are at low concentrations. The majority of the migration current is carried out by non-electractive species called the supporting electrolyte which is added at high concentration. The addition of the supporting electrolyte can not only eliminate the contribution of migration to the mass transfer of the electroactive species but also decreases the solution resistance and hence the uncompensated resistance drop.

3.2.2. *Diffusion*

Diffusion is a spontaneous and random movement of a species from a region of higher concentration to a low concentration. Fick's first law states that the diffusion is proportional to the concentration gradient (Figure 3.4).

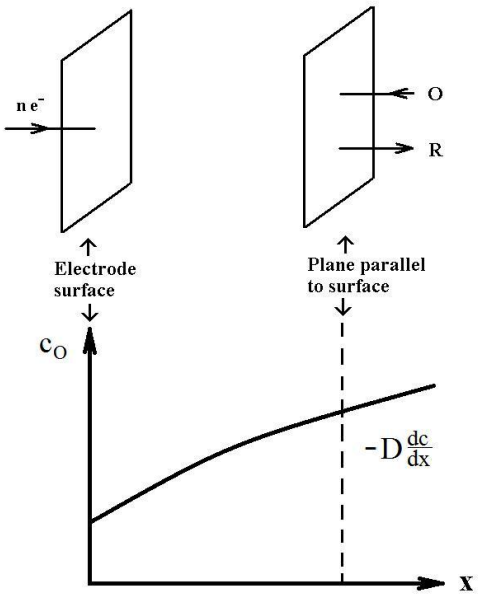

Figure 3.4. Fick's law for linear diffusion.

Hence, the rate of movement by diffusion can be predicted as:

$$N = j / n F = – D \, dc / dx \qquad (37)$$

where N is the diffusional flux of a species, dc/dx is the concentration gradient and D is the diffusion coefficient or diffusivity of the species. The negative sign signifies that the diffusion movement is from the region of high concentration to that of lower. In a diffusion process as shown in Figure 3.5, the flux balance between the flux of electrons on the electrode and the soluble species in the electrolyte exists due to the mass conservation as follows:

Reactant loss flux = electron transfer flux = product formation flux

$$-D_O (dc_o / dx)_{x=} = \quad j / n F \quad = \quad D_R (dc_R / dx)_{x=0} \qquad (38)$$

In the case of zinc electrodeposition at the negative, metallic zinc was deposited and accumulated on the carbon substrate, hence no reaction product is removed from the electrode surface.

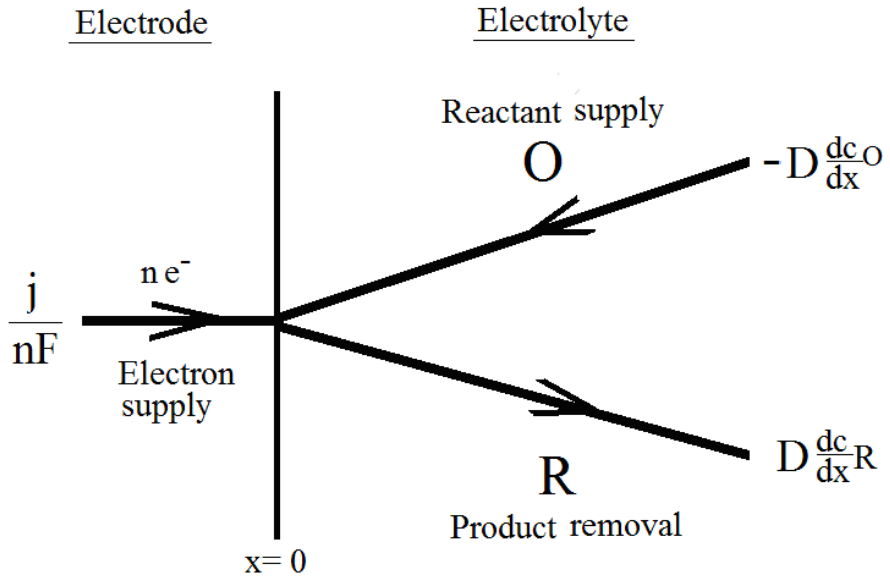

Figure 3.5. Flux balance perpendicular to the surface.

3.2.3. *Convection-diffusion*

Reactants and products can be transferred to or from an electrode by mechanical sources of natural convection. Mechanical agitation includes movement of an electrode or an electrolyte by techniques, such as reciprocation, vibration or rotation using pump, stirring or a flow of gas. Natural convection is generated by the small thermal or density differences in the electrolyte layer near the electrode, in which the movement is random and unpredictable. Forced convection can be controlled by rotating electrodes or controlled fluid flow and can be described by the Nernst diffusional layer model.

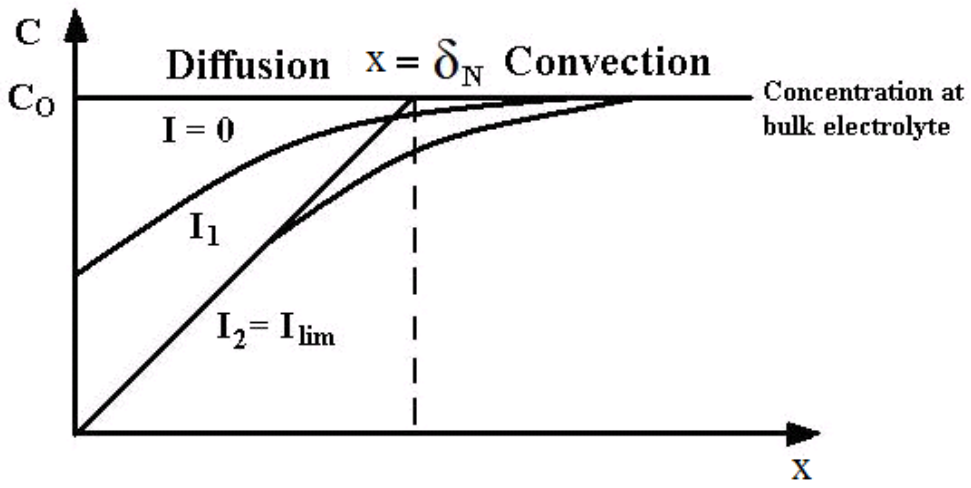

Figure 3.6. The Nernst diffusion layer profile and the reactant concentration versus distance profiles at different applied current densities.

As shown in figure 3.6, the electrolyte layer close to the electrode surface can be divided into two zones. Close to the electrode surface, there is a totally stagnant layer with a thickness, δ_N, where diffusion due to concentration differences dominates. Outside this region (at x >= δ_N,), it is convection controlled. In reality, there is a gradual transition of concentrations rather than two distinct regions as mass transport is neither pure

diffusion nor pure convection controlled at x = δ_N. At open circuit where no electrochemical net reaction takes place, the concentration of reactant is the same as in the bulk electrolyte value, c_o. However, if a current, I_1, is applied, O is converted to R and the reactant concentration eventually declines near the electrode surface. Further increase the applied current to I_2, will decrease the reactant concentration making the concentration gradient more pronounced and eventually reaching zero in the limiting case. This current is often regarded as the limiting current, I_L, which is ideally independent of electrode potentials and can be expressed as a function of reactant concentration at bulk electrolyte and the Nernst diffusion layer thickness:

$$I_L = A\ n\ F\ D\ C / \delta_N \tag{39}$$

where A is the active electrode area [cm^2], D is the diffusion coefficient [$cm^2\ s^{-1}$] and δ_N is the Nernst diffusion layer [cm].

Although the concept of a diffusion layer has been studied extensively, the length of diffusion layer is often difficult to measure experimentally. Hence, the equation is often used by electrochemical engineers as:

$$I_L = A\ n\ F\ D\ k_m\ C \tag{40}$$

where k_m, the mass transport coefficient [$m\ s^{-1}$] and is defined as the ratio of the diffusion coefficient to the Nernst diffusion layer thickness:

$$k_m = D / \delta_N \tag{41}$$

Since k_m is highly influenced by the electrolyte flow conditions and the reactor geometry, it is generally found that a relationship between k_m and v^a as expressed in relationship (42).

$$k_m \ \alpha \ v^a \tag{42}$$

where v is the characteristic velocity, such as the mean linear flow velocity of the electrolyte and a is the velocity exponent, which typically lies between 0.3 and 1 and is highly dependent on the electrode geometry and the flow regime.

3.2.3.1. *Dimensionless quantities*

Dimensionless quantities are important for design and scale-up applications in engineering. Common dimensionless groups include Reynolds number (*Re*), Sherwood number (*Sh*) and Schmidt number (*Sc*) are usually used to characterise the flow conditions of an electrolyte in particular reactor geometry. The expressions of common dimensionless groups are summarized in Table 3.2.

Dimensionless Group	Definition	Eq.
Reynolds number,	$Re = \mathrm{v}\, l / \nu$	(43)
Sherwood number	$Sh = k_m\, l / D$	(44)
Stanton number	$St = k_m / \nu$	(45)
Schmidt number	$Sc = \nu / D$	(46)

Table 3.2. Common dimensionless group used in electrochemical engineering under mass transport flow condition. v is the characteristic velocity, l is the characteristic length, ν is the kinematic viscosity, k_m is the mass transport coefficient, D is the diffusion coefficient.

By combining equations (41) and (44), Sherwood number can be rewritten as a function of Nernst diffusion layer thickness, δ_N :

$$Sh = 1 / \delta_N \quad (47)$$

The characteristic length and the characteristic velocity depend upon the reactor or electrode geometry. In any case, the characteristic length chosen for the Reynolds number must be the same with that chosen for the Sherwood Number and vice versa. As shown in Figure 3.7, a parallel plate filter-press cell was used as the flow battery in this work. The characteristic length for defining both Reynolds and Sherwood numbers is the equivalent hydraulic diameter, d_e, which is defined by the following expression:

$$d_e = 4\ B\ S\ /\ (2B + 2S) = 2\ B\ S\ /\ (B + S) \quad (48)$$

where B and S are the breadth of the channel and the electrode separation, respectively. The electrode separation can be referred as the electrode-membrane gap in a divided cell and the gap between two electrodes in an undivided system. The characteristic velocity is the mean linear flow velocity, which is based on the cross sectional area for the flow (B $\times$ S).

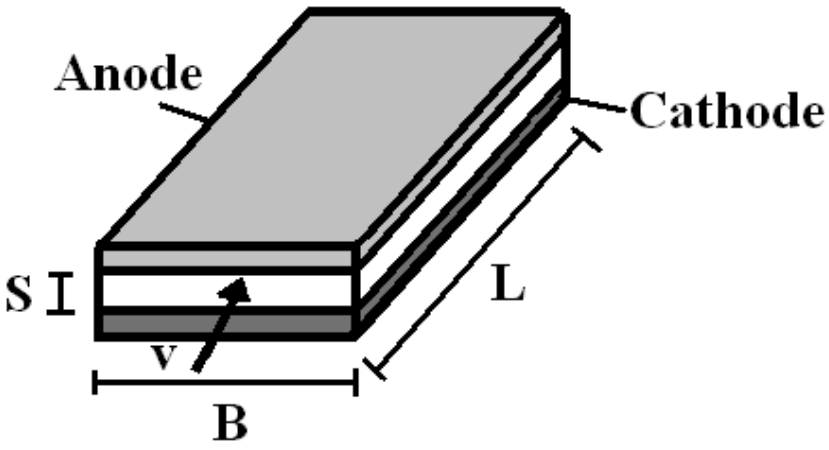

Figure 3.7. Schematic of electrolyte flowing through an undivided parallel plate filter-press cell.

The correlation of the dimensionless group can be taken as the following general form:

$$Sh = \text{a}\ Re^{\text{b}}\ Sc^{\text{c}}\ Le^{\text{d}} \quad (49)$$

where a, b, c, d are constants that can be obtained empirically from the experiment. Le is the dimensionless length quantity, which is the ratio of hydraulic diameter to the length of the electrodes in the direction of flow.

For simplicity, constants c and d are usually assumed to be 1/3 and 1, respectively. Hence, the empirical correlation usually takes the form:

$$Sh = \text{a}\ Re^{\text{b}}\ Sc^{0.333} \quad (50)$$

3.3. Figures of merit

The main figures of merit defined for a redox flow battery are:

3.3.1. *Cell voltage*

For self-driving system, such as flow battery, cell voltage operating away from equilibrium contains several components: cathode potential, $E_{C,}$ anode potential, E_A, ohmic drop within the cell, IR_{CELL}, and in the electrical circuit, IR_{CIRC}:

$$E_{CELL} = E_C - E_A - IR_{CELL} - IR_{CIRC} \quad (51)$$

The predicted available cell voltage decreased by the ohmic components within the cell and the electrical circuit. Equation (51) can be rewritten in the form of the equilibrium electrode potentials, E_e, and the overpotentials, η as follows:

$$E_{CELL} = (E_e^{\text{C}} - E_e^{\text{A}}) - |\eta_C| - |\eta_A| - IR_{CELL} - IR_{CIRC} \quad (52)$$

Overpotentials at each electrode are required to overcome the activation energy of each half cell reaction. The rate of the reaction is highly dependent on the magnitude of the overpotential, $|\eta|$. For instance, a fast reaction might require smaller overpotential and a low reaction require larger overpotential.

3.3.2. *Current efficiency*

Current efficiency, also known as Faradaic efficiency, is the ratio between the theoretically calculated mass of the products generated in an electrochemical reaction and the mass obtained experimentally.

$$\varphi = (m_{experimental} / m_{theoetical}) \times 100 \quad (53)$$

The theoretical value of the mass generated can be calculated by using Faraday's law - equation (2). This efficiency describes the efficiency of how charge is transferred into a reaction conversion. Inefficiencies are due to the secondary reactions, usually side-reactions, other than the intended reaction taking place at the electrode.

3.3.3. Coulombic efficiency

Coulombic or charge efficiency is the ratio of the electrical charge released from the battery during discharge to the charge used at battery charge.

$$\eta_{\text{Columbic}} = Q_{\text{Discharge}} / Q_{\text{Charge}} = I_{\text{Discharge}}\, t_{\text{Discharge}} / I_{\text{Charge}}\, t_{\text{Charge}} \quad (54)$$

where Q is the electrical charge [C], I is the current [A] and t is the time [s] during battery charge or discharge. The loss in coulombic efficiency is mainly due to the side reactions as well as the ion-transfer across the membrane.

3.3.4. *Voltage efficiency*

Voltage efficiency is the ratio of cell voltage between discharge and charge of a battery, which describes the losses in the potential term through Ohmic resistance within the cell and the electrical circuit as well as the overpotential (or polarization) losses during charge/ discharge cycles.

$$\eta_{\text{Voltage}} = V_{\text{Discharge}} / V_{\text{Charge}} \quad (55)$$

Voltage efficiency can be enhanced by decreasing the resistance of electrical contact, wiring, electrode, electrolyte and membrane and by improving the electro-catalytic properties of the electrodes used in the redox reactions of a battery.

3.3.5. *Energy efficiency*

Energy can be expressed as a product of cell voltage, current and the reaction time. Energy efficiency (Electrical energy) is the ratio of the energy released from the battery during discharge to the energy supplied to the battery during charge. In this work, it is also written as round-trip DC energy efficiency, which does not include the energy consumed by the pump and temperature controlling devices.

$$\eta_{\text{Energy}} = E_{\text{Discharge}} / E_{\text{Charge}} = V_{\text{Discharge}} I_{\text{Discharge}} t_{\text{Discharge}} / V_{\text{Charge}} I_{\text{Charge}} t_{\text{Charge}} \quad (56)$$

which can also be represented as:

$$\eta_{\text{Energy}} = \eta_{\text{Coulombic}} \eta_{\text{voltage}} \quad (57)$$

3.3.6. *Electrolytic energy consumption*

The electrolytic energy consumption, W_{CELL} [W], can be expressed as the power cost for the total cell resistance, R_{CELL} [Ω], as given by equation (51).

$$W_{CELL} = I\, E_{CELL} = I^{2}\, R_{CELL} \tag{58}$$

Sometimes, it can be represented by referring to a unit amount, mass or volume of an electroactive species via Faraday's Law. The molar energy consumption, $E_{S,amount}$ [J mol^{-1}], can be given by:

$$E_{S,amount} = W_{CELL} / m = - n\, F\, E_{CELL} / \varphi \tag{59}$$

where m is the number of mols [mol] and φ is the current efficiency [dimensionless].

The specific energy consumption, $E_{S,mass}$ [J kg^{-1}], is:

$$E_{S,mass} = W_{CELL} / w = - n\, F\, E_{CELL} / \varphi\, M \tag{60}$$

where w is the mass [kg] and M is the molecular weight [kg / mol].

The volumetric energy consumption, $E_{S,mass}$ [J m^{-3}], is:

$$E_{S,mass} = W_{CELL} / V_{m} = - n\, F\, E_{CELL} / \varphi\, V_{m} \tag{61}$$

where V_m is the molar volume [m^3 / mol].

Chapter 4

Experimental details and apparatus

Chapter 4 Experimental details and apparatus

4.1. Chemical reagents and solutions

All chemicals reagents, shown in Table 4.1, are used as received from the supplier without further purification. All solutions were prepared with ultrapure water (18 M Ω cm resisitivity, Elga Elgastat UHQ PS). Since there is no methanesulfonate salt commercial available for electroactive species, such as zinc, cerium and sodium, these salts were prepared by stirring metal carbonate (zinc carbonate basic: Fluka Analytical 96466; cerium carbonate: Treibacher; sodium carbonate: Alfa Aesar A17484) in aqueous methanesulfonic acid (Sigma Aldrich 471348) using a PTFE-coated steel magnetic stirrer bar to convert carbonate into the methanesulfonate following the reactions (1), (2) and (3) below, respectively:

Zinc (II) methanesulfonate:

$$[ZnCO_3]_2 \cdot [Zn(OH)_2]_3 + 10CH_3SO_3H \rightarrow 5\,Zn(CH_3SO_3)_2 + 2CO_2 + 8H_2O \qquad (1)$$

Cerium (III) methanesulfonate:

$$Ce_2(CO_3)_3 + 6CH_3SO_3H \rightarrow 2Ce(CH_3SO_3)_3 + 3CO_2 + 3H_2O \qquad (2)$$

Sodium (I) methanesulfonate:

$$Na_2CO_3 + 2CH_3SO_3H \rightarrow 2\,NaCH_3SO_3 + CO_2 + H_2O \qquad (3)$$

Chemicals	Comment	Suppliers
Zinc (II) carbonate basic	$[ZnCO_3]_2 \cdot [Zn(OH)_2]_3$ purum p.a., ≥58% Zn basis Molecular weight = 548.96	Fluka
Cerium (III) carbonate	$Ce_2(CO_3)_3 \cdot x\ H_2O$, 99 % purity Molecular weight = 460.27	Treibacher Industrie AG., Germany
Sodium (I) carbonate	$Na_2CO_3 \cdot 10\ H_2O$, 99.5 % purity Molecular weight = 286.14	Alfa Aesar
Methanesulfonic acid	CH_3SO_3H, 70 vol. % (Sigma Aldrich), 99.8 % (BASF) Molecular weight = 96.11	Sigma Aldrich, BASF
Ultra-pure water	18 MΩ cm resisitivity, Elgastat UHQ PS	ELGA
Nitrogen (oxygen free)	99.99 % purity	BOC Gases
Electrolytic additives	-	Sigma Aldrich, Fluka

Table 4.1. List of chemical reagents used in the electrochemical studies.

4.2.Cyclic voltammetry

Cyclic voltammetry was carried out in a divided, three-electrode electrochemical cell like the one shown in Figure 4.1. The electrolyte volume of the working electrode compartment was approximately 120 cm^3. This glass cell was equipped with a water jacket connected to a Grant LV FG water thermostat controller. The temperature was varied in the range of 20 – 60 ^oC. For the half-cell reactions of zinc and cerium, the working electrodes (area: 0.13 cm^2) were static glassy carbon and platinum disc electrodes, respectively. The counter electrode was a platinum mesh (area: 1 cm × 1 cm). The working and counter electrode compartments were separated by a Nafion® membrane (Dupont, NF117/H^+). This arrangement precluded the products formed at the counter electrode from reacting with the working electrode. The silver/silver chloride reference electrode (ABB instrumentation Ltd) was located at approximately 2 mm from the rotating disc electrode surface via a Luggin capillary. The electrochemical instrumentation was a Metrohm Autolab potentiostat (PGASTAT20) with Electrochemical software (GPES Version 4.5 software).

All reagents were analytical grade and prepared with ultrapure water (Elga water purification system). The solutions were purged with a fast stream of nitrogen gas for 10 minutes to avoid interference from the reduction of oxygen dissolved in solution. Prior to each experiment, the working electrode (glassy carbon disc) was manually polished with alumina powder (Leco) of 3 μm then 0.05 μm on a moist polishing cloth (Beuhler). After each experiment, the electrodes were rinsed well with ultra-pure water to remove contamination from the polishing cloth. The polishing procedures were repeated until a mirror finish was obtained.

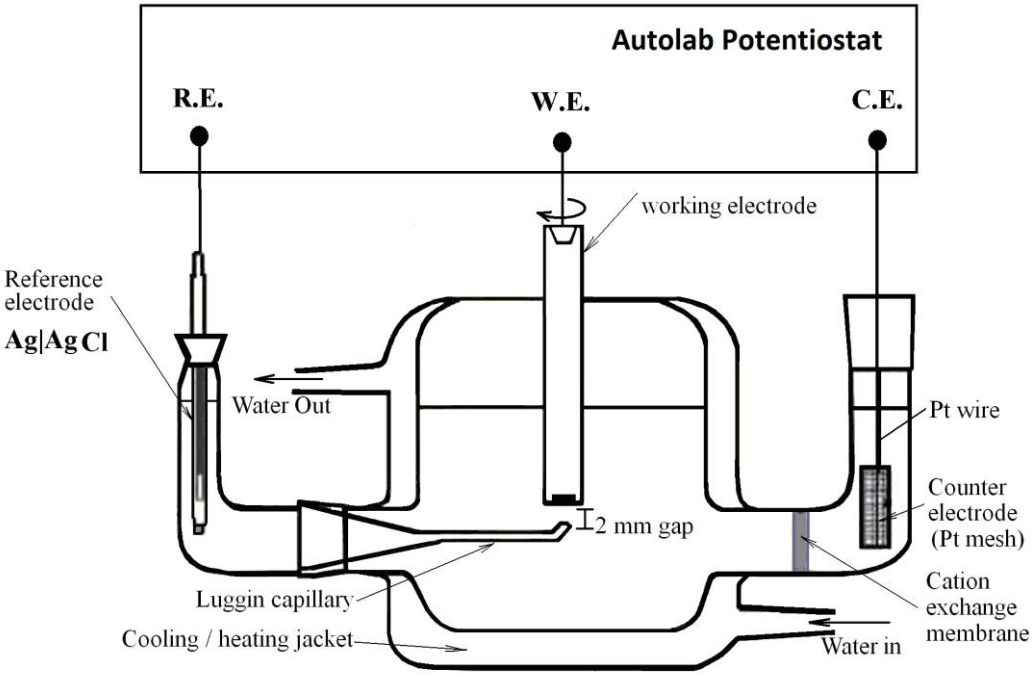

Figure 4.1. Instrumentation used for electrochemical voltammetry.

4.3. Zinc electrodeposition and microscopy

Figure 4.2 shows the set-up used for zinc electrodeposition. Carbon polyvinyl-ester composite (Entegris Inc., BMC 18649, Germany) electrodes were used as both cathode and anode. The electrodes were 8 cm × 1 cm nylon-made holder from the top. Before each experiment, the electrodes were polished using silicon carbide paper Grade P120, degreased with detergent and then left in ultrasonic bath for 10 minutes.

The back and sides of both cathode and anode were covered with an insulating tape (polyester tape, Cole-Parmer) to ensure the current density for each experiment is approximately similar and to make sure that zinc deposition occurs only were the electrodes face each other. As a result, the effective areas for both electrodes are maintained to be 4 cm × 1 cm. A double walled water jacket allows water circulation from the thermostat bath

to maintain the solution temperature at 50 ^{o}C. Throughout the experiment, the solution was stirred at 400 rpm using an IKa yellowline® magnetic stirrer.

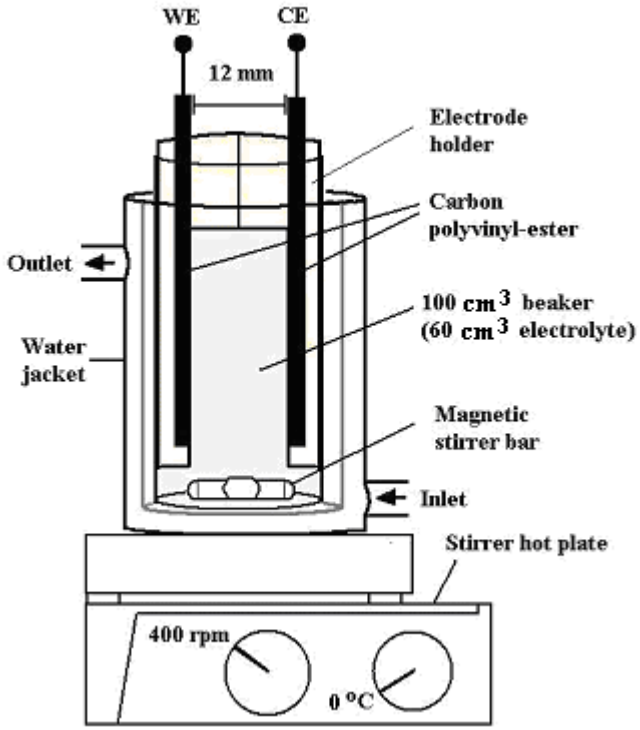

Figure 4.2. Zinc electrodeposition in a beaker cell at controlled temperature, stirred at 400 rpm.

The 100 cm^3 glass beaker was filled with 60 cm^3 of 1.5 mol dm^{-3} zinc methanesulfonate in 1 mol dm^{-3} methanesulfonic acid aqueous electrolyte. All chemicals used were Analytical Reagent grade. Zinc electrodeposition with and without additives was carried out for 4 hours at 50 mA cm^{-2}. The electronic equipment was the battery test system of BaSyTec GmbH (5 A/ 12 V). At the end of each experiment, the samples were rinsed with Ultra-pure water (Elga water purification system) for 10 seconds, air-dried and carefully stored in a sample bag placed in a container with silica gel granules. The images of the zinc electrodeposits were taken with a JEOL scanning electron microscope (model

JSM 6500 F) equipped with an energy-dispersive spectroscopic analyzer, which was used to estimate the elemental composition.

4.4. Hydrogen and weight loss measurements

Measurement of hydrogen evolution and weight loss of a metallic zinc sample was carried out in a volume-calibrated polyethylene syringe (Plastipak Industries, Canada) of 60 cm^3 volume, in which a zinc sample of approximately 3.5 g was immersed in solutions at different electrolyte compositions and temperatures as shown in Figure 4.3 The dimensions of the zinc sample were 2 cm × 2 cm × 0.15 cm and at 99.0 % purity (Rudgwick Metals, UK). Prior to the experiments, the zinc samples were pretreated by manually polishing their surface using silicon carbide paper grade P120, degreasing with detergent (Teepol, UK), etching in 30 % V/V methanesulfonic acid for 20 seconds to obtain a light, matt and clean surface, following by ultrasonic cleaning for 1 minute and then rinsing with plenty of ultrapure water (18 M Ω cm resistivity, Elga water purification system). The back surface of the zinc sample was covered with a polyester insulating tape (Cole-Parmer) to ensure the exposed area was 4 cm^2. The weight of the zinc sample was measured by an electronic balance (Scout Pro SP202, Ohaus, USA).

In order to measure the hydrogen evolved during corrosion, the 60 cm^3 syringe was filled by pulling up 50 cm^3 of electrolyte from the beaker through the orifice at the bottom. The syringe was immersed in the other 50 cm^3 of electrolyte contained in the bottom end of the beaker as shown in Figure 4.3. When the zinc sample was exposed to the electrolyte, hydrogen evolves and displaces the solution contained inside the syringe. As the accumulated hydrogen gas increases at the top of the syringe, the liquid level of the syringe drops, which represent the volume of hydrogen generated by the corrosion reaction. The

amount of hydrogen gas was recorded and the zinc sheet was taken out to be weighted every 30 minutes. Once the measurements have been done, the zinc sheet was placed back in the syringe and the electrolyte was replaced inside. The experimental procedures described above were repeated over a period of 10 hours or until the zinc sample dissolved completely.

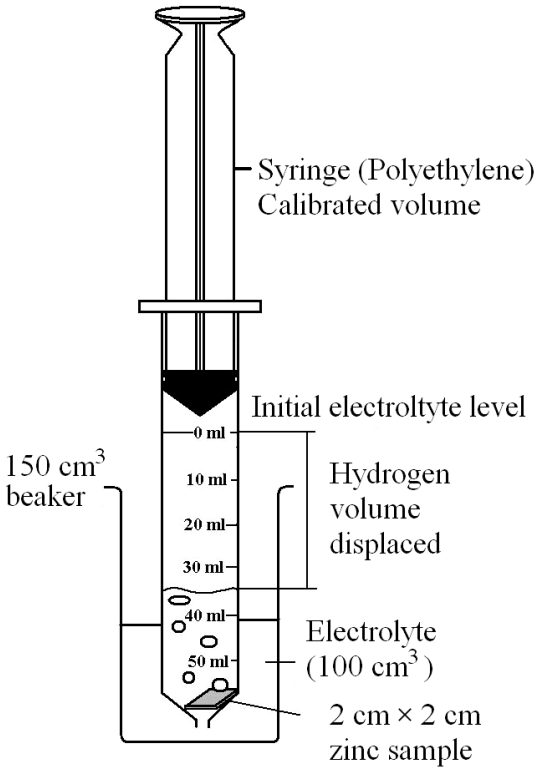

Figure 4.3. Experimental set-up for the measurement of hydrogen evolution from a 2 cm × 2 cm zinc sample.

4.5. Polarization measurements on the zinc plate electrode

The open circuit potential of the immersing zinc sample in the electrolyte of 1 mol dm^{-3} methanesulfonic acid in the presence and absence of corrosion inhibitor was typically measured by using a silver-silver chloride reference electrode (ABB, Series 1400, 0.1 mol dm^{-3} KNO_3) in a 150 cm^3 glass beaker containing 100 cm^3 of electrolyte as shown in

Figure 4.4. The zinc sample being tested was 7 cm × 2 cm × 0.15 cm and at 99.0 % purity supplied from Rudgwick Metals (U.K.). The pretreatment of the zinc sample was the same as that in Section 4.4. The zinc sample was the working electrode and was covered with an insulating polyester tape (Cole-Parmer) to ensure the exposed area to the solution was 4 cm^2 (2 cm × 2 cm). The counter electrode was a platinum mesh of 1 cm^2 (1 cm × 1 cm). Reference electrode was located at about 2 mm from the surface of the zinc plate through a luggin capillary.

Using the same experimental set-up, the cathodic and anodic polarization measurements for the surface condition of the zinc sample were carried out by linearly sweeping the potential of the zinc at 2 mV s^{-1} using a computer controlled potentiostat (Metrohm Autolab BV, Netherlands) immersed in 1 mol dm^{-3} methanesulfonic acid at 22 ^oC for 1 — 10 hours. Since two zinc samples were needed for the cathodic and anodic measurements in each hour, 20 zinc samples were used in this work. For the cathodic polarization, the electrode potential was swept from the equilibrium potential up to 130 mV positive, and 130 mV negative during the anodic polarization. The characterization of the specimen was analyzed by the X-ray diffraction (XRD) using a Siemens D5000 X-ray diffractometer with Ni-filtered Cu Kα radiation (λ = 1.5406 Å).

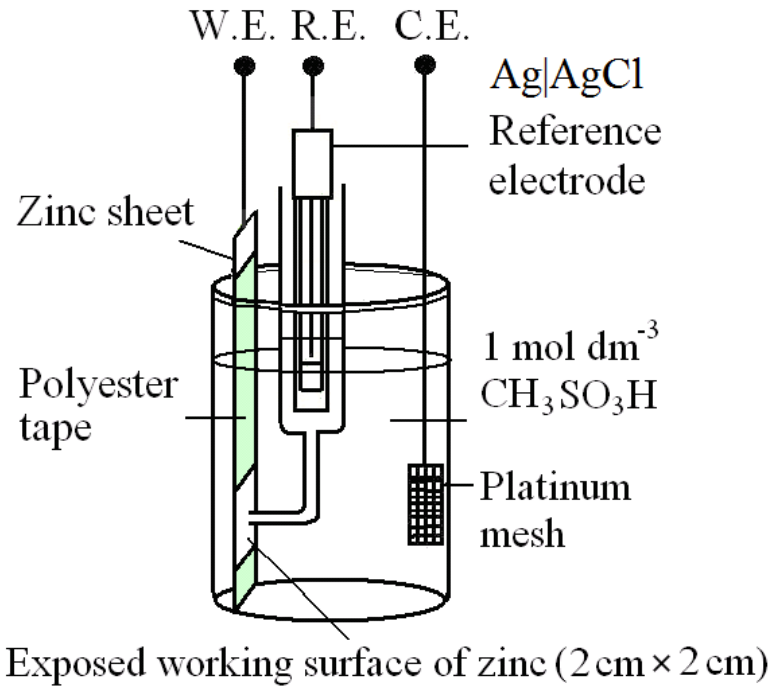

Figure 4.4. Experimental set-up for the polarization measurement of the zinc samples have been immersed in the solution for different lengths of time.

4.6. Chemical titration of Ce(IV)

The concentration of Ce(IV) in methanesulfonic acid was determined via a titration method as outlined in previous studies [1-3]. An aliquot of 0.5 cm^3 of an unknown concentration of Ce(IV) was taken from the electrolyte storage reservoir and mixed with 9.5 cm^3 of 2.0 mol dm^{-3} methanesulfonic acid a droplet of ferroin (1,10–orthophenanthroline-ferrous sulphate complex, Fluka) as a colorimetric redox indicator. A freshly prepared solution of 0.01 mol dm^{-3} $NH_4Fe(II)SO_4$ was then titrated into this electrolyte, which is more susceptible to be oxidized comparing with $Fe(II)SO_4$. The concentration of Ce(IV) was determined from the amount of Fe(II) added to the solution to achieve complete reduction of Ce(IV) to Ce(III) indicated when the solution changed colour from blue to red.

4.7. Flow battery experiment

4.7.1. A divided flow battery experiment

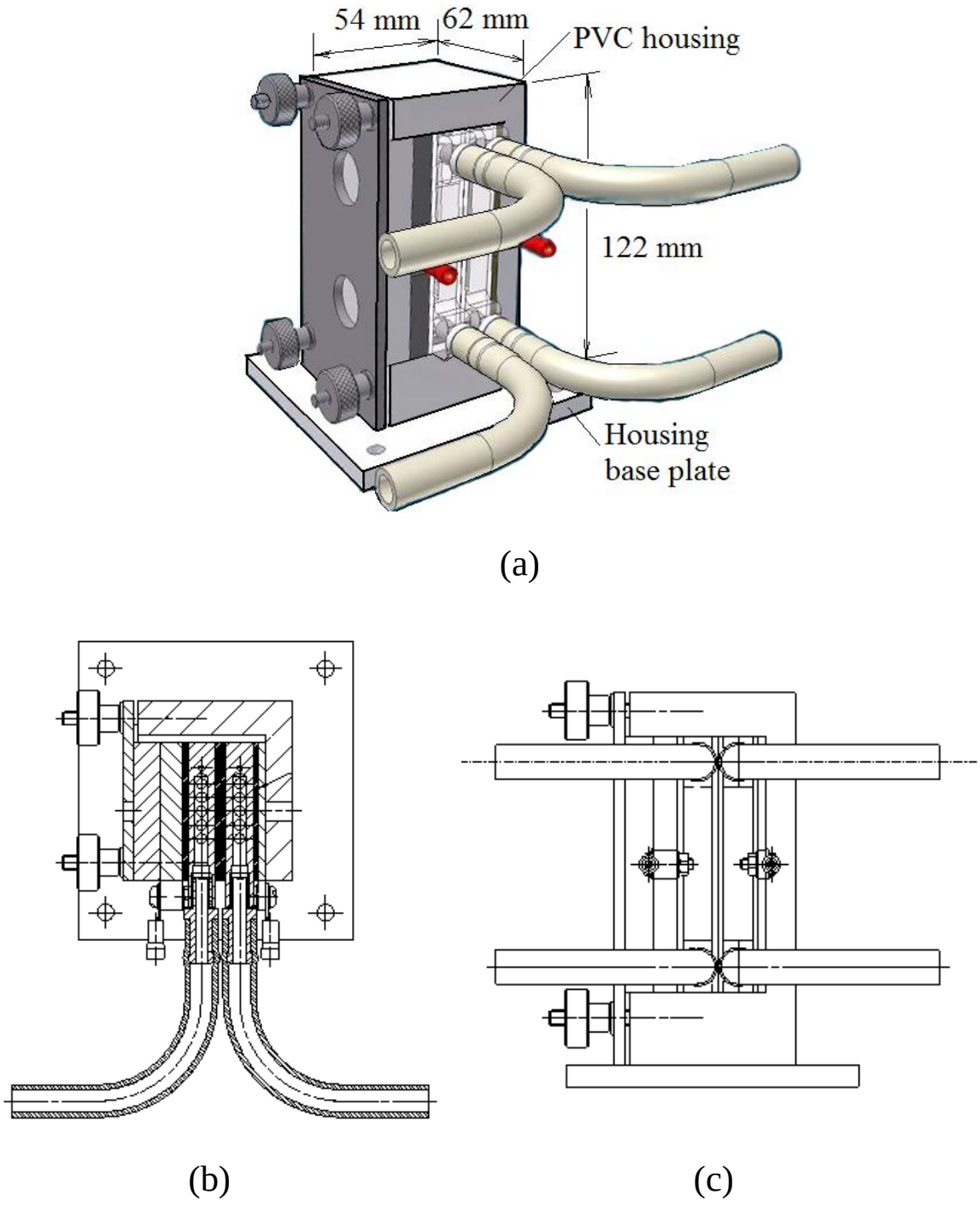

Figure 4.5. Divided flow battery (a) AutoCAD drawing (b) Sectional plan and (c) Side view.

Figure 4.5 shows the AutoCAD drawing of the divided flow battery used in this thesis. The electrical circuit and the expanded view of the components of a divided flow battery is shown in Figure 4.6a and 4.6b. The cell consisted of a polyvinyl chloride (PVC) casing, two acrylic flow channels, four 1.5 mm thickness rubber silicon gaskets as well as the negative and positive electrodes separated by a cation-conducting Nafion® membrane (DuPont, NF117/H^+). Each electrode had a geometric area of 70 mm × 50 mm, which was covered by a silicon rubber gasket to expose an active surface area of 45 mm × 20 mm to the electrolyte. The membrane-electrode gap was 23 mm.

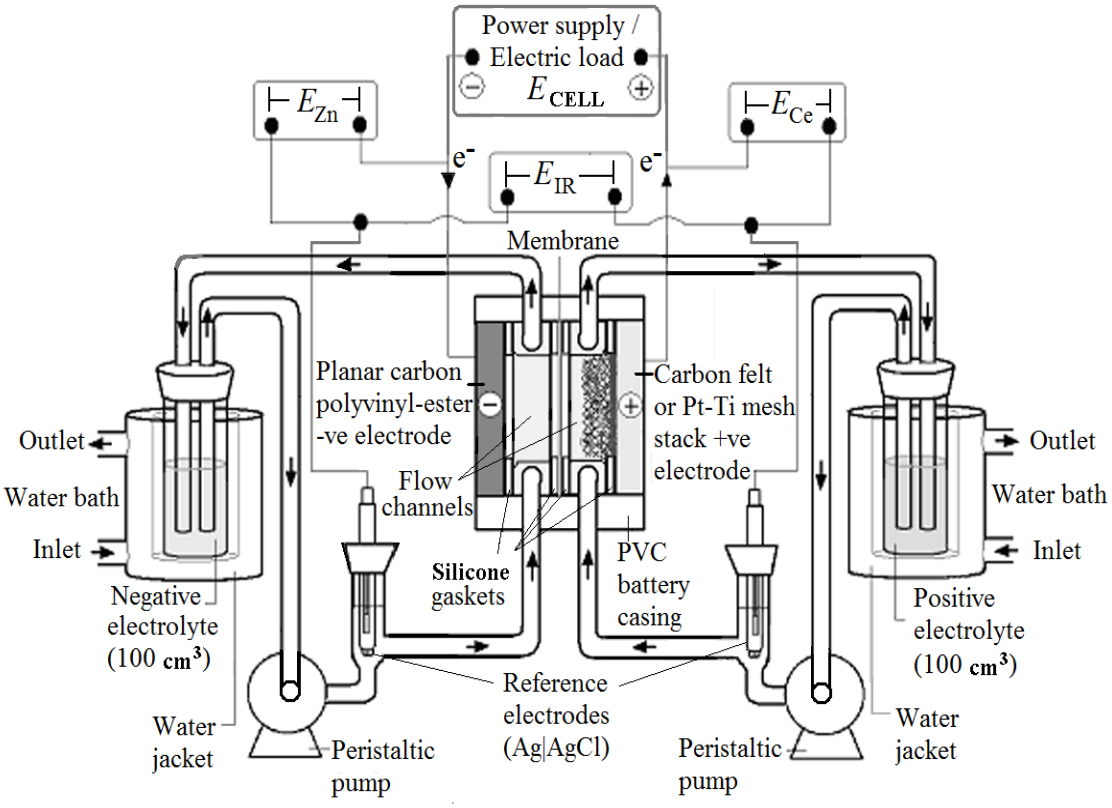

(a)

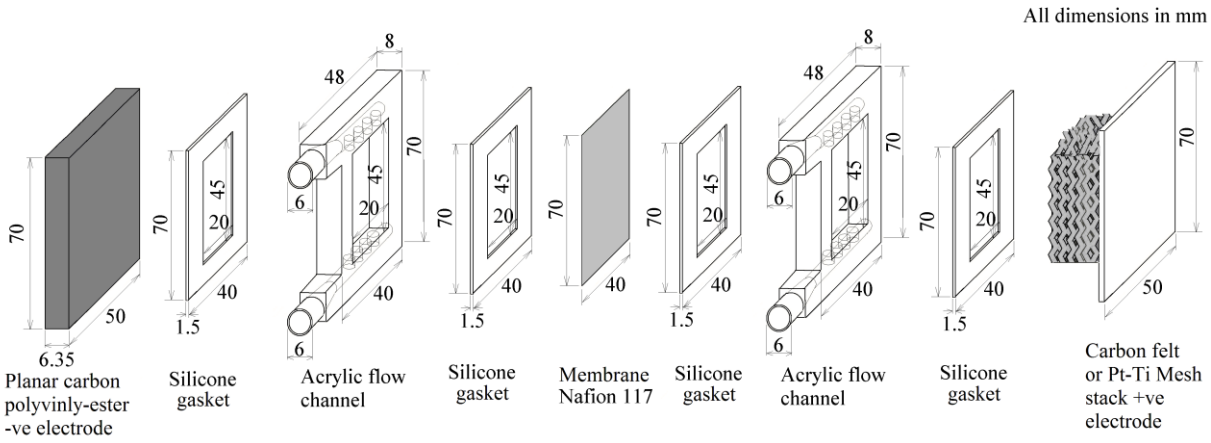

(b)

Figure 4.6. Experimental arrangement and electrical circuit of a divided zinc-cerium redox battery. (a) Overall set-up, (b) expanded view of the components of a flow battery. The units are shown in mm.

Carbon polyvinyl-ester composite (BMC 18649, Engtegris Inc, Germany) was used as the negative electrode material and a range of positive electrode materials was tested. Detailed description of the positive electrode materials are described in the chapter 8. As shown in Figure 4.7, the three-dimensional platinised titanium mesh was manufactured by spot welding four pieces of platinised titanium mesh (44 mm × 16 mm) onto a planar platinised titanium plate (Magneto GmbH, Netherlands). Other 3-dimensional positive electrode materials, such as reticulated vitreous carbon and carbon felt were heat bonded to a graphite plate using a conductive carbon adhesive (931 Binder & Cotronics Corp., USA) by curing in the oven at 130 ^{o}C for 4 hours.

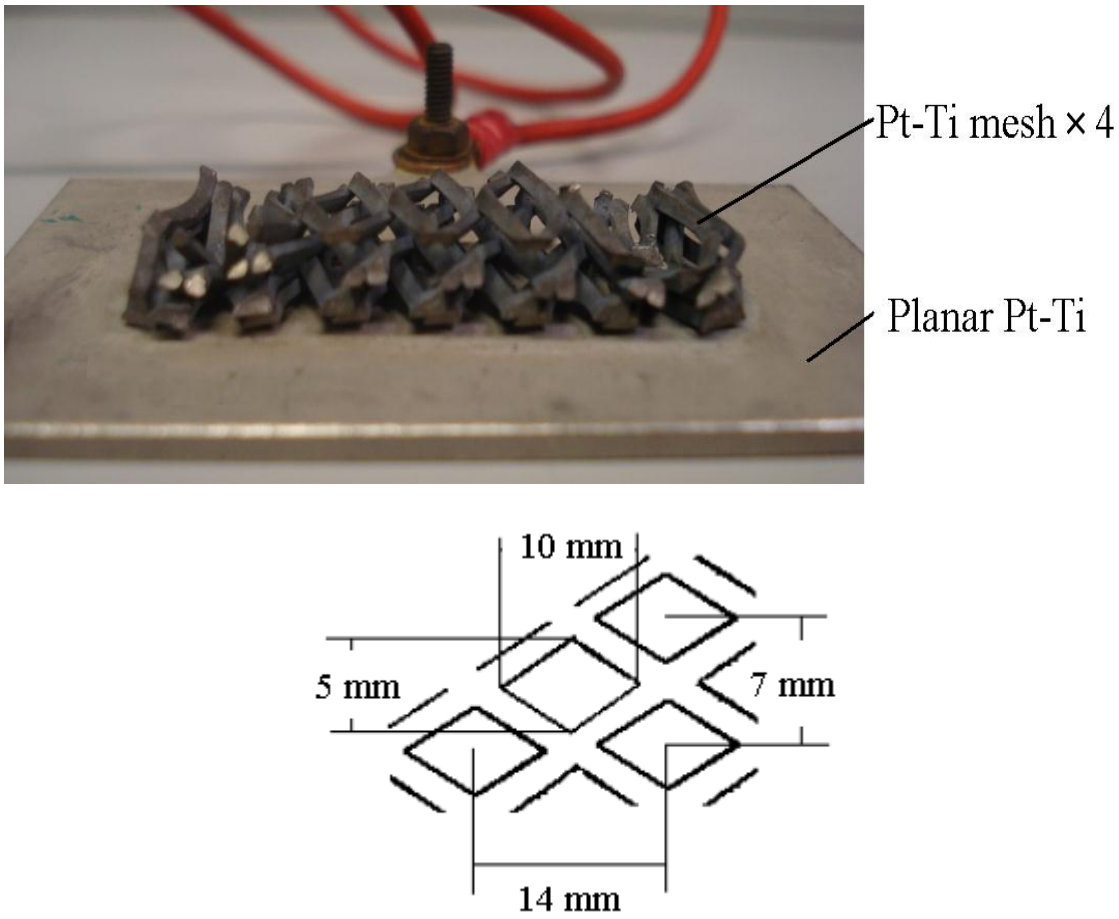

Figure 4.7. Photograph and the dimension of the three-dimensional platinised-titanium mesh stack electrodes.

The volume of each electrolyte compartment was 100 cm^3. Unless otherwise indicated, the positive electrolyte contained 0.8 mol dm^{-3} cerium(III) methanesulfonate in 4.0 mol dm^{-3} methanesulfonic acid while the negative electrolyte compartment contained 1.5 mol dm^{-3} zinc(II) methanesulfonate in 1.0 mol dm^{-3} methanesulfonic acid. The electrolytes were maintained at 50 ^oC by a water thermostat (Grant Model LV FG) through water jackets. Both positive and negative electrolytes were circulated at 3.9 cm s^{-1} by a peristaltic pump (Masterflex® Model 7553079, Cole-Parmer) using high-pressure tubings (Masterflex® Norprene®, Cole-Parmer). Reference electrodes were saturated silver-silver chloride electrode, Ag|AgCl (ABB, Series 1400, 1.0 mol dm^{-3} KNO_3) placed about 3 cm away from the entrance of each flow channel, in line with the electrolyte circuit.

In a typical experiment, the battery was charged at 450 mA (50 mA cm^{-2} considering the 2-dimensional negative electrode) for 4 hours. It was then left at open-circuit for 1 minute and discharged at the same current. Cut-off voltages were set up at 3.4 V and 0.5 V during battery charge and discharge, respectively. In order to determine the change in cerium concentration, an aliquot of 0.5 cm^3 of positive electrolyte solution was taken from the reservoir during the charge and discharge cycles at regular intervals of time. All electrochemical measurements were made by BaSyTec (Germany) battery test system (5A/12 V). The anode-, cathode- and cell potentials were continuously monitored through-out the experiment.

4.7.2. *An undivided flow battery experiment*

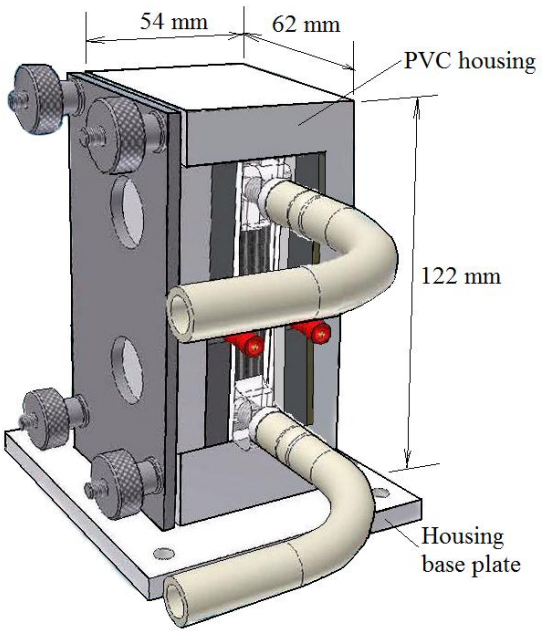

(a)

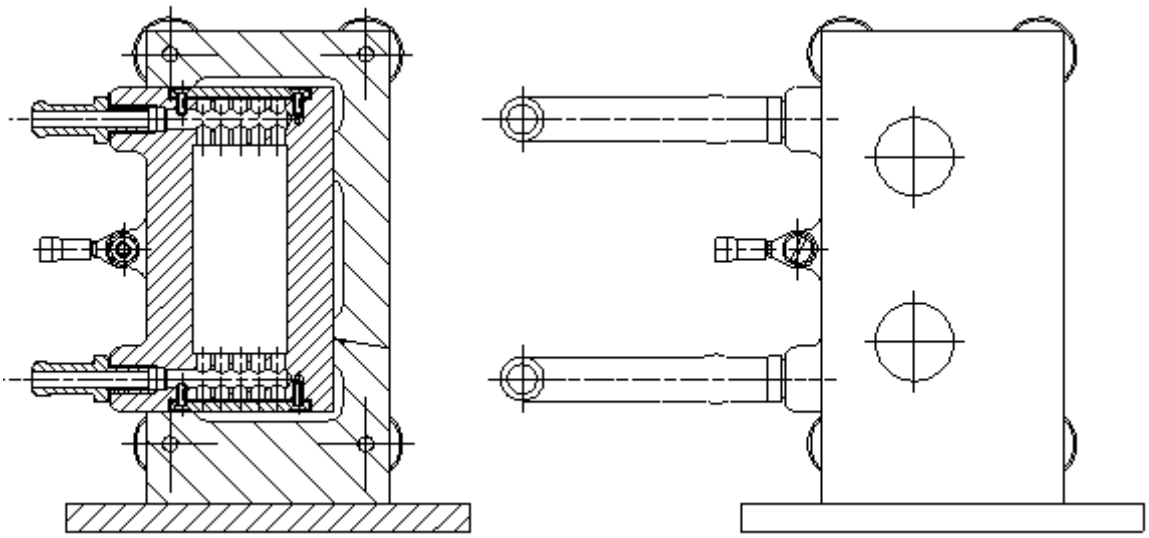

(b) (c)

Figure 4.8. Undivided flow battery (a) AutoCAD drawing (b) Sectional side view and (c) Side view.

Figure 4.8 shows the AutoCAD drawing of the undivided flow battery used in this thesis. The electrical circuit and the expanded view of the components of a membraneless zinc-cerium redox flow battery are shown in Figure 4.9a and 4.9b, respectively. Carbon polyvinyl-ester electrode (BMC 18649, Engtegris Inc., Germany) was the substrate for the zinc electrodeposition and dissolution at the negative electrode. The positive electrode was with three pieces of carbon felts (Sigratherm® GFA-05, 4.5 cm × 2.0 cm × 0.5 cm, SGL Group, Germany), which were compressed to the carbon polyvinyl-ester substrate by a Perspex compressing gasket, which avoids the felts from contacting the zinc negative electrode. The inlet and outlet of the electrolyte was designed with acrylic flow channels. Several gaskets were used to form a negative electrolyte compartment and to prevent leakage. For both negative and positive electrodes, carbon polyvinyl ester substrates were covered with a polyester insulating tape (Cole-Parmer) to ensure the exposed surface area was 2 cm × 0.8 cm. The distance between the two electrodes was 2 cm.

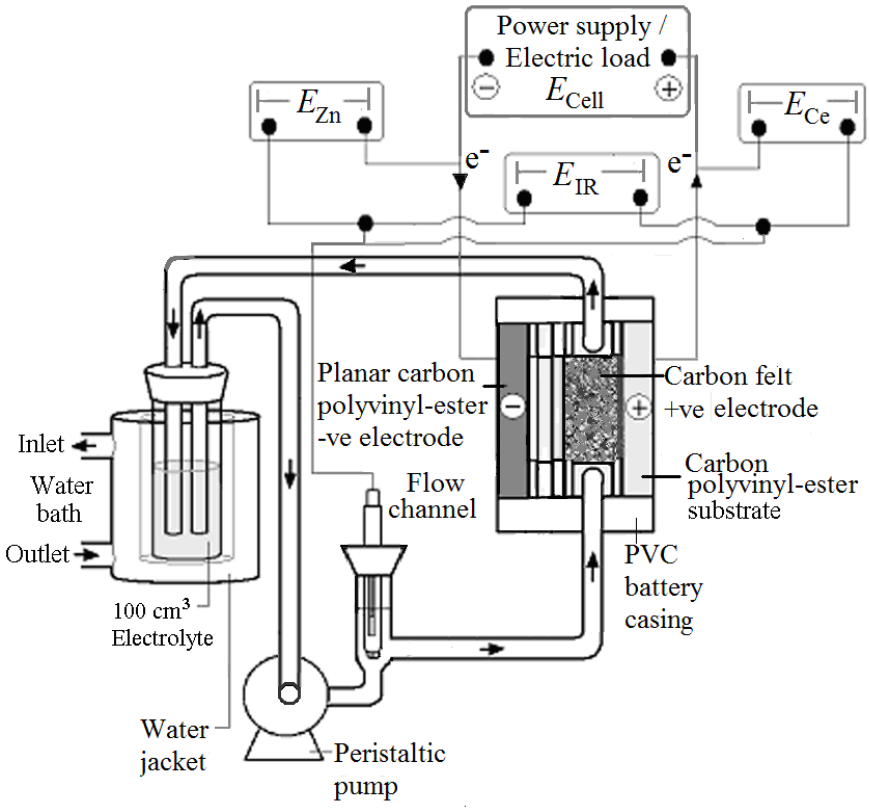

(a)

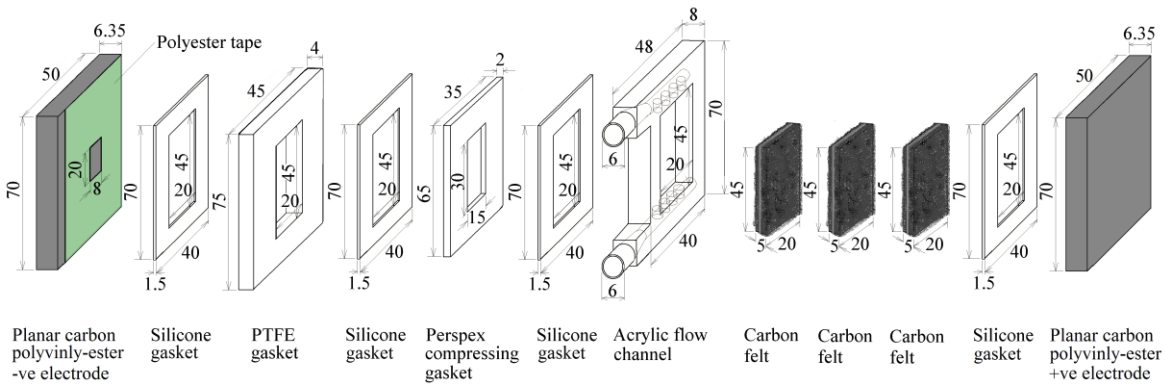

(b)

Figure 4.9. Experimental arrangement and electrical circuit of an undivided zinc-cerium redox battery. (a) Overall set-up, (b) expanded view of the components of the flow battery. The units are shown in mm.

In a typical experiment, 100 cm^3 of electrolyte contained 1.5 mol dm^{-3} zinc methanesulfonate and 0.2 mol dm^{-3} cerium(III) methanesulfonate in 0.5 mol dm^{-3}

methanesulfonic acid. Unless otherwise indicated, the battery was charged and discharged at 32 mA during 30 minutes, which corresponds to a current density of 20 mA cm^{-2} at the negative electrode. The electrolyte was maintained at a range of temperature by a water thermostat (Grant Model LV FG) through water jackets and circulated past the electrode surfaces at an average linear flow velocity of 3.9 cm s^{-1} using a peristaltic pump (Masterflex® Model 7553079, Cole-Parmer). A saturated silver-silver chloride electrode was used as the reference electrode (ABB, Series 1400, 1.0 mol dm^{-3} KNO_3), which was placed about 3 cm away from the inlet of the flow channel. All electrochemical measurements were made by BaSyTec (Germany) battery test system (5 A / 12 V). The anode-, cathode- and cell potentials were continuously monitored throughout.

4.7.3. Dimensionless quantities of the flow battery compartment

Dimensionless quantities are important for design and scale-up applications in engineering. Common dimensionless groups including Reynolds number (Re), Sherwood number (Sh) and Schmidt number (Sc) are used to characterise the flow conditions of an electrolyte in the reactor geometry with different types of electrode materials. In order to increase the electrode reaction rate, three dimensional electrodes, such as reticulated vitreous carbon, carbon felt and three-dimensional platinised titanium mesh electrodes, have been used in this work. Scanning Electron micrographs of the three-dimensional electrodes of 30, 100 ppi Duocel® reticulated vitreous carbon (RVC) foams (ERG Material and Aerospace Corp., USA), SGL Sigratherm® GFA-05 (SGL Group, Germany), Alfa-Aesar carbon felt (Stock 42107, UK) and the three-dimensional mesh stack electrode, are shown in Figures 4.10 a – e, respectively.

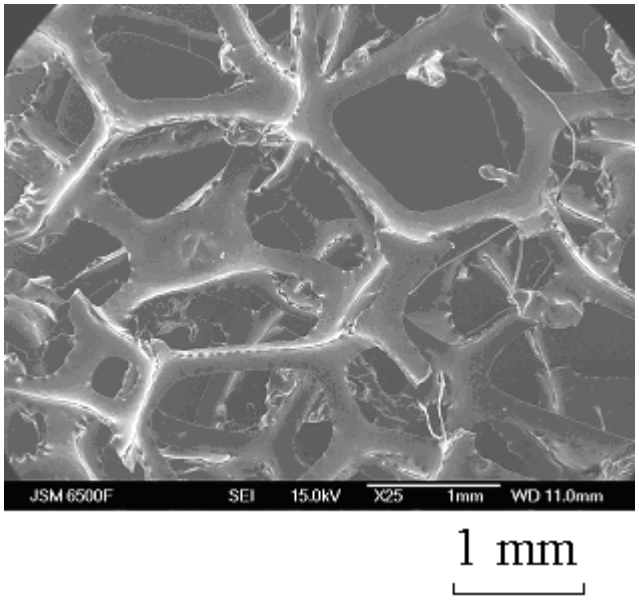

(a) 30 ppi RVC

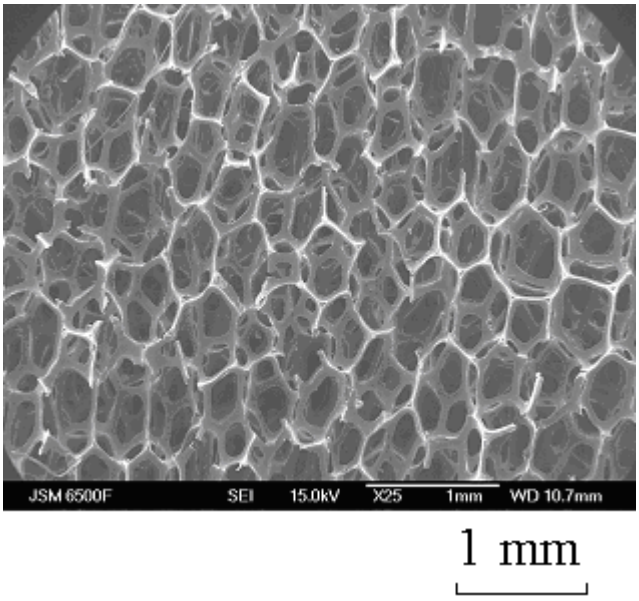

(b) 100 ppi RVC

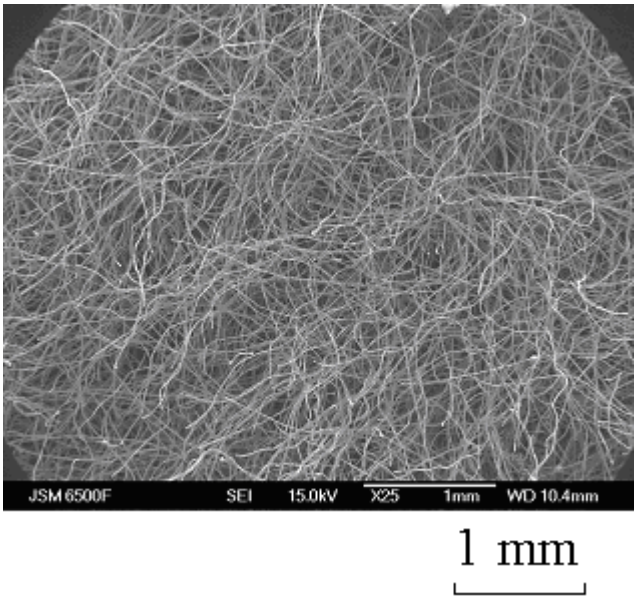

(c) SGL Sigratherm® carbon felt

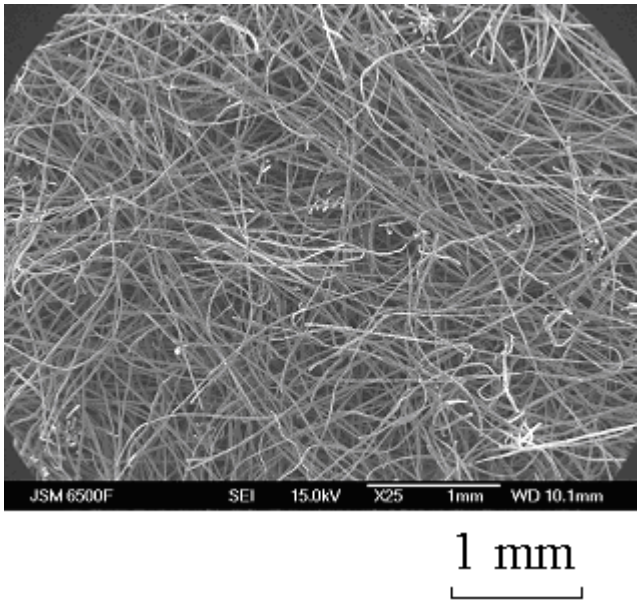

(d) Alfa-Aesar carbon felt

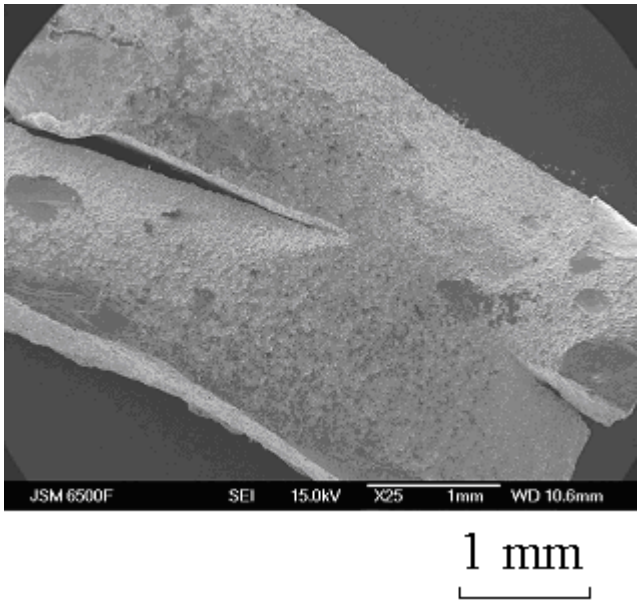

(e) Platinised titanium mesh stack

Figure 4.10. Scanning electron micrographs (× 25 magnification) of five types of three-dimensional electrode materials: (a) 30 ppi reticulated vitreous carbon, (b) 100 ppi reticulated vitreous carbon, (c) SGL Sigratherm® carbon felt, (d) Alfa-Aesar carbon felt and (e) platinised titanium mesh stack.

The mass transport with the above mentioned electrode materials in the flow battery compartment has been examined by the oxidation of ferrocyanide using the solution containing 10×10^{-3} mol dm^{-3} potassium ferricyanide and 1×10^{-3} mol dm^{-3} potassium ferrocyanide in 1 mol dm^{-3} potassium nitrate solution. Figure 4.11 shows the plot of limiting current density *vs.* the mean linear flow velocity (possible range) for the electrode materials: two-dimensional carbon polyvinyl-ester, two-dimensional platinised titanium, three-dimensional platinised titanium mesh stack, 100 ppi reticulated vitreous carbon and SGL carbon felt. The limiting current densities are based on the geometric area of the two-dimensional electrode (substrate). With the three-dimensional electrodes, such as carbon felt, the anodic current densities increase by a factor of more than ten and highly depend on the mean linear flow velocity. Among the tested electrodes, higher limiting current densities were observed in the following order: two-dimensional platinised titanium

< two-dimensional carbon polyvinyl-ester < three-dimensional platinised titanium mesh stack < 100 ppi reticulated vitreous carbon < SGL carbon felt.

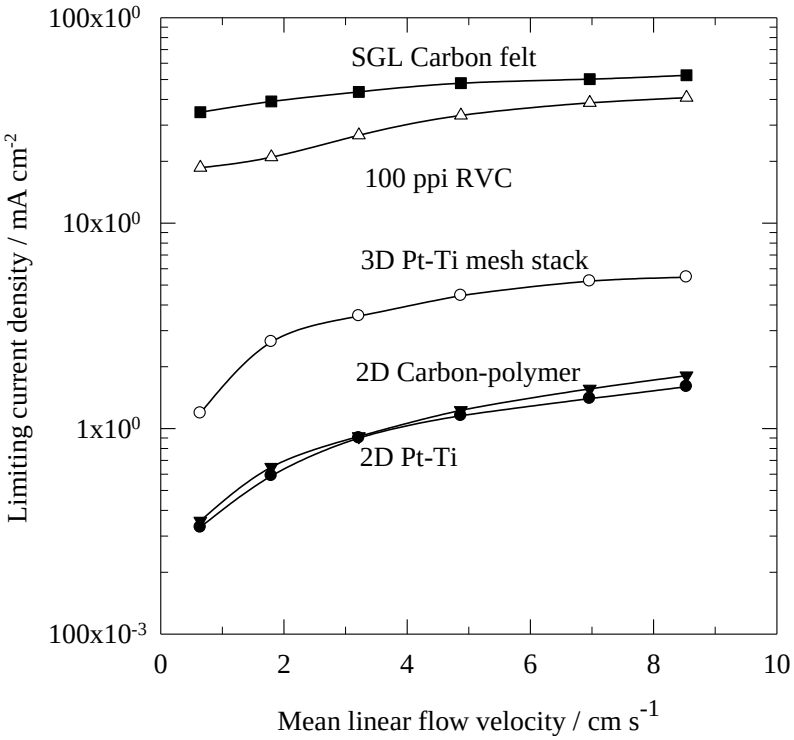

Figure 4.11. Plots of log j_L, against mean linear flow velocity for the oxidation of ferrocyanide at different electrode materials in the flow battery compartment. The electrolyte was 10×10^{-3} mol dm^{-3} potassium ferricyanide and 1×10^{-3} mol dm^{-3} potassium ferrocyanide in 1 mol dm^{-3} potassium nitrate solution. T = 22 ^{o}C. ● Two-dimensional platinised titanium, ▼ two-dimensional carbon polyvinyl ester, ○ three-dimensional platinised titanium mesh stack, △ 100 ppi reticulated vitreous carbon and ■ SGL Sigratherm® carbon felt.

According to Brown *et al.* [4], the dynamic viscosity, μ, and the diffusion coefficient, D, of potassium ferrocyanide at the similar electrolyte composition are 0.0102 g cm^{-1} s^{-1} and 6.2×10^{-6} cm^2 s^{-1}, respectively. The hydraulic diameter of the cell, d_e, is calculated based on equation (48) in chapter 3, which is 1.42 cm for this case. With these values and the equations defined in chapter 3, dimensionless Reynolds and Sherwood numbers can be determined. Figure 4.12 shows the double logarithmic plot of Sherwood

number against Reynolds number for each electrode material in the flow battery compartment.

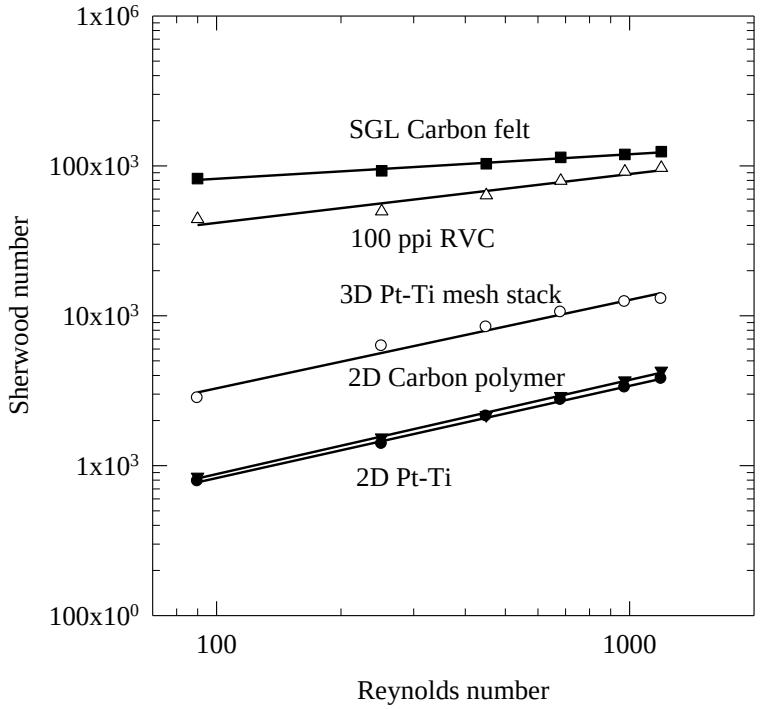

Figure 4.12. Plots of log Sherwood number and log Reynolds number for the oxidation of ferrocyanide at different electrode materials in the flow battery compartment. The electrolyte composition as in Figure 4.10. T = 22 ^{o}C. ● Two-dimensional platinised titanium, ▼ two-dimensional carbon polyvinyl ester, ○ three-dimensional platinised titanium mesh stack, △ 100 ppi reticulated vitreous carbon and ■ SGL Sigratherm® carbon felt.

The correlation of Sherwood number against Reynolds number is calculated in the following form:

$$Sh = a\, Re^{b}$$

For two-dimensional platinised titanium electrode,

$$Sh = 48.66\, Re^{0.63}$$

For two-dimensional platinised carbon polyvinyl-ester electrode,

$$Sh = 48.61\, Re^{0.62}$$

For three-dimensional platinised titanium mesh electrode,

$$Sh = 217.4\ Re^{0.59}$$

For 100 ppi reticulated vitreous carbon electrode,

$$Sh = 9293.9\ Re^{0.33}$$

For SGL Sigratherm® GFA-05 carbon felt electrode,

$$Sh = 38574.5\ Re^{0.16}$$

4.8. Instrumentation and analytical equipments

Instrumentations	Comments	Supplier
Potentiostat/ Galvanostat	PGSTAT20	Metrohm Autolab B.V.
Rotating motor	EG & G Model 636	Ametek Inc.
Battery test system	5 channels, 5 A/ 12 V	BaSyTec GmbH
Scanning Electron Microscopy	JSM 6500 F	JEOL Ltd.
Water bath	LV-FG	Grant

Table 4.2. The main instrumentations used in this project.

4.9. References

1. P. Patnaik, Dean's Analytical Chemistry Handbook, 2nd ed. McGraw-Hill, (2004).
2. I.M. Kolthoff, E.B. Sandell, Texture of Quantitative Inorganic Analysis, 3rd ed. The Macmillan Company, 463-481.
3. A.I. Vogel, Textbook of Quantitative Inorganic Analysis, 5th ed. Wiley, New York.
4. C.J. Brown, D. Pletcher, F.C. Walsh, J.K. Hammond, D. Robinson, J. Appl. Electrochem. 23 (1993) 38-43.

Chapter 5
Electrochemistry of the zinc half-cell reaction

Chapter 5 Electrochemistry of zinc half-cell reaction

Introduction

Due to the electronegativity of zinc in aqueous medium (– 0.76 V *vs.* SHE) and its widespread availability, zinc redox couple has been considered as the negative electroactive species in the redox flow batteries with other positive couples. During the charge-cycle of a redox flow battery, the electrodeposition of zinc is the reaction at the negative electrode:

$$Zn^{2+} + 2e^- \underset{\text{Discharge}}{\overset{\text{Charge}}{\rightleftharpoons}} Zn \qquad E^{\ominus} = -0.76 \text{ V } vs. \text{ SHE} \qquad (1)$$

Recent attention has focused on the application of aqueous methanesulfonic acid as an electrolyte for redox flow batteries, as this electrolyte allows a high solubility for a wide range of metal ions, including the highly electropositive lead [1] and cerium ions [2]. Although zinc electrodeposition has been used for a long time at acidic chloride [3-8] and sulphate [9-12] baths, there is no study of zinc electrodeposition in methanesulfonic acid to date. Several recent patents suggested that methanesulfonic acid can reduce the dendritic growth significantly [13, 14], which lead to a limited cycle life in a zinc-based flow battery.

Different from electroplating industry, carbon-based materials are the commonest electrode materials used in redox flow batteries [15-17], as they are chemically inert and do not undergo dissolution and formation of oxides. In this work, the electrochemistry of zinc in methanesulfonic acid was studied via cyclic voltammetry on a glassy carbon rotating disk electrode. In order to optimize the conditions for a zinc-based redox flow battery, a range of electrodeposition and dissolution experiments have been carried out in a parallel plate flow-cell at controlled electrolyte compositions and operating parameters.

5.1 Cyclic voltammetry and electrochemical behaviour

Figure 5.2a shows the cyclic voltammogram of Zn(II) ions at a glassy carbon electrode at 20 mV s^{-1} potential sweep rate in an electrolyte containing 0.01 mol dm^{-3} zinc methanesulfonate and 0.5 mol dm^{-3} sodium methanesulfonate adjusted at pH 4 with methanesulfonic acid at 22 ^{o}C. The potential was firstly swept from – 0.8 V to – 1.4 V *vs.* Ag|AgCl.

The voltammogram is similar to those reported in other acid media. The cathodic scan shows the nucleation potential at – 1.15 V *vs.* Ag|AgCl, which is comparable to *c.a.* – 1.2 V *vs.* SCE reported in sulphate, chloride and acetate electrolyte [18]. The sharp increase in current reduction was due to the formation of fresh zinc nuclei, which further increases the available deposition area. The peak current density reached *c.a.* 2.57 mA cm^{-2} at – 1.22 V *vs.* Ag|AgCl due to the reaction of Zn(II) ions already on the electrode surface. After the peak, the current density decreases as no more Zn(II) ions exist on the surface and new Zn(II) species diffuse from the bulk of the electrolyte. The concentration profile is similar to that as shown in Figure 3.6. Since the standard electrode potential of the zinc deposition is more negative than the hydrogen one, hydrogen gas could evolve by the cathodic reduction of hydrogen ions on the newly formed zinc nuclei. Although the cyclic voltammogram does not show the evolution of hydrogen gas, a fraction of the current is probably due to the reduction of protons. The scan was reversed at – 1.4 V *vs.* Ag|AgCl in order to avoid further evolution of hydrogen.

While sweeping the potential towards the positive direction, zinc ions are still being reduced until the crossover potential at – 1.16 V *vs.* Ag|AgCl on the foot of the stripping peak. At – 1.14 V *vs.* Ag|AgCl, solid zinc was no longer thermodynamically stable on the electrode surface and the metallic zinc deposit on the electrode oxidizes very quickly as the

oxidation process is not diffusion controlled and a sharp high current peak is observed. The forward and reverse scan forms a nucleation loop between – 1.16 V and – 1.18 V *vs.* Ag|AgCl. The slightly more negative potential during Zn(II) reduction observed during the forward scan shows that the deposition of zinc on the less-conductive glassy carbon substrate required slightly more energy than on the zinc metallic surface recently formed.

In this study, the overpotential of zinc electrodeposition was *c.a.* 20 mV, as the nucleation potential on glassy carbon electrode is more negative than that on metallic electrode. For instance, Gomes and Pereira [19] reported that the nucleation potential of zinc electrodeposition was observed at c.a. – 0.8 V *vs.* SCE on stainless steel electrode from the sulphate bath in the absence of electrolytic additive. Such an overpotential was reported to have important implications on the morphology nature of the deposit and the current efficiency. Volmer and Weber [20] suggested that larger overpotential could lead to faster nucleation rate and prevent further grain growth [20-24], which has been reviewed by Budevski *et al.* [25]. Finer grain size and sometimes more uniform deposits have been obtained at larger deposition overportentials, which was found to be largely dependent on anions [18, 26], electrolytic additives [23, 27, 28], temperature [18, 29] or the influence of pH on the formation of zinc complexes [30, 31]. As suggested by Morón *et al* [32], the crystal size of zinc deposit was also influenced by the exchange current density. Due to the reduced exchange current density induced by the adsorption of electrolytic additives on the electrode surface, compact and shiny coating has been obtained in an acid chloride bath.

In terms of electron transfer, the Zn(II)/Zn(0) reaction in methanesulfonate bath is considered to be a quasi-reversible reaction, as the separation of peak potentials was 160 mV. Literature reports show that the separation of peak potentials for the Zn(II)/Zn(0) reaction in chloride and sulfate electrolytes were *c.a.*100 mV and 150 mV, respectively, in

an electrolyte containing 0.01 mol dm^{-3} Zn(II) ions and 0.5 mol dm^{-3} Na(I) ions. The results in this paper suggest that zinc electrodeposition in methanesulfonaic bath has similar electrochemical behaviour as that in sulphate bath. Moreover, the ratio of anodic to cathodic charge was found to be consistent with the previous finding in sulphate bath. The charge ratio between the anodic and cathodic processes in methaneulfonate bath was 82 % while the reported value in a sulfate bath was 81 % [33]. This suggests that some of the charge during the zinc electrodeposition was used in hydrogen reduction. Other possibilities can be due to incomplete stripping of zinc electrodeposit at glassy carbon substrate.

Plotting the logarithm of the current density versus the potential range of zinc nucleation, a Tafel slope of 52 ± 2 mV $decade^{-1}$ was obtained which is almost double the magnitude of the theoretical calculation of 30 mV $decade^{-1}$ for a two electrons transfer reaction. The value agrees with other works reported in the literature: Ibrahim reported that the Tafel slope was 56 mV s^{-1} at 0.09 mol dm^{-3} zinc in 0.2 mol dm^{-3} sodium sulfate [29]. In the investigation of Guerra in zinc sulfate, the Tafel slope was *c.a.* 60 mV $decade^{-1}$ in neutral pH solution and *c.a.* 30 mV $decade^{-1}$ in highly acidic electrolyte. The smaller Tafel slope was due to the surface condition, as the hydrogen adsorbed on the newly formed zinc nuclei. This resulted in a combined cathodic reactions of hydrogen and zinc, further leading to a sharp increase in current density [34].

In this work, linear sweep voltammetry based on cathodic peak current densities was used to determine the diffusion coefficient of zinc ion. Standard anodic stripping voltammetry requires a thin-film mercury working electrode, under which circumstances the metal is rapidly depleted from the amalgam, while complete stripping of zinc electrodeposit on glassy carbon could lead to inaccuracy, and therefore is not analyzed in

this section. Figure 5.1b shows the plot of the cathodic peak current densities *vs.* the square root of the potential sweep rate. For a mass transport controlled reaction, a linear increase of the peak current density with the square root of the potential sweep rate can be predicted according to Randles-Sevcik equation:

$$j_p = 2.69 \times 10^5 \, z^{1.5} \, D^{0.5} \, v^{0.5} \, c \qquad (2)$$

where j_p is the peak current density, c is the zinc ion concentration in the electrolyte, z is the number of electrons involved the electrode process, v is the potential sweep rate and D is the diffusion coefficient of the zinc ions. By using the Randles-Sevcik plot, the diffusion coefficient was 7.2×10^{-6} cm^2 s^{-1}. This value is comparable to previous estimations reported in the literature in other acid electrolytes: Yu *et al.* [18] calculated 2.1, 5.5 and 8.4 $\times$ 10^{-6} cm^2 s^{-1} in acetic, sulphuric and hydrochloric acids, respectively, while Meas *et al.* [35] reported 7.27×10^{-6} cm^2 s^{-1} in hydrochloric acid. Therefore, the current used for zinc electrodeposition in methanesulfonic acid would be expected to be similar to that used in other common acids but the less-corrosive nature of methanesulfonic acid makes it more attractive for energy storage applications [1].

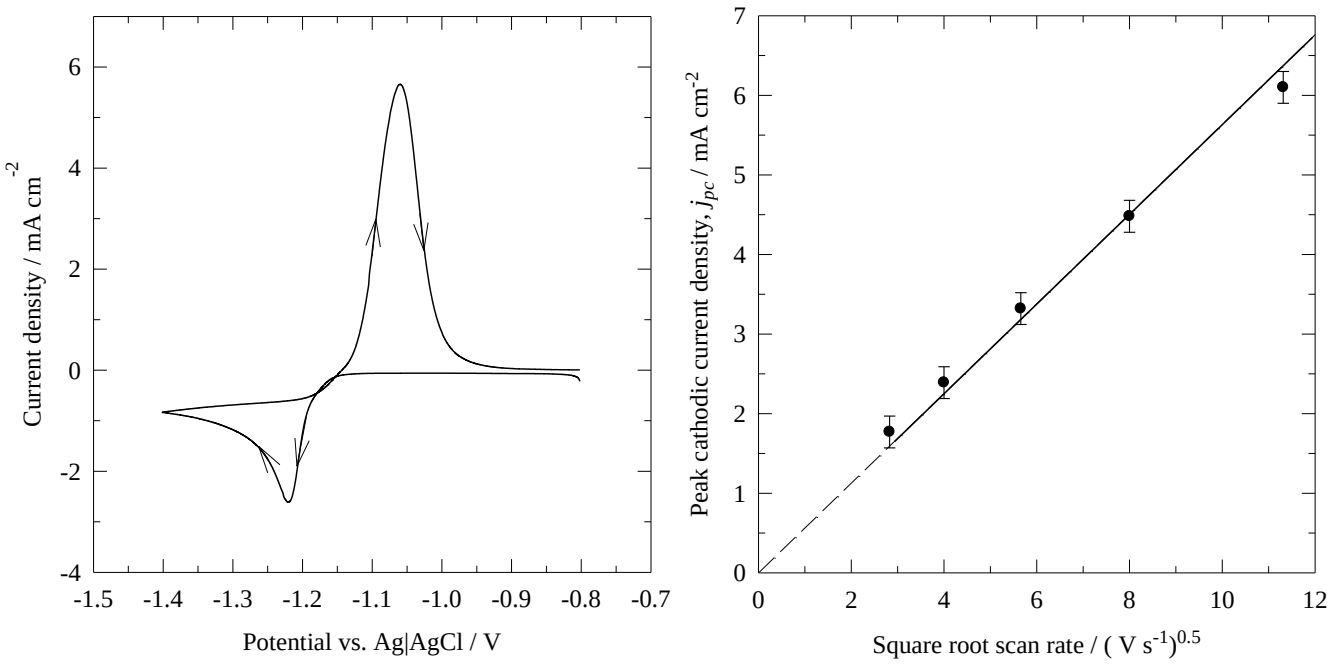

(a) (b)

Figure 5.1 Electrochemistry of zinc electrodeposition at a glassy carbon electrode in methanesulfonic acid. (a) Cyclic voltammogram, (b) Randles-Sevćik plot, Electrolyte: 0.01 mol dm^{-3} $Zn(CH_3SO_3)_2$ in 0.5 mol dm^{-3} $NaCH_3SO_3$ adjusted at pH 4 with CH_3SO_3H. The electrode was swept from – 0.80 to – 1.40 V *vs.* Ag|AgCl at 20 mV s^{-1} and 20 ^oC. The potential sweep rates were 8, 16, 32, 64, 128 mV s^{-1}.

5.2. Linear sweep voltammetry

5.2.1 *Mass transport*

As well as the charge-transfer process taking place on the electrode surface, mass transport of the Zn(II) ions towards the electrode also contributes to the reaction. As the electrode potential becomes gradually more negative during the linear sweep voltammetry, the reduction of Zn(II) becomes dominated by the rate at which the ions reach the electrode

surface. Figure 5.2a shows a family of linear sweep voltammograms of Zn(II) reduction on a glassy carbon rotating disk electrode at various speeds: 400, 900, 1600, 2500 and 3600 rpm. The electrolyte composition was the same as that used in the experiments of Figure 5.1a and b. In order to avoid excessive hydrogen evolution, the electrode potential was swept from – 1.0 V to – 2.0 V *vs.* Ag|AgCl at 20 mV s^{-1}. The reduction of zinc was observed at the same potential as in the cyclic voltammogtam, – 1.2 V *vs.* Ag|AgCl, and well defined plateaus of constant current density where observed after – 1.4 *vs.* Ag|AgCl. The constant supply of the zinc ions to the electrode surface due to the rotation of the electrode at different rates helps to maintain Zn(II) ion concentration constant on the surface. Increased rotation speed was found to shorten the plateau region and lead to earlier evolution of hydrogen.

The limiting current density for each rotating speed was measured at the mid-point of the plateau give the potential value. The supply rate of zinc ions to the cathode surface is necessary to equalize with the electrodeposition rate. If the limiting current density of such electrochemistry is too low compared to the applied current density, hydrogen evolution takes place instead of zinc electrodeposition and hence increases the electrolyte resistance reducing the effective plating area, which can result in burnt deposit [36]. At such conditions, the supply rate of zinc ion to the negative electrode needs to be increased. As shown in Figure 5.1b, a linear relationship between the limiting current density with the square root of the rotating rate is observed and follows the Levich equation.

$$j_{lim} = 0.620\, zFD^{2/3}\omega^{1/2}\, v^{1/6}\, c \qquad (3)$$

where j_{lim} is the limiting current density (A cm^{-2}), F is Faraday's constant, ω is the rotation rate of the disk (radians s^{-1}) and v is the kinematic viscosity of the electrolyte (cm^2 s^{-1}).

The linear behaviour of this process indicates that the reduction of Zn(II) ions is under complete mass transport control. By using the gradient of Figure 5.2b, a diffusion coefficient of 7.8×10^{-6} cm^2 s^{-1} was estimated. This value is slightly larger than the one obtained from the Randles-Sevik equation as possibly both hydrogen adsorption and oxygen reduction reactions are more significant under the mass transport controlled regime and contribute to higher degree to the observed limiting current than in the cyclic voltammetry experiment. In this study, the average diffusion coefficient of zinc ion obtained from the Levich and Randles-Sevik equations in the electrolyte of 0.01 mol dm^{-3} zinc methanesulfonate and 0.5 mol dm^{-3} sodium methanesulfonate at pH 4 is 7.5×10^{-6} cm^2 s^{-1}.

In the industry of high speed electroplating, increasing mass transport is a common technique to provide a high current density and a fast electrodeposition rates. Literature reported that powdery and burnt deposits can be avoided by increasing the limiting current density via mass transport techniques [22, 36]. Turbulent flow is often used for industrial high speed zinc electrodeposition [37].

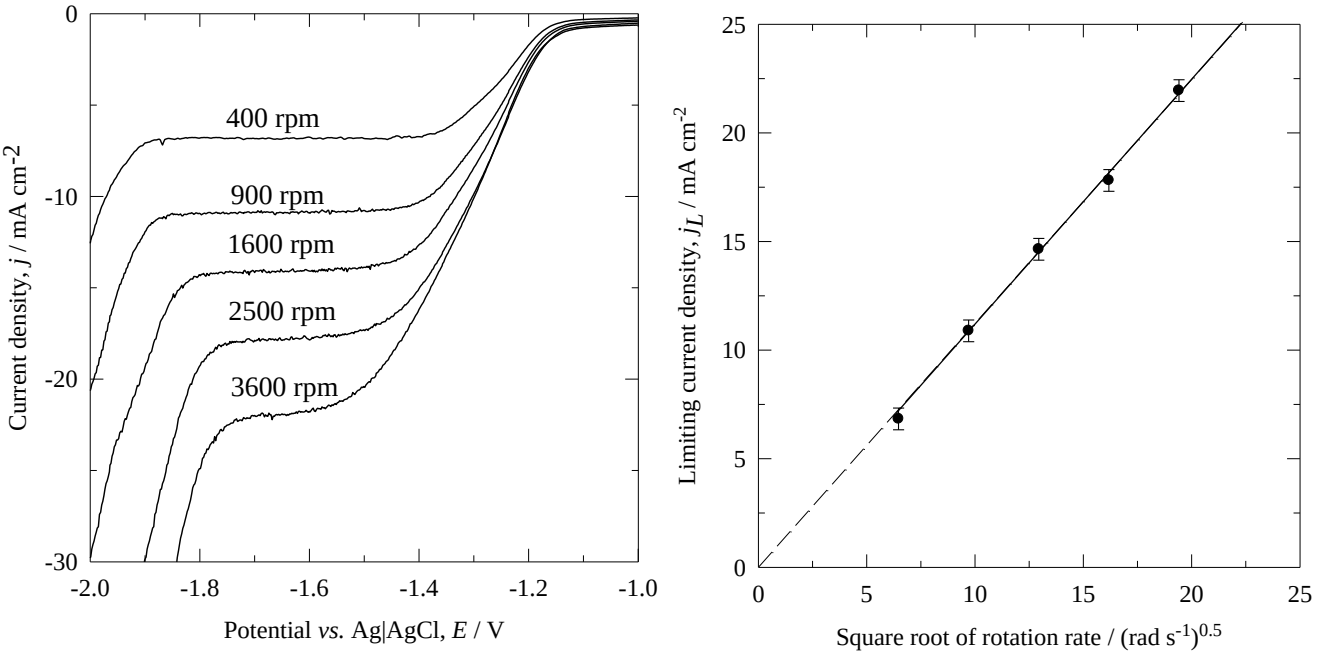

Figure 5.2. Effect of rotation speed on zinc electrodeposition in methanesulfonic acid at glassy carbon electrode. (a) Cyclic voltammogram and (b) Levich plot. Electrolyte: as in Figure 5.1. Rotation speeds were 400, 900, 1600, 2500, 3600 rpm. The electrode was swept from – 1.0 to – 2.0 V *vs.* Ag|AgCl scanning at 20 mV s^{-1} and 20 ^{o}C.

5.2.2. *Zinc ion concentration*

Figure 5.3a shows the linear sweep voltammogram of zinc electrodeposition at a range of zinc concentrations of 10, 20, 40, 60 and 80 $\times$ 10^{-3} mol dm^{-3} at 600 rpm rotation speed in 0.5 mol dm^{-3} sodium methanesulfonate at pH 4 and 295 K. The electrode potential was swept from – 1.0 to – 2.0 V *vs.* Ag|AgCl at 20 mV s^{-1}. As the concentration of zinc increases, the nucleation potentials shift towards positive values linearly with the logarithm of Zn(II) ion concentration by 58 $\pm$ 2 mV per 10-fold change in concentration. The

magnitude of such potential shift is similar to the that obtained in sulphate electrolyte reported in the literatures [29] .

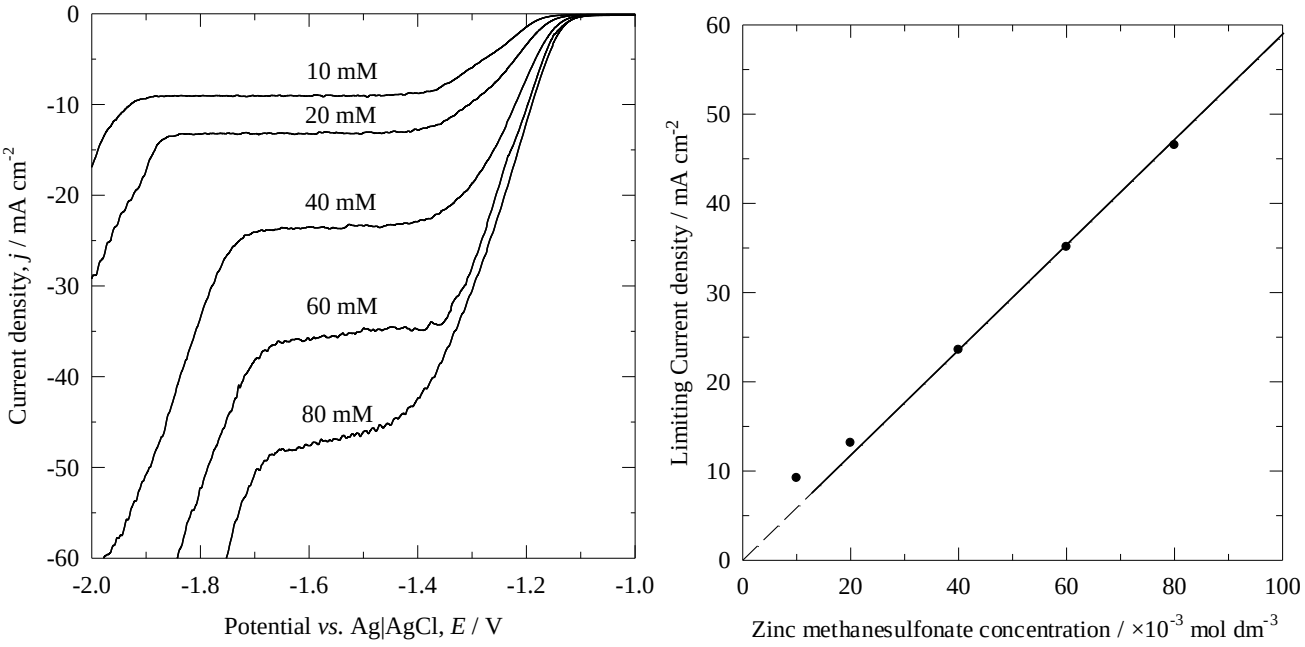

(a) (b)

Figure 5.3. Effect of zinc ion concentration on zinc electrodeposition in methanesulfonic acid at glassy carbon electrode (20 ^{o}C). (a) Linear sweep voltammogram and (b) the plot of zinc ion concentrations against the limiting current densities. Electrolyte: as in Figure 5.1. Zinc concentrations: 10, 20, 40, 60 and 80 × 10^{-3} mol dm^{-3}. The electrode was swept from – 1.0 to – 2.0 V *vs.* Ag|AgCl scanning at 20 mV s^{-1} at 600 rpm and 20 ^{o}C.

Figure 5.3b shows the limiting current densities as a function of the concentration of the zinc ion. The limiting current density of zinc electrodeposition increased by *c.a.* 10 mA cm^{-2} per every 10 mM zinc ion concentration. The linear plot confirms the fact that the system was under hydrodynamic condition according to the Levich equation. The potential window at which the limiting current plateau decreases as the concentration of zinc

increases suggesting that hydrogen evolution is less favourable as more zinc is deposited.

5.2.3. *Concentration of protons*

Figure 5.4 shows the linear sweep voltammogram of zinc electrodeposition at a range of pHs from 0 to 4 at the rotation speed of 600 rpm. The electrolyte composition is the same as in Figure 5.1. The electrode potential was swept from – 1.0 to – 2.0 V *vs.* Ag|AgCl at 20 mV s^{-1}. At lower pH values, the nucleation potentials were shifted towards more positive values, which is due to the higher conductivity of the electrolyte and to the increased concentrations of protons. Smaller limiting current plateaus were observed at pHs 4 and 3 than at lower values.

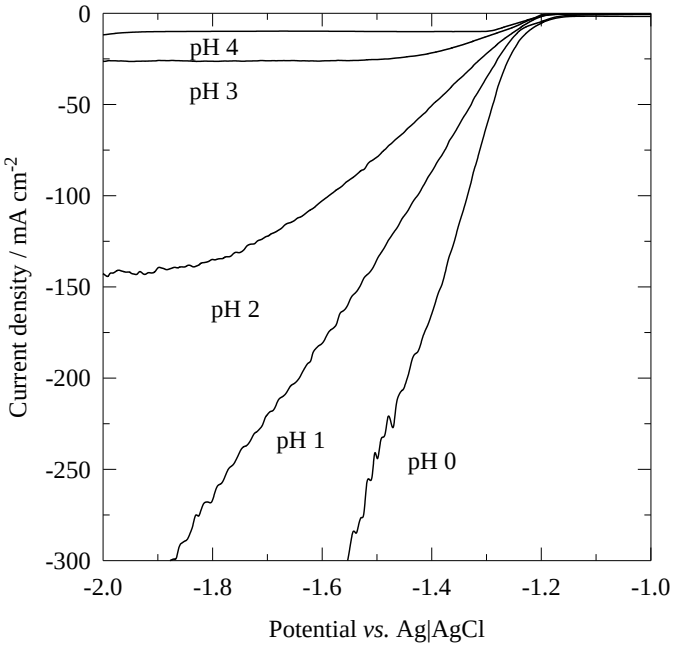

Figure 5.4. Effect of electrolyte acidity on zinc electrodeposition in methanesulfonic acid at glassy carbon electrode at 600 rpm. Electrolyte: as in figure 5.1. Solution acidity was pH 4, 3, 2, 1 and 0. The electrode was swept from – 1.0 to – 2.0 V *vs.* Ag|AgCl at 20 mV s^{-1} and 20 ^{o}C.

At increased electrolyte acidity from pH 2 to 0, the stability of the zinc methanesulfonate complexes decreases and the reduction of protons occurs on the newly formed zinc nuclei. This results in a larger current density plateau at pH 2 but undefined plateau at pH 0 and 1. In these two cases, zinc electrodeposition takes place simultaneously with hydrogen evolution and the two reactions compete and the sharp increase in current density was due to the excessive hydrogen evolution. The competition of the deposition of zinc and hydrogen evolution has been confirmed by the reaction model reported by C. Cachet and R. Wiart [38], which stated that the discharge of zinc ion is firstly inhibited by hydrogen adsorption following by the hydrogen evolution on the surface of the zinc deposit. At such highly acidic media, the zinc ion concentration on the electrode surface is relatively low and hydrogen adsorption on the electrode is therefore easy. In this case, the current is mainly used for hydrogen evolution and the current efficiency of zinc deposition decreases.

The suppression of hydrogen evolution is necessary to promote zinc electrodeposition. Indium has been suggested as an additive to increase the hydrogen overpotential giving a current efficiency almost 95 % compared to 70 – 80 % without the additive [39, 40]. Other finding suggests that additives, such as Na-benzylnicotinate [41], polyethylene glycol (PEG) [9, 41], cetyltrimethyl ammonium bromide (CTAB) [19], tetrabutylammonium bromide (TEBACl) [42], perfluorosurfactants [43], tartaric acid [44], succinic acid [44], thallium [39], indium [45], cellulose [46] are capable of suppressing the hydrogen evolution reaction. In the plating industry, buffer reagents are often incorporated to stabilize the pH and avoid excessive hydrogen evolution [47].

5.2.4. *Operating temperature*

Figure 5.5 shows the linear sweep voltammograms of zinc electrodeposition at a range of electrolyte temperatures from 20 to 60 ^{o}C on a glassy carbon rotating disk electrode at 600 rpm. The electrolyte composition is the same as in the experiments of Figures 5.1. Both, the nucleation potential of zinc ions and hydrogen evolution potential shift towards more positive values as the temperatures increased. The change in such electrode potential obeys the Nernst equation, as a lower driving force for zinc electrodeposition is required as the temperature increases.

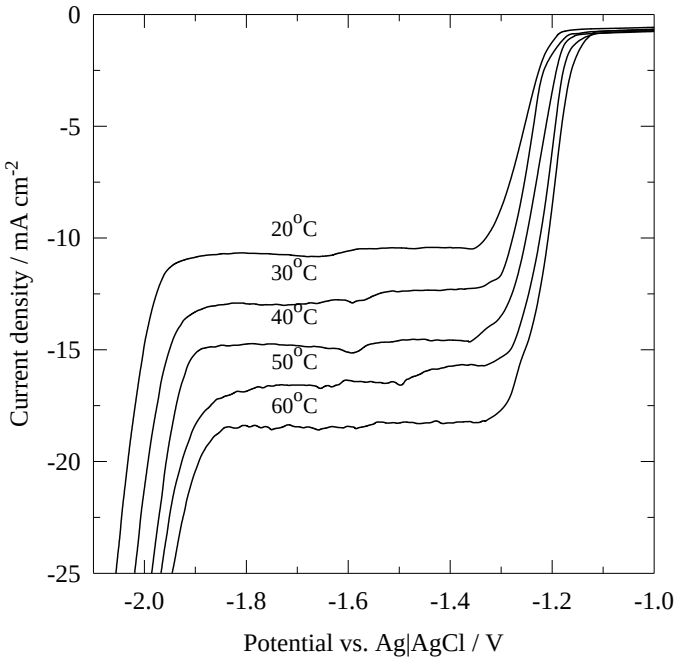

Figure 5.5. Effect of operating temperatures on zinc electrodeposition in methanesulfonic acid at glassy carbon electrode at 600 rpm. Electrolyte: as in Figure 5.1. Electrolyte temperature: 20, 30, 40, 50 and 60 ^{o}C. The electrode was swept from – 1.0 to – 2.0 V *vs.* Ag|AgCl at 20 mV s^{-1}.

The electrode potential for the deposition of Zn(II) shifted 60 mV from – 1.19 V *vs.* Ag|AgCl at 20 ^{o}C to – 1.13 V *vs.* Ag|AgCl at 60 ^{o}C. Similar findings were observed by

Zhang *et al.* [48] who reported that the cathode potential decreased by *c.a.* 65 mV when the temperature increased from 30 ^{o}C to 45 ^{o}C during zinc deposition in a sulfate electrolyte with 1-butyl-3-methylimidazolium hydrogen sulphate as an electrolytic additive. Elevated temperature can hence reduce the polarization of zinc ions reduction effectively. Since diffusion coefficient is a function of temperature, limiting current densities will increase with temperature. Every 10 ^{o}C increase in electrolytic temperature would lead to an increase in current density of *c.a.* 5 mA cm^{-2}. During the zinc dissolution process, the charge of the zinc stripping peak was higher at elevated temperature confirming that zinc electrodeposition has been facilitated.

5.2.5. *Effect of electrolytic additives*

Electrolytic additives are often employed in the plating industry to obtain endurable, uniform, and more compact coatings as well as to decrease the rate of unfavourable reactions. Figure 5.6a shows the cyclic voltammogram of zinc electrodeposition with the addition of three selected electrolytic additives: tetrabutylammonium hydroxide, potassium sodium tartarate and indium oxide at a glassy carbon static disk electrode. All additives were tested at 2 × 10^{-3} mol dm^{-3} concentration in an electrolyte containing 0.01 mol dm^{-3} zinc methanesulfonate and 0.5 mol dm^{-3} sodium methanesulfonate adjusted to pH 4 with methanesulfonic acid at 295 K. The potential was swept from – 0.8 V to – 1.5 V *vs.* Ag|AgCl and then reversed. The reduction and oxidation processes can be analyzed at the charge and discharge cycles of a half-cell zinc battery, respectively. Larger anodic peaks were observed with the addition of another two electrolytic additives, except with tetrabutylammonium hydroxide. The discharge/charge ratio between the anodic and cathodic processes (Table 5.1), using indium oxide and potassium sodium tartarate were approximately 88 %. This is an improvement to the experiments in the absence of additives (82 %).

Linear sweep voltammograms in the presence of the three electrolytic additives were also carried out on a rotating vitreous carbon electrode at rotation speed of 600 rpm as shown in Figure 5.6b. Well-defined plateau of limiting current densities were observed in all the experiments but each additive presented different limiting current density, this could be due to the additive reacting or adsorbing on the newly formed zinc deposit on the carbon electrode thus decreasing the above area. Nucleation potentials of zinc in the presence of indium oxide and potassium sodium tartarate shifted to more positive values as shown in Table 5.1. This can be beneficial for battery efficiencies, as lower charge voltages can be expected due to the reduced overpotential and zinc electrodeposition taking place prior to hydrogen evolution. The coulombic efficiency slightly improved except when tetrabutylammonium hydroxide was used. Although larger overpotentials obtained with tetrabutylammonium hydroxide result in lower voltage efficiency, such overpotentials were reported to be useful for refining the grain size and hence brightening the electrodeposit by partly covering the electrode surface and blocking the growing of the zinc crystals in different directions [49].

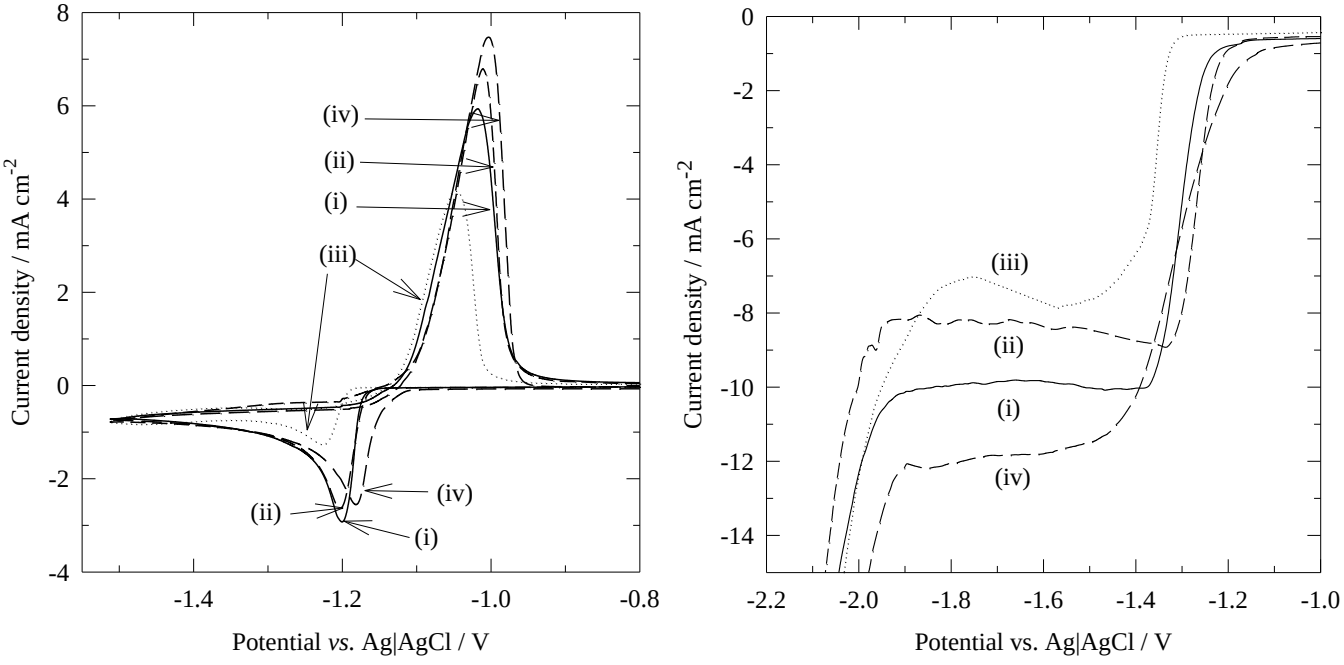

Figure 5.6. Effect of electrolytic additive on cyclic voltammogram of zinc electrodeposition in methanesulfonic acid (a) at static electrolyte and (b) at 600 rpm. Electrolyte: as in Figures 5.1. Electrolytic additives were at 2×10^{-3} mol dm^{-3}, (i) no additive, (ii) potassium sodium tartarate, (iii) tetrabutylammonium hydroxide and (iv) indium oxide.

	Electrolytic additive	Static electrode						Electrolyte stirring at 600 rpm
		Nucleation potential *vs.* Ag|AgCl / V	Cathodic peak		Anodic peak		Charge ratio / %	Limiting current density, j_{lim} / $mAcm^{-2}$
			Voltage *vs.* Ag|AgCl / V	Current density / $mAcm^{-2}$	Voltage *vs.* Ag|AgCl / V	Current density / $mAcm^{-2}$		
(i)	No additive	− 1.16	− 1.19	− 2.86	− 1.03	5.8	82.3	− 9.8
(ii)	Potassium sodium tartarate	− 1.15	− 1.20	− 2.60	− 1.01	6.7	87.6	− 8.3
(iii)	Tetrabutylammonium hydroxide	− 1.18	− 1.22	− 1.21	−1.05	4.2	66.6	− 7.7
(iv)	Indium oxide	− 1.12	− 1.18	− 2.58	− 1.01	7.5	87.7	− 11.8

Table 5.1. The electrochemical behaviour of the electrolytic additives: (i) no additive, (ii) potassium sodium tartarate, (iii) tetrabutylammonium hydroxide and (iv) indium oxide at static and rotating glassy carbon electrode. Electrolyte composition as in Figure 5.6. All potentials were measured *vs.* Ag|AgCl.

5.3. Zinc half-cell efficiencies in a divided parallel plate flow cell

Aiming to achieve the optimum electrolyte compositions and operating conditions for a zinc-based redox flow battery, the electrodeposition and stripping of zinc was carried out over a wide range of concentrations, electrolyte flow rates, temperatures, applied current densities and electrolytic additives in a divided parallel flow cell. Unless indicated otherwise, the electrolyte composition used for the negative electrolyte compartment was 1.5 mol dm^{-3} zinc methanesulfonate in 1 mol dm^{-3} methanesulfonic acid while the positive compartment contained 1 mol dm^{-3} methanesulfonic acid. Electrodeposition of zinc on a carbon polyvinyl-ester composite substrate was carried out at 50 mA cm^{-2} and 50 ^{o}C for four hours. Table 5.2 summarizes the estimated half-cell efficiencies in terms of voltage, charge and energy at different operating conditions.

5.3.1. *Effect of operating parameters*

Figures 5.7a, b and c show the effects of current density, temperature and electrolyte flow rate, respectively, on the charge-discharge curves of zinc half cell reaction. Without the addition of additives, the largest energy efficiency was 70 %, which was obtained at a low current density of 20 mA cm^{-2} (Table 5.2). The highest efficiency at 20 mA cm^{-2} was attributed to the reduced ohmnic drop and improved voltage efficiency as the self-discharge (current density) of zinc became more significant while discharging at low current density. At higher applied current density, coulombic efficiencies were found to be higher but overall efficiency decreased. Similar findings were also reported by Saba and Elsherief [50] over a range of sulfuric acid and Zn(II) ion concentrations.

Figure 5.7b shows the electrode potential *vs.* time at different temperatures during reduction and oxidation of zinc. Higher energy efficiency was obtained at lower operating temperatures, despite the fact that the solution conductivity and the resulting voltage efficiency increased with higher temperature. The coulombic efficiency significantly decreases from 94 % at 20 ^{o}C to 68 % at 70 ^{o}C. This is because higher temperature can lead to stronger depolarizing effect on hydrogen evolution than zinc deposition [51], therefore less zinc was deposited at such a high temperature. As the mean linear electrolyte flow velocity increased from 1.8 to 5.8 cm s^{-1}, an increase in coulombic efficiency was observed as shown in Figure 5.7c. This is because the increased mean linear flow velocity can reduce the diffusion layer and facilitate the transport of zinc ions to the working electrode. Despite this, larger voltage drop was also observed at increased mean linear flow velocity possibly due to the bypass of the electrolyte formed. Therefore, there was no significant improvement on the overall energy efficiencies of the zinc half-cell reaction.

5.3.2. *Effect of zinc ions and acid concentrations*

Electrolyte compositions, especially the concentration of acid, were found to be crucial for the flow cell performance. Energy efficiency was as high as 62 % at 1 mol dm^{-3} methanesulfonic acid compared to 41 % at 3 mol dm^{-3} methanesulfonic acid. Alfantazi and Dreisinger reported that electrical conductivity increase linearly with sulfuric acid concentration, therefore higher voltage efficiency was obtained [52]. Due to more dominant hydrogen evolution and faster corrosion rate at higher acid concentration, a significant decrease in coulombic efficiency was observed. The increase in zinc ion concentration was found to facilitate the electrodeposition process indicated by the improvement of the coulombic efficiency but this does not benefit the energy efficiency [52].

The lower charge cell voltages observed as the concentration of Zn(II) ions increases can be explained by the Nernst equation. Since the dissolution of zinc back to Zn(II) species becomes more difficult at higher Zn(II) ion concentration in the vicinity of the electrode surface, lower discharge voltages were obtained. Despite this, higher Zn(II) ion concentration can be advantageous for redox flow battery as it allows the battery to charge at high current densities without the mass transport limitation. Such a high concentration ensures that enough Zn(II) ions exist at all state of charges. Additionally, two mole of methanesulfonic acid are formed per each mole of zinc methanesulfonate is used in the electrodeposition as shown in equation (1) [53]. In order to minimize the hydrogen evolution and facilitate zinc electrodeposition, higher Zn(II) ion concentration is preferred in the negative electrolyte.

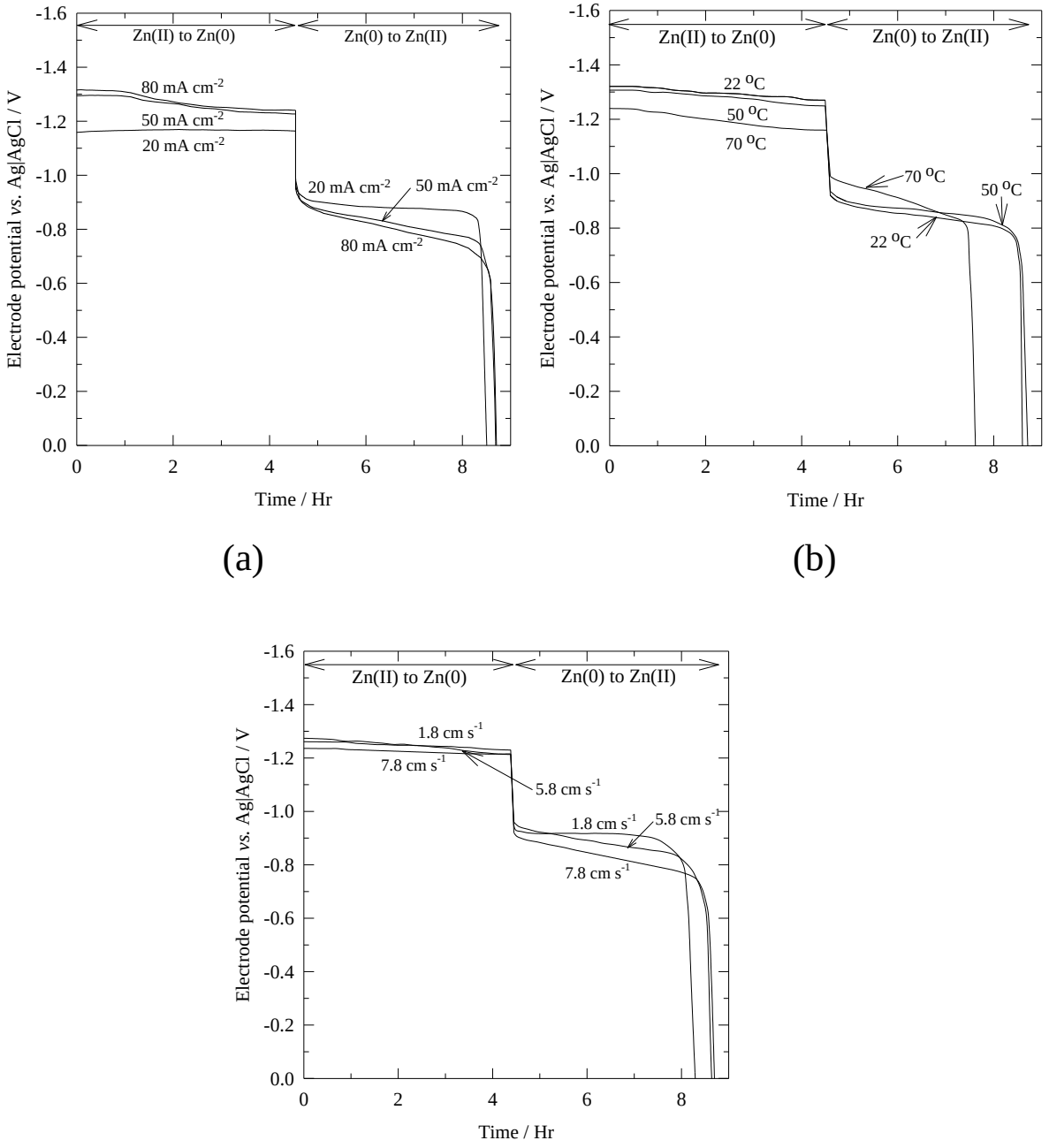

Figure 5.7. The effect of current density, temperature and mean linear electrolyte flow rate of zinc half cell on a carbon polyl-ester composite substrate from a methanesulfonic acid bath in a parallel plate flow cell. Unless indicated, the current density was 50 mA cm^{-2}, deposition time 4 hours, temperature 50 ^{o}C, mean linear flow velocity 3.9 cm s^{-1} and the solution was 1.5 mol dm^{-3} $Zn(CH_3SO_3)_2$ and 1 mol dm^{-3} CH_3SO_3H.

Operating parameter	Zinc half cell overpotential, η / V	Zinc half-cell charge voltage *vs.* Ag|AgCl / V	Zinc half-cell discharge voltage *vs.* Ag|AgCl / V	Zinc half-cell efficiencies / %		
				Voltage	Coulombic	Energy
Current density / mA cm^{-2}						
20	0.26	− 1.17	− 0.91	78	90	70
50	0.41	− 1.28	− 0.85	68	91	62
80	0.41	− 1.30	− 0.87	63	92	62
Temperature / ^{o}C						
22	0.45	− 1.32	− 0.87	66	94	62
40	0.43	− 1.31	− 0.88	67	94	62
50	0.41	− 1.28	− 0.85	68	91	62
70	0.27	− 1.19	− 0.92	71	68	52
CH_3SO_3H concentration / mol dm^{-3}						
0.5	0.42	− 1.26	− 0.84	67	94	62
1	0.41	− 1.26	− 0.85	68	91	62
2	0.36	− 1.28	− 0.88	71	87	62
3	0.34	− 1.24	− 0.89	72	57	41
Zn^{2+} concentration / mol dm^{-3}						
0.5	0.33	− 1.27	− 0.94	74	78	58
1	0.34	− 1.24	− 0.91	74	83	62
1.5	0.41	− 1.28	− 0.85	68	91	62
2	0.38	− 1.21	− 0.83	69	92	64
Mean linear flow velocity / cm s^{-1}						
1.8	0.33	− 1.24	− 0.92	74	86	63
3.9	0.41	− 1.28	− 0.85	68	91	62
5.8	0.37	− 1.25	− 0.88	70	92	64
7.8	0.41	− 1.27	− 0.86	67	92	62
Additive / × 0.002 mol dm^{-3}						
No additive	0.41	− 1.28	− 0.85	68	91	62
Potassium sodium tartarate	0.35	− 1.26	− 0.91	72	86	62
Tetrabutylammonium bromine	0.44	− 1.37	− 0.93	68	39	26
Indium oxide	0.27	− 1.21	− 0.94	78	94	73

Table 5.2. Half-cell efficiencies of electrodeposition and stripping of zinc on a carbon polyvinyl-ester composite substrate from a methanesulfonic acid bath in a parallel plate flow cell. Unless indicated otherwise, electrolyte compositions and operating conditions are the same as in Figure 5.7.

5.3.3. *Effect of electrolytic additives*

Three electrolytic additives from different categories were tested at a concentration of 2×10^{-3} mol dm^{-3}. For instance, both indium oxide [54] and potassium sodium tartarate [55] are inorganic additives, while tetrabutylammonium hydroxide is a surface active agent. In order to determine whether they are suitable additives for battery performance, charge-discharge experiments were carried out with these additives as shown in Figure 5.8. With the addition of indium oxide, the energy efficiency improved significantly from 62 % without additive to 73 % (Table 5.2). In this case, higher coulombic and voltage efficiencies were obtained. The high coulombic efficiency obtained could be attributed to the large hydrogen overpotential of indium as an additive also observed in the Plurion Inc.'s zinc-cerium system [45], hence more current can be used for zinc electrodeposition. As presented in the voltammetry study in section 5.2.5., lower deposition overpotential was observed. Hence, an improved voltage efficiency was expected in this electrolysis study, which is consistent with the previous finding of Yang and Lin [54] in their alkaline zinc-air battery.

The remaining two additives did not have any improvement on the half-cell efficiencies. This is probably due to the strong adsorption and inhibiting effect of the additives (the levelling property). Ganne *et al.* reported that some electrolytic additives could slow down the charge transfer reactions, poisoning the active kink sites and increasing the deposition overpotential [24]. For instance, the coulombic and energy efficiencies in the presence of tetrabutylammonium hydroxide were only 39 % and 26 %, respectively (Table 5.2). As a result, only indium oxide was suitable to be used as an electrolytic additive in a zinc-based flow battery.

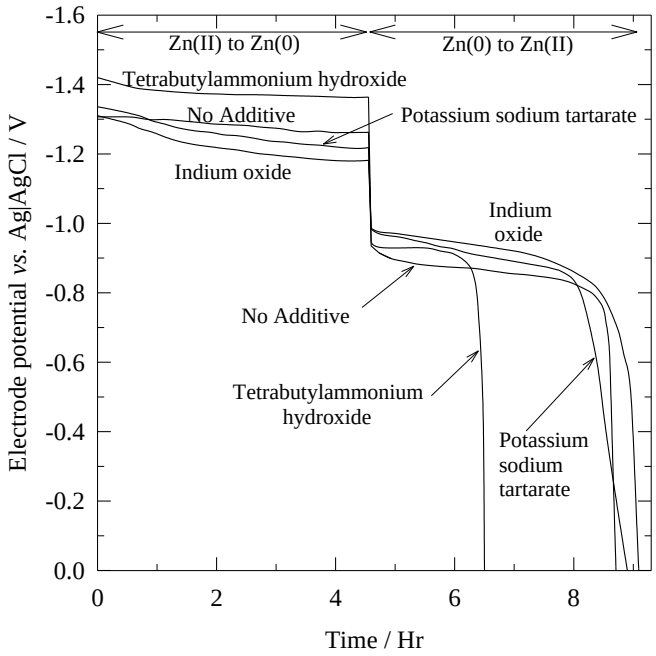

Figure 5.8. The effect of electrolytic additives of zinc half cell on a carbon polyl-ester composite substrate from a methanesulfonic acid bath in a parallel plate flow cell. Unless indicated, electrolyte compositions and operating conditions are the same as in Figure 5.7.

5.4. Coating morphologies

Figure 5.9(a) – (d) show the microstructures of the zinc electrodeposits when the addition of electrolytic additives were used at 2×10^{-3} mol dm^{-3}: (a) no additive, (b) potassium sodium tartarate, (c) tetrabutylammonium hydroxide and (d) indium oxide. In the absence of additive, hexagonal-like crystalline structure was aligned plate-by-plate parallel to the substrate (Figure 5.9a). This morphology is typical and has been observed in various literatures [52, 56]. On the uppermost of such hexagonal plates, a relatively rough, irregular plate-like structure was observed because of the continued growth and the stacking of the hexagonal platelet on the top of one another during the prolonged deposition for 4 hours. The mechanisms of such stacking behavior from nucleation to growth have been discussed by a proposed model of Lee *et al.* [57] with schematic diagrams and microscope images in the medium of zincate.

In general, the microstructure of the zinc deposit without additive is quite smooth indicated by a shiny appearance without any nodule or dendrite. This finding is consistent with previous investigations that methanesulfonic acid can reduce the dendritic growth [13, 14], which has been a major problem in the zinc-halogen redox flow batteries, leading to short circuit and hence reduced life cycle [58-61]. In a zinc-bromine system, zinc dendrite was observed at current density as low as 15 mA cm^{-2} [62]. Therefore, methanesulfonic acid is attractive for zinc-based redox flow battery, as it not only minimizes the dendritic growth but also maintain high coulombic efficiency (91 %) as discussed in section 5.2.5.

With the addition of potassium sodium tartarate, similar microstructure of the rough, irregular plate-like structure was observed as in the absence of additive (Figure 5.9b). Comparing with the previous micrograph, the hexagonal platelets were more difficult to distinguish and were mostly covered by the irregular plate structures. This was due to the faster growth rate of the zinc platelets at the lower overpotential of potassium sodium tartarate as suggested in the voltammetric study of this work. In the presence of tetrabutylammonium hydroxide (Figure 5.9c), the microstructure was very different and was formed by nano size needle-shaped structures. Similar morphology has been reported by Gomes *et al.* [56] in the presence of cetyl trimethyl ammonium bromide in the sulfate medium. The needle-shaped microstructure was due to the competitions between nucleation and crystal growth by the strong blocking effect of the absorbed surfactant as discussed in section 3.5. The strong blocking effect and the adsorption of tetrabutylammonium hydroxide has been examined by the low coulombic and voltage efficiencies in the deposition and stripping experiment in a parallel flow cell (Section 5.3.3).

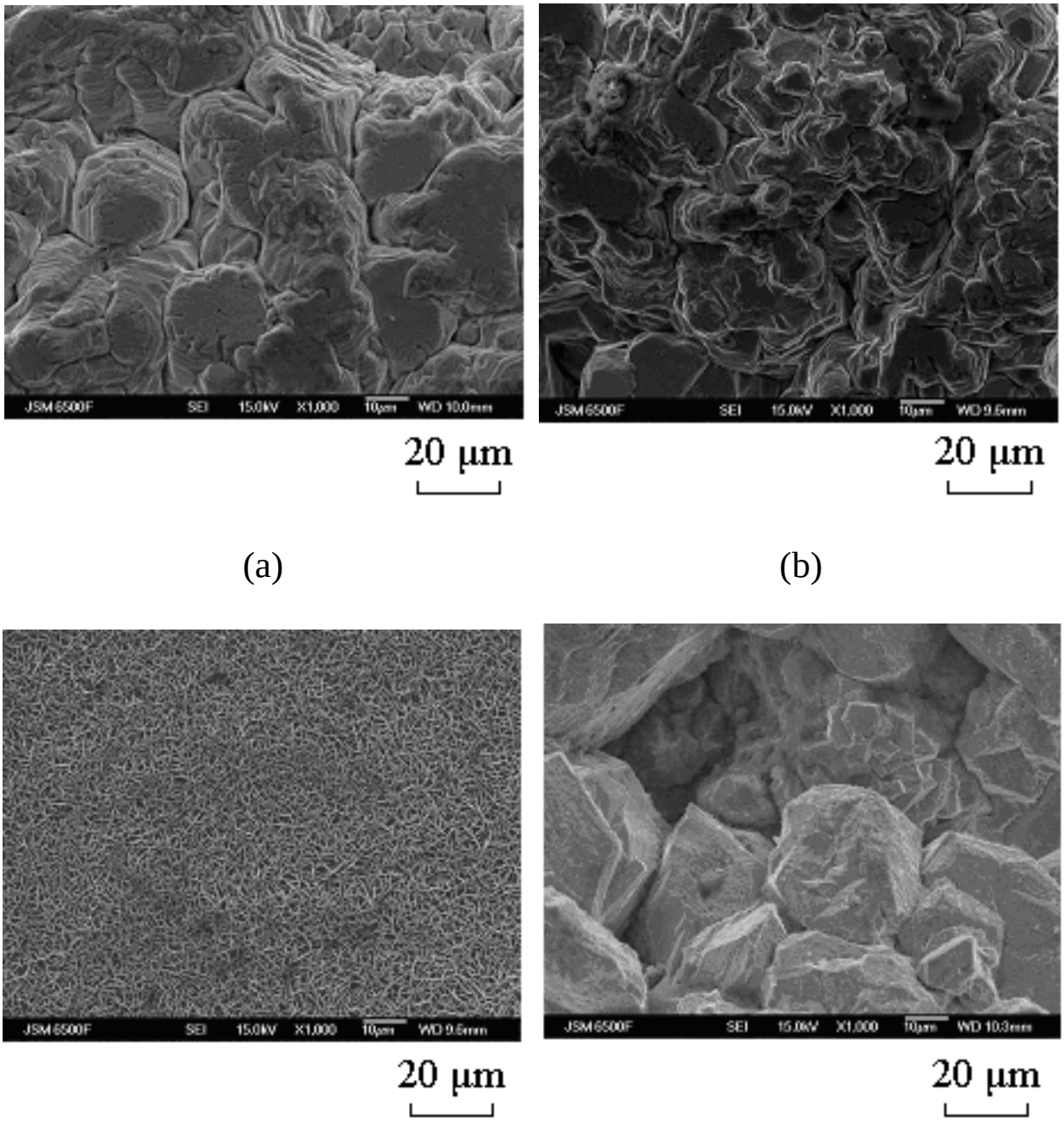

Figure 5.9. The effect of electrolytic additives on microstructures of zinc electrodeposits obtained on a carbon polyvinyl-ester composite for a methanesulfonic acid bath in a beaker. Electrolytic additives 2×10^{-3} mol dm^{-3}, (a) no additive, (b) potassium sodium tartarate, (c) tetrabutylammonium hydroxide and (d) indium oxide. Electrolyte compositions and operating conditions were as in Figure 5.8 but stirring at 400 rpm.

Among the additives tested, indium oxide had the highest half-cell efficiencies and a significant effect on the cell voltage. Due to the low deposition overpotential, zinc deposited at a faster rate and boulder-like agglomerate was observed with the addition of indium oxide. The boulder structure as shown in Figure 5.9d has been considered to be a precursor of a dendrite but not necessarily developed [63]. In this work, relatively rough and nodular morphology was observed rather than dendrites. On the coating surface, a small amount of indium (0.55 wt. %) has been detected by the energy-dispersive spectroscopy. In all electrodeposits, no dendrite has been observed after depositing for 4 hours at 50 mA cm^{-2} in the presence and absence of the electrolytic additives.

5.5. Conclusions

1. Zinc electrodeposition at 0.01 mol dm^{-3} Zn(II) ions in methanesulfonate medium was a mass transport controlled process and with a diffusion coefficient of 7.5×10^{-6} cm^2 s^{-1} for Zn^{2+} obtained from the average estimations of the Randles-Sevik and Levich equations.

2. At higher acid concentration, a significant decrease in coulombic efficiency was observed due to more dominant hydrogen evolution and a faster corrosion rate. Although higher zinc ion concentration led to more difficult dissolution process, it is still advantageous for redox flow battery application as not only facilitates the deposition process, but also allows the battery to charge at high current densities without the mass transport limitation and ensures enough Zn(II) ions at all state of charges. The optimum electrolyte compositions for flow battery application were suggested at high zinc(II) methanesulfonate concentration (1.5 – 2 mol dm^{-3}) and at low methanesulfonic acid concentration (i.e. 0.5 mol dm^{-3}).

2. No dendrite was observed (with or without electrolytic additive) in any of the zinc electrodeposits at 50 mA cm^{-2} and 60 ^{o}C for 4 hours. The low deposition overpotential observed with the addition of 2×10^{-3} mol dm^{-3} potassium sodium tartarate and indium oxide led to irregular, rough layer-like and boulder granular microstructures, respectively, giving an appearance of relatively rough surface. Among the three additives tested, only indium oxide was found to be suitable for zinc-based redox flow battery as energy efficiency improved significantly from 62 % in the absence of additives to 73 % due to the improvement of both coulombic and voltage efficiencies in the presence of additives.

5.6. References

1. M.D. Gernon, M. Wu, T. Buszta, P. Janney, Green Chem. 1 (1999) 127-140.
2. R.P. Kreh, R.M. Spotnitz, J.T. Lundquist, J. Org. Chem. *54* (1989) 1526-1531.
3. J.Y. Lee, J.W. Kim, M.K. Lee, H.J. Shin, H.T. Kim, S. M. Parka, J. Electrochem. Soc. 151 (2004) C25-C31.
4. K. Saber, C.C. Koch, P.S. Fedkiw, J. Mater. Sci. Eng. A341 (2003) 174-181.
5. M. Mouanga, L. Ricq, G. Douglade, J. Douglade, P. Berçot, J. Surf. Coat. Technol. 201 (2006) 762-767.
6. J.X. Yu, Y.Y. Chen, H.X. Yang, Q.A. Huang, J. Electrochem. Soc. 146 (1999) 1789-1793.
7. D.S. Baik, D.J. Fray, J. Appl. Electrochem. 31 (2001) 1141- 1147.
8. G. Trejo, R. Ortega, Y. Meas, P. Ozil, E. Chaînet, B. Nguyen, J. Electrochem. Soc. 145 (1998) 4090-4097.
9. M.C. Li, S.Z. Luo, Y.H. Qian, W.Q. Zhang, L.L. Jiang, J.I. Shen, J. Electrochem. Soc. 154 (2007) D567-D571.
10. Shanmugasigamani, M. Pushpavanam, J. Appl. Electrochem. 36 (2005) 315-322.
11. M.C. Li, L.L. Jiang, W.Q. Zhang, Y.H. Qian, S.Z. Luo, J.N. Shen, J. Solid State Electrochem. 11 (2007) 549-553.
12. C.K. Sarangi, B.C. Tripathy, I.N. Bhattacharya, T. Subbaiah, S.C. Das, B.K. Mishra, 22 (2009) 1266-1269.
13. G. Brodt, J. Haas, W. Hesse, H.U. Jäqer, US 2003/0141195 Al, 31/07/2003, (2003).
14. R. Clarke, USP 7582385 B2, 01/09/2009, (2009).
15. M. Skyllas-Kazacos, F. Grossmith, J. Electrochem. Soc. 134 (1987) 2950-2953.

16. H.T. Zhou, H.M. Zhang, P. Zhao, B.L. Yi, Electrochim. Acta 51 (2006) 6304-6312.
17. C.M. Hagg, M. Skyllas-Kazacos, J. Appl. Electrochem. 32 (2002) 1063-1069.
18. J.X. Yu, H.X. Yang, X.P. Ai, Y.Y. Chen, Russian J. Electrochem. 38 (2002) 321-325.
19. A. Gomes, M.I. da Silva Pereira, Electrochim. Acta 52 (2006) 863-871.
20. A.M. Volmer, Z. Weber, J. Phys. Chem. 119 (1926) 277.
21. J.C. Ballesteros, P. Díaz-Arista, Y. Meas, R. Ortega, G. Trejo, Electrochim. Acta 52 (2007) 3686-3696.
22. F.C. Walsh, M.E. Herron, J. Phys. D: Appl. Phys. 24 (1991) 217.
23. R.C. Kerby, H.E. Jackson, T.J. O'Keefe, Y.M. Wang, Metall. Mater. Trans. B 8 (1977) 661-668.
24. F. Ganne, C. Cachet, G. Maurin, R. Wiart, E. Chauveau, J. Petitjean, J Appl. Electrochem. 30 (2000) 665-673.
25. E. Budevski, G. Staikov, W.J. Lorenz, Electrochimica Acta 45 (2000) 2559-2574.
26. B.Z. Jugović, T.L. Trišović, J.S. Stevanović, M.D. Maksimović, B.N. Grgur, Electrochim. Acta 51 (2006) 6268-6274.
27. H. Fischer, Electrochim. Acta 2 (1960) 50-91.
28. Fischer, Elektrolytische Absecheichung and Electrokrystallisation der Metallen Springer Berlin, (1954).
29. M.A.M. Ibrahim, J. Chem. Technol. Biotechnol. 75 (2000) 745-755.
30. A. Zirino, M.L. Healy, Limnology and Oceanography 15 (1970) 956-958.
31. A.E. Dong, J. Appl. Spectrosc. 27 (1977) 124-128.
32. L.E. Morón, Y. Meas, R. Ortega-Borges, J.J. Perez-Bueno, H. Ruiz, G. Trejo, Int. J. Electrochem. Sci. 4 (2009) 1735-1753.
33. J. Torrent-Burgués, E. Guaus, J. Portugaliae Electrochim. Acta 21 (2003) 179-189.
34. E. Guerra, Evaluation of zinc electrodeposition kinetics from acidic zinc sulfate solutions using a UPD modified platinum substrate, University of British Columbia (2003) https://circle.ubc.ca/handle/2429/16770 accessed on 1 September 2010.
35. G. Trejo, H. Ruiz, R. Ortega Borges, Y. Meas, J. Appl. Electrochem. 31 (2001) 685-692.
36. K. Sato, K. Yamato, K. Iozumi, Transactions ISIJ 23 (1983) 946-953.
37. L.J. Durney, W.H. Safranek, Electroplating engineering handbook; Chapter 39: High speed electroplating, common technique for sustaining high current density and a fast deposition rate, Chapman & Hall, (1998).
38. C. Cachet, R. Wiart, Electrochim. Acta 44 (1999) 4743-4751.
39. R.L. Clarke, B.J. Dougherty, S. Harrison, P.J. Millington, S. Mohanta, US 2004/ 0202925 A1, (2004).
40. M. Yano, S. Fujitani, K. Nishio, Y. Akai, M. Kurimura, J. Power Sources 74 (1998)

129-134.
41. L. Mirkova, G. Maurin, I. Krastev, C. Tsvetkova, J. Appl. Electrochem. 31 (2001) 647-654.
42. B.C. Tripathy, S.C. Das, G.T. Hefter, P. Singh, J. Appl. Electrochem. 28 (1998) 915-920.
43. J.L. Zhu, Y.H. Zhou, C.Q. Gao, J. Power Sources 72 (1998) 231-235.
44. C.W. Lee, K. Sathiyanarayanan, S.W. Eom, H.S. Kim, M.S. Yun, J. Power Sources 159 (2006) 1474-1477.
45. Plurion Systems Inc. http://plurionsystems.com/contact.html accessed on 1 September 2010.
46. C.W. Lee, K. Sathiyanarayanan, S.W. Eom, H.S. Kim, M.S. Yun, J. Power Sources 160 (2006) 161-164.
47. Jr. Diaddario, L. Leonard, USP 6143160, (2000).
48. Q.B. Zhang, Y.X. Hua, T.G. Dong, D.G. Zhou, J. Appl. Electrochem. 39 (2009) 1207-1216.
49. E.M. Hofer, H.E. Hintermann, J. Electrochem. Soc. (1963) 103-112.
50. A.E. Saba, A.E. Elsherief, Hydrometallurgy 54 (2000) 91-106.
51. F. Galvani, I.A. Carlos, J. Met. Finish. 95 (1997) 70-72.
52. A.M. Alfantazi, D.B. Dreisinger, J. Hydrometallurgy 69 (2003) 99-107.
53. A. Hazza, D. Pletcher, R. Wills, J. Phys. Chem. Chem. Phys. 6 (2004) 1773 - 1778.
54. C.C. Yang, S.J. Lin, J. Power Sources 112 (2002) 497-503.
55. C.C. Hu, C.Y. Chang, J. Mater. Chem. Phys. 86 (2004) 195-203.
56. A. Gomes, M.I. da Silva Pereira, Electrochim. Acta 51 (2006) 1342-1350.
57. S.K. Lee, J.H. Lee, Y.H. Kim, J. Electronic Materials 36 (2007) 1442-1447.
58. Y. Ando, T. Ochiai, USP 4510218, 04/09/1985, (1985).
59. Y. Ando, USP 4479856, (1984).
60. F.G. Will, USP 4074028, 02/14/1978, (1978).
61. R.A. Putt, M.J. Montgomery, USP 4218521 08/19/1980, (1980).
62. C. Ponce de León, A. Frías-Ferrer, J. González-García, D.A. Szánto, F.C. Walsh, J. Power Sources 160 (2006) 716-732.
63. I.N. Justinijanović, J.N. Jovićević, A.R. Despić, J Appl. Electrochem. 3 (1973) 193-200.

Chapter 6
Prevention of zinc corrosion in methanesulfonic acid

Chapter 6 Prevention of zinc corrosion in methanesulfonic acid

Introduction

Zinc is an active (anodic) material, dissolution of zinc and cathodic evolution of hydrogen have a high tendency to take place in acidic electrolytes at the same time as the mixed electrode system consisting of the following reaction:

At anodic sites,

$$Zn - 2\ e^- \rightarrow Zn^{2+} \qquad -0.76\ V\ \textit{vs.}\ SHE \quad (1)$$

At cathodic sites,

$$2H^+ + 2\ e^- \rightarrow H_2 \qquad 0\ V\ \textit{vs.}\ SHE \quad (2)$$

The equilibrium potentials of the couples in equations (1) and (2) are labeled as $E_{eq,Zn}$ and $E_{eq,H2}$, respectively. The actual corrosion potential is the potential at which the rate of zinc oxidation is equal to the rate of reduction of proton (H^+). For batteries, zinc corrosion and hydrogen evolution are undesirable reactions that lead to a reduced charge capacity and in need to introduce an additional hydrogen venting system. Prior to this work, there were only a few investigations of zinc dissolution at higher acid concentration in sulphuric [1], hydrochloric [2,3] and phosphoric acids [4]. Recently, increasing attention has been given to the use of methanesulfonic acid in energy storage applications [5-8]. Methanesulfonic acid has advantages over conventional acids in terms of lower corrosivity, higher conductivity and solubility for some common metal cations, such as Ce(III) [9], Pb(II) and Ag(I) [10]. Additionally, zinc electrodeposition in such medium has been reported to have minimal dendritic growth after long hours of deposition [8,11,12]. Therefore, a longer cycle life can be achieved. In this work, the mechanism of zinc corrosion and the corresponding hydrogen evolution were investigated under a wide range of electrolyte temperatures, zinc ions and acid concentrations. Instead of using toxic

mercury, a small amount of corrosion inhibitors were evaluated to inhibit the zinc corrosion process.

6.1. Corrosion of zinc in methanesulfonic acid

Corrosion of zinc in methanesulfonic acid was studied by measuring the weight loss and hydrogen evolution. Figure 6.1a illustrates the dependence of the weight loss over time in 1 mol dm^{-3} methanesulfonic acid at two electrolyte volumes of 100 and 500 cm^3. By immersing the zinc sample in a 100 cm^3 electrolyte, zinc dissolution started to increase slowly. After the second hour, the dissolution rate increased and levelled off after the sixth hour. The rate of hydrogen evolution followed similar trend against time as shown in Figure 6.1b. According to the equations 1 and 2, the charge for zinc dissolution is the same with that of the simultaneous hydrogen evolution. By using Faraday's law, the amount of hydrogen evolution should be proportional to the mass of zinc dissolved in the electrolyte: 1 gram of the dissolved zinc is equivalent to an electrical charge of 822 mA h and evolves 329 cm^3 of hydrogen (1 μ A cm^{-2} = 2.92 mg dm^{-2} day^{-1} of Zn = 0.4 μ L h^{-1} cm^{-2} of H_2) by using ideal gas law (V = n R T / P) at room temperature and atmospheric pressure [13]. As shown in Figure 6.1b, the estimated hydrogen volume based on the weight loss data is in agreement with the evolved hydrogen evolution volume observed experimentally during zinc dissolution. Due to the limited electrolyte volume of 100 cm^3, the amount of proton concentration decreased to *c.a.* 0.31 mol dm^{-3} (Figure 6.2) after 10 hour of immersion. The slow down of zinc dissolution was attributed to the decreased proton concentration and the increased zinc ion concentrations after time. When the zinc sample was immersed in a larger volume of 500 cm^3 solution, zinc corrosion was observed to take place at a steady rate as shown in Figure 6.1a due to higher proton concentration (> 0.6 mol dm^{-3}) maintained. As a result, the electrolyte compositions of zinc and acid concentration can have a great influence on zinc corrosion.

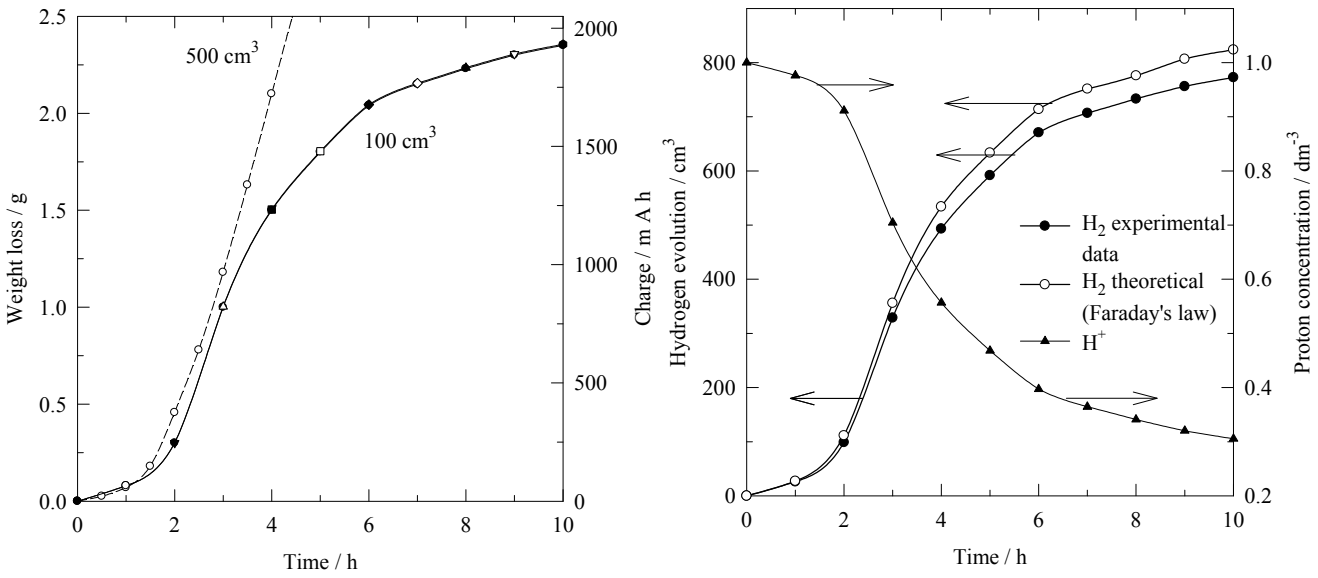

Figure 6.1 Corrosion of zinc immersed in 1 mol dm^{-3} methanesulfonic acid for 10 hours at 22 ^{o}C; as a function of (a) weight loss and charge density in electrolyte volume of 100 and 500 cm^3 and (b) hydrogen evolution of the zinc plate.

Figure 6.2 illustrates the dependence of the zinc dissolution rate with time is related to the zinc electrode potential. Once the zinc sample was immersed in the solution, a drop of zinc half-cell potential was observed in the initial 20 minutes as the surface condition of the zinc sample underwent a change from its initial condition exposed to the atmosphere (after etching) and zinc corrosion began take place. Since then, zinc dissolution rate in terms of weight loss increased rapidly during the first 3 hours of immersion. As in previous research in the literature, the corroded zinc layer was black in colour. The black colour was suggested by Feitnecht [14] was due to the small dispersed zinc particles scattering the light rather than reflecting it, hence a larger surface area. During the formation of this film, the open circuit potential increased from − 1.13 to − 1.03 V *vs.* Ag|AgCl and the dissolution rate increased from 0.12 g h^{-1} in the first 20 minutes of immersion to the maximum rate of 0.7 g h^{-1} in the 3rd hour (Figure 6.2). The positive shift of the open circuit

potential can be due to higher zinc ion concentration in the solution according to Nernst equation. Figure 6.3 shows the XRD pattern of a < 1 mm thickness corroded zinc specimen after immersing in 1 mol dm^{-3} CH_3SO_3H for 2 hours. XRD revealed that the composition on the corroded specimen was only metallic zinc, which is in agreement with the Poubaix diagram of zinc that no oxide layer is formed at the acidic medium but is still possible to form zinc oxide as the surface of the corroded specimen becomes alkaline due to a large amount of hydrogen evolution. According to the X-ray diffraction (XRD) data, the strongest diffraction peaks were observed at 36.6 ^{o}, 43.3^{o} and 70.1^{o} (2θ), which represent the preferential orientation were along planes (002), (101) and (110), respectively [15,16]. By using the Debye-Sherrer equation [17], the meaned grain size was estimated to be 18 nm from the width of the strongest diffraction peak of the (101) plane.

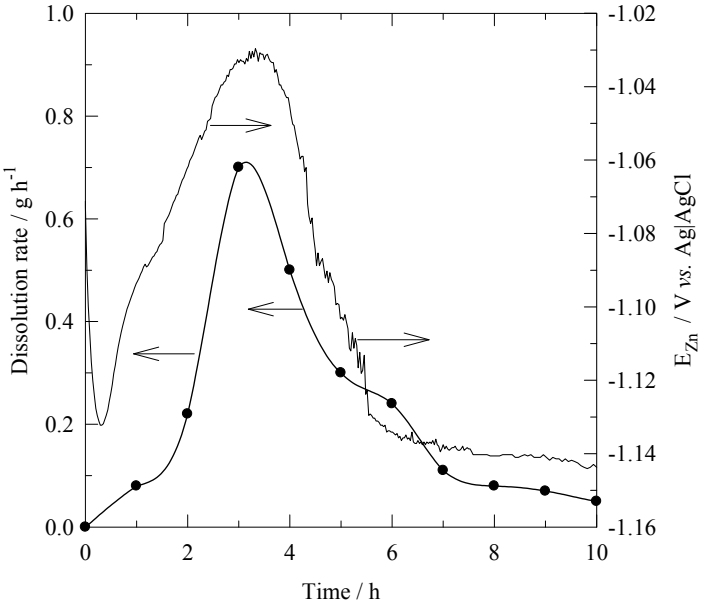

Figure 6.2. Corrosion of zinc immersed in 1 mol dm^{-3} methanesulfonic acid for 10 hours at 22 ^{o}C; as a function of the zinc dissolution rate and its open circuit half-cell potential.

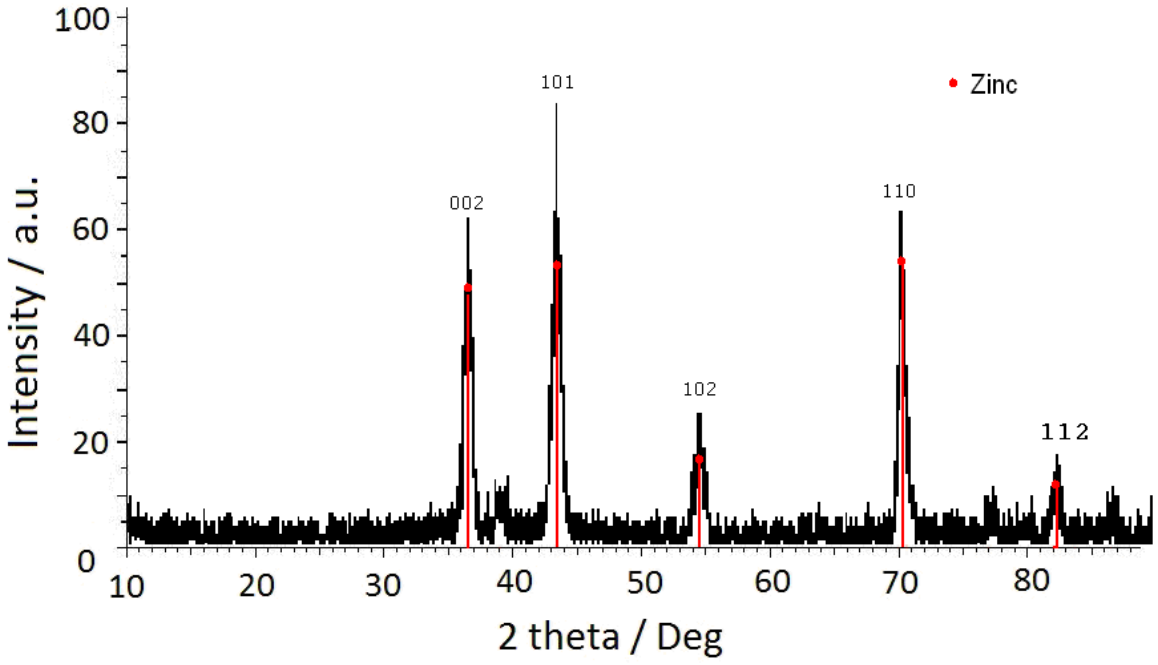

Figure 6.3. X-ray diffractogram of corroded zinc samples (< 1 mm) after immersing in 100 cm^3 of 1 mol dm^{-3} methanesulfonic acid for 2 hours.

Corrosion current densities and corrosion potentials of each hour were obtained electrochemically from the polarization measurement throughout the 10 hour immersion as described in the experimental section. Figure 6.4a and 6.4b were the plots of the zinc half cell potential against the logarithm of current density when the metallic zinc sheet was immersed in methanesulfonic acid at different hours during the periods of 1 — 4 h and 4 — 10 h, respectively. The electrode kinetic data were including cathodic, β_c, and anodic, β_a, Tafel gradients, corrosion current density, j_{cor}, corrosion potential, E_{cor}, and linear polarization resistance, R_P were compared with the data obtained from the weight loss experiment and summarized in Table 6.1. The value of the linear polarization resistance, R_P, was calculated using the Stern-Geary equation:

$$R_P = B / (j_{cor} \times A) \quad (3)$$

where A is the electrode area exposed to the solution, which was 4 cm^2. B parameter is the

proportionality constant and is obtained from the cathodic, β_c, and anodic, β_a, Tafel gradients.

$$B = (\beta_c \cdot \beta_a) / (2.3 (\beta_c + \beta_a)) \quad (4)$$

Hours	Weight loss		Cathodic and anodic polarization				
	Weight loss rate / g h^{-1}	j / mA cm^{-2}	j_{cor} / mA cm^{-2}	E_{cor} / V vs. Ag|AgCl	$-\beta_c$ / mV $decade^{-1}$	β_a / mV $decade^{-1}$	R_p / Ω cm^2
1st h	0.08	16.4	12	– 1.091	165	143	0.69
2nd h	0.22	45.2	38	– 1.060	209	188	0.28
3rd h	0.70	143.8	103	– 1.036	164	184	0.09
4th h	0.50	102.7	79	– 1.044	214	228	0.15
5th h	0.30	61.6	40	– 1.107	230	206	0.30
6th h	0.24	49.3	28	– 1.129	240	174	0.39
7th h	0.11	22.6	16	– 1.141	207	155	0.60
8th h	0.08	16.4	13	– 1.137	203	148	0.71
9th h	0.07	14.4	10	– 1.138	191	140	0.88
10th h	0.05	10.3	6	– 1.138	202	140	1.50

Table 6.1. Electrochemical parameters of zinc dissolution from the weight loss and polarization measurements at different times in 1 mol dm^{-3} methanesulfonic acid solution at 22 ^oC.

In the first 3 or 4 hour, corrosion current density increased significantly. As shown in Table 6.1, corrosion current densities obtained from the Tafel plot were lower than the gravimetric ones based on the weight loss measurements. Certain degree of such differences were also reported in previous literatures [18-20], some of the possibilities have been discussed in detailed by Zhang [13].

In aqueous methanesulfonic acid, the rate of zinc dissolution decreased and lower

corrosion current densities (Table 6.1) were observed after immersing in the solution for 4 hours, in which the proton concentration decreased and the zinc ion concentration increased after time. The resulting zinc open circuit potential and the corrosion potential also shifted towards more negative values and are in consistent with the zinc potential in Figure 6.2. Since no decrease in current densities was observed when the zinc potential was swept towards the anoidic direction in the potentiodynamic measurement as shown in Figures 6.3a and 6.3b, there was no evidence that a passive film was formed.

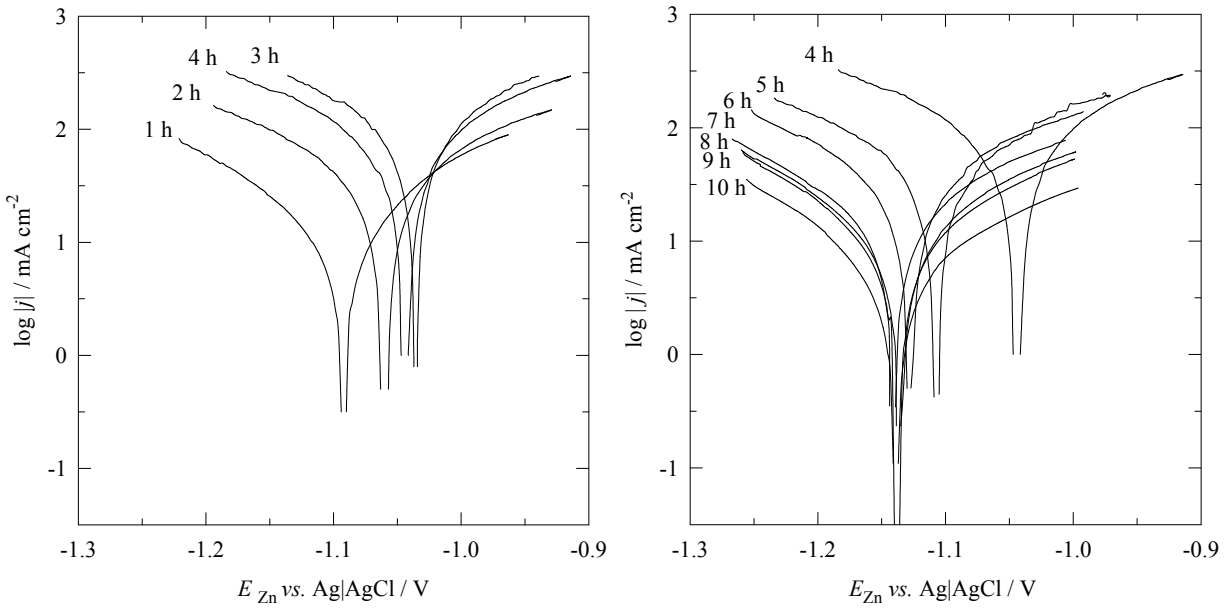

(a) (b)

Figure 6.4. Potentiodynamic polarization of zinc sample in 1 mol dm^{-3} methanesulfonic acid for the period of (a) 1 — 4^{th} hour and (b) 4 — 10^{th} hour.

After seven hours of immersion, the rate of zinc weight loss remained as low as < 0.10 g h^{-1} and the open circuit potential became steady at *c.a.* — 1.15 V *vs.* Ag|AgCl. The general trend of zinc weight loss and the zinc open circuit potential during the 10 hours immersion in methanesulfonic acid was similar to the previous work of Stanojevic *et al*. [1] in sulfuric acid and the work of Mouanga *et al*. in the sodium chloride solution, respectively [21].

6.2. Effect of methanesulfonic acid concentration

During the zinc corrosion and the simultaneous hydrogen evolution reactions, hydrogen ion is the main reactant and therefore is important to investigate the influence of methanesulfonic acid concentration on the corrosion rate. Figure 6.5 illustrates the corrosion rates in terms of weight loss over a wide range of methanesulfonic acid concentrations (1 to 12 mol dm^{-3}) over a period of 10 hours. Zinc dissolution rate increased significantly with the acid concentrations and reached the highest at 6 mol dm^{-3}, *c.a.* 3 g h^{-1}. In aqueous methanesulfonic acid, the rate of zinc dissolution was relatively fast. As indicated in the zinc-cerium flow battery developed by Plurion Inc.(UK), approximately 4.5 g of zinc deposit dissolved in the electrolyte after two hours at open circuit. The electrolyte composition was approximately at *c.a.* 1.5 mol dm^{-3} zinc(II) methanesulfonate in 3 mol dm^{-3} methanesulfonic acid. Their zinc dissolution rate higher than this work was probably due to their high battery operating temperature at 60 ^{o}C [22].

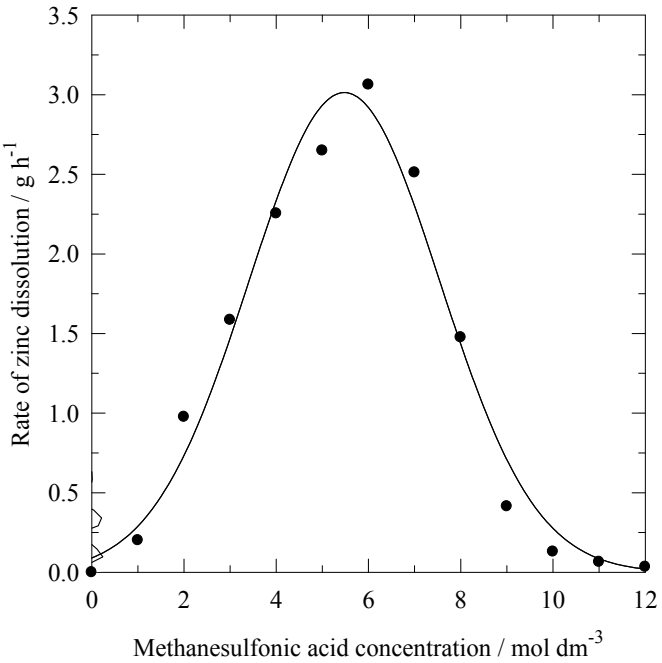

Figure 6.5. Zinc corrosion in term of weight loss at which the zinc dissolution rate *vs.* methanesulfonic acid concentration in the range 0 − 12 mol dm^{-3}.

A decrease in zinc corrosion rate in methanesulfonic acid at acid concentration of higher than 6 mol dm^{-3} was observed due to the reduced amount of dissociated hydrogen ions (H^+) at such acid concentrations. The effect of methanesulfonic acid concentration on the zinc weight loss as a function of time is shown in Figure 6.6a. At higher methanesulfonic acid concentration, the dependency of dissolution rate on time became less significant and more linear relationship was observed due to the higher reactivity of acid and the larger amount of proton in the electrolyte. Comparable trend of zinc dissolution at a similar range of immersion time has been observed at 0.1 — 3.5 mol dm^{-3} hydrochloric acid [23]. The volumes of hydrogen evolution in this study were summarized in Table 6.2 and are highly comparable to the theoretical conversion of weight loss as discussed in section 6.1.

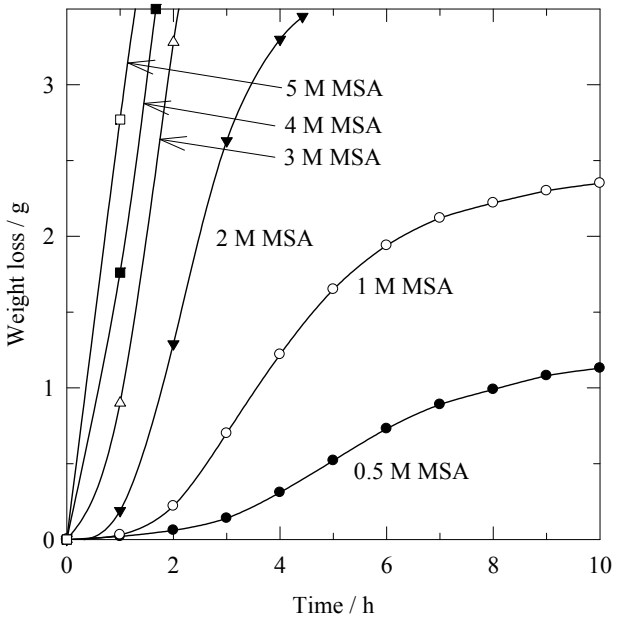

(a)

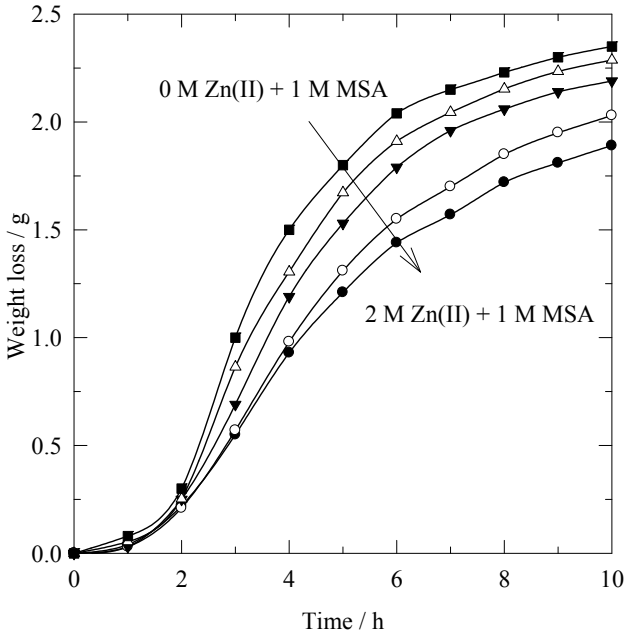

(b)

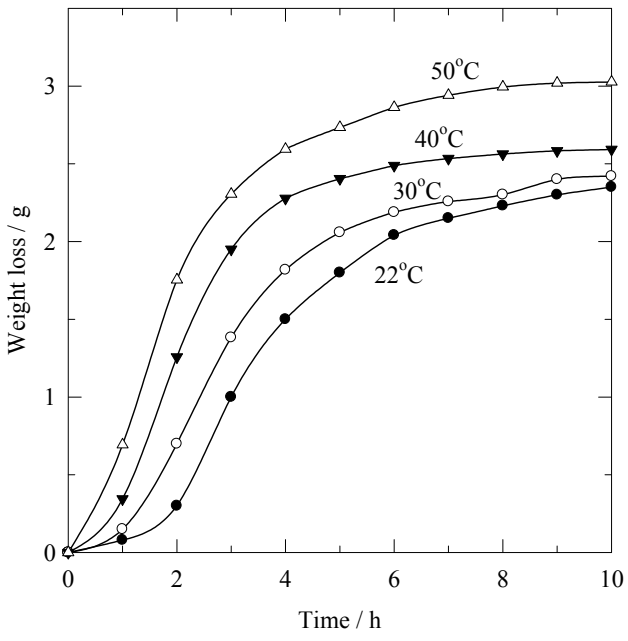

(c)

Figure 6.6. Zinc corrosion in term of weight loss, the dependency of time at (a) 0.5 − 5 mol dm^{-3} methanesulfonic acid, (b) 0 − 2 mol dm^{-3} zinc(II) methanesulfonate and (c) solution temperatures of 22 − 50 ^{o}C.

Parameters	Current density / mA cm^{-2}	Weight loss rate / g h^{-1}	Hydrogen evolution rate / cm^3 h^{-1}
Methanesulfonic acid concentration / mol dm^{-3}			
5	57.1	0.28	82.5
3	67.4	0.33	102.9
2	67.8	0.33	106.0
1	48.3	0.24	77.3
Zinc(II) methanesulfonate concentration / mol dm^{-3}			
0	48.3	0.24	77.3
0.5	47.5	0.23	76.4
1	45.0	0.22	72.2
2	38.8	0.19	62.3
Temperature / ^oC			
22	44.7	0.22	71.5
40	49.3	0.24	84.5
50	57.5	0.28	102.3

Table 6.2. The dissolution rates of zinc samples in term of weight loss and hydrogen evolution at various electrolyte compositions and solution temperatures. Unless specified, the zinc sample was immersed in 1 mol dm^{-3} methanesulfonic acid solution at 22 ^oC.

6.3. Effect of zinc(II) methanesulfonate concentration

Figure 6.6b shows the effect of the zinc(II) methanesulfonate concentration on the weight loss of zinc at a range of 0 − 2 mol dm^{-3} when a zinc plate was immersed in the solutions containing different zinc(II) methanesulfonate concentrations in 1 mol dm^{-3} methanesulfonic acid for 10 hours. The rates of zinc dissolution and hydrogen evolution were recorded in Table 6.2. Both rates were proportional to each other and decreased significantly when zinc(II) methanesulfonate concentrations increased.

The amounts of zinc weight loss and hydrogen evolution were decreased by *c.a.* 20 % when the zinc(II) methanesulfonate concentration increased from 0 to 2 mol dm^{-3}. Similar

findings have been reported in alkaline media according to previous investigations; in the media of potassium hydroxide solution [24-27], Bockris [28] reported that corrosion current density was reduced to 1 μ A cm^{-2} with the addition of 0.03 − 1 mol dm^{-3} zincate ions compared to 45 μ A cm^{-2} in its absence. In the work of Meesus *et al.* [29], more than 50 % of hydrogen volume was reduced by increasing the content of zinc powder from 5 to 100 g in the electrolyte. Besides, a higher zinc ion concentration can be advantageous for rechargeable batteries as it allows the battery to charge at high current densities regardless of mass transport limitations and ensures that an adequate concentration of the Zn(II) species is present at all states of charge.

6.4. Effect of electrolyte temperature

The effect of electrolyte temperature during the zinc weight loss experiment was investigated by immersing the zinc sample in 1 mol dm^{-3} methanesulfonic acid at 22, 30, 40 and 50 ^{o}C over an immersion period of 10 hours. Like many other reactions, the zinc corrosion rate increased rapidly at elevated temperatures as indicated by the higher rates of the zinc weight loss and the hydrogen evolution as summarized in Table 6.2. Figure 6.6c shows that the total weight loss of the zinc sample after immersing for 10 h was *c.a.* 2.4 g at 22 ^{o}C but increased to *c.a.* 3.0 g at 50 ^{o}C, which was in agreement with previous studies reported in the literature [25,27,30]. A higher zinc dissolution rate at elevated solution temperatures was due to the faster reaction kinetics. Since the total amount of hydrogen evolved was larger at elevated temperature and resulted in a lower proton concentration (lower acidic solution), a slower dissolution rate was observed at all temperatures after immersion for four hours.

6.5. Effect of corrosion inhibitors

Due to the relatively fast reaction of zinc corrosion in methanesulfonic acid, addition of corrosion inhibitors is crucial to inhibit such reaction in rechargeable batteries to maintain the dischargeable capacity for a period of time after battery charge. In this work, four selected inhibitors: indium oxide, lead methanesulfonate, cetyltrimethylammonium bromide (CTAB) and butyltriphenyl phosphonium chloride were tested due to previous research in the literatures [31,32] and their large hydrogen overpotentials [33,34].

Figure 6.7a and 6.7b show the effect of the four corrosion inhibitors on the electrode potential and hydrogen evolution respectively, for an immersion of 10 hours in 1 mol dm^{-3} methanesulfonic acid. The open circuit potentials of the zinc sample with the addition of indium and lead were − 1.12 and − 1.11 V *vs.* Ag|AgCl at the second hour of immersion, which were lagging behind the one in the absence of inhibitor towards the anodic direction (− 1.08 V *vs.* Ag|AgCl) during the formation of the black corroded zinc layer. It was due to the thin metallic layers of indium and lead reduced at the top of the corroding zinc surface as determined by x-ray diffraction as shown in Figures 6.8a and 6.8b, respectively, in which both samples have been immersed in the solution with inhibitors for 2 hours. Such metallic layers were chemically less reactive and slowed down the formation of the active layer.

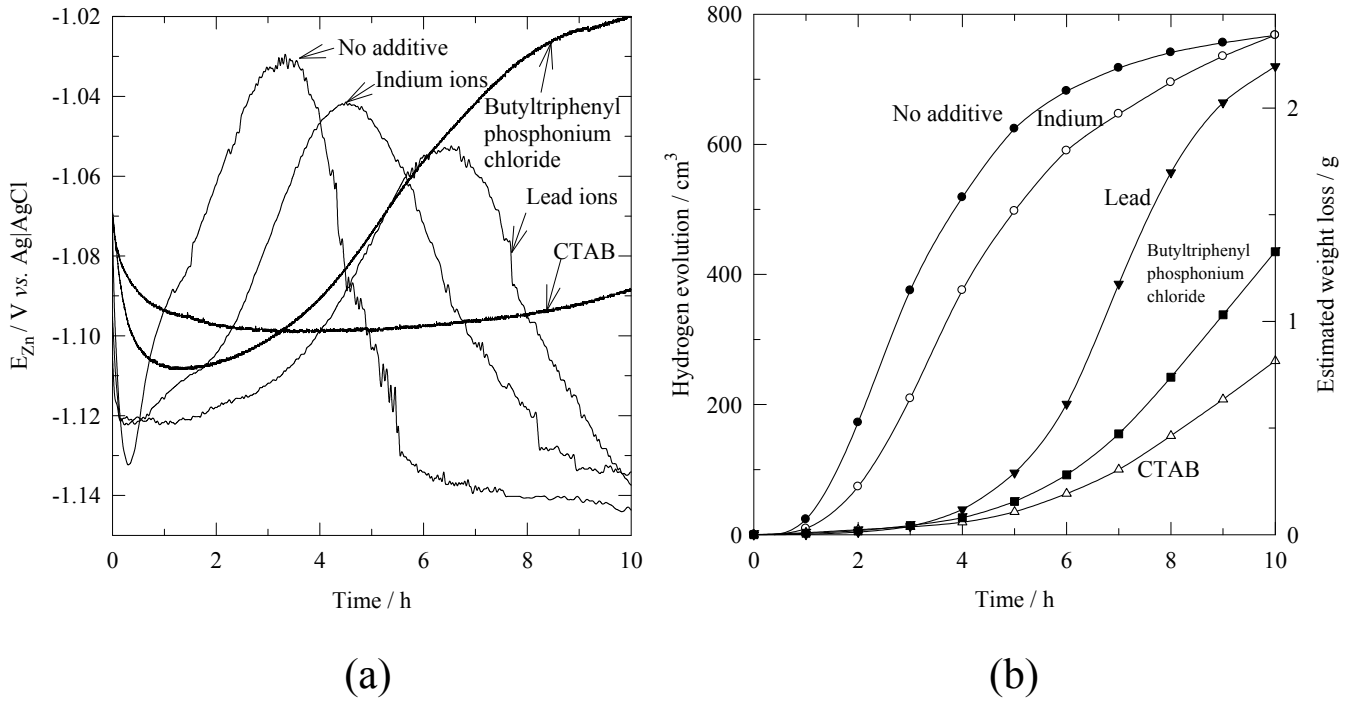

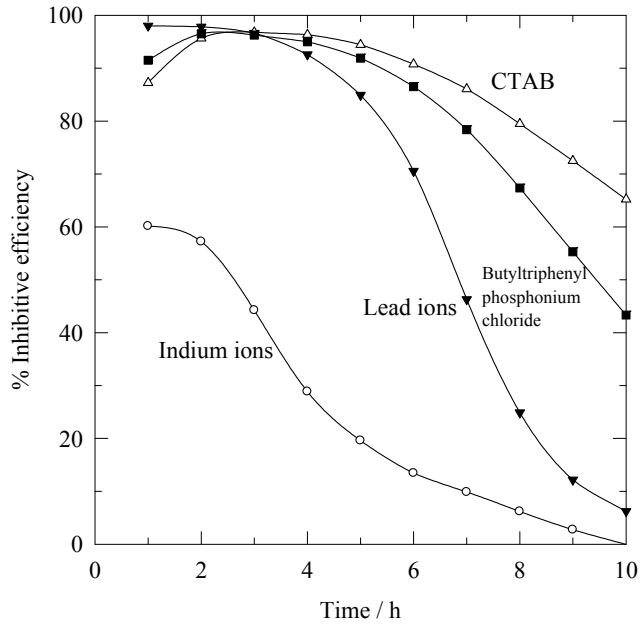

Figure 6.7. The effect of corrosion inhibitors, indium oxide, lead methanesulfonate, cetyltrimethylammonium bromide and butyltriphenyl phosphonium chloride at 2×10^{-3} mol dm^{-3} on (a) the zinc electrode potentials, (b) the hydrogen evolutions and the estimated weight losses and (c) the inhibitive efficiencies.

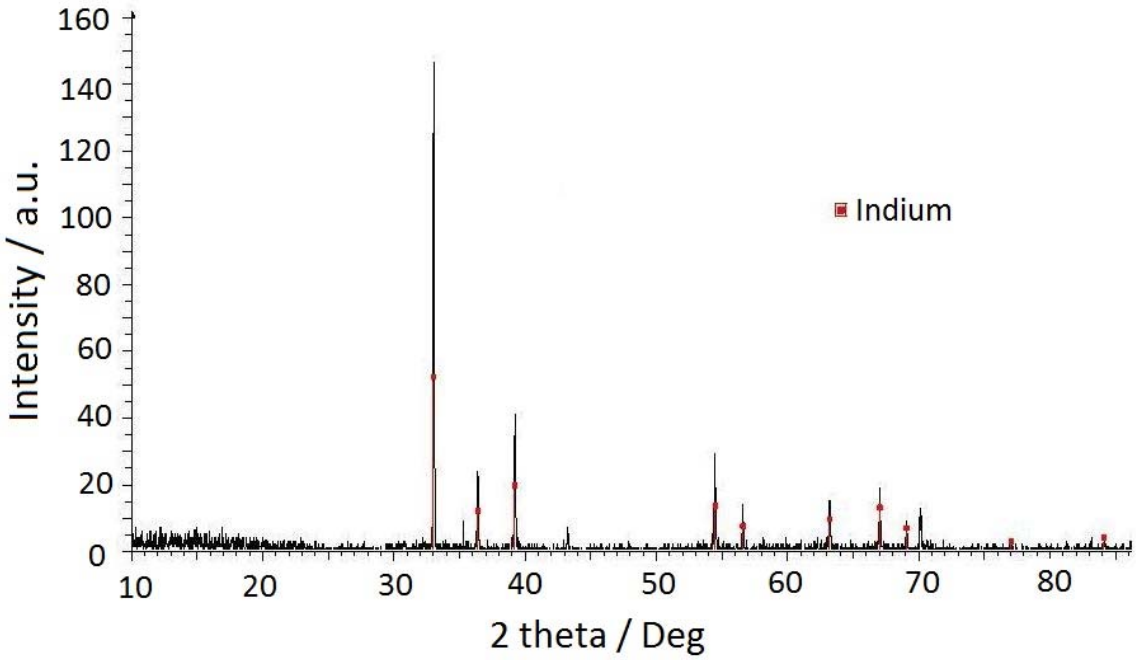

(a)

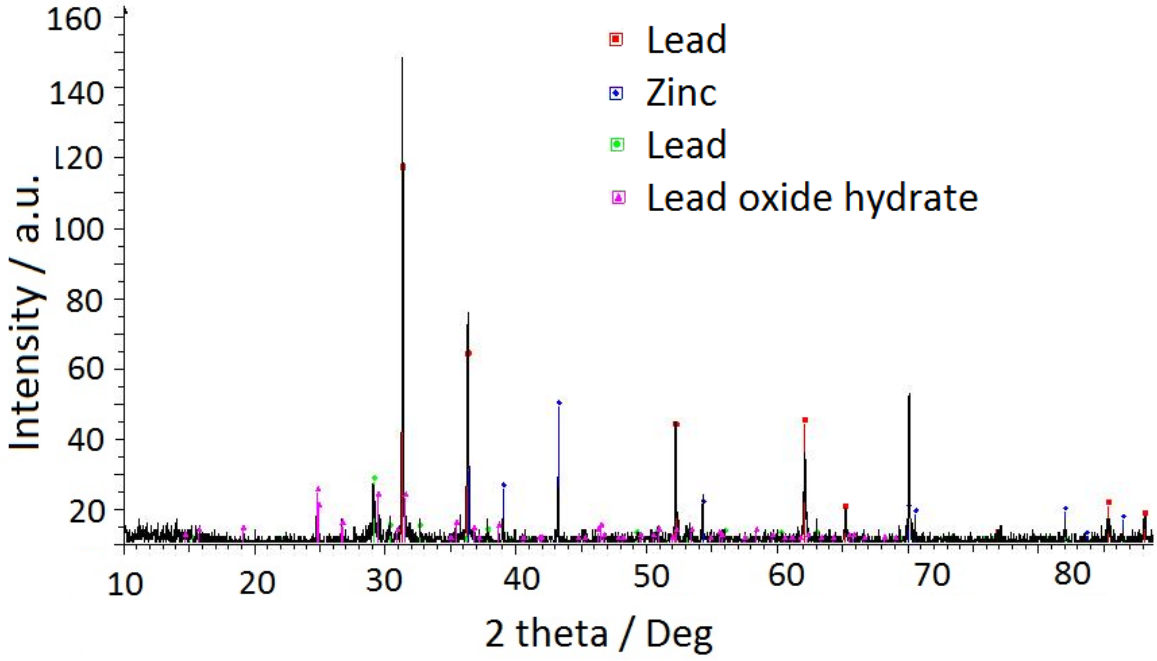

(b)

Figure 6.8. X-ray diffractograms of corroded zinc samples after immersing in 100 cm^3 of 1 mol dm^{-3} methanesulfonic acid with the addition of 2 × 10^{-3} mol dm^{-3} inhibitors, (a) indium ion and (b) lead ion for 2 hours.

Unlike indium and lead compounds, organic additives, such as cetyltrimethylammonium bromide (CTAB) and butyltriphenyl phosphonium chloride do not form any metallic layer but inhibit corrosion by adsorption and geometric blocking the zinc surface [35,36]. In the presence of such organic inhibitors, the open circuit potentials of the zinc samples were more negative than that in the absence of inhibitor and shifted toward more positive values after time. In the presence of the inhibitors tested, zinc corrosion was inhibited effectively or temporarily, which was verified by the decrease in the hydrogen evolution rate as shown in Figure 6.7b. With the addition of CTAB and butyltriphenyl phosphonium chloride, the total amount of hydrogen evolved was decreased significantly from *c.a.* 800 cm^3 in the absence of inhibitor to less than 200 cm^3 after 10 hour of immersion. Although CTAB and butyltriphenyl phosphonium chloride have the advantages of superior inhibitive performance and lower toxicity, the strong adsorption and blocking effects of such inhibitors may inhibit the zinc electrodeposition process leading to higher deposition overpotential and lower current efficiency [37]. Since dendritic growth of the zinc deposits was not significant in methanesulfonic acid as reported in the previous literatures [8,11], large deposition overpotential is not favourable for battery application and cause lower voltage efficiency. Optimisation of corrosion inhibition and zinc electrodeposition is under development.

With the addition of lead methanesulfonate, hydrogen evolution remained as low as *c.a.* 100 cm^3 after five-hours immersion compared to *c.a.* 600 cm^3 in the absence of inhibitor. Due to the formation of the metallic layers, weight loss measurement of the zinc sample was no longer comparable to the hydrogen evolution data. The estimated weight loss of the zinc sample (Figure 6.7b) was calculated by using the charge density consumed according to the hydrogen evolution data as discussed in section 6.1. Since the zinc open circuit potentials were more negative when the metallic layers of indium and lead were

formed on the zinc surface, such inorganic inhibitors served as anodic inhibitors to slow down the corrosion rate. Despite this, the metallic layers formed were not completely covered on the zinc surface due to the continued hydrogen evolution during the process. Once the bare zinc was in contact with the solution, the zinc sample corroded instead of the less chemically active metallic coating of indium or lead and resulted in a sharp increase in hydrogen evolution (Figure 6.7b) after the 1st and 3rd hours, respectively. The zinc electrode potential then shifted towards more positive values and an active oxide layer was formed as shown in Figure 6.7a.

After a sharp increase in the amounts of hydrogen evolved, the open circuit potentials of the zinc sample stabilized in the 5th and 7th hours with the addition of indium or lead ions, respectively. At that time, the total amount of hydrogen evolved were similar, approximately 500 — 600 cm^3, the proton concentration in the electrolytes were depleted to about 0.5 mol dm^{-3}. This was indicated by the cathodic shift of zinc electrode potential (Figure 6.7a) and the slow rate of hydrogen evolution (Figure 6.7b). In the presence and absence of indium and lead compounds, the total amounts of hydrogen evolved after 10 hours of immersion were eventually similar (*c.a.* 700 cm^3). Therefore, zinc corrosion cannot be inhibited with such inorganic inhibitors in the long term but can be effectively slowed down in the first few hours. By adding lead as an inhibitor, the corrosion of zinc was delayed nearly approximately three hours. The percentage inhibitive efficiency, % *P*, of the inhibitor can be calculated;

$$\% \ P = [1 - (H_{2 \ \text{inhibitor}} / H_{2\text{-without inhibitor}})] \times 100 \ \% \qquad (5)$$

where $H_{2\ \text{inhibitor}}$ and $H_{2\ \text{without inhibitor}}$ are the amounts of hydrogen evolution in the presence and absence of inhibitor, respectively. Figure 6.7c show that all inhibitive efficiencies of

the four inhibitors tested decreased over time. In the first four hours, the inhibitive efficiency of lead methanesulfonate was more than 90 % and dropped to lower than 6.2 % after immersing for 10 hours, while the inhibitive efficiencies of CTAB and butyltriphenyl phosphonium chloride were still more than 40 % over the 10 hours.

6.6. Conclusions

1. The rate of zinc corrosion was highly dependent on the electrolyte compositions during the process. The corroded zinc layer was black in colour with high surface area and formed after 20 minutes. Since then, the rate of zinc dissolution in terms of weight loss and hydrogen evolution increases significantly, while the corrosion rate decreased once the proton concentration dropped below *c.a.* 0.56 mol dm^{-3}.

2. Zinc corrosion in terms of weight loss and hydrogen evolution increased significantly at lower zinc(II) methanesulfonate concentration, higher methanesulfonic acid concentration and at elevated temperature.

3. With the addition of CTAB and butyltriphenyl phosphonium chloride, zinc corrosion in terms of hydrogen evolved was inhibited significantly with inhibitive efficiencies of more than 40 % after immersing in 1 mol dm^{-3} methanesulfonic acid for 10 hours. Despite this, the strong adsorption and blocking effects of such organic inhibitors may inhibit the zinc electrodeposition process leading to higher deposition overpotential and lower the voltage and current efficiency.

4. Due to the continued hydrogen evolution, the metallic layers formed by indium oxide and lead methanesulfonate were not covered perfectly on the zinc surface. Once the bare zinc was in contact with the solution, zinc preferentially corroded instead of such

metallic coatings and results in fast dissolution. In the presence and absence of indium and lead compounds, the total amounts of hydrogen evolved after 10 hours of immersion were eventually similar. Therefore, zinc corrosion cannot be inhibited with such inorganic inhibitors in the long term but can be effectively slowed down in the first few hours.

6.7. References

(1) D. Stajevic; D. Toskovic; M.B. Rajkovic, J, Mining and Metallurgy B: Metallurgy, 41, (2005) 47-66.

(2) A.S. Fouda; L.H. Madkour; A.A. EI-Shafel; S.A. Abd EIMaboud, Bull. Korean Chem. Soc., 16, (1995) 454-458.

(3) O.K. Abiola; A.O. James, Corros. Sci., 52, (2010) 661-664.

(4) L. Wang; J.X. Pu; H.C. Luo, Corros. Sci., 45, (2003) 677-683.

(5) P.C. Symons, J. Electrochem. Soc. , International Conference on electrolytes for power sources, Brighton, (1973).

(6) P.C. Symons, USP 3713888, Process for electrical energy using solid halogen hydrates, (1970).

(7) J.Q. Pan; Y.Z. Sun; J. Cheng; Y.H. Wen; Y.S. Yang; P.Y. Wan, Electrochem. Comm., 10, (2008) 1226-1229.

(8) R. Clarke, USP 7582385 B2, Zinc air battery with acid electrolyte, (2009).

(9) R.P. Kreh; R.M. Spotnitz; J.T. Lundquist, J. Org. Chem., *54*, (1989) 1526-1531.

(10) M.D. Gernon; M. Wu; T. Buszta; P. Janney, Green Chem., 1, (1999) 127-140.

(11) G. Brodt; J. Haas; W. Hesse; H.U. Jäqer, US 2003/0141195 Al, Method for electrolytic galvanizing using electrolytes containing alkane sulphonic acid, (2003).

(12) P.K. Leung; C. Ponce de León; C.T.J. Low; F.C. Walsh, in preparation, (2010).

(13) X.G. Zhang Corrosion and Electrochemistry of Zinc; 1 ed.; Springer, (1996).

(14) W. Feitnecht, Chem. Ind., (1959) 1102-1109.

(15) P.D.F.A. Index, International Center for Diffraction Data, Swarthmore, PA, File 4-831, ICDD, (1988).

(16) A. Gomes; M.I. da Silva Pereira, Electrochim. Acta, 51, (2006) 1342-1350.

(17) A.L. Patterson, Phys. Rev., 56, (1939) 978 http://prola.aps.org/abstract/PR/v56/i10/p978_1.

(18) A. Macias; C. Andrade, Br. Corros. J. , 22, (1987) 113-118.

(19) J.C. Chang; H.H. Wei, Corros. Sci., 30, (1990) 831-837.

(20) V.S. Muralidharan; K.S. Rajagopalan, J. Electroanal. Chem., 94, (1978) 21-36.
(21) M. Mouanga; P. Berçot, Corros. Sci., 52, (2010) 3993-4000.
(22) R.L. Clarke; B. Dougherty; S. Harrison; J.P. Millington; S. Mohanta, USP 20040197651, Lanthanide Batteries, (2004).
(23) K. Orubite-Okorosaye; N.C. Oforka, J. Appl. Sci. Environ. Mgt., 8, (2004) 57-61.
(24) R.N. Snyder; J.J. Lander, Electrochem. Technol., 3, (1965) 161.
(25) P. Ruetschi, J. Electrochem. Soc., 114, (1967) 301-305.
(26) T.P. Dirkse; R. Timmer, J. Electrochem. Soc., 116, (1969) 162-165.
(27) D.P. Gregory; P.C. Jones; D.P. Redfearn, J. Electrochem. Soc., 119, (1972) 1288 - 1292.
(28) J.O.M. Bockris; Z. Nagy; A. Danjavic, J. Electrochem. Soc., 119, (1972) 285-295.
(29) M. Meesus; Y. Strauven; L. Groothaert, J. Power Sources, 9, (1986) 303-323.
(30) W. Glaeser, J. Power Sources, 12, (1989) 265-296.
(31) G.L. Henriksen, USP 4036003, Zinc halogen battery electrolyte composition with lead additive, (1981).
(32) R.L. Clarke; B.J. Dougherty; S. Harrison; P.J. Millington; S. Mohanta, US 2004/ 0202925 A1, Cerium Batteries, (2004).
(33) A. Era; Z. Takehara; S. Yoshizawa, Electrochim. Acta, 13, (1968) 383-396.
(34) Y. Sato; M. Takahashi; M. Assakura; H. Yoshida; T. Tada; K. Kobayakawa; N. Chiba; K. Yoshida, J. Power Sources, 38, (1992) 317-325.
(35) J.L. Zhu; Y.H. Zhou; C.Q. Gao, J. Power Sources, 72, (1998) 231-235.
(36) M.S. Morad, Corrosion Science, 42, (2000) 1307-1326.
(37) Shanmugasigamani; M. Pushpavanam, J. Appl. Electrochem., 36, (2005) 315-322.

Chapter 7
Electrochemistry of the cerium half-cell reaction

Chapter 7 Electrochemistry of the cerium half-cell reaction

Introduction

The Ce(III)/Ce(IV) redox couple [1-3] has recently been suggested as the positive electrode reaction in zinc-cerium [4-6] and vanadium-cerium flow batteries [7] as it offers a large positive potential which leads to a high potential difference for a charged battery. At the positive electrode, the standard electrode potential of the Ce(III)/Ce(IV) redox couple, reaction (1), lies between 1.28 V and 1.72 V *vs.* SHE depending on the supporting electrolytes [8]:

$$Ce^{3+} - e^{-} \underset{\text{Discharge}}{\overset{\text{Charge}}{\rightleftharpoons}} Ce^{4+} \qquad E^{\ominus} \approx +\ 1.28 - 1.72\ \text{V}\ \textit{vs.}\ \text{SHE} \quad (1)$$

Cerium in methanesulfonic acid is highly attractive for flow battery application as it can be easily prepared at concentration as high as 1 mol dm^{-3} compared to less than 0.5 mol dm^{-3} in sulphuric acid. In order to optimise the resulting cerium half-cell as the positive electrode reaction in a redox flow battery, an improved understanding of the electrochemical kinetics of the Ce(III)/Ce(IV) redox couple in methanesulfonic acid at different conditions is crucial. To date, only a limited number of studies have been directed to the electrochemistry of cerium in methanesulfonic acid, the reduction of Ce(IV) and to the reversibility of the Ce(III)/Ce(IV) system. Earlier studies have mainly focused on the oxidation of Ce(III) in sulfuric and nitric acid electrolytes. Previous studies of the oxidation of Ce(III) and reduction of Ce(IV) in methanesulfonic acid have typically used 0.01 to 0.1 mol dm^{-3} cerium (III) methanesulfonate [9-11]. Such a low concentration of the electroactive species is not practical in a redox flow battery since the amount of energy that can be made available depends on the concentration of the electroactive species. These investigations are useful to calculate the kinetic parameters of the Ce(III)/Ce(IV) redox

couple but a cerium based flow battery requires a higher concentration of cerium (III) methanesulfonate, typically 0.5 to 2.0 mol dm^{-3} in a wide range of methanesulfonic acid concentration e.g. from 1.0 to 6.0 mol dm^{-3}. This is mainly due to changes in the electrolyte concentration during the charge-discharge cycles. During battery charge, proton is transferred to the negative electrolyte from its positive counterpart, where methanesulfonate anions are complexed with the Ce^{4+} ion oxidized in the charge process.

In this work, we report the electrochemistry of the Ce(III)/Ce(IV) redox couple in methanesulfonic acid over a range of electrolyte compositions typically found in a redox flow battery. The oxidation of Ce(III) and reduction of Ce(IV) are studied via cyclic voltammetry at a platinum disc electrode and at constant current electrolysis in a divided, two compartment parallel plate flow reactor. The reversibility of the Ce(III)/Ce(IV) redox couple as a function of cerium (III) methanesulfonate and methanesulfonic acid concentrations at various electrolyte temperatures is also investigated. A suitable electrolyte composition for the positive electrode reaction in a redox flow battery using a cerium half-cell is suggested.

7.1. Electrochemical behaviour

Figure 7.1 shows the cyclic voltammetry of the Ce(III)/Ce(IV) redox couple recorded at platinum and glassy carbon disk electrodes in an electrolyte containing 0.8 mol dm^{-3} cerium (III) methanesulfonate and 4.0 mol dm^{-3} methanesulfonic acid at 22 ± 2 ^{o}C at a potential sweep rate of 50 mV s^{-1}. The oxidation of Ce(III) started at approximately + 1.2 V *vs.* Ag|AgCl on both electrodes and the anodic current rose steadily as the potential became more positive.

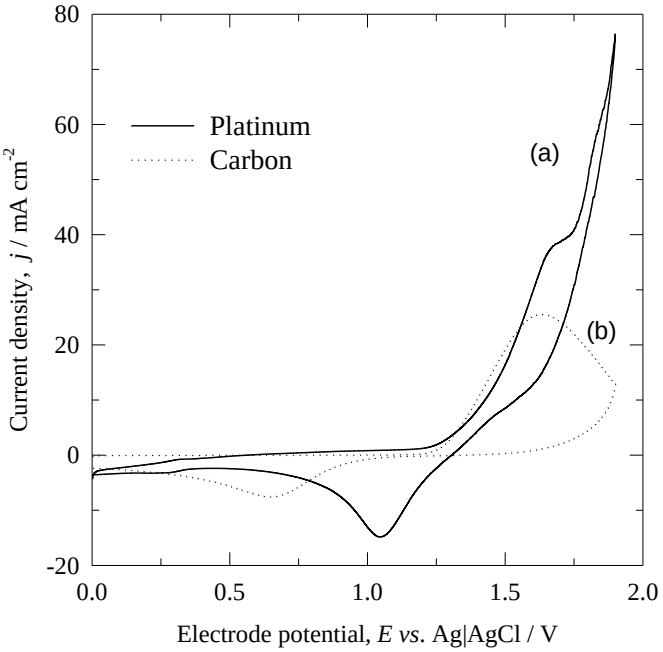

Figure 7.1. Cyclic voltammograms of the Ce(III)/Ce(IV) redox couple in methanesulfonic acid at (a) platinum and (b) glassy carbon electrodes. Electrolyte: 0.8 mol dm^{-3} cerium (III) methanesulfonate in 4.0 mol dm^{-3} methanesulfonic acid at 22 ^{o}C. The electrode potential was swept from 0 to + 1.9 V *vs.* Ag|AgCl then from + 1.9 to 0 V *vs.* Ag|AgCl at 50 mV s^{-1}.

A higher current density, *c.a.* 39 mA cm^{-2} was recorded on the platinum electrode compared with *c.a.* 25 mA cm^{-2} on the glassy carbon electrode at around 1.65 V *vs.* Ag|AgCl for both electrodes. At a more positive potential, the anodic current at the glassy carbon electrode decayed while at the platinum electrode continued to rise sharply due to the oxygen evolution reaction (and the formation of platinum oxides) [12, 13]. The influence of oxygen evolution reaction does not seem to be significant on the glassy carbon electrode as the current during the oxidation of Ce(III) on this electrode did not increase at more positive potentials. However, this can also be attributed to the oxidation of carbon at such potential.

On the reverse scan, a more negative potential was required for the reduction of Ce(IV) on the glassy carbon than on the platinum electrode. A maximum cathodic peak current density of 15 mA cm^{-2} on platinum was observed at *c.a.* + 1.05 V *vs.* Ag|AgCl while only 7.5 mA cm^{-2} at + 0.65 V *vs.* Ag|AgCl at the glassy carbon electrode. The separation between the oxidation and reduction peaks on each electrode was approximately 0.7 V on platinum and 1.0 V on carbon. The anodic current was higher than the cathodic one and the ratio of cathodic to anodic peak current was approximately 0.4 to 0.6 on both electrodes. Platinum gives a more favourable electrochemical response than carbon for the oxidation of Ce(III) and reduction of Ce(IV) in methanesulfonic acid because the peak separation is smaller. Several features in the voltammogram are worth mentioning: the separation of peak potentials is relatively high (several hundreds of millivolts) and the ratio of cathodic to anodic peak current is far below 1, the value expected for an ideally reversible system. The magnitude of oxygen evolution as a secondary reaction on the platinum electrode also needs to be reduced in order to improve the current and conversion efficiencies. Since platinum gave higher oxidation current than glassy carbon and the separation between the oxidation and reduction peaks is smaller than using the glassy carbon electrode in the cyclic voltammograms, the following studies were carried out on a platinum electrode only.

7.2 Potential sweep rate

Figure 7.2a shows the effect of the potential sweep rate on the cyclic voltammetry of the Ce(III)/Ce(IV) redox couple on a platinum electrode in an electrolyte containing 0.8 mol dm^{-3} cerium (III) methanesulfonate and 4.0 mol dm^{-3} methanesulfonic acid at 22 ^{o}C. The peak current density of the oxidation and reduction processes increased linearly with the square root of the potential sweep rate. Figure 7.2b shows the linear Randles-Sevćik relationship [8, 14-16] indicating that the oxidation of Ce(III) and reduction of Ce(IV) in

methanesulfonic acid were diffusion limited. In this work, the diffusion coefficient of cerium(III) ion was determined using the anodic current densities as the experiment was carried out in the cerium(III) electrolyte. Using the value of the slope from this plot during the oxidation process, the diffusion coefficient of Ce(III) ion in methanesulfonic acid was estimated to be 1.67×10^{-6} cm^2 s^{-1} at 22 ^oC. This value agrees with previous measurements of diffusion coefficients that where in the range of 0.27 to 0.72 x 10^{-6} cm^2 s^{-1} [17], using a glassy carbon electrode in an electrolyte containing 0.034 to 0.152 mol dm^{-3} cerium (III) methanesulfonic in 1.0 and 4.0 mol dm^{-3} methanesulfonic acid at room temperature.

The diffusion coefficient of Ce(III) ions in methanesulfonic acid was slightly larger than those reported for many metal ions in aqueous electrolytes, which are typically (4.0 to 6.0) $\times$ 10^{-6} cm^2 s^{-1} [18, 19] possibly due to the complexation with methanesulfonate ion show equilibrium reaction [11]. Indeed, a lower diffusion coefficient value was found at increased methanesulfonic acid concentration, e.g. in an electrolyte containing 0.152 mol dm^{-3} cerium (III) methanesulfonate, the diffusion coefficient of Ce(III) was approximately 0.69×10^{-6} cm^2 s^{-1} in 1.0 mol dm^{-3} methanesulfonic acid but only 0.27×10^{-6} cm^2 s^{-1} in 4.0 mol dm^{-3} methanesulfonic acid [17]. Due to the tedious preparation procedure of cerium(IV) methanesulfonate involving insoluble cerium(IV) oxide, diffusion coefficient of cerium(IV) ion was not studied as it requires cerium(IV) methanesulfonate as the initial electrolyte to obtain accurate data.

For all potential sweep rates, the ratio of cathodic to anodic peak current was approximately 0.5. The charge density for the reduction of Ce(IV) was lower than the charge involved in the oxidation of the Ce(III) ion possibly due to the oxygen evolution secondary reaction during and after the oxidation of Ce(III) but no visible side reactions occurred during the reduction of Ce(IV). Earlier investigations also suggested that the

larger anodic peak current could also be due to the contribution of the weak adsorption of Ce(III) ions on the electrode surface, which was demonstrated via cyclic voltammograms of the Ce(III)/Ce(IV) redox couple in sulfuric and methanesulfonic acids [11].

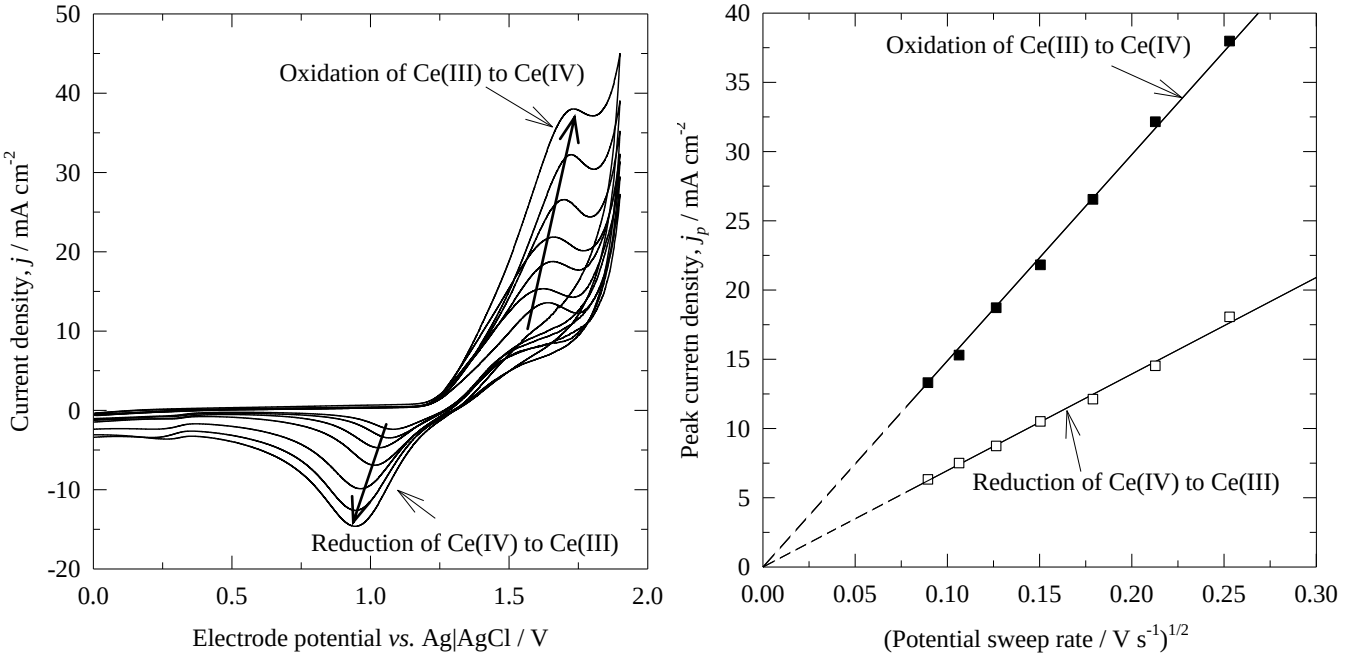

Figure 7.2. The effect of potential sweep rate on the Ce(III)/Ce(IV) redox couple in methanesulfonic acid. (a) Cyclic voltammogram and (b) Randles-Sevćik plot. Electrolyte: as in Figure 7.1. The potential sweep rates were 8, 11, 16, 22.6, 32, 45.3 and 64 mV s^{-1}. ■ oxidation of Ce(III) and □ reduction of Ce(IV).

Recent studies have also showed that the cathodic and anodic peak currents can be brought closer via the complexation of Ce(III) and Ce(IV) ions with ligands such as ethylenediaminetetraacetic acid and diethylenetriaminepentaacetic acid [20, 21]. Such strategy has been advantageous since the reversibility of the Ce(III)/Ce(IV) redox couple was significantly improved and higher charge densities were obtained [22]. The work also showed that the faster electrochemical kinetics in the presence of the ligands are due to a

higher charge transfer coefficient and an increased rate constant for the Ce(III) ⇆ Ce(IV) redox reaction. The electron transfer rates were also found to be similar for the oxidation of Ce(III) and the reduction of Ce(IV), confirming that an improvement in the reversibility of these reactions using complexing ligands [22] can be achieved.

By increasing the potential sweep rate during the oxidation of Ce(III), the peak potential shifted to more positive values while for the reduction of Ce(IV) to more negative potentials. The separation of the peak potentials increased at higher potential sweep rates e.g. 560 mV at 8 mV s^{-1} compared to 790 mV at 64 mV s^{-1}. This finding suggests slow electrochemical kinetics of the Ce(III)/Ce(IV) redox couple. Previous results reported similar observation in an electrolyte containing 0.034 mol dm^{-3} cerium (III) methanesulfonate in 4.0 mol dm^{-3} methanesulfonic acid at a glassy carbon electrode [9] e.g. the reduction peak shifted by approximately -100 mV as the potential sweep rate increased from 10 to 160 mV s^{-1}. Earlier investigations also showed a quasi-reversible behaviour of the Ce(III)/Ce(IV) redox couple in commodity electrolytes, such as sulfuric acid [1, 23].

7.3. Concentration of methanesulfonic acid

Cyclic voltammograms of the Ce(III)/Ce(IV) redox couple were recorded at a platinum electrode in a wide range of methanesulfonic acid concentration from 0.1 to 5.0 mol dm^{-3}. Figure 7.3a shows that the anodic current density for the oxidation of Ce(III) decreases as the concentration of methanesulfonic acid increased when the electrolyte contained 0.8 mol dm^{-3} Ce(III) methanesulfonate. For example, the anodic peak current density was approximately 50 mA cm^{-2} in 2.0 mol dm^{-3} methanesulfonic acid but no oxidation peak was observed with 5.0 mol dm^{-3} acid concentration, although the current density reached 20 mA cm^{-2}. The change in the peak current density was due to the

increase in the solution viscosity at high acid concentrations and high conductivity of the acid at low concentrations in aqueous electrolytes [1, 24]. Other findings reported in the literature also showed similar observation: the anodic peak current was 3.6 mA cm^{-2} in 1.0 mol dm^{-3} methanesulfonic acid and decreased to 1.6 mA cm^{-2} in 6.0 mol dm^{-3} methanesulfonic acid in a solution where the starting electroactive species was Ce(IV) at 0.033 mol dm^{-3} concentration [11].

Further increase in the anodic current after the oxidation of Ce(III) was caused by oxygen evolution, which was found to be influenced by the methanesulfonic acid concentration. The linear sweep voltammograms in the absence of Ce(III) with different concentrations of the acid in Figure 7.3b shows that oxygen evolution shifted to more positive potentials at a higher acid concentration. For example, at an electrode potential of *c.a.* +1.8 V *vs.* Ag|AgCl, the anodic current density was *c.a.* 80 mA cm^{-2} in 2.0 mol dm^{-3} methanesulfonic acid, but at the same potential the current density was only 40 mA cm^{-2} in 5.0 mol dm^{-3} methanesulfonic acid. Although a similar behaviour has been found in sulfuric acid, the cathodic current density in such media was smaller [25]. These findings suggest that the oxidation of Ce(III) is the dominant reaction at a higher concentration of methanesulfonic acid and is consistent with observations during the experiment where less oxygen bubbles appeared on the electrode surface during the oxidation of Ce(III) at high acid concentrations. The decrease in oxygen evolution at higher methanesulfonic acid concentration can be possibly due to the less dominant amount of hydroxide ion in the electrolyte for the oxygen oxidation reaction.

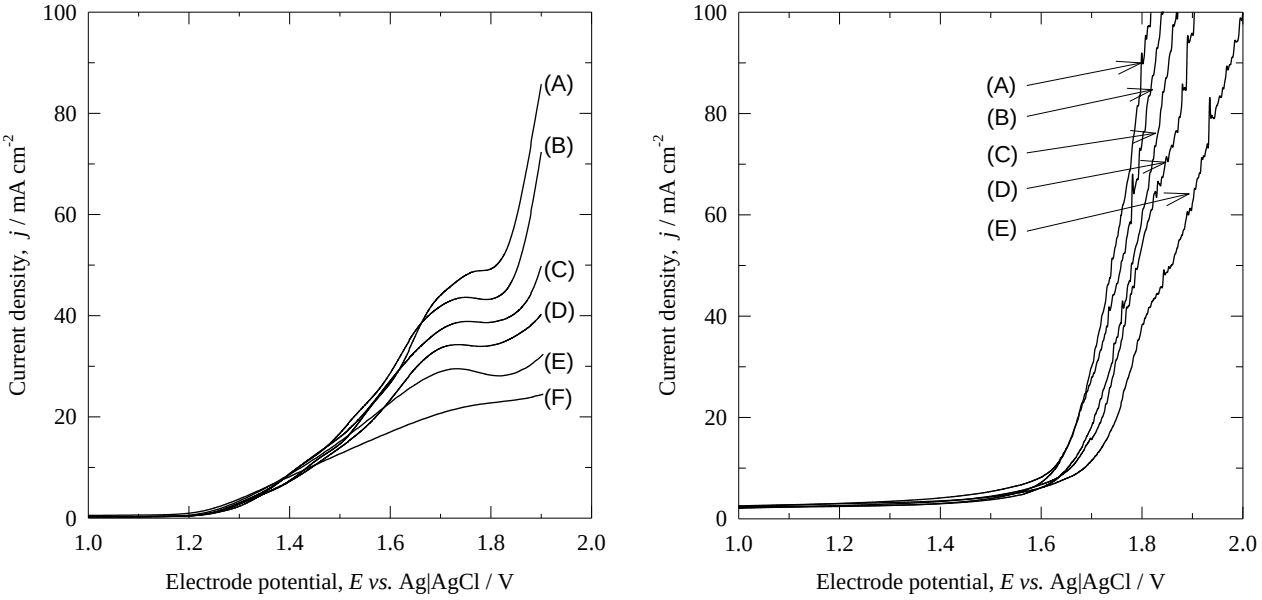

(a) (b)

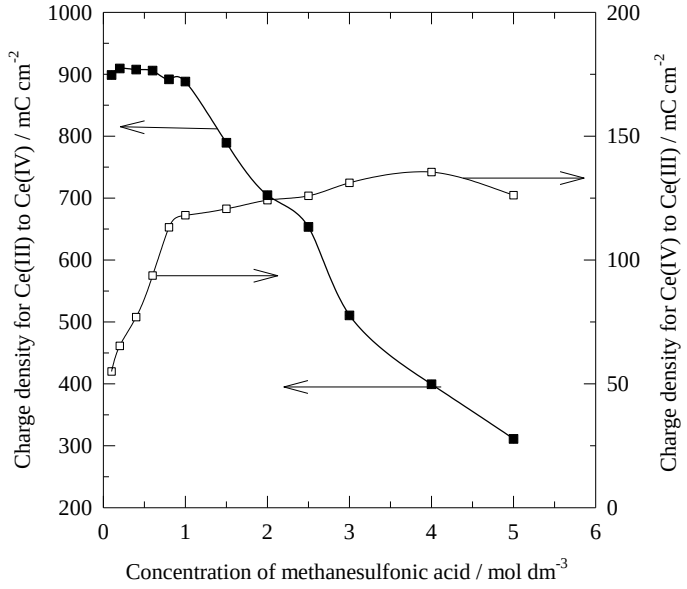

(c)

Figure 7.3. The effect of methanesulfonic acid on (a) oxidation of Ce(III) to Ce(IV): (A) 2, (B) 2.5, (C) 3, (D) 4, (E) 4.5 and (F) 5 mol dm^{-3} CH_3SO_3H, respectively, (b) oxygen evolution at platinum without Ce(III) ions: (A) 1, (B) 2, (C) 3, (D) 4 and (E) 5 mol dm^{-3} CH_3SO_3H, respectively and (c) charge density for Ce(III)/Ce(IV) redox couple. Other electrolyte conditions were similar to those in Figure 7.1. ■ oxidation of Ce(III) and □ reduction of Ce(IV).

Figure 7.3c shows the charge density involved in the oxidation and reduction of Ce(III) and Ce(IV) ions respectively, *vs.* the concentration of methanesulfonic acid. The charge density, calculated from the area under the curve of the cyclic voltammogram, during the oxidation of Ce(III) is constant up to 1 mol dm^{-3} of methanesulfonic acid and then decreases sharply as the acid concentration increases. This is consistent with the observations made on the cyclic voltammograms shown in Figure 7.3a and 7.3b. The charge density for the reduction of Ce(IV) increased significantly with the concentration of acid up to 1 mol dm^{-3}, after that the charge increase is slow and reaches a maximum at 4.0 mol dm^{-3} methanesulfonic acid. A further increase in the acid concentration led to a slight reduction in both charge and current density for the reduction of Ce(IV). This is attributed to an increase in solution viscosity [26] and the solubility limit of Ce(III) in 5.0 mol dm^{-3} in methanesulfonic acid, which might have been exceeded. At such a high acid concentration, the solubility limit of Ce(III) was estimated to be approximately 0.7 mol dm^{-3} [10].

7.4. Concentration of cerium (III) methanesulfonate

Figure 7.4 shows that the charge density for both the oxidation of Ce(III) and reduction of Ce(IV) increased when the Ce(III) methanesulfonate changed from 0.1 to 1.0 mol dm^{-3} in a solution containing 4.0 mol dm^{-3} methanesulfonic acid. A further increase in the concentration of cerium (III) methanesulfonate to 1.2 mol dm^{-3}, which was a relatively viscous solution and led to a reduction in the charge density for both processes. This was due to the limited solubility of Ce(III) at such acid concentration as previous results showed that 1.0 mol dm^{-3} was the solubility limit for Ce(III) and Ce(IV) in 4.0 mol dm^{-3} methanesulfonic acid at room temperature [10, 27]. This observation is also consistent with previous results where a high concentration of Ce(III) could only be achieved in a low

concentration of methanesulfonic acid. The concentration of Ce(IV) however, could only be increased in higher methanesulfonic acid concentrations [10].

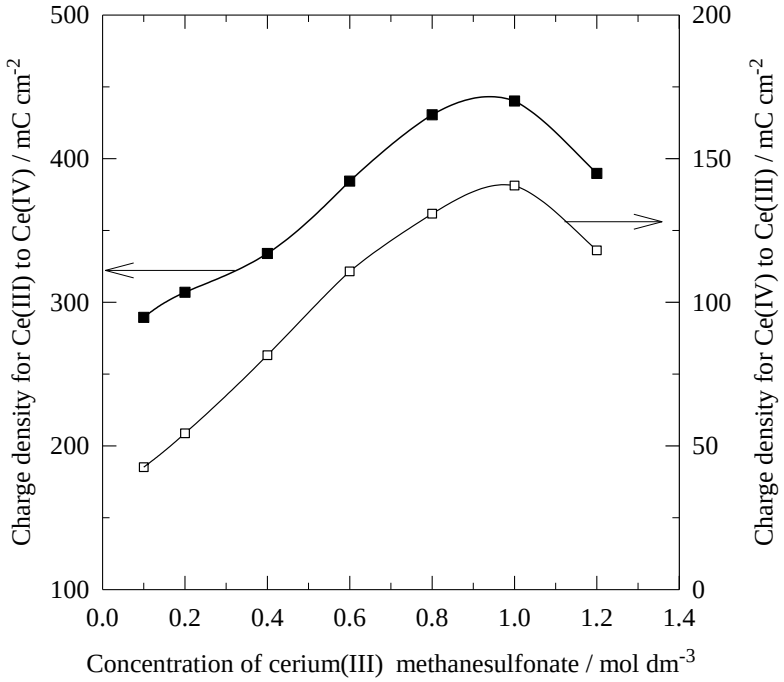

Figure 7.4. The effect of Ce(III) concentration on the charge density of the Ce(III)/Ce(IV) redox couple in methanesulfonic acid. Other electrolyte conditions: as in Figure 7.1. The charge density was calculated from the area under the cyclic voltammograms between 0 to + 1.9 V *vs.* Ag|AgCl at 50 mV s^{-1}. ■ Oxidation of Ce(III) and □ reduction of Ce(IV).

Since the acidity of the electrolyte in the flow battery will change during charge-discharge cycles, the challenge is to use an appropriate concentration of methanesulfonic acid which provides sufficient solubility for both Ce(III) and Ce(IV) species. The results above show that a solution with higher concentration of Ce(III), e.g. 1.5 to 2.0 mol dm^{-3} could be prepared in a low acid concentration. However, the Ce(IV) solution obtained during or from a constant current electrolysis under this conditions was highly viscous and slurry [28]. A high concentration of Ce(IV) could be prepared if the concentration of acid is high but the solubility of Ce(III) became limited and the

Ce(III)/Ce(IV) redox couple demonstrated poor reversibility. Therefore, a solution of 0.8 mol dm^{-3} cerium (III) methanesulfonate was prepared in 4.0 mol dm^{-3} methanesulfonic acid as a compromise in order to maximize the solubility of both Ce(III) and Ce(IV) ions.

7.5 Electrolyte temperature

Figure 7.5 shows that the charge density during the oxidation of Ce(III) increases with temperature. The reduction of Ce(IV) also increased but reached a maximum at 323 K. The higher charge density for the oxidation of Ce(III) could be due to the simultaneous oxygen evolution reaction which is favourable at high temperatures. Cyclic voltammograms recorded for 0.01 mol dm^{-3} Ce(III) in 1.0 mol dm^{-3} sulfuric acid also showed an increase in the charge density at elevated electrolyte temperature, e.g. 60 ^{o}C [1]. During the electrolysis of Ce(III) ions in both undivided and divided electrochemical cells using nitric acid electrolyte, the applied cell potential difference decreased slightly as the temperature increased due to improved reaction kinetics, increased electrolyte conductivity and reduced viscosity. The study also showed that the current efficiency of the electrolysis of Ce(III) to Ce(IV) improved from 77 % at 40 ^{o}C to 93 % at 90 ^{o}C in nitric acid [26].

Previous work also demonstrated that the conversion of Ce(III) to Ce(IV) was higher at high electrolyte temperature, e.g. conversion increased from 45 % to 93 % when the temperature was raised from 40 ^{o}C to 90 ^{o}C in 1.0 mol dm^{-3} Ce(III) contained in 3.0 mol dm^{-3} nitric acid [26]. An increase in the diffusion coefficient of Ce(III) ions and the rate constant for Ce(III) oxidation have also been observed at elevated electrolyte temperature [25]. Literature studies confirm that an Arrhenius, semi-logarithmic plot of the diffusion coefficient against the inverse of the electrolyte temperature is a linear relationship for the Ce(III) ⇆ Ce(IV) redox reaction in nitric and sulphuric acid electrolytes [24].

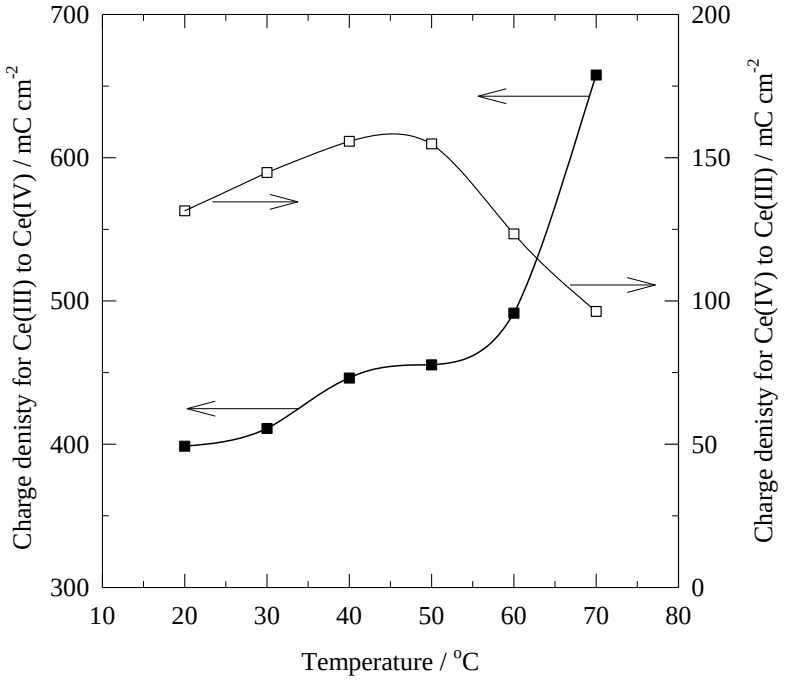

Figure 7.5. The effect of electrolyte temperature on the charge density for Ce(III)/Ce(IV) redox couple. Other electrolyte conditions: as in Figure 7.1. The charge density was calculated from the area under the cyclic voltammograms between 0 to + 1.9 V *vs.* Ag|AgCl at 50 mV s^{-1}. ■ Oxidation of Ce(III) and □ reduction of Ce(IV).

7.6. Reversibility of the Ce(III)/Ce(IV) redox couple

A series of cyclic voltammograms were recorded at a platinum electrode in various electrolyte compositions and the reversibility of the Ce(III)/Ce(IV) redox couple was investigated in terms of the separation of peak potentials and the ratio of cathodic to anodic peak currents. Table 7.1 shows the measured values. Since the separation of the peak potentials was more than 59 mV and the ratio of the peak currents was less than unity, the Ce(III)/Ce(IV) redox couple in methanesulfonic acid can be considered as a quasi-reversible system [8, 14]. The increase in the separation of peak potentials at increasing potential sweep rate shows that the redox reaction involved a slow electrochemical kinetic. The separation of peak potentials decreased at lower

concentrations of cerium (III) methanesulfonate and methanesulfonic acid as well as at higher electrolyte temperatures. The ratio of cathodic to anodic peak current density varied from 0.3 to 0.65 depending on the electrolyte composition. The ratio was closer to unity in an electrolyte containing a higher concentration of methanesulfonic acid and cerium (III) methanesulfonate as well as at an elevated electrolyte temperature.

At higher concentrations of cerium (III) methanesulfonate and methanesulfonic acid, the separation of oxidation and reduction peak potentials increased due to an increase in the ohmic drop associated with larger current response and changes in the solution viscosity and conductivity. The high concentration also reduced the reversibility of the Ce(III)/Ce(IV) redox couple. At such concentration, the oxidation potential remained fairly constant but the reduction potential became more negative leading to lower discharge cell potential difference of a cerium-based redox flow battery. Such observations agree with other studies, for example the separation of peak potentials increased from 140 mV to 240 mV when the acid concentration changed from 2 to 5 mol dm^{-3} in a solution containing 0.033 mol dm^{-3} of Ce(III) [11].

Operational parameter	Separation of the peak potentials / mV	Ratio of cathodic to anodic peak current
Potential sweep rate / mV s^{-1}		
8	558	0.51
16	557	0.54
32	736	0.50
64	788	0.51
Concentration of methanesulfonic acid / mol dm^{-3}		
1.0	654	0.42
2.0	710	0.43
4.0	738	0.53
5.0	965	0.65
Concentration of cerium (III) methanesulfonate / mol dm^{-3}		
0.1	591	0.32
0.4	632	0.49
0.8	738	0.53
1.0	857	0.53
Temperature of the electrolyte / ^{o}C		
22	738	0.53
30	659	0.54
40	631	0.56
50	619	0.65
60	660	0.62

Table 7.1. The effect of operational parameters on the separation of the peak potentials and the ratio of peak currents. Unless stated, the temperature of the electrolyte was 22 ^{o}C and the electrolyte contained 0.8 mol dm^{-3} cerium (III) methanesulfonate in 4.0 mol dm^{-3} methanesulfonic acid. The data was estimated from cyclic voltammograms recorded in the potential range from 0 to + 1.9 V *vs.* Ag|AgCl at a potential sweep rate of 50 mV s^{-1}.

Although a low concentration of cerium (III) methanesulfonate leads to a narrower separation of the peak potentials, such a low concentration of Ce(III) ions would not be

practical for a flow battery. Besides, the use of a low concentration of methanesulfonic acid also limits the solubility of Ce(IV) in the solution, hence the energy density available in a flow battery will be restricted. As mentioned earlier, in this study, a solution of 0.8 mol dm^{-3} cerium (III) methanesulfonate in 4.0 mol dm^{-3} methanesulfonic acid was suggested for flow battery applications. The use of elevated electrolyte temperature could also provide a more reversible redox reaction but will be limited by the properties of the materials used to construct the cell.

7.7. Constant current electrolysis in a zinc-cerium redox flow battery

The electrochemical oxidation of Ce(III) followed by the reduction of Ce(IV) ions was investigated in an electrolyte containing 0.8 mol dm^{-3} Ce(III) methanesulfonate in 4.0 mol dm^{-3} methanesulfonic acid. The reaction on the negative electrode was the electrodeposition and stripping of zinc onto a carbon polyvinyl-ester composite using 1.5 mol dm^{-3} zinc (II) methanesulfonate in 1.0 mol dm^{-3} methanesulfonic acid electrolyte. Both electrolytes were contained in external tanks and were approximately 100 cm^3, circulated through the cell at a mean linear flow rate of 3.9 cm s^{-1} at 50 ^oC temperature. Figure 7.6a shows the concentration of Ce(IV) as a function of the electrolysis time using two types of platinised titanium electrodes (70 g Pt m^{-2}): a 2-dimensional planar electrode and a 3-dimensional mesh electrode described in the experimental section. During the first 4.5 hours, a charge current density of 50 mA cm^{-2} was applied through the cell and it was found that the concentration of Ce(IV) ion was higher when the 3-dimensional mesh electrode was used rather than the 2-dimensional planar electrode. At the end of the first 4.5 hours, a current density of 50 mA cm^{-2} of opposite sign was applied to discharge the flow battery, reducing Ce(IV) ions to Ce(III) ions. As shown in Figure 7.6a, the concentration of Ce(IV) ion appears to increase and decrease linearly when the 3-dimensional electrode was used but not linear behaviour was observed on the

2-dimensional electrode. The linear behaviour of using the three-dimensional electrode suggested that Ce(IV) concentration was proportional to the faradaic charge and seems no mass transport limitation was observed. Hence, the reaction was likely to be a charge-transfer reaction.

The logarithm of the normalised cerium (IV) concentration *vs.* the electrolysis time was plotted in Figure 7.6b. This graph shows that a linear behaviour was observed during the oxidation of Ce(III) and the reduction of Ce(IV) processes using a 2-dimensional planar electrode. This indicates that the increase and decrease in concentration of Ce(IV) ions on this electrode are mass transport controlled processes and follow a first order reaction kinetics with a continuous stirred tank batch model [29] given by the following equations:

During oxidation:

$$ln\left(\frac{c_{after\,charge} - c_{(t)}}{c_{after\,charge}}\right) = -kt \qquad (2)$$

During reduction:

$$ln\left(\frac{c_{(t)}}{c_{after\,charge}}\right) = -kt \qquad (3)$$

where $c_{\text{after charge}}$ is the Ce(IV) concentration (mol m^{-3}) after battery charge, $c_{(t)}$ is the Ce(IV) concentration (mol m^{-3}) at the time t, k is the apparent first order rate constant (s^{-1}) and t is the time (s). This result is consistent with the previous findings in the cyclic voltammograms which showed that the oxidation of Ce(III) and reduction of Ce(IV) at a platinum rotating disk electrode were diffusion controlled reactions following the Randles-Sevćik equation. The apparent first order rate constant k, is equal to k_mA/V, where k_m is the mass transport coefficient (m s^{-1}), A is the electrode area (m^2) and V is the volume of electrolyte within the reactor (m^3).

Table 7.2 shows several reactor performances obtained using constant current electrolysis during the oxidation of Ce(III) and reduction of Ce(IV) ions. The parameters were calculated based on a simplified batch reactor model [30], while the current efficiency (%) and the specific electrochemical energy consumption (Wh g^{-1}) were calculated according to the equations (4) and (5) below, respectively.

$$\text{Current efficiency, } (\varphi) = \left(\frac{m_{experimental}}{m_{theoetical}}\right) \times 100 \quad (4)$$

$$\text{Specific electrochemical energy consumption} = \frac{E\,I\,t}{m} \quad (5)$$

where $m_{experimental}$ is the amount of product determined experimentally during the electrolysis and $m_{\text{theoretical}}$ is the theoretical value calculated by Faraday's law. E is the cell potential difference (V), I is the applied current (A), t is the duration of the electrolysis (s) and m (g) is the mass of the reaction product.

In the case of the oxidation of Ce(III) and reduction of Ce(IV) on the 3-dimensional mesh electrode, the relationship between log $c_{(t)}/c_{(0)}$ and time was not linear as can be seen in Figure 7.6b. This indicates that the reaction on this electrode was charge transfer controlled, when 50 mA cm^{-2} current density was applied during the first three hours of electrolysis. After these three hours of electrolysis the concentrations of Ce(III) and Ce (IV) during charge and discharge respectively, are low and the processes appear to become mass transport controlled. The parameters reported in Table 7.2 for this electrode were calculated using the linear region indicated as mass transport region in the Figure 7.6b. The

apparent first-order rate constant for the reduction of Ce(IV) ion was lower than the apparent first-order rate constant for the oxidation of Ce(III) when the 2-dimensional electrode was used. The percentage of conversion and current efficiency for the reduction of Ce(IV) was lower than the oxidation of Ce(III), as shown in Table 7.2 and Figure 7.6c, on both electrodes. The lower current efficiency observed in the 2-dimensional electrode at high current densities could be due to the leakage of Ce(IV) ions towards the negative electrolyte compartment across the membrane and the secondary reactions such as oxygen evolution during oxidation of Ce(III) and hydrogen evolution during Ce(IV) reduction process. The ionic transport of Ce(IV) ions through the membrane was confirmed by a very slightly yellow colouration observed in the negative electrolyte compartment [31]. The low current efficiency for the reduction of Ce(IV) also suggests that the current density was too high and that a significant part of the current was used in the hydrogen evolution reaction, which was indicated by a negative cell potential difference value of the zinc-cerium redox flow battery during discharge, as shown in Table 7.2. Current efficiencies of the cerium redox reactions were high (>94 %) when employing a 3-dimensional mesh electrode.

Current efficiency could be increased by enhancing the mass transport of cerium (III) ions. Previous investigation has shown that the oxidation of Ce(III) in nitric acid improved at a higher electrolyte flow rate in a divided flow cell [24]. For example, to achieve 0.84 mol dm^{-3} Ce(IV) using an applied constant cell potential difference of 2.5 V, approximately 2 hours were required at an electrolyte flow rate of 50 cm^3 min^{-1} but only 1.5 hours were required at 100 cm^3 min^{-1} to obtain the same concentration. This effect was also seen when the reaction was carried out in a beaker where the rate of Ce(III) oxidation increased with the stirring rate [32, 33]. These findings will be included in the chapter 7, where the current efficiency of Ce(III) oxidation increased from 95.2. % at 1.2 cm s^{-1} to

99.6 % at 5.8 cm s^{-1} using a 3-dimensional platinised mesh electrode in a divided parallel plate flow reactor [34].

Table 7.2 shows that, both the apparent first order rate constant and the mass transport coefficient improved at increased current densities. At higher applied current densities, cerium (III) and cerium (IV) conversion improved but the current efficiency decreased. Since more oxygen evolved at increased current density during the oxidation of Ce(III), more specific electrochemical energy was consumed. The specific electrochemical energy consumption during the oxidation of Ce(III) was reported to be dependent on different electrode materials. For example, on a mixed RuO-IrO-TiO_2 electrode the specific electrochemical energy consumption was 0.9 W h g^{-1} but approximately 2.1 W h g^{-1} was required at a SnO_2/Ti electrode [17]. These values are higher than those obtained in this work on 2- and 3-dimensional platinised titanium (see table 7.2). Since hydrogen evolution is the only side reaction possible at such negative potentials (< − 0.5 V *vs.* Ag|AgCl) during the Ce(IV) reduction using a 2-dimensional planar electrode, negative cell potential differences were obtained which resulted in no energy released from the battery during discharge; this is indicated by the positive value of the specific electrochemical energy consumption in Table 7.2. The cell potential value when the cell was fitted with the 3-dimensional platinised titanium mesh electrode was positive (1.8 V) and provided 0.35 W h g^{-1} specific energy output during discharge at 50 mA cm^{-2}, this is indicated by the minus sign in Table 7.2. Therefore, a 3-dimensional platinised titanium mesh positive electrode were found to be crucial to discharge a zinc-cerium redox flow battery at 50 mA cm^{-2} and 50 ^{o}C in the positive electrolyte containing 0.8 mol dm^{-3} cerium (III) methanesulfonate in 4 mol dm^{-3} methanesulfonic acid.

Parameters	Oxidation of Ce(III)				Reduction of Ce(IV)			
Electrode	2-d			3-d	2-d			3-d
Applied current density / mA cm^{-2}	20	50	80	50	20	50	80	50
Cell potential difference / V	3.0	3.4	3.7	3.0	−0.5	−0.8	−0.9	1.8
Apparent first order rate constant / $\times 10^{-5}$ s^{-1}	3.3	6.1	9.2	4.7 (mass-transport region)	2.1	5.0	7.7	5.6 (mass-transport region)
Mass transport coefficient/ $\times 10^{-6}$ s^{-1}	3.6	6.8	10.2	5.3 (mass-transport region)	2.4	5.6	8.5	6.2l (mass-transport region)
Change in concentration of Ce(IV) in the anolyte compartment at the end of the electrolysis / mol dm^{-3}	0.30	0.50	0.63	0.71	0.23 (4.0 h)	0.34 (4.0 h)	0.46 (4.0 h)	0.55 (3.3 h)
Specific electrochemical energy consumption / W h g^{-1}	0.58	0.98	1.36	0.61	0.11 (4.0 h)	0.30 (4.0 h)	0.40 (4.0 h)	−0.35 (3.3 h)
Overall current efficiency / %	99.3	66.2	52.1	94.0	86.0	50.0	43.0	97.6

Table 7.2 Calculated parameters of the electrolysis of Ce(III) and Ce(IV) in methanesulfonic acid using a divided, parallel plate zinc-cerium flow cell. The positive electrolyte contained 0.8 mol dm^{-3} cerium (III) methanesulfonate in 4.0 mol dm^{-3} methanesulfonic acid. Negative electrolyte was 1.5 mol dm^{-3} zinc methanesulfonate in 1.0 mol dm^{-3} methanesulfonic acid. Both electrolytes were circulated at 3.9 cm s^{-1} and at 50 ± 2 ^{o}C. The values were estimated using the assumption of a first order reaction in a constant volume stirred well mixed batch reactor.

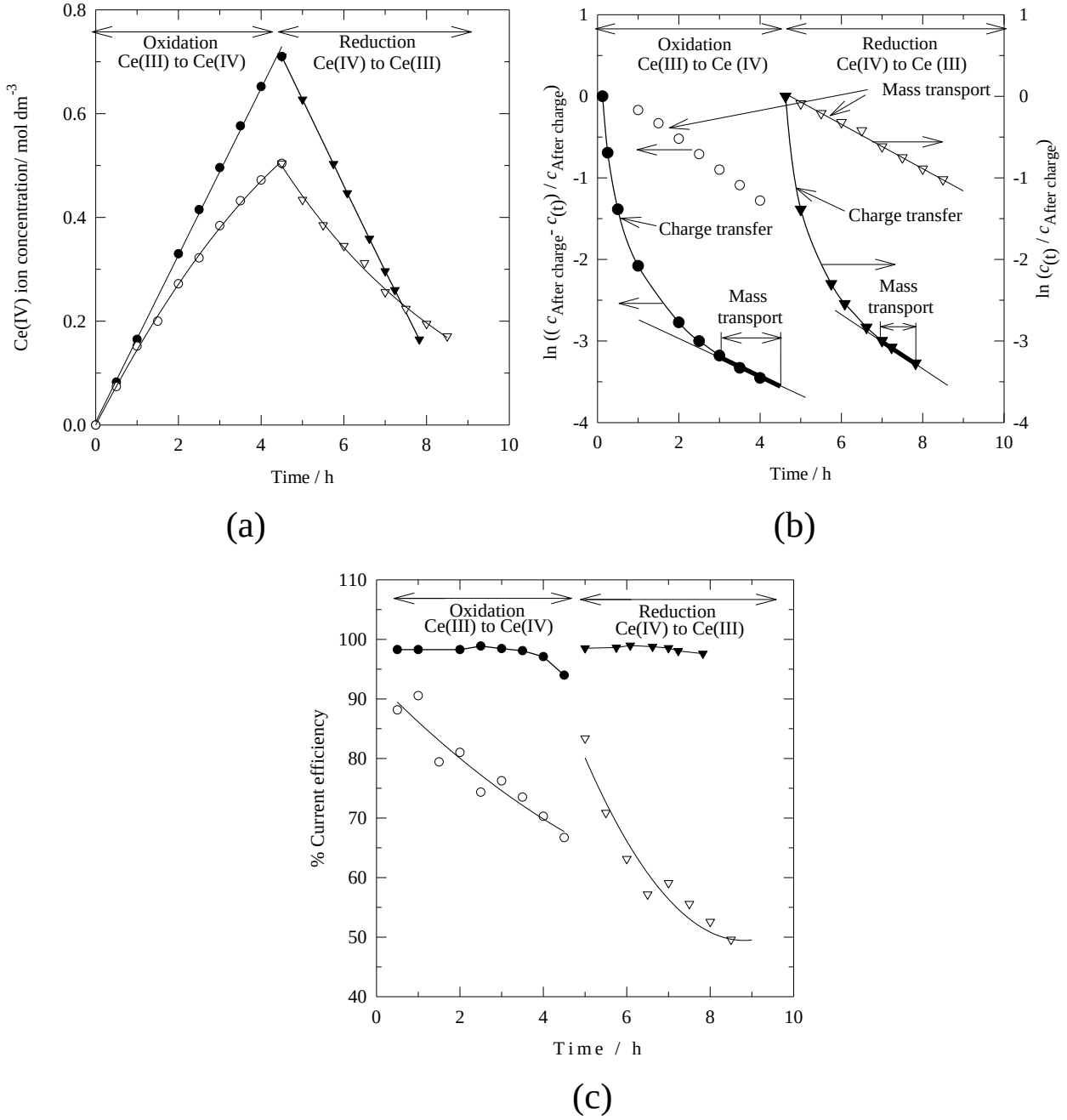

Figure 7.6. Electrolysis at a constant current (50 mA cm^{-2}) in a zinc-cerium flow cell. (a) Concentration of Ce(IV) *vs.* time. (b) Logarithmic plot of Ce(III) and Ce(IV) concentration *vs.* time and (c) Current efficiency. ○ oxidation of Ce(III) using a 2-d planar electrode, ● oxidation of Ce(III) using a 3-d mesh electrode, ▽ reduction of Ce(IV) using a 2-d planar electrode and ▼ reduction of Ce(IV) using a 3-d mesh electrode. Electrolyte compositions and operating conditions are the same as in Table 7.2.

7.8. Conclusions

1. The Ce(III)/Ce(IV) redox couple in methanesulfonic acid is a quasi-reversible and diffusion limited redox reaction at a platinum disc electrode. The magnitude of reversibility was found to be strongly dependent on the concentration of cerium (III) methanesulfonate in 0.1 to 5.0 mol dm^{-3} methanesulfonic acid between 0 and 70 ^{o}C. On a carbon electrode the electrochemistry of the Ce(III) ⇆ Ce(IV) redox reaction was found to be less favourable than on a platinum electrode.
2. Cyclic voltammograms show that higher concentrations of cerium (III) and methanesulfonic acid lead to an increase in the cathodic-anodic peak current ratio but wider the peak separation. The reversibility of the Ce(III)/Ce(IV) redox reaction in methanesulfonic acid was found to be improved at elevated electrolyte temperature.
3. The acid strength needed to be sufficiently high to maintain solubility of Ce(IV), however, the solubility of Ce(III) decreased at higher acid concentrations. As a compromise to maximize the solubility of both ions, an electrolyte composition for the positive electrode reaction in a flow battery using cerium half-cell was suggested as: 0.8 mol dm^{-3} cerium (III) methanesulfonate in 4.0 mol dm^{-3} methanesulfonic acid at 70 ^{o}C.
4. This quasi-reversible characteristic, at current densities of 20 to 80 mA cm^{-2} during the charge-discharge cycles at a relatively high concentration of electroactive species, e.g. 0.5 to 1.0 mol dm^{-3}, suggests that the Ce(III)/Ce(IV) redox couple can be used as a high cell potential difference and a high energy capacity positive electrode reaction in a flow battery. The methanesulfonic acid concentration had a crucial influence on the efficiencies of the Ce(III)/Ce(IV) redox reaction.
5. With a 2-dimensional planar platinised titanium electrode, the redox reactions of Ce(III)/Ce(IV) were under mass-transport controlled regime, while reactions at the 3-dimensional mesh electrode appear to be charge-transferred controlled but became

mass-transport controlled after 2.5 – 3 h of electrolysis when the concentrations of Ce(III) and Ce(IV) were lower.

6. At 50 mA cm^{-2}, hydrogen evolution takes place during the reduction of Ce(IV) at the 2 dimensional planar electrode, which resulted in negative cell potential differences and no energy output released from the flow battery. Using a 3-dimensional platinised titanium mesh electrode instead to discharge the battery, the cell potential difference reached 1.8 V and the energy output was 0.35 W h g^{-1}.

7.9. References

1. B. Fang, S. Iwasa, Y. Wei, T. Arai, M. Kumagai, Electrochim. Acta 47 (2002) 3971-3976.
2. A. Paulenova, S.E. Creager, J.D. Navratil, Y. Wei, J. Power Sources 109 (2002) 431-438.
3. P. Trinidad, C. Ponce de Leon, F.C. Walsh, J. Environ. Manage. 88 (2008) 1417-1425.
4. R.L. Clarke, B. Dougherty, S. Harrison, J.P. Millington, S. Mohanta, USP 20040197651, (2004).
5. R.L. Clarke, B. Dougherty, S. Harrison, J.P. Millington, S. Mohanta, US2008233484 (A1), (2008).
6. R.L. Clarke, B. Dougherty, S. Harrison, J.P. Millington, S. Mohanta, US2004197649 (A1), (2004).
7. Y. Liu, X. Xia, H. Liu, J. Power Sources 130 (2004) 299-305.
8. J. Bard, L.R. Faulkner, Electrochemical Methods-Fundamentals and Applications, 2nd ed. Wiley, (2001).
9. V. Devadoss, M. Noel, K. Jayaraman, C. Ahmed Basha, J. Appl. Electrochem. 33 (2003) 319-323.
10. R.P. Kreh, R.M. Spotnitz, J.T. Lundquist, J. Org. Chem. *54* (1989) 1526-1531.
11. T. Vijayabarathi, D. Velayutham, M. Noel, J. Appl. Electrochem. 31 (2001) 979-986.
12. E. Bishop, P. Cofré, J. Analyst 106 (1981) 316-322.
13. M. Breiter, P. Delahay, C.W. Tobias, Advances in Electrochemistry and Electrochemical Engineering Vol. 1, Interscience New York, (1961).

14. D. Pletcher, A First Course in Electrode Processes, The Electrochemical Consultancy, Romsey, (1991).
15. F.C. Walsh, A First Course in Electrochemical Engineering, Electrochemical Consultancy, Romsey, (1993).
16. C.M.A. Brett, M.O. Brett, Electrochemistry Principles, Methods and Applications, Oxford University Press, (1993).
17. V. Devadoss, C.A. Basha, K. Jayaraman, J. Ind. Eng. Chem. Res. 47 (2008) 4607-4616.
18. T.H. Randle, A.T. Kuhn, J. Chem. Soc., Faraday Trans. 1: Physical Chemistry in Condensed Phases 79 (1983) 1741-1756.
19. Y. Maeda, K. Sato, R. Ramaraj, T.N. Rao, D.A. Tryk, A. Fujishima, Electrochim. Acta 44 (1999) 3441-3449.
20. A. Abbaspour, M.A. Mehrgardi, J. Talanta 67 (2005) 579-584.
21. P. Glentworth, B. Wiseall, C.L. Wright, A.J. Mahmood, J. Inorg. Nucl. Chem. 30 (1968) 967-986.
22. P. Modiba, A.M. Crouch, J. Appl. Electrochem. 38 (2008) 1293-1299.
23. D. Pletcher, E.M. Valdes, Electrochim. Acta 33 (1988) 499-507.
24. Y. Wei, B. Fang, T. Arai, M. Kumagai, J. Appl. Electrochem. 35 (2005) 561-566.
25. K. Kramer, P.M. Robertson, N. Ibl, J. Appl. Electrochem. 10 (1980) 29-36.
26. M. Matheswaran, S. Balaji, S.J. Chung, I.S. Moon, Bull. Korean Chem. Soc. 28 (2007) 1329-1334.
27. T. Raju, C.A. Basha, J. Ind. Eng. Chem. Res. 47 (2008) 8947-8952.
28. T. Raju, C.A. Basha, J. Portugaliae Electrochim. Acta 23 (2005) 367-378.
29. P. Trinidad, F.C. Walsh, I. Chem. E. Symp. Series 145 (1999) 281-290.
30. P. Trinidad, F. Walsh, D. Gilroy, Int. J. Eng. Educ. 14 (1998) 431-441.
31. S. Harrison, USP 5679235, (1997).
32. T.A. Sedneva, J. Appl. Chem. 78 (2005) 907-911.
33. T. Raju, C.A. Basha, Chem. Eng. J. 114 (2005) 55-65.
34. P.K. Leung, C. Ponce-de-Leon, C.T.J. Low, A.A. Shah, F.C. Walsh, J. Power Sources 196 (2011) 5174-5185.

Chapter 8
Characterisation of a divided zinc-cerium redox flow battery

Chapter 8 Characterisation of a zinc-cerium redox flow battery

Introduction

An improved understanding of the flow battery performance under various operating conditions and electrolyte compositions are presented. In addition, a comprehensive investigation is carried out to optimize the electrode materials. The charge and discharge characteristics of the redox flow battery were studied under different operating conditions and Zn/Ce reactant, as well as methanesulfonic acid concentrations.

8.1. Electrochemistry of zinc and cerium in methanesulfonic acid

Figure 8.1 shows the combined cyclic voltammogram of the zinc and cerium redox couples under static conditions as a function of temperatures (22, 40 and 60 ^{o}C). The voltammogram of zinc was carried out between – 0.7 to – 1.2 V *vs.* Ag|AgCl at 128 mV s^{-1} in the negative electrolyte containing 1.5 mol dm^{-3} zinc(II) methanesulfonate and 1 mol dm^{-3} methanesulfonic acid on a glassy carbon disc electrode of 0.13 cm^2. The behaviour of the cerium half-cell reaction was recorded between + 0.5 to + 1.9 *vs.* Ag|AgCl at 128 mV s^{-1} in the positive electrolyte containing 0.8 mol dm^{-3} cerium(III) methanesulfonate and 4 mol dm^{-3} methanesulfonic acid of a platinum electrode (0.13 cm^2).

The cyclic voltammograms show that the influence of temperature on the peak current of the zinc reaction was much larger than the cerium one. The current density of zinc reduction increased tenfold when the temperature changed from 22 to 60 ^{o}C whereas the oxidation of Ce(III) increased only twice in the same temperature range. It is also likely that the current for zinc electrodepositon has some contributions from the hydrogen evolution, while the oxidation of Ce(III) might involve some oxygen evolution. During the battery charge, Zn(II) electrodeposition and Ce(III) oxidation take place at *c.a.* – 1.08 and

+ 1.84 V *vs.* Ag|AgCl, respectively, at 22 ^{o}C. Upon discharge, dissolution of Zn(0) occurs at – 0.94 V *vs.* Ag|AgCl and the reduction of Ce(IV) at + 1.05 V *vs.* Ag|AgCl . A simple estimation of the charge and discharge cell voltages can be obtained by subtracting the zinc potential from the cerium potential, which do not take account of the ohmic drop of the electrolyte and the electrodes as the working electrodes were pointed to the reference electrodes through luggin capillaries. At 22 ^{o}C, the estimated values for charge and discharge would be 2.92 V and 1.99 V, respectively. The estimation of charge and discharge cell voltages at 60 ^{o}C was 2.81 V and 2.08 V, respectively. These values do not consider the ohmic losses across the electrolyte, electrodes and membrane but show the improvement in cell voltage with temperature for the charge and discharge cycles.

As the temperature increases, the separation between the oxidation and reduction peaks of each redox couple decreased. For the Zn(0)/Zn(II) redox couple, the oxidation and reduction peaks became 30 mV closer when the temperature increased from 22 to 60 ^{o}C while for the Ce(III)/Ce(IV) redox couple the improvement was 150 mV from 830 mV at 22^{o}C to 680 mV at 60 ^{o}C. At increased temperature, the oxidation and reduction peak current density of both zinc and cerium reactions increased. As the cyclic voltammetry shows that the positive electrode reaction could limit the use of higher current, high surface area electrodes could be used to solve this problem. A range of 2- and 3-dimensional positive electrodes are investigated in the next section.

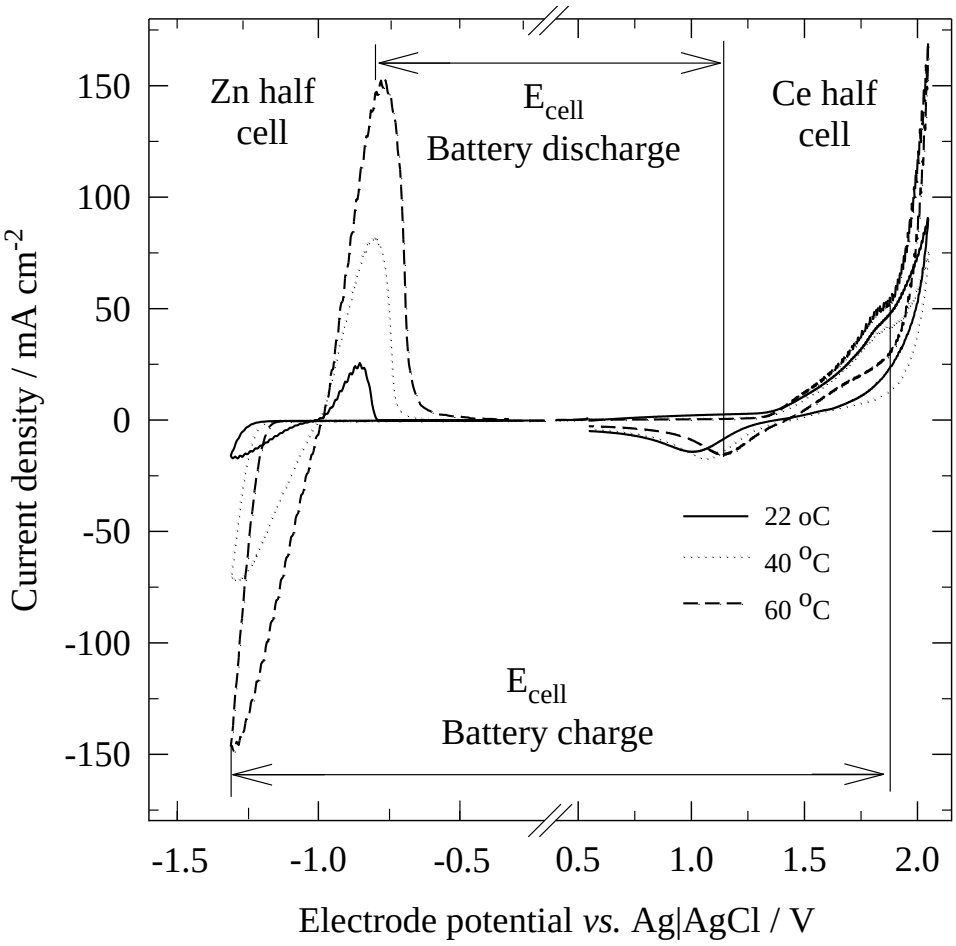

Figure 8.1. A combined cyclic voltammetry of zinc half-cell at glassy carbon electrode and cerium half-cell reaction at platinum sweeping the potential linearly at 128 mV s^{-1} from – 0.7 to – 1.2 V *vs.* Ag|AgCl and + 0.5 to + 1.9 V *vs.* Ag|AgCl, respectively at electrolyte temperatures of 20, 40 and 60 °C. Negative electrolyte: 1.5 mol dm^{-3} zinc(II) methanesulfonate and 1 mol dm^{-3} methanesulfonic acid. Positive electrolyte: 0.8 mol dm^{-3} cerium(III) methanesulfonate and 4 mol dm^{-3} methanesulfonic acid.

8.2. Selection of positive electrode materials

A summary of the characteristics and behaviour of the eight positive electrode materials tested during the operation of a Zn/Ce redox flow battery at 50 °C is shown in Table 8.1. For the Zn(0)/Zn(II) redox couple, carbon polyvinyl-ester composite was the

negative electrode material. Both positive and negative electrolyte compositions were the same as that in the cyclic voltammetry experiments described in section 3.1 and were circulated mean linear velocity of 3.9 cm s^{-1} through the cell. The battery was first charged at 50 mA cm^{-2} for 4 hours using different electrodes and the concentration of Ce(IV) was measured after the battery was charged, these concentrations are shown in Table 8.1. The battery was then discharged at a range of constant current densities (5 – 50 mA cm^{-2}) and constant cell voltages (2.2 – 1.0 V). In order to maintain the Ce(IV) ion concentration approximately constant, each discharge current or voltage was applied for only 2 minutes, enough time to measure the cell voltage or current generated. The battery was recharged frequently to restore the concentration of Ce(IV) ions and maintain the same state of charge (SOC) for each experiment.

Table 8.1 shows that during battery charge at 50 mA cm^{-2}, the conversion of Ce(III) was the highest when the two carbon felts and the 3-dimensional platinised titanium mesh were used. Ce(IV) concentrations reached more than 0.60 mol dm^{-3} at current efficiencies of > 90 % using these electrodes. This value is consistent with previous results where the current efficiencies of the electrochemical oxidation of Ce(III) were 70 – 85 % using platinum, RuO_x−IrO_x−TiO_x coated titanium and dimensionally stable anode [DSA]/O_2 or [DSA]/Cl_2 at 50 mA cm^{-2} [1]. In these experiments, platinum-based positive electrode materials were stable through the battery charge and discharge cycles. Other materials, such as reticulated vitreous carbon, graphite and carbon polyvinyl-ester composite have less stable performance and poor Ce(IV) conversion. These electrodes either exfoliated or expanded and carbon debris appeared in the electrolytes during battery cycling.

Type	Electrode Materials	Details	Specific surface area / cm^2 cm^{-3}	Total Surface area / cm^2	Observations		Ce(IV) after 4 hours charge at 50 mA cm^{-2} / mol dm^{-3}
					Electrode	Electrolyte	
1	Platinised titanium (7 cm × 5 cm × 0.2 cm)	70 g Pt m^{-2} loading, 3. 5μm thick, Magneto GmbH (Netherlands)	Nil (2D)	9	Stable, no observable change	Clear yellowish solution	0.456
2	Graphite (7 cm × 5 cm × 0.6 cm)	Grade S plate, Le Carbone Lorraine S.A. (France)	Nil (2D)	9	Graphite plate exfoliated, as particles came off after 10 min	Very dark solution with carbon particles	0.104
3	Carbon-polyvinylester (7 cm × 5 cm × 0.6 cm)	BMC 18649 Vinyl ester bipolar plate Entegris Inc. (Germany)	Nil (2D)	9	Carbon plate exfoliated, as particles came off after 10 min	Very dark solution with carbon particles	0.08
4	30 ppi reticulated vitreous carbon (4.5 cm × 2 cm × 2 cm)	Duocel®, ERG Material and Aerospace Corp. (USA)	19 [2]	342	Slightly expanded, and carbon particles came off after 2 hours and 15 min	Dark solution with carbon particles	0.16
5	100 ppi reticulated vitreous carbon (4.5 cm × 2 cm × 2 cm)	Duocel®, ERG Material and Aerospace Corp. (USA)	65 [2]	1170	Slightly expanded, and carbon particles came off after 2 hours and 15 min	Dark solution with carbon particles	0.128
6	Alfa Aesar carbon felt (4.5 cm × 2 cm × 0.8 cm)	Stock 42107, 99 %, Alfa Aesar (UK)	452.3 [3]	3256	Became darker the appearance after the experiment	Clear orange solution with very few carbon particles	0.632
7	Sigratherm® carbon felt (4.5 cm × 2 cm × 0.8 cm)	GFA -05, SGL Group (Germany)	240 – 600 [4]	1728 – 4320	No observable change in appearance	Clear orange solution with very few carbon particles	0.656
8	4 platinised titanium mesh (4.4 cm × 1.6 cm × 0.25 cm each) welded on a platinised titanium plate (7 cm ×5 cm × 0.2 cm)	70 g Pt m^{-2} loading, 3.5 μm thick, Magneto GmbH (Netherlands)	19.3	72.7	Stable, no observable change	Clear Orange solution	0.652

Table 8.1. Positive electrode materials evaluated for the zinc-cerium redox flow battery.

8.2.1. *Constant current density discharge*

The patented Plurion Inc. zinc-cerium system discharges at a constant cell voltage of 1.8 V [5, 6], at which the current density undergoes an exponential decay. Despite a high initial current density, the full discharge of the battery requires a prolonged period of time [7]. In practice, constant current density discharge is preferred due to lower cost and a more steady power output. Therefore, the eight positive electrode materials were tested at constant current densities during discharge. Figure 8.2a shows the cell voltages of the eight positive electrode materials *vs.* discharge current density (5 – 50 mA cm^{-2}). In all materials, the cell voltage decreases as the applied current density increases. This is attributed to the electrode overpotentials and ohmic drop across the electrodes, electrolytes and membrane. Most of the 2-dimensional materials and the reticulated vitreous carbon electrodes had a large cell voltage drop attributed to their resistance during discharge at increased current densities, the initial cell voltages were *c.a.* 2.0 V at 5 mA cm^{-2} and dropped to values below 0 V at 50 mA cm^{-2}.

The initial cell voltage of the carbon felts and the 3-dimensional platinised titanium mesh were all above 1.8 V in a current density range between 5 and 50 mA cm^{-2} with less than 0.55 V voltage drop. The high cell voltages were due to the high Ce(IV) concentration generated in the positive electrolyte (Table 8.1) and to the low local current density of the large surface area of the electrodes. On the contrary, the battery equipped with a 2-dimensional platinised titanium electrode, carbon polyvinylester and reticulated vitreous carbon 3-dimensional electrodes had a voltage drop of more than 1.5 V when the discharge current density increased from 20 to 25 mA cm^{-2}. Such discharge current density seems to be too high for these electrodes and is perhaps due to the low of concentration Ce(IV) ions near the electrode surface to be reduced, which lead to hydrogen evolution. It is important to notice that despite having high surface area, the reticulated vitreous carbon electrodes

behave similarly to a 2-dimentional electrode.

8.2.2. *Constant cell voltage discharge*

Figure 8.2b shows the discharge performance of the eight positive electrode materials when a range of constant cell voltages (1.0 – 2.2 V) was applied after 4 hours of charge at 50 mA cm^{-2}. For all positive electrode materials, the discharge current density decreased when the applied constant cell voltage increased. A similar trend was also observed in the previous study of a zinc-bromine redox flow battery [8]. The data (Figure 8.3b) is comparable to the discharge performance at constant current density shown in the last section. For instance, the initial current density of the 3-dimensional platinised titanium mesh electrode at 1.9 V discharge was *c.a.* 50 mA cm^{-2}, while at constant current density of 50 mA cm^{2}, cell voltage was 1.92 V (Figure 8.2a).

The highest initial current densities were obtained with the two carbon felts and the 3-dimensional platinised titanium mesh electrodes. These materials have initial current densities of > 14 and > 120 mA cm^{-2} at constant cell voltage discharge of 2.2 V and 1.0 V, respectively. The initial discharge current densities of the other 2-dimensional electrodes and the reticulated vitreous carbon materials were less than 5 and 30 mA cm^{-2} during a cell voltage discharge at 2.2 V and 1.0 V, respectively. In the case of the two carbon felts and the 3-dimensional platinised titanium mesh electrode, the large current densities obtained at low discharge cell voltages were also due to the gaseous evolution reaction. Discharging the zinc-cerium battery at such low voltages is not a practical approach, as it not only leads to the side reaction but also lowers the voltage and the charge efficiencies.

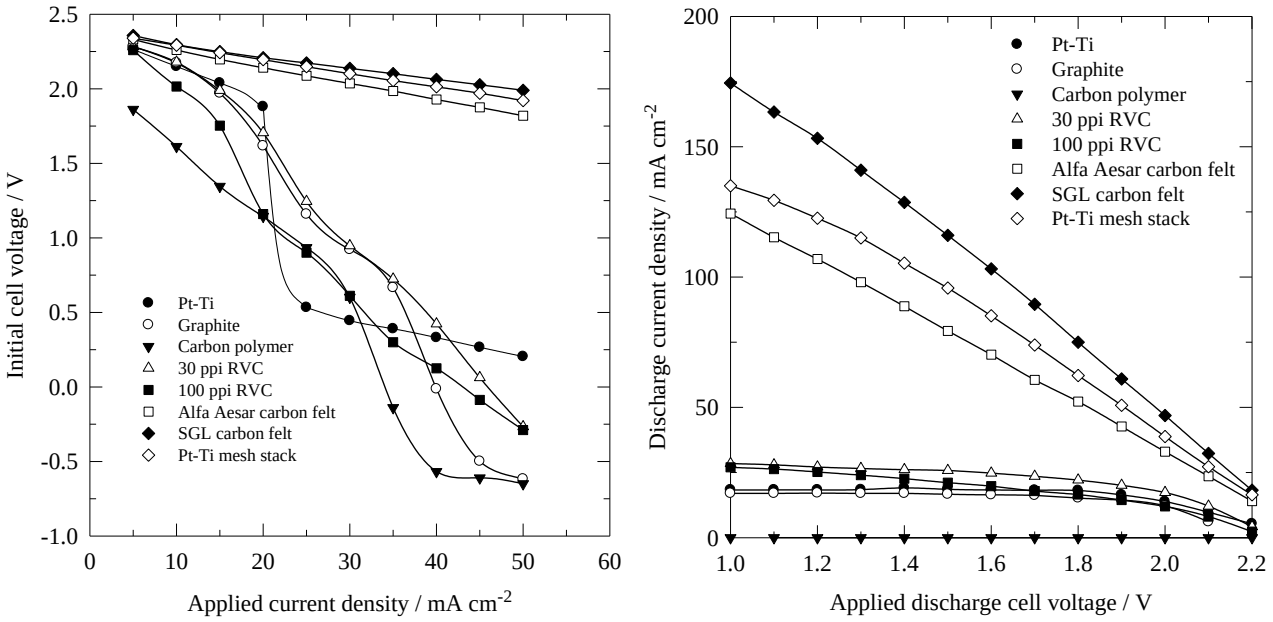

(a) (b)

Figure 8.2. Performance of 8 positive electrode materials in a zinc-cerium redox flow battery during the discharge cycle. (a) constant current density. (b) Constant cell voltage; A carbon-polyvinylester composite was used as a negative electrode material. The negative electrolyte was a 100 cm^3 solution containing 1.5 mol dm^{-3} zinc(II) methanesulfonate in 1 mol dm^{-3} methanesulfonic acid. Positive electrolyte was 100 cm^3 solution containing 0.8 mol dm^{-3} cerium(III) methanesulfonate in 4 mol dm^{-3} methanesulfonic acid. Both negative and positive electrolytes were circulated at 3.9 cm s^{-1} by a peristaltic pump and maintained at 50 ^oC by a water bath.

8.3. Charge/discharge performance of a zinc-cerium redox flow battery

After testing a number of electrode materials, the carbon felt and the 3-dimensional platinised titanium mesh were found to be the optimum materials for the positive electrode reaction. This agrees with the data reported in the literature as glassy carbon and platinized titanium were used as the positive electrode materials in the Plurion Inc.'s system [5, 6].

The charge-discharge performances of the redox flow battery was studied when the Sigratherm® GFA-05 carbon felt and the 3-dimensional platinised titanium mesh were fitted as the positive electrodes, while the negative electrode was a carbon polyvinyl-ester composite. Detailed descriptions on operating conditions and electrolyte compositions were described in the experimental section.

Figures 8.3a and 8.3b show the cell voltage and the electrode potentials *vs.* time characteristics of the zinc-cerium flow battery when Sigratherm® carbon felt and the 3-dimensional platinised titanium mesh, respectively were used. Also, the figures show the IR drop across the membrane and electrolyte during the 4-hour charge/ discharge cycle. The charge/discharge performance with the Sigratherm® carbon felt was more favourable than that of the 3-dimensional platinised titanium mesh system as it shows very flat cell voltage profile. In the 3-dimensional platinised titanium mesh system (Figure 8.3b), cell voltage started to rise after charging for three hours due to the consumption of Ce(III) ions and the oxygen evolution becoming more significant at the positive electrode. With the Sigratherm® carbon felt, coulombic efficiency was 92.4 % while the average charge and discharge cell voltages were 2.79 V and 1.90 V, respectively. Since the surface area is higher than the 3-dimensional platnised titanium mesh, the cerium ion can reach the electrode easier at the same flow condition, hence Ce(III) oxidation (conversion of Ce(III) ion to Ce(IV) ion) is more efficient and less oxygen evolved during charge. The very large surface area of carbon felt can make reduction of cerium(IV) reaction becomes possible even at low Ce(IV) ion concentration during discharge. The energy efficiency was 63 % at charge/discharge current density of 50 mA cm^{-2} which compare well with other systems such as the soluble lead acid flow battery which is about 58 % at current density of 40–60 mA cm^{-2} [9]. Using the 3-dimensional platinised titanium mesh electrode (Figure 8.3b), the coulombic efficiency was 71 % and the energy efficiency was 43% at 50 mA cm^{-2}. The

charge and discharge voltages were 2.98 V and 1.79 V, respectively. The difference between these and the predicted values in the cyclic voltammetry study are attributed to the ohmic resistance and the depleted electroactive species during battery charge and discharge cycles.

The cell voltage during discharge is expressed as the sum of the cerium half-cell potential, the zinc half-cell potential, the ohmic loss and the overpotentials.

$$E_{CELL} = E_{Ce} - E_{Zn} - \Sigma IR - |\Sigma \eta| \quad (1)$$

The ohmic losses in the battery were mainly attributed to the proton-exchange membrane, the electrodes, the electrolytes and to the electrical contacts. In the zinc-cerium battery fitted with a Sigratherm® carbon felt positive electrode, the change in cerium half-cell voltage between the charge and discharge cycle was remarkably small, at just 0.07 V compared to 0.29 V observed in the 3-dimensional platinised titanium mesh electrode as shown in Figures 8.3a and 8.3b, respectively. This value is also smaller than those of the positive half-cell reactions in the zinc-chlorine [10] and zinc-bromine [8] systems reported in the literature. In addition to the overpotential advantages of this electrode, carbon felt is less expensive than platinum and does not form any oxide layer during the oxidation of Ce(III) [11]. This suggests that the cerium redox reaction at the carbon felt electrode shows better reversibility than at platinised titanium and could be a promising prospect for future use in this system.

The carbon polyvinyl-ester composite negative electrode material in both systems (Figures 8.3a and 8.3b) showed 0.35 V difference between charge and discharge cycles. This value is larger than those found in the electrolyte of zinc chloride [10] or zinc bromide [8] systems, possibly due to the high stability of the zinc(II) methanesulfonate complexes.

Additives, such as indium oxide [12], can be used to reduce such overpotential in aqueous methanesulfonic acid. The reduction of the Ce(IV) took slightly longer in the battery with the Sigratherm® carbon felt than with the 3-dimensional platinised titanium mesh electrode (see Figure 8.3a and 8.3b). Also, with the 3-dimensional mesh electrode, Figure 8.3b shows that zinc deposits were still on the electrode at the end of the discharge cycles, while with the carbon felt electrode zinc electrodeposits were stripped off after discharging for 3.4 h as shown by the potential increase towards the end of the cycle in Figure 8.3a. Both zinc and cerium electrodes were completely utilized during battery discharge using the carbon felt, while with the 3-dimensional platinised-titanium mesh electrode the cerium half-cell reaction was the main limiting factor in the system. Despite the high efficiency of carbon felts as positive electrodes, poor conductivity and poor adherence of the carbon adhesive were observed after 2 to 3 charge/discharge cycles. Further developments on the construction of such electrode and the electrical connections in the highly acidic, oxidizing cerium(IV) methanesulfonate electrolyte are required.

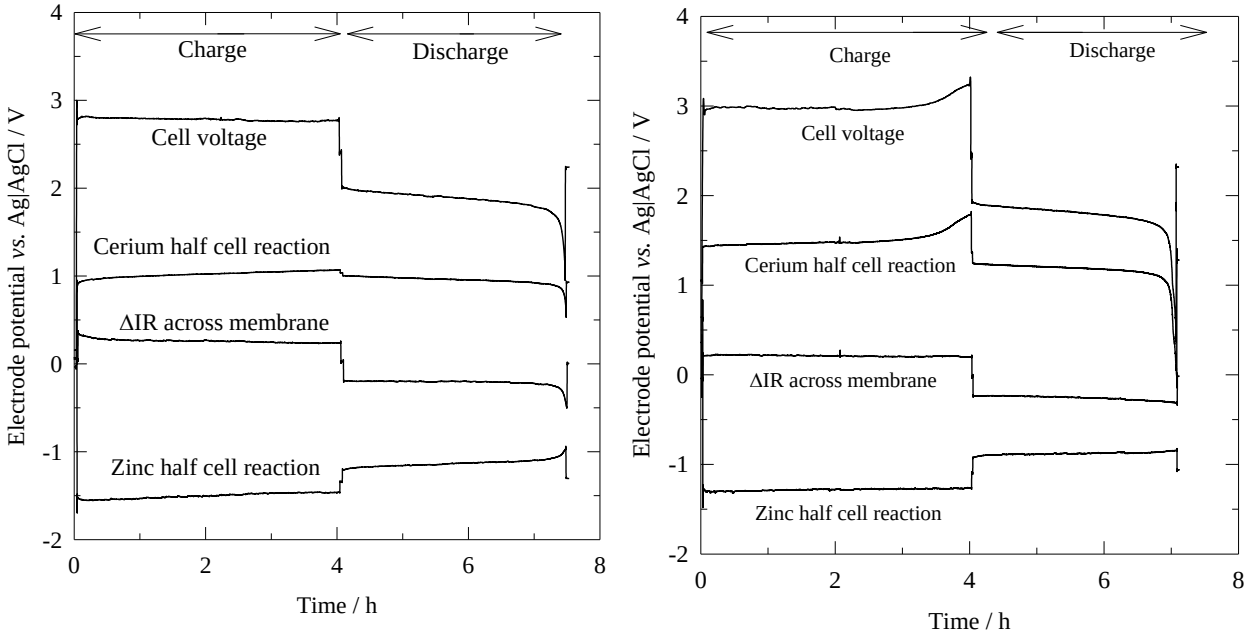

Figure 8.3. A voltage *vs.* time characteristic of a zinc-cerium redox flow battery equipped with high surface areas of positive electrodes: (a) Sigratherm® carbon felt and (b) platinised titanium mesh electrodes. Electrolyte composition and operating conditions as in Figure 8.2.

8.4. Effect of flow conditions on battery discharge

Redox flow battery differs from conventional energy storage because mass transport conditions play an important role to deliver large power output. The effect of the mean linear flow velocity of the electrolyte on the battery performance was studied under two discharge modes: (1) constant cell voltage and (2) constant current density. Sigratherm® carbon felt and the 3-dimensional platinised titanium mesh were fitted in the flow battery as the positive electrodes, while the negative electrode was a carbon-polyvinylester composite. Operating conditions and electrolyte compositions were described in the experimental section. The battery was first charged at current density of 50 mA cm^{-2},

referred to the negative electrode area for 4 hours in order to achieve the same state of charge (SOC) before all the tests. The battery was then discharged at a range of constant current densities (10 – 70 mA cm^{-2}) and cell voltages (1.0 – 2.2 V) under a wide range of mean linear electrolyte flow velocities (1.2 – 7.8 cm s^{-1}). In order to maintain the Ce(IV) concentration constant, each current and potential was applied for 2 minutes only and the battery was frequently charged between measurements to restore the Ce(IV) consumed and maintain the same SOC.

8.4.1. *Constant cell voltage discharge*

Similar to the previous section, the effect of the mean linear electrolyte flow velocity on the discharge current densities during the application of a range of constant cell voltage discharge is shown in Figures 8.4a and 8.4b, respectively. As the mean linear flow velocity increased, the current density was larger at all the applied cell voltages but the effect of mean linear electrolyte flow velocity was more pronounced at Sigratherm® carbon felt as shown in Figure 8.4a, where the discharge current densities increased at higher mean linear electrolyte flow velocity and reached the maximum values at 3.9 cm s^{-1}. Further increase in the velocity caused a slight decrease in the discharge current densities. In the system with the 3-dimensional platinised titanium mesh, the mean linear electrolyte flow velocity had less influence on discharge current density at higher cell voltage discharge (Figure 8.4b). At a 2.2 V discharge, the current density obtained was *c.a.* 16 mA cm^{-2} over mean linear electrolyte flow velocities of 1.2 – 7.8 cm s^{-1}. Similar to the battery with a carbon felt positive electrode, the discharge current densities reached the maximum values at a mean linear electrolyte flow velocity of 3.9 cm s^{-1} but leveled off at higher velocities. As a result, 3.9 cm s^{-1} was an optimum value for the flow conditions of both systems to discharge at constant cell voltage. As the velocity increased, the polarization losses were expected to be lower at equivalent states of charge since the charge since the reactants would be

distributed more evenly and the width of any Nernst diffusion layer decreased.

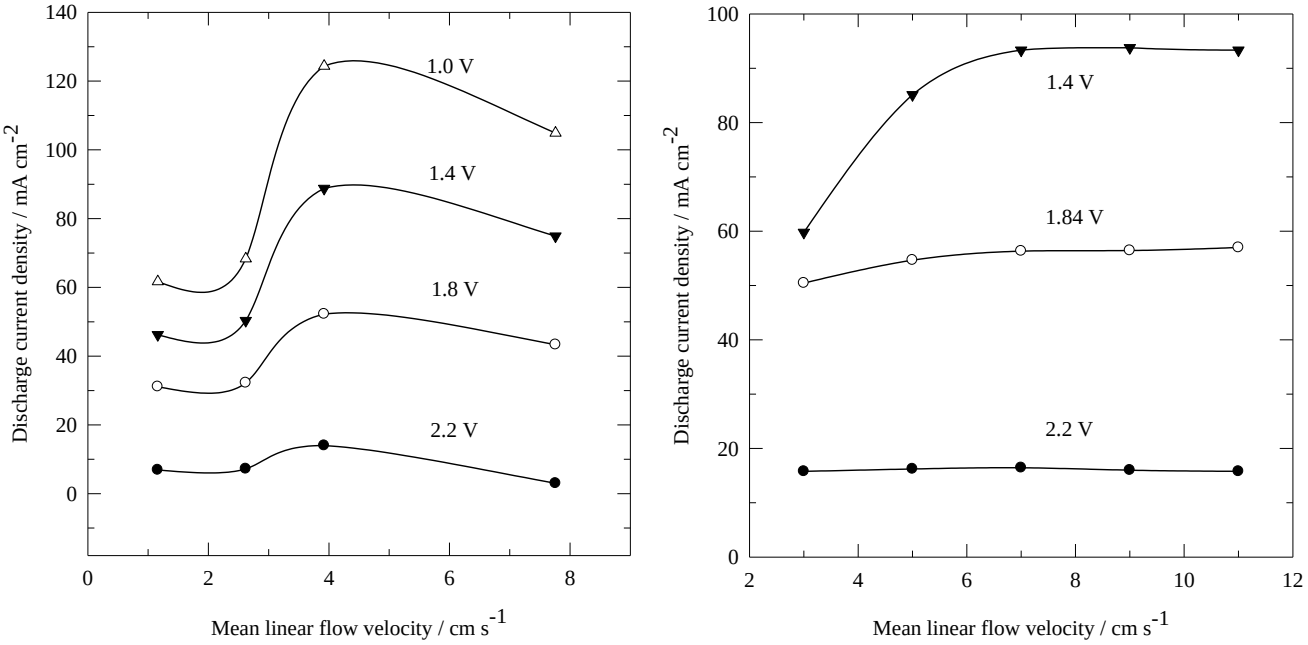

Figure 8.4. Effect of flow condition on constant voltage discharge of a zinc-cerium redox flow battery at (a) Sigratherm® carbon felt and (b) platinized titanium mesh electrode. Electrolyte compositions and operating conditions as in Figure 8.3.

8.4.2. *Constant current density discharge*

Figure 8.5a and 8.5b show the effect of the mean linear flow velocity on discharge voltage at a range of constant current densities during the discharge of the zinc-cerium flow battery equipped with the carbon felt and the 3-dimensional platinised titanium mesh electrodes, respectively. In both systems, the cell voltage decreases at higher discharge current densities, which is comparable to the results obtained in the section 8.2.1. at constant current density discharge. As shown in Figure 8.5a, the effect of the mean linear electrolyte flow velocity was significant on the cell voltage in the Sigratherm® carbon felt system: discharge voltages increased with the mean linear electrolyte flow velocity until

reaching maximum values at 3.9 cm s^{-1} for all current densities.

On the contrary, Figure 8.5b shows that the discharge cell voltages of the battery for the 3-dimensional platinised titanium mesh system remained almost the same over a wide range of mean linear electrolyte flow velocities except when the discharge current density was 70 mA cm^{-2}. At these conditions the mass transport is still important and the supply rate of Ce(IV) ions to the positive electrode should be higher. For instance, the discharge cell voltage at 70 mA cm^{-2} was as low as *c.a.* 0.1 V at a mean linear electrolyte flow velocity of 1.16 cm s^{-1}. When the mean linear flow velocity of the electrolyte increased above 2.62 cm s^{-1}, discharge cell voltages of *c.a.* 1.5 V were obtained. As given by equation (2) below, higher discharge current densities can be obtained by increasing the cerium(IV) ion concentration and by reducing the diffusion layer with higher electrolyte velocity and temperature:

$$j_L = z\,\mathrm{F}\,D\,c_o / \delta_N \qquad (2)$$

where j_L is the limiting current density (A cm^{-2}), z is the number of electrons, F is the Faraday constant, D is the diffusion coefficient (cm^2 s^{-1}), c_o is the cerium concentration in the bulk of the solution (mol cm^{-3}) and δ_N is the thickness (cm) of the Nernst diffusion layer.

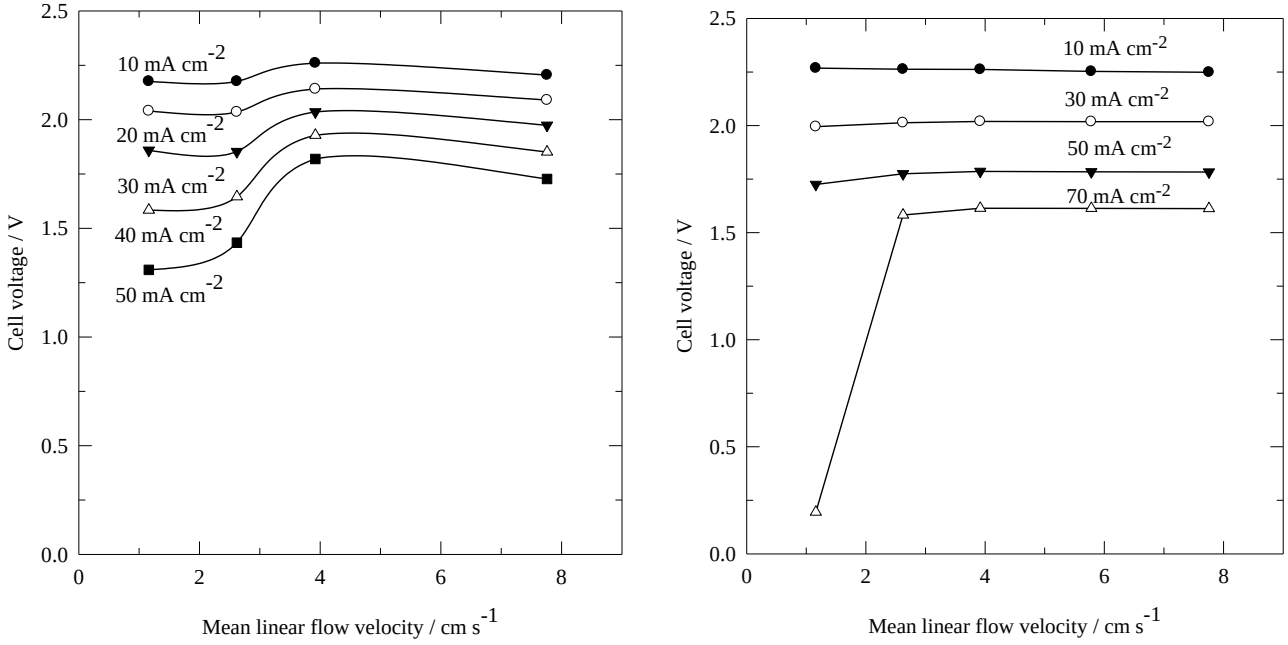

(a) (b)

Figure 8.5. Effect of constant current density discharge at (a) Sigratherm® carbon felt and (b) platinized titanium mesh electrode. Electrolyte compositions and operating conditions were the same as in Figure 8.3.

8.5. Efficiencies of a zinc-cerium redox flow battery

In order to determine the optimum operating conditions and electrolyte compositions of a zinc-cerium flow battery, a wide range of experiments was carried out over a range of applied current densities (20 – 80 mA cm^{-2}), operating temperatures (25 – 60 ^{o}C), mean linear flow velocities of the electrolyte (1.8 – 7.8 cm s^{-1}), zinc(II) methanesulfonate concentrations (0.5 – 1.5 mol dm^{-3}), cerium(III) methanesulfonate concentrations (0.4 – 1.2 mol dm^{-3}) and methanesulfonic acid concentrations (2 – 5 mol dm^{-3}) in the positive electrolyte. Since the carbon adhesive was no longer conductive or adherent to the carbon-polymer substrate after a few cycles, a 3-dimensional platinised titanium mesh positive electrode was preferred in this study. The flow battery was first charged for four hours and discharged at the same current

until the cell voltage dropped below 0.5 V. Unless indicated otherwise, the operating conditions were the same as those described in the experimental section.

Table 8.2 summarizes the charge-discharge voltages and the system efficiencies when the parameters mentioned above changed. However, the energy consumptions due to the peristaltic pumps and water baths have not been taken into the account in the energy efficiency. The highest energy efficiency was obtained at 50 ^{o}C with a mean linear electrolyte flow velocity of 3.9 cm s^{-1}, while the optimum composition for the positive electrolyte was 0.8 mol dm^{-3} cerium(III) methanesulfonate in 4.0 mol dm^{-3} methanesulfonic acid. In all cases, cerium half-cell was the limiting reaction for battery discharge, as the redox reaction of zinc lasted longer than that of the cerium reaction, both during charge and discharge cycles.

Operating parameters	Average charge voltage /V	Average discharge voltage / V	[Ce(IV)] after charge / mol dm^{-3}	[Ce(IV)] after discharge / mol dm^{-3}	% Coulombic efficiency	% Voltage efficiency	% Energy efficiency
Current density / mA cm^{-2}							
20	2.67	1.98	0.264	0.098	63.1	74.2	46.8
50	2.98	1.79	0.652	0.184	71.4	60.1	42.9
80	3.33	1.57	0.728	0.271	43.6	47.1	20.5
Temperature / ^{o}C							
25	3.30	1.55	0.600	0.288	47.6	47.0	22.4
40	3.13	1.61	0.616	0.218	60.7	51.4	31.2
50	2.98	1.79	0.652	0.184	71.4	60.1	42.9
60	2.86	1.82	0.672	0.260	62.8	63.6	39.9
Mean linear electrolyte flow velocity / cm s^{-1}							
1.16	3.15	1.61	0.640	0.396	37.3	51.1	19.1
1.79	3.02	1.74	0.616	0.280	51.4	57.6	29.6
3.92	2.98	1.79	0.652	0.184	71.4	60.1	42.9
5.78	2.93	1.74	0.669	0.201	71.4	59.4	42.4
[Ce(III)] / mol dm^{-3}							
0.4 (2.5 h electrolysis)	3.08	1.73	0.395	0.166	56.0	56.2	31.5
0.8	2.98	1.79	0.652	0.184	71.4	60.1	42.9
1.0	3.01	1.72	0.632	0.237	60.3	57.1	34.5
1.2	3.04	1.65	0.628	0.293	51.1	54.3	27.7
[Zn(II)] / mol dm^{-3}							
0.5	2.99	1.80	0.652	0.204	68.4	60.2	41.2
1	2.98	1.77	0.652	0.179	72.2	59.4	42.9
1.5	2.98	1.79	0.652	0.184	71.4	60.1	42.9
2	3.13	1.51	0.652	0.201	69.0	48.2	33.3
[Methanesulfonic acid] in positive electrolyte / mol dm^{-3}							
2	3.01	No discharge (Insoluble)	0.616	No discharge	Nil	Nil	Nil
3	3.01	1.74	0.608	0.307	46.0	57.8	26.6
4	2.98	1.79	0.652	0.185	71.4	60.1	42.9
5	3.00	1.68	0.656	0.291	55.7	56.0	31.2

Table 8.2. System efficiencies of a zinc-cerium redox flow battery at different operating compositions and electrolyte compositions. Unless specified, the operating conditions are the same as in Figure 8.3.

8.5.1. *Effect of operating parameters*

Figure 8.6a shows the charge-discharge performance *vs.* time under the effect of current density. Smaller cell voltage drop between the charge and discharge cycles was observed at low current densities, hence the voltage efficiency improved; at 80 mA cm^{-2} (Figure 8.6a), the charge voltage started at *c.a.* 3.3 V and rose to 3.5 V after charging for two hours. This is because larger concentration of Ce(IV) ions were produced, depleting the Ce(III) ion concentration in the positive electrolyte leading to a more dominant oxygen evolution which occurs at higher potential. Similarly, more gases evolved during battery discharge at 80 mA cm^{-2}. The low coulombic efficiencies observed at 20 and 80 mA cm^{-2} (Table 8.2) were due to limited mass transport of Ce(IV) ions and the gaseous evolution of the secondary reactions. For instance, Ce(IV) concentration after battery discharge at 20 and 80 mA cm^{-2} were just 0.098 and 0.271 mol dm^{-3}, respectively. Such Ce(IV) ion concentration and mean linear electrolyte flow velocity of 3.9m cm s^{-1} may not have been sufficient for a high reaction rate at the positive electrode.

Figure 8.6b shows the effect of the mean linear flow velocity *vs.* time on the charge-discharge cycle. Small cell voltage drop was observed at high mean linear flow velocity. Longer and more stable discharge times and higher cell voltages were obtained as the mean linear electrolyte flow velocity increased indicating that mass transport of Ce(IV) ion is important during battery discharge. Meanwhile, faster convection of zinc and cerium ions towards the electrodes allowed more efficient electrode reactions [13] and side reactions became less dominant. A further increase in mean linear electrolyte flow velocity above 3.9 cm s^{-1} did not yield significant, higher discharge voltage as the reaction was no longer mass transport controlled. At lower electrolyte mean flow velocities of 1.16 and 1.79 cm s^{-1}, the charge cell voltage rose after charging for 2.5 hours. This is mainly due to the side reaction of oxygen evolution and the limited mass transport of the Ce(III) ion

towards the positive electrode. Increase of the mean linear electrolyte flow velocity led to lower charge voltages and higher discharge voltages, hence higher voltage efficiency.

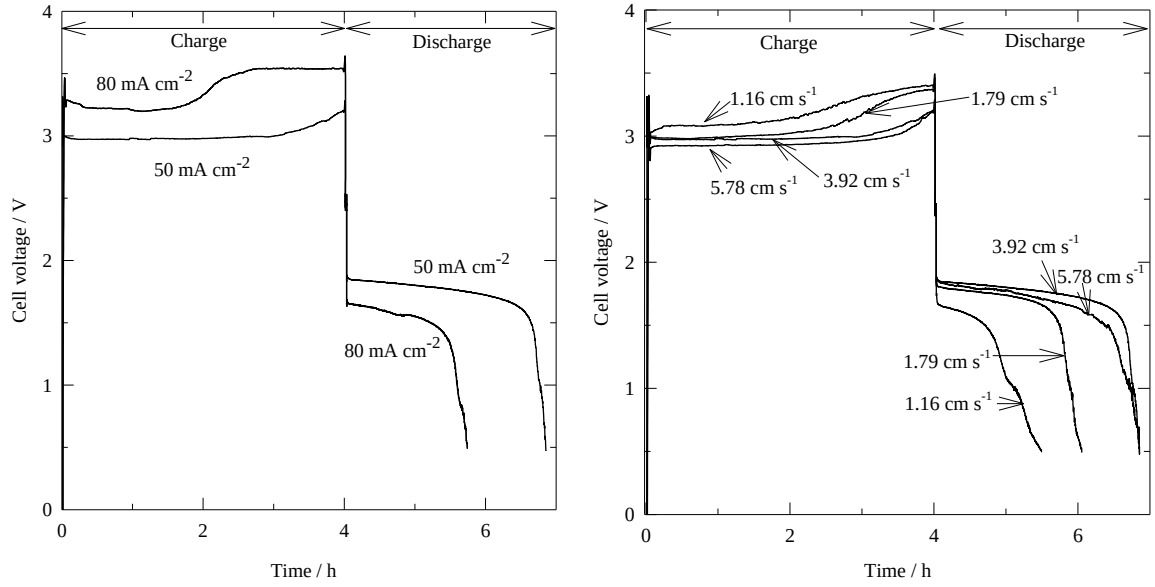

(a) (b)

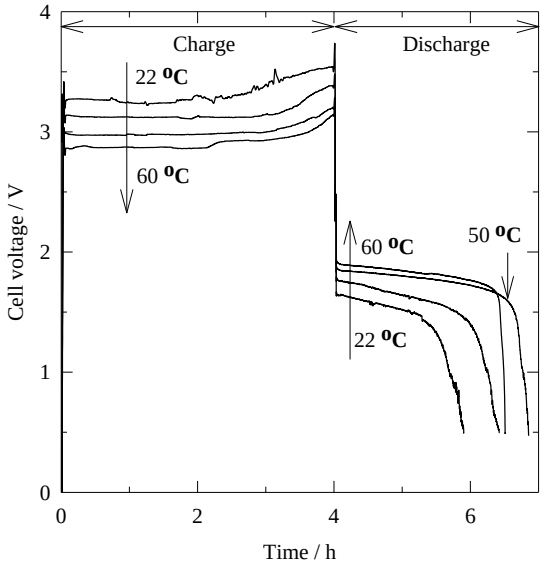

(c)

Figure 8.6. Effect of operating conditions on charge-discharge performance of a zinc-cerium redox flow battery: (a) current density, (b) mean linear electrolyte flow velocity and (c) temperature. Unless indicated, electrolyte compositions and operating conditions were the same as in Figure 8.3.

Figure 8.6c shows the effect of temperature on the charge-discharge performance of a zinc-cerium battery. Substantial improvement of both charge and voltage efficiencies were obtained as the temperature increased from 25 to 50 ^{o}C. The coulombic efficiency increased due to faster reaction kinetics, increased diffusion rate and reduced viscosity. Higher voltage efficiencies were due to the increased electrolyte conductivity and a decrease in the overpotential resulted in higher voltage efficiencies [13, 14].

8.5.2. *Effect of electrolyte compositions*

Electrolyte compositions have a large influence on the charge/discharge performance of a zinc-cerium battery. As shown in previous section, the zinc deposit in the negative electrolyte was still not completely stripped off while there was no more Ce(IV) ions to be reduced towards the end of the early cycles, cerium half-cell reaction was the limiting factor in all operating parameters. Therefore, it is crucial to optimize the composition of the positive electrolyte. Figure 8.7a and 8.7b show the cell voltage *vs.* time characteristic of a zinc-cerium battery under the effect of the concentrations of Ce(III) ions and methanesulfonic acid in the positive electrolyte, respectively. By increasing the Ce(III) ion concentration from 0.8 to 1.2 mol dm^{-3}, the voltage and coulombic efficiencies decreased as the solutions became viscous and milky. This is mainly due to the low Ce(III) solubility in 4 mol dm^{-3} methanesulfonic acid. Previous study reported that high concentration of Ce(III) ion could only be obtained at low methanesulfonic acid concentration [15]. On the contrary, higher Ce(IV) ion concentration can only be soluble in more concentrated methanesulfonic acid [15]. The solubility limit of both Ce(III) and Ce(IV) ions in 4.0 mol dm^{-3} methanesulfonic acid was *c.a.* 1.0 mol dm^{-3} at room temperature [15, 16].

Figures 8.7a and 8.7b show that the cell voltage increased after 2 hours charge with

oxygen evolution becoming the main reaction when the concentration of Ce(III) ions gradually falls. The data in Table 8.2 shows that at Ce(III) ion concentrations higher than 0.8 mol dm^{-3}, less Ce(IV) ion has been converted at the end of the charge cycle, which is consistent with previous results using platinum as the positive electrode [13]. Due to the lower conversion of Ce(III) ions, reduced coulombic efficiencies and discharge voltages were obtained. This characteristic was also observed at lower Ce(III) ion concentration, e.g. at 0.4 mol dm^{-3}.

Figure 8.7b shows that increasing the methanesulfonic acid concentration up to 4 mol dm^{-3} in the positive electrolyte can improve both voltage and coulombic efficiencies on the charge-discharge cycle of the zinc-cerium redox flow battery. At higher methanesulfonic acid concentration, there was a slight decrease in the cell voltage during charge while a slight increase on discharge. At 2 and 3 mol dm^{-3} methanesulfonic acid concentration, the positive electrolyte was highly viscous after battery charge. This suggest that high concentrations of Ce(IV) solution will be difficult to achieve in methanesulfonic acid concentration lower than 4 mol dm^{-3}. The discharge performances of such electrolytes were unfavorable and resulted in poor coulombic efficiencies. No battery discharge was observed at 2 mol dm^{-3} methanesulfonic acid in the positive electrolyte. Taking into account the battery performance and the solubility of Ce(IV) ions in low concentration of acid, the optimum positive electrolyte composition was 0.8 mol dm^{-3} Ce(III) methanesulfonate in 4 mol dm^{-3} methanesulfonic acid.

The solubility problem of zinc(II) methanesulfonate is less complicated. As summarized in Table 8.2, higher cell voltage during charge and lower discharge cell voltages were observed at 2 mol dm^{-3} Zn(II) as such concentration is approaching the solubility limit (2.16 mol dm^{-3}) in methanesulfonic acid [17]. At a range of zinc(II) methanesulfonate concentration from 0.5 to 1.5 mol dm^{-3}, there was no significant effect on both coulombic and voltages efficiencies. A higher Zn(II) ion concentration, e.g. 1.5 mol dm^{-3}, can be advantageous for a redox flow battery. For instance, it allows the battery to charge at high current densities without the mass transport limitation. Such a high concentration ensures that the Zn(II) ions maintain the same state of charge for longer period of time. During battery charge, one mole of zinc(II) methanesulfonate used in electrodeposition would lead to a formation of two mole methanesulfonic acid [18] as proton is transferred to the negative electrolyte to its positive counterpart, where methanesulfonate anions are complexed with the Ce^{4+} ion oxidized in the charge process. In order to facilitate zinc electrodeposition and avoid the hydrogen evolution side-reaction, higher Zn(II) ion concentration is preferable in the negative electrolyte.

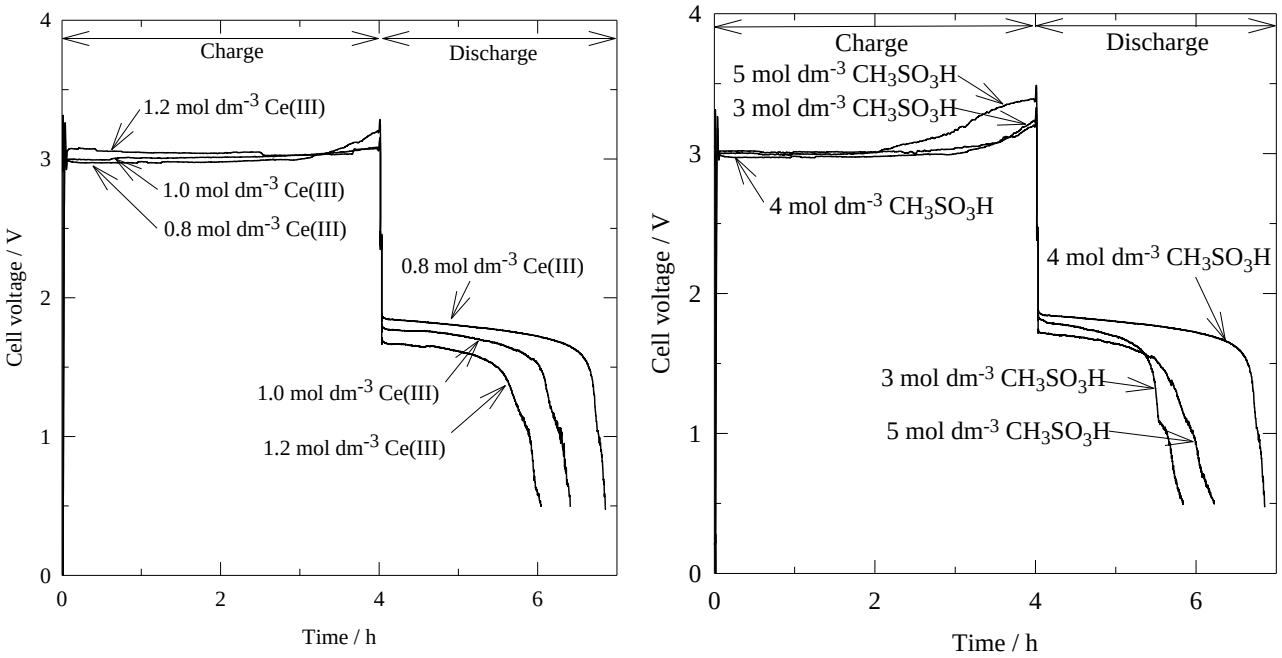

(a) (b)

Figure 8.7. Effect of positive electrolyte compositions on charge-discharge performance of a zinc-cerium redox flow battery: (a) cerium(III) concentration and (b) methanesulfonic acid concentration. Unless indicated, electrolyte compositions and operating conditions were the same as in Figure 8.3.

8.6. Life cycle

A number of charge-discharge experiments at the optimum operating conditions and the positive electrolyte compositions; 0.8 mol dm^{-3} cerium(III) methanesulfonate in 4.0 mol dm^{-3} methanesulfonic acid and the negative electrolyte was 1.5 mol dm^{-3} zinc(II) methanesulfonate in 1.0 mol dm^{-3} methanesulfonic acid and electrolyte compositions found in the previous sections were carried out on the zinc-cerium flow battery to investigate its life cycle. The charge-discharge characteristics at different state of charge were recorded by charging the zinc-cerium battery at 50 mA cm^{-2} for different lengths of time: 15 minutes (Figure 8.8a), 1 hour, 2 hours and 4 hours (Figure 8.8b). In a further experiment, the

battery was first charged at 50 mA cm^{-2} for 3 hours following 15 minutes charge/discharge cycles for approximately 14 hours (see Figure 8.8c). During battery charge and discharge, cut-off voltages were set at 3.4 V and 0.5 V, respectively. 3-dimensional platinised titanium mesh was used as the positive electrode, while the negative electrode was a carbon-polyvinylester composite.

The life cycle and system efficiencies of these experiments are summarized in Table 8.3. As shown in Figures 8.8a and 8.8b, the number of cycles that the battery was able to perform reasonably before no discharge could be obtained increases from 4 cycles in the 4 hour charge/discharge experiments (Figure 8.8b) to 57 cycles in the 15 minutes one (Figure 8.8a). Column 5 in Table 8.3 shows that the average coulombic efficiency of the zinc-cerium battery was below 100 % in all the experiments indicating that the products formed during battery charge did not return completely to their initial conditions and that a secondary reaction possibly took place. At longer charging times, more Ce(III) ions reacted and therefore the product, Ce(IV) ions seem to accumulate over time and not been reduced completely during discharge cycles. This caused the depletion of the electroactive species of Ce(III) and cycle numbers were hence diminished. In all experiments, the life of the battery was between 25 – 30 hours, except in Figure 8.8c where the cell was charged for 3 hours before 15 minutes charge/ discharge cycles.

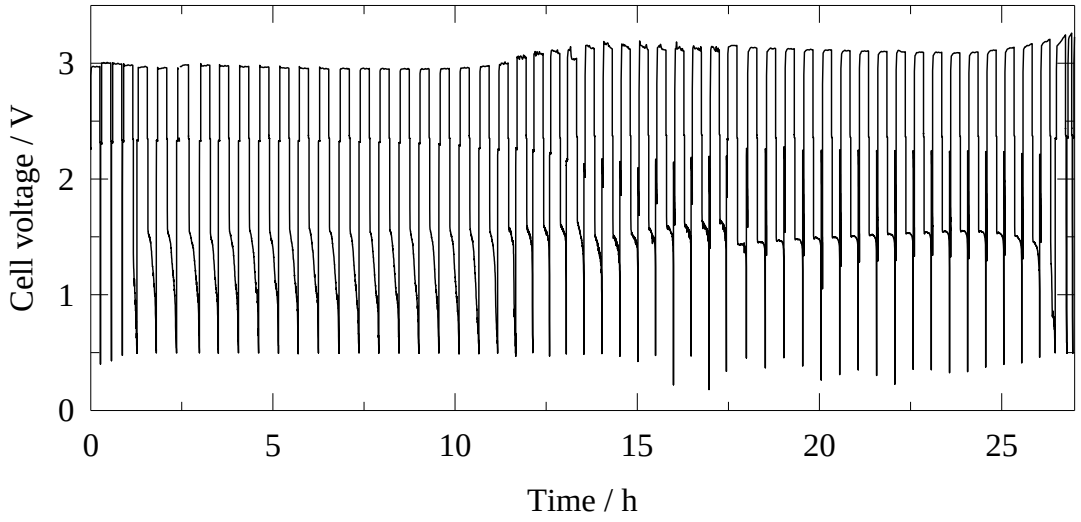

(a)

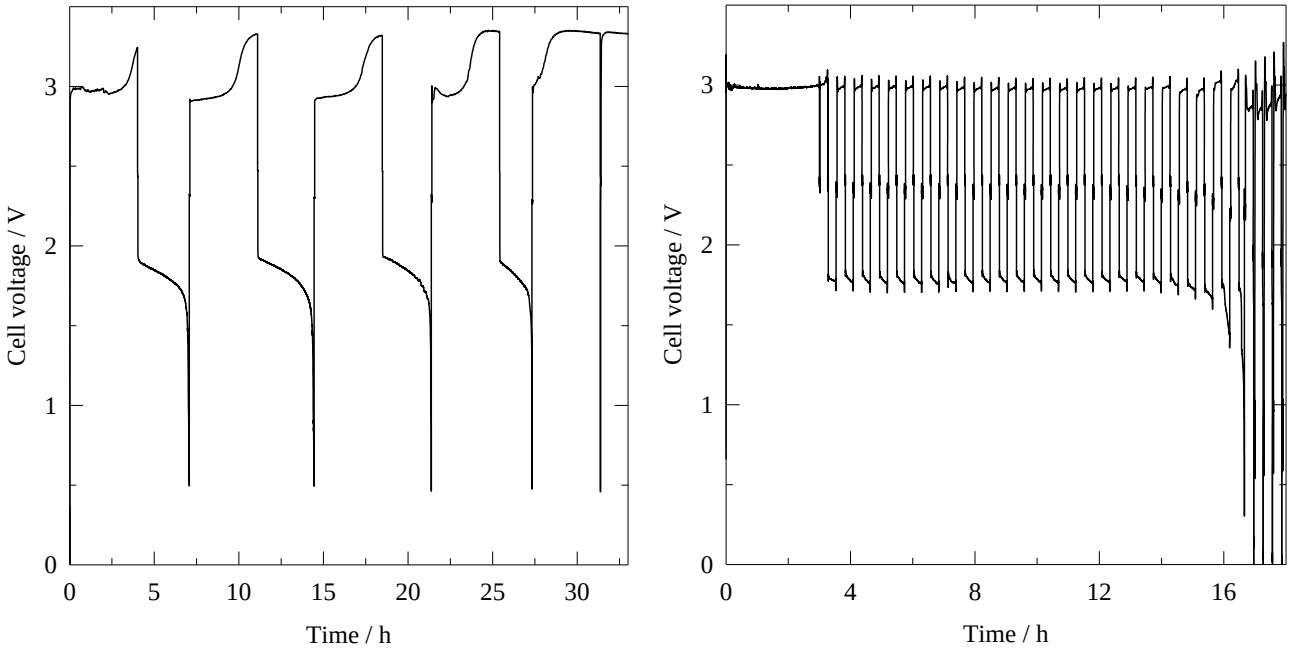

(b) (c)

Figure 8.8. Life cycle of a zinc-cerium battery charging at 50 mA cm^{-2} for different lengths of time: (a) 15 minutes, (b) 4 hours and (c) the experiment of first charging for 3 hours following 15 minutes charge/discharge cycles. Electrolyte compositions and operating conditions were the same as in Figure 8.3.

Due to the initial higher acid concentration in the positive compartment and the formation of acid in the negative electrode during battery charge, the negative electrolyte became more acidic after prolonged charge/discharge cycling, which led to a more inefficient zinc electrodeposition. For this reason, in all charge/discharge modes studied in this section, zinc half-reaction was also a limiting factor for long life-time cycle experiments. The acid concentration change and the diffusion of proton across the membrane were more significant towards the end of the four hour charge/discharge cycle.

More cycles at longer charge-discharge times can be easily achieved by increasing the ratio of electrolyte volume to electrode area. As shown in Figures 8.8a, the cell voltages during discharge dropped very quickly in the early cycles at the modes of 15 minutes. This is because the concentration of Ce(IV) ions generated was still too low for the battery to be able to discharge at 50 mA cm^{-2}. After a number of cycles, Ce(IV) ions accumulated and higher discharge cell voltages could be obtained. At later cycles, depletion of Ce(III) ion led to a sharp increase in charge cell voltages.

In order to achieve long life cycle and a relatively high discharge cell voltage, the battery was first charged at 50 mA cm^{-2} for three hours to obtain high concentrations of Ce(IV) ions. Following the three hours charge, a charge/discharge cycle regime of 15 minutes each was applied. This ensured less acid concentration change and depletion of Ce(III) ions. Figure 8.7c shows that for this experiment, 25 cycles at an average discharge voltage of *c.a.* 1.77 V were obtained with an average coulombic and energy efficiencies of 99.4 % and 59.3 %, respectively, higher than any of the other charge/discharge cycles regime tested.

8.7. Conclusions

1. A zinc-cerium redox flow battery with high surface area carbon felt or platinised titanium mesh electrodes was discharged at constant current density (5 – 50 mA cm^{-2}) or constant cell voltage (1.0 – 2.2 V).

2. Carbon felts positive electrodes were capable of discharge at 50 mA cm^{-2} with high coulombic (> 92%) and voltage (> 68 %) efficiencies.

3. Due to the poor electrical conductivity and the poor adherence of the carbon adhesive, used to attach the carbon felts, after a few cycles, a 3-dimensional platinized titanium mesh electrode was preferred as the positive electrode material in this work.

4. The highest energy efficiency was obtained at 50 ^{o}C with a mean linear electrolyte flow velocity of 7.8 cm s^{-1}, while the optimum composition for the positive electrolyte was 0.8 mol dm^{-3} cerium(III) methanesulfonate in 4.0 mol dm^{-3} methanesulfonic acid. In all cases, the positive cerium half-cell was the limiting reaction for battery discharge as the discharge reaction of zinc lasted longer than that of the cerium reaction in the early cycles.

5. Due to the initial higher acid concentration in the positive compartment and the formation of acid during charge at the negative electrolyte, this became more acidic after prolonged charge/discharge cycling, which led to more difficult electrodeposition of zinc.

6. In all charge/discharge modes at different charging times, the zinc half-cell reaction was the limiting factor for life cycle at longer times. This was because the negative electrolyte becoming more acidic due to the migration of proton from the positive electrolyte and the proton generation during zinc electrodeposition when the battery was tested for larger number of cycles.

8.8. References

1. V. Devadoss, C.A. Basha, K. Jayaraman, J. Ind. Eng. Chem. Res. 47 (2008) 4607-4616.
2. J.M. Friedrich, C. Ponce-de-León, G.W. Reade, F.C. Walsh, J. Electroanal. Chem. 561 (2004) 203-217.
3. A.P. Borole, C.Y. Hamilton, T.A. Vishnivetskaya, D. Leak, C. Andras, J. Morrell-Falvey, M. Keller, B. Davison, J. Power Sources 191 (2009) 520-527.
4. J. Gonza´lez-Garcıa, P. Bonete, E. Exposito, V. Montiel, A. Aldaz, R. Torregrosa-Macia, J. Mater. Chem. 9 (1999) 419-426.
5. R.L. Clarke, B.J. Dougherty, S. Harrison, P.J. Millington, S. Mohanta, US 2004/ 0202925 A1, (2004).
6. R.L. Clarke, B.J. Dougherty, S. Harrison, J.P. Millington, S. Mohanta, US 2006/0063065 A1, (2005).
7. C. Ponce de León, A. Frías-Ferrer, J. González-García, D.A. Szánto, F.C. Walsh, J. Power Sources 160 (2006) 716-732.
8. H.S. Lim, A.M. Lackner, R.C. Knechtli, J. Electrochem. Soc. 124 (1977) 1154-1157.
9. D. Pletcher, R. Wills, J. Power Sources 149 (2005) 96-102.
10. J. Jorné, J.T. Kim, D. Kralik, J. Appl. Electrochem. 9 (1979) 573-579.
11. Y. Liu, X. Xia, H. Liu, J. Power Sources 130 (2004) 299-305.
12. P.K. Leung, C. Ponce de León, C.T.J. Low, F.C. Walsh, Electrochimica Acta (2011) Accepted.
13. T. Raju, C.A. Basha, Chem. Eng. J. 114 (2005) 55-65.
14. B. Fang, S. Iwasa, Y. Wei, T. Arai, M. Kumagai, Electrochim. Acta 47 (2002) 3971-3976.
15. R.P. Kreh, R.M. Spotnitz, J.T. Lundquist, J. Org. Chem. *54* (1989) 1526-1531.
16. T. Raju, C.A. Basha, J. Ind. Eng. Chem. Res. 47 (2008) 8947-8952.
17. M.D. Gernon, M. Wu, T. Buszta, P. Janney, Green Chem. 1 (1999) 127-140.
18. A. Hazza, D. Pletcher, R. Wills, J. Phys. Chem. Chem. Phys. 6 (2004) 1773 - 1778.

Chapter 9

Preliminary study of an undivided zinc-cerium redox flow battery

Chapter 9 Preliminary study of an undivided zinc-cerium RFB

Introduction

In the previous chapter, a divided zinc-cerium redox flow battery has been characterized at different operating parameters and the life cycle at different state of charge has been tested. In all the long life-cycle experiments, zinc half-cell reaction has been the limiting factor for discharge due to the high acid concentration in the negative compartment caused by the diffusion of protons across the membrane. The use of such proton exchange membranes also increases the cost, design complexity and maintenance requirements. Therefore, an investigation of a divided zinc-cerium redox flow battery has been carried out in the previous chapter in order to propose a simple and reliable membraneless system.

Prior to this work for a soluble lead acid flow battery, the first membraneless system was introduced by Hazza *et al.* [1] in 2004. Since then, a few more undivided systems, including, zinc-nickel [2, 3], copper-lead dioxide [4] and cadmium-chloranil [5], have been developed. However, these flow battery systems have shortcomings in either a low operating cell voltage or a limited storage capacity associated with the positive electrode materials, such as lead dioxide and nickel hydroxide [6]. In order to enhance the prospect of zinc-cerium system further, the flow battery was operated at room temperature using less expensive carbon felt as the positive electrode and carbon polyvinyl-ester electrode as the negative electrode. The charge-discharge performance at different operation conditions is investigated and future research direction is suggested.

9.1. Electrolyte formulations

Aiming to determine the electrolyte compositions to be used in the flow battery

experiments, the zinc half-cell reaction was studied first. The negative electrode potential during the deposition and stripping of zinc using different concentrations of reactants and methanesulfonic acid was monitored. High concentration of zinc at 1.5 mol dm^{-3} in 0.5 mol dm^{-3} methanesulfonic acid, was used avoid mass transport limitation. At such electrolyte, a high coulombic efficiency of 91.4 % was observed (curve a), which was consistent with our previous results reported in chapter 4. Despite this, coulombic efficiency decreased to 85.3 % when 0.2 mol dm^{-3} cerium(III) ions were added in the electrolyte (curve b). This can be due to the competition of Ce(III) ion on the electrode surface, which led to an increased overpotential. The curves in Figure 9.1 indicates that the zinc half-cell potential shifted towards more negative and positive values during zinc electrodeposition and stripping, respectively, when cerium was added. Additionally, the higher concentration of Ce(IV) ion required for a zinc-cerium battery can be made soluble only at high methanesulfonic acid concentration. Increasing methanesulfonic acid concentration to 3 mol dm^{-3}, could decrease the coulombic efficiency of zinc deposition/ stripping process to approximately 61.4 % although a reduced potential drop due to improved conductivity was observed (curve c). Therefore, the use of higher concentration of cerium species is further limited unless suitable supporting electrolytes, such as Lewis acid and trifluromethanesulfonic acid, or mixture of these are used. In the following flow battery experiments in this chapter, an electrolyte of 1.5 mol dm^{-3} Zn(II) and 0.2 mol dm^{-3} Ce(III) in 0.5 mol dm^{-3} methanesulfonic acid was, therefore, used.

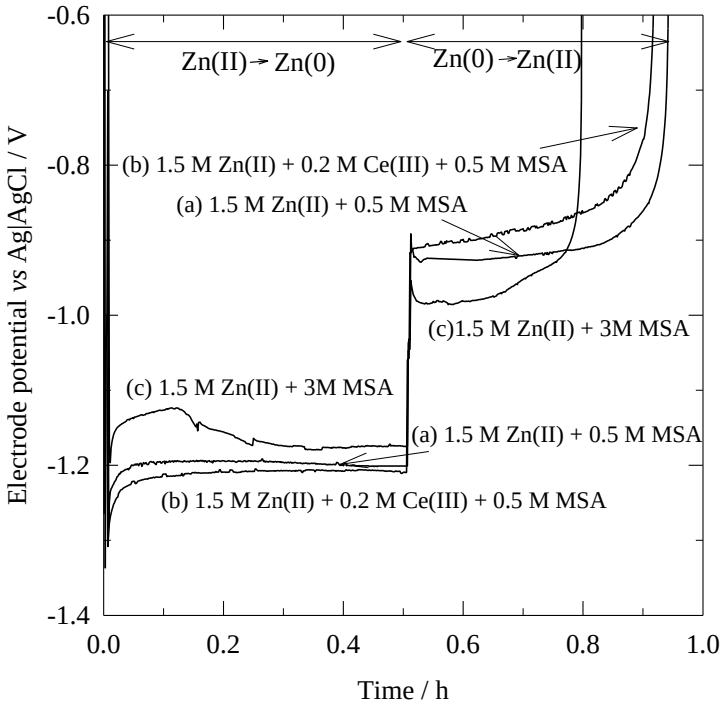

Figure 9.1. The effect of electrolyte composition on zinc electrodeposition and stripping at 20 mA cm^{-2}. The electrolyte was maintained at 22.5 ^{o}C and circulated at 3.9 cm s^{-1}.

9.2. Charge-discharge characteristic of an undivided zinc-cerium RFB

The cell voltage and the half-cell potentials *vs.* time characteristic of the initial ten charge-discharge cycles of an undivided zinc-cerium redox flow battery is shown in Figure 9.2. These were obtained by charging and discharging the battery at 32 mA (20 mA cm^{-2}) for 30 minutes. The experimental open circuit cell voltage was 2.34 V, which lies in the range of the predicted value. In general, the curve shows a relatively flat charge voltage at approximately 2.5 V. At the start of the discharge cycle, the cell voltage decreased gradually from 2.1 V to 2.0 V towards a sharp voltage drop at the end of the cycle.

As can be seen in the half-cell potentials shown in Figure 9.2, the change in cell voltage during charge-discharge was mainly attributed to the polarization of the zinc negative electrode, which underwent a two-phase transformation. The half-cell potentials between charge and discharge of zinc and cerium reactions were approximately 300 mV

and less than 15 mV, respectively. Hence, the redox reaction Ce(III)/Ce(IV) was highly reversible when carbon felts was used, especially at such low concentrations of cerium and methanesulfonic acid. The cell voltage between the charge and discharge cycles is similar to the vanadium-cerium redox flow battery reported by Fang *et al.* [7], in which carbon felt was also used as the positive electrode material in 1 mol dm^{-3} sulfuric acid. Despite this, inconsistent findings of electrochemistry of Ce(III)/Ce(IV) at carbon materials have been reported [7-10]. These studies suggest that the electrochemical behaviour of cerium redox reaction at carbon felt electrode can be very different for various forms of carbon materials.

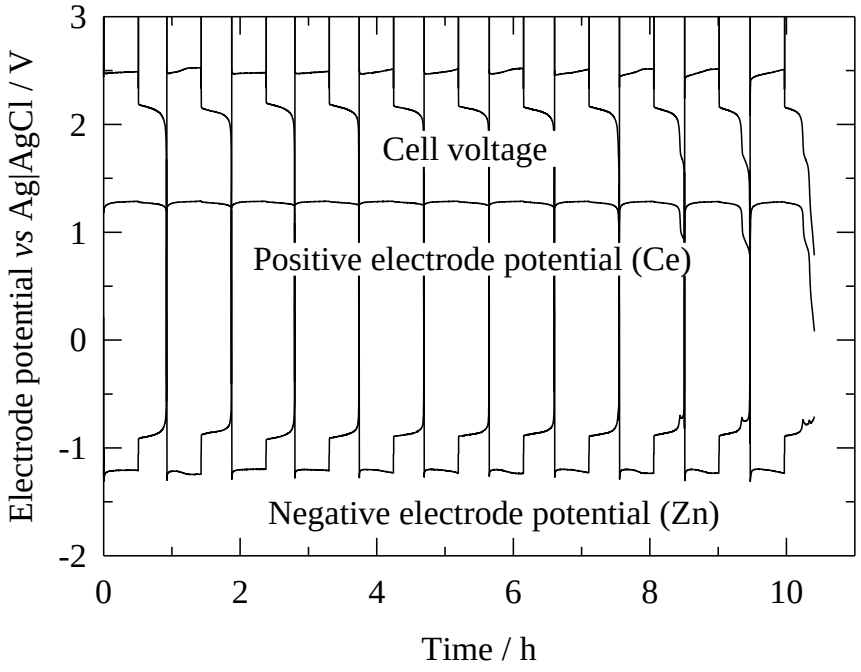

Figure 9.2. The voltage *vs.* time characteristic of an undivided zinc-cerium redox flow battery during the initial 10 charge-discharge cycles; at 20 mA cm^{-2}, 22.5 ^{o}C and 3.9 cm s^{-1} electrolyte mean linear flow velocity. Electrolyte: 1.5 mol dm^{-3} $Zn(CH_3SO_3)_2$ and 0.2 mol dm^{-3} $Ce(CH_3SO_3)_3$ in 0.5 mol dm^{-3} CH_3SO_3H.

During discharge, the cut-off cell voltage was set at 0.8 V. At the end of each discharge cycle, zinc dissolved back to the electrolyte as Zn(II) species and carbon polyvinyl ester substrate was exposed to the electrolyte. This resulted in a drastic move of

zinc-half cell potential towards a positive value and hence a sharp drop in cell voltage. Therefore, zinc half-cell reaction seems to be the limiting reaction for discharge during the cycling. The coulombic, voltage and energy efficiencies of the undivided zinc-cerium battery during charge-discharge cycles are presented in Figure 9.3. The energy and coulombic efficiencies increased slightly from 68 to 76 % and from 76 to 90 % respectively, with the number of cycles, and a small drop was observed at the tenth cycle. The voltage efficiency remained stable at 88 within the ten cycles as shown in Figure 9.3.

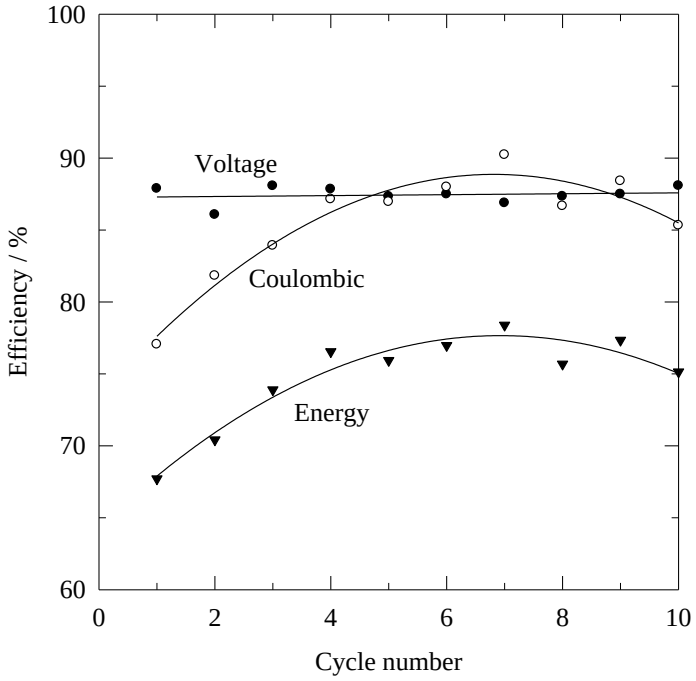

Figure 9.3. System efficiencies of an undivided zinc-cerium redox flow battery during the initial 10 charge-discharge cycles. Electrolyte compositions and operating conditions as in Figure 9.2.

The increase of the coulombic efficiency during the first few cycles from 76 % to nearly 90 %, indicates that the zinc half-cell reaction was less efficient in the early cycles. With further increase in cycle number, a deterioration in both, zinc and cerium half cell reactions was observed, which resulted in a slight decline in coulombic efficiency after the 7^{th} charge-discharge cycle. As shown in Figure 9.2, some fluctuations of the zinc half-cell

potential were observed at the end of each discharge cycle due to the residual zinc remained on the substrate surface. At this point, carbon polyvinyl-ester substrate was exposed to the electrolyte and zinc half-cell potential had the tendency to shift towards positive values and cause a significant drop in cell voltage. The residual zinc could also lead to fall-off of zinc deposit as powdery zinc coating is easily removed from the electrode by aggressive flow after subsequent cycles. Electrolytic additives may be needed to prevent such 'shape-change' effect and to extend the cycle life of the zinc half-cell reaction. Considering the cerium half-cell, the possibilities of the deterioration of this reaction are still unknown and can be due to various factors, such as electrolyte compositions and electrode condition. Despite this, the highly reversible nature and stable electrode potential of cerium half-cell reaction suggests that the change in electrode condition should be insignificant. Therefore, further investigation is necessary to define the possible problems in order to seek solutions for any remedial treatment in large scale operation.

9.3. Effect of current densities

Figure 9.4a shows the negative and positive electrode potentials together with the cell voltage at different discharge current densities in the range of 0 and 80 mA cm^{-2}. The polarization of cerium half-cell remained almost unchanged and increased negligibly with the current density. This is possibly due to the very large surface area available in the three pieces of compressed carbon felts. Therefore, the local current density was very small and resulted in a charge-transfer reaction in the low overpotential region. In contrast to the cerium positive reaction, cell voltage was mainly attributed to the polarization of the zinc half-cell reaction. At 80 mA cm^{-2}, polarization of up to 600 mV was recorded. In this case, this value was approximately similar to the total cell voltage drop.

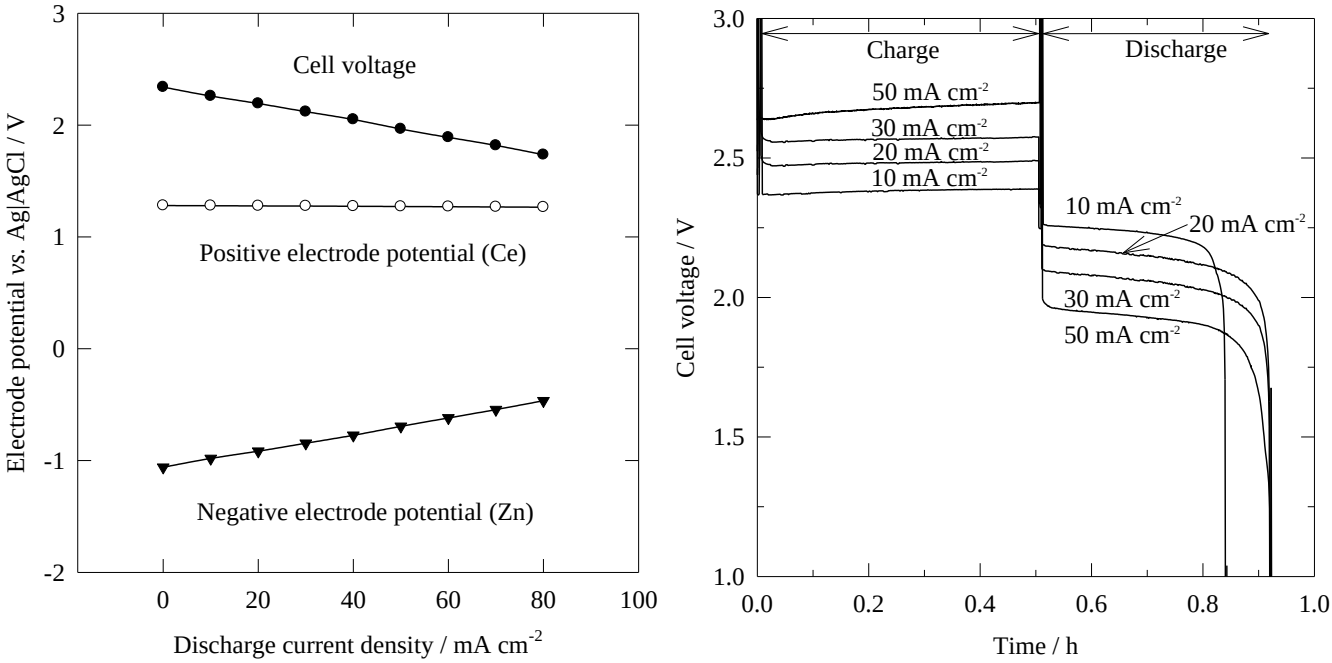

(a) (b)

Figure 9.4. Effect of current density on (a) the half-cell potentials during discharge and (b) the charge-discharge performance of an undivided zinc-cerium redox flow battery. Operating condition and electrolyte compositions as in Figure 9.2.

Although overpotential and ohmic losses were less significant at lower current density, shorter discharge time was observed in the charge-discharge cycle at 10 mA cm^{-2} (Figure 9.4b). As reported in the chapter 4, shorter time for zinc stripping was also observed at lower current density. Since zinc is electrodeposited on the substrate surface, mass transport limitation is not a limiting factor during discharge. Hence, lower coulombic efficiencies during low current density charge-discharge cycle can be attributed to the self-discharge of zinc and the significance of zinc nucleation on the carbon substrate surface. When current densities were in the range between 20 and 50 mA cm^{-2}, a similar discharge time was obtained and the coulombic efficiencies were approximately 80 %. Although local current densities at the zinc electrode can be reduced with the use of high surface area three dimensional electrodes, such as reticulated vitreous carbon and carbon felt, local current densities needs to be maintained at sufficiently high values to ensure a

high coulombic efficiency. Therefore, the ratio between the positive and negative electrode areas could be further investigated in the future work.

9.4. Effect of flow conditions

In an undivided zinc-cerium redox flow battery, the common electrolyte for the negative and positive electrodes was circulated through the cell and reservoir loop by a peristaltic pump. The effect of two mean linear flow velocities on the charge-discharge cycle at 20 mA cm^{-2} is shown in Figure 9.5a: 0.64 cm s^{-1} and 3.9 cm s^{-1}. Slightly higher coulombic and voltage efficiencies were observed at increased flow of 3.9 cm s^{-1}, these can be explained by the improved supply of the reactants. Since the concentration of Ce(III) ion was prepared at 0.2 mol dm^{-3}, increased mass transport of the cerium ions can be effective in reducing the side reactions, such as the gas evolution, hence lower charge and higher discharge cell voltages were obtained.

As shown in Figure 9.5b, the discharge cell voltages were investigated at a wide range of mean linear flow velocities between 0.64 and 7 cm s^{-1} under different constant current densities of 20, 50 and 80 mA cm^{-2}. At higher discharge current densities, cell voltages became lower and are comparable to the results obtained in the current density section (Section 9.3). In general, the effect of mean linear flow velocity was not very significant on the discharge cell voltage, especially at mean linear flow velocities higher than 2 cm s^{-1}. This could be due to the very large surface area of the carbon felt electrode, hence the mass transport of cerium ion towards the electrode surface becomes less crucial. Similar effects were also observed in the divided zinc-cerium system (Chapter 7). Despite this, a sharp discharge cell voltage drop was observed at 80 mA cm^{-2} while circulating the electrolyte at low velocity. At such a fast reaction, faster electrolyte flow velocity is necessary to offset the rapid Ce(IV) depletion at the electrode surface.

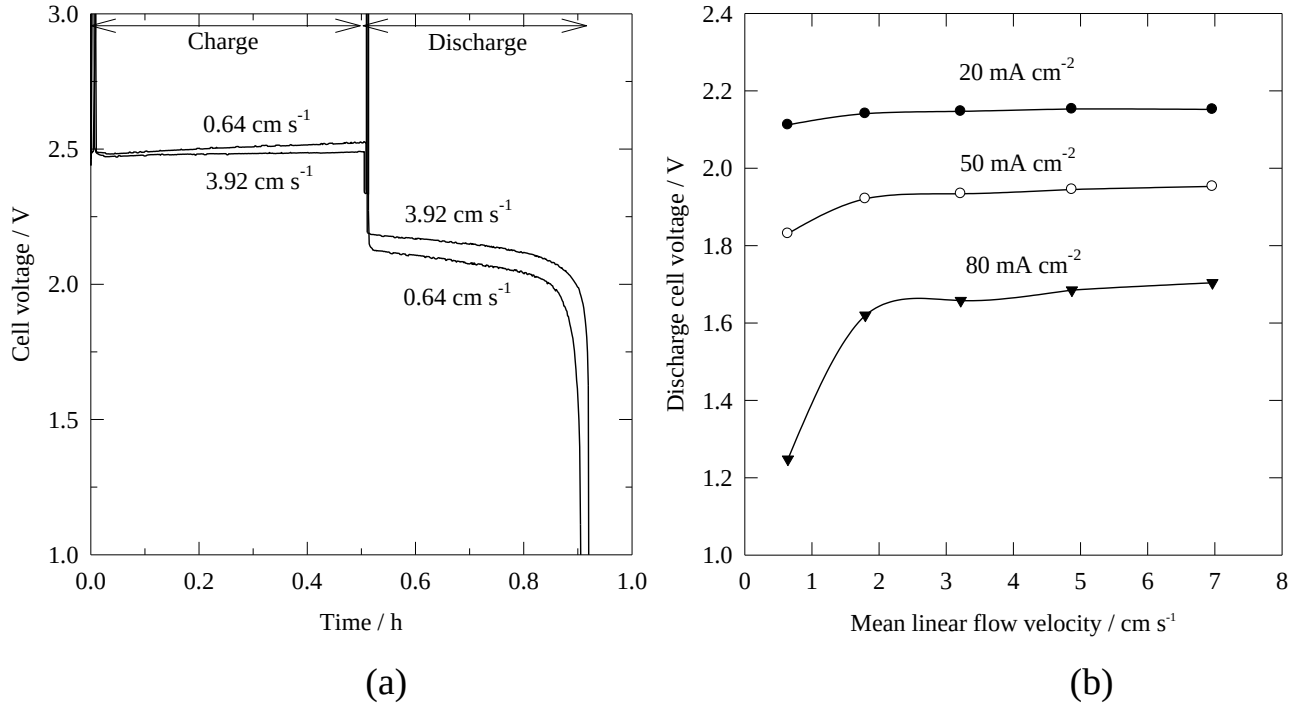

Figure 9.5. Effect of flow condition on (a) charge-discharge performance and (b) cell voltages of an undivided zinc-cerium redox flow battery. Operating condition and electrolyte compositions as in Figure 9.2.

9.5. Effect of operating temperature

Figure 9.6 shows the effect of temperature on the battery charge-discharge cycle. Although higher temperature improves conductivity and reduces polarization, tremendous decrease in coulombic efficiency has been seen in this study as temperature increases. Unlike the divided flow battery as discussed in chapter 7, both coulombic and voltage efficiencies optimized at operating temperature of 50 ^{o}C. The low coulombic efficiencies in this case are attributed to the poor conversion of Ce(IV) ions as an insignificant yellow coloration was observed after charge. Since the Ce(III) ion concentration was only 0.2 mol dm^{-3} and the diffusion coefficient of water molecule [11] is higher than that of cerium ions [10], oxygen evolution seems to become dominant at higher temperature. Based on the voltammetric study in chapter 6, the low methanesulfonic acid concentration is favorable

for oxygen evolution. Therefore, the future work should focus on the use of higher cerium ion concentration by solving the solubility issues to allow operation at wider temperature range and to enable efficient zinc electrodeposition at higher acidic concentration.

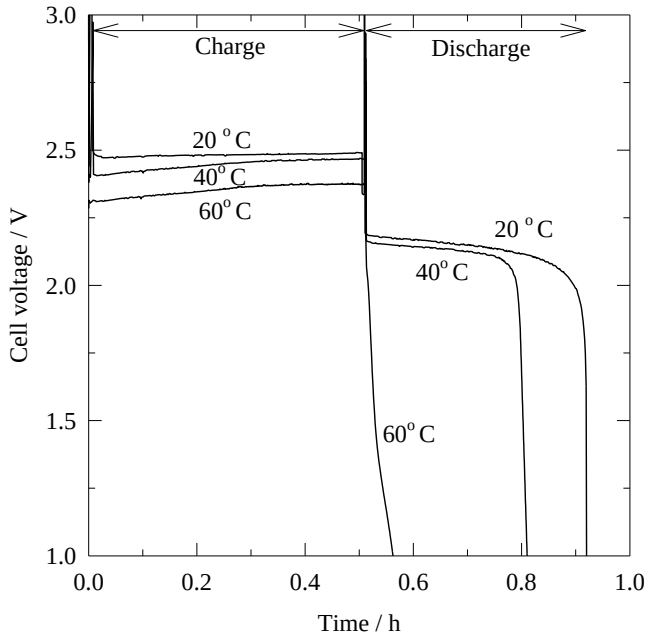

Figure 9.6. Effect of temperatures on charge-discharge performance of an undivided zinc-cerium redox flow battery. Operating condition and electrolyte compositions as in Figure 9.2.

9.6. Self-discharge

Since both zinc and cerium are electroactive species mixed in a single electrolyte, self-discharge at open circuit could be a problem. This was evaluated by leaving the cell at open circuit and monitoring the cell voltage and the half-cell potentials after charging at 20 mA cm^{-2} for 30 minutes. As shown in Figure 9.7, a slightly decrease in the open circuit cell voltage and zinc half-cell potentials was observed after four hours followed by a sharp decrease at around seven hours. The positive shift of the zinc half-potential from initially *c.a.* – 1.03 to *c.a.* 0.13 V *vs.* Ag|AgCl indicates that most of the zinc deposit was dissolved back into the electrolyte. In this work, the self-discharge was comparable to those of the conventional systems, such as all-vanadium redox flow battery. For instance, the capacity

of an all-vanadium redox flow battery was reported to last for only 11 hours after being charged for 1.6 A h [12].

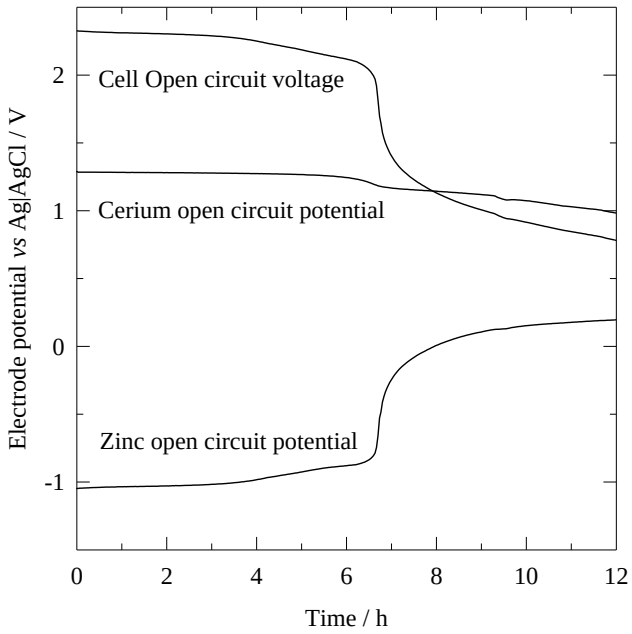

Figure 9.7. Open circuit potential *vs.* time characteristics of an undivided zinc-cerium redox flow battery after charging at 20 mA cm^{-2} for 30 minutes. Operating condition and electrolyte compositions as in Figure 9.2.

Although self-discharge of all-vanadium redox flow battery is mainly attributed to the crossover of vanadium ions across the membrane, vanadium ions are susceptible to be oxidized, therefore nitrogen gas is often purged into the electrolyte during the operation [13]. Due to the electropositive nature of the cerium redox reactions and the experimental observations, Ce(III) and Ce(IV) ions are less likely to be oxidized or reduced by dissolved oxygen, respectively [7], compared to their vanadium counterparts [7]. Moreover, as zinc is deposited on the electrode surface, self-discharge of zinc is not an issue while discharging the battery. In the short term, zinc corrosion can be effectively inhibited with corrosion inhibitors, such as cetyltrimethyl ammonium bromide and butyltriphenyl phosponium chloride [14]. If the battery needs to be discharged after being charged for a

long period of time, the electrolyte can be pumped out from the cell to prevent the reactions of metallic zinc with protons or with Ce(IV) ions. In terms of storing energy over a long term, an undivided zinc-cerium redox flow battery could have some attractive advantages over the all-vanadium redox flow battery.

9.7. Conclusions

An undivided zinc-cerium redox flow battery is proposed for the first time. This system features several advantages over conventional redox flow battery, such as the use of a single electrolyte, simple cell design, high open-circuit cell voltage (2.34 V) and the capability to operate at room temperature. At a current density of 20 mA cm^{-2}, an average coulombic and energy efficiencies up to 90 and 76 %, respectively can be obtained. The change in half-cell cerium potential between charge and discharge cycles was very small (*c.a.* < 50 mV) over a wide range of current densities (0 — 80 mA cm^{-2}) suggesting that cerium redox reaction was highly reversible at a high surface area carbon felt electrode. Despite these, oxygen evolution was found to become dominant at higher temperature; this suggests that higher cerium ions concentration in the electrolyte is important. Since a relatively low concentration of 0.2 mol dm^{-3} Ce(III) was used to avoid hydrogen evolution at the zinc negative electrode in this work, the energy density of this system is currently *c.a.* 11 W h dm^{-3} compared to 20 – 35 W h dm^{-3} of an all-vanadium redox flow battery [15]. However, Paulenova *et al.* reported that up to 0.7 mol dm^{-3} Ce(IV) can be dissolved at low sulfuric acid conccentration. Hence, further investigation should focus on the use of mixed acid electrolyte, such as with sulphuric acid and trifluromethanesulfonic acid, for the zinc-cerium redox flow battery.

9.8. References

1. A. Hazza, D. Pletcher, R. Wills, J. Phys. Chem. Chem. Phys. 6 (2004) 1773 - 1778.
2. J. Cheng, L. Zhang, Y.S. Yang, Y.H. Wen, G.P. Cao, X.D. Wang, Electrochem. Comm. 9 (2007) 2639-2642.
3. Y.H. Wen, J. Cheng, S.Q. Ning, Y.S. Yang, J. Power Sources 188 (2009) 301-307.
4. J.Q. Pan, Y.Z. Sun, J. Cheng, Y.H. Wen, Y.S. Yang, P.Y. Wan, Electrochem. Comm. 10 (2008) 1226-1229.
5. Y. Xu, Y.H. Wen, J. Cheng, G.P. Cao, Y.S. Yang, Electrochem. Comm. 11 (2009) 1422-1424.
6. J. Pan, L. Ji, Y. Sun, P. Wan, J. Cheng, Y. Yang, M. Fan, Electrochemistry Communications 11 (2009) 2191-2194.
7. B. Fang, S. Iwasa, Y. Wei, T. Arai, M. Kumagai, Electrochim. Acta 47 (2002) 3971-3976.
8. D. Pletcher, E. Valdes, Electrochimica Acta 33 (1988) 509-515.
9. A. Paulenova, S.E. Creager, J.D. Navratil, Y. Wei, J. Power Sources 109 (2002) 431-438.
10. P.K. Leung, C. Ponce-de-Leon, C.T.J. Low, F.C. Walsh, Electrochimica Acta 56 (2011) 2145-2153.
11. A.A. Shah, M.J. Watt-Smith, F.C. Walsh, Electrochimica Acta 53 (2008) 8087-8100.
12. X.L. Luo, Z.Z. Lu, J.Y. Xi, Z.H. Wu, W.T. Zhu, L.Q. Chen, X.P. Qiu, J. Phys. Chem. B 109 (2005) 20310-20314.
13. S. Kim, J. Yan, B. Schwenzer, J. Zhang, L. Li, J. Liu, Z. Yang, M.A. Hickner, Electrochemistry Communications 12 (2010) 1650-1653
14. P.K. Leung, C. Ponce de León, F.C. Walsh, In preparation for Corrosion Science

(2011).

15. M. Skyllas-Kazacos, J. Power Sources 124 (2003) 299-302.

Chapter 10

Summary and future work

Chapter 10 Summary and future work

10.1. Summary

In this work, the development of the divided and undivided zinc-cerium redox flow batteries from their fundamental chemistry in aqueous methanesulfonic acid to laboratory flow cells has been described. This comprehensive investigation has focused on the selection of electrode material, evaluation of zinc corrosion, characterization of the redox flow battery and the cycling performance of an unit zinc-cerium cell. Experimental variables included: the metal ion concentration, the acid concentration, the controlled flow rate, electrolyte temperature and the applied current density.

During battery charge, Zn(II) was reduced and deposited onto a carbon polyvinyl-ester composite substrate at the negative electrode and the Ce(III) ion was oxidized to Ce(IV) at a positive platinized titanium electrode. In aqueous methanesulfonic acid, cyclic voltammetry suggested that hydrogen evolution was a highly competitive reaction with zinc electrodeposition. Tests on the zinc negative electrode in a parallel plate flow cell at 50 mA cm^{-2} and 50 ^{o}C for 4 hours showed that the coulombic efficiency was as high as 91 % at 1 mol dm^{-3} methanesulfonic acid and decreased to 57 % at 3 mol dm^{-3} methanesulfonic acid. The increase in Zn(II) ion concentration can facilitate the electrodeposition process as indicated by the improved coulombic efficiency but does not benefit the energy efficiency of the zinc half-cell reaction.

At increased Zn(II) ion concentration, a lower charge voltage was observed as would be predicted by the Nernst equation. Since the oxidation of zinc back to Zn(II) species becomes more difficult at higher Zn(II) ion concentration in the vicinity of the electrode

surface, lower discharge voltages were obtained. However, higher Zn(II) ion concentration is still advantageous for redox flow battery as it not only facilitates the deposition process, but also allows the battery to charge at high current densities without mass transport limitations and ensures enough Zn(II) ions are available at all states of charge. The optimum electrolyte compositions were experienced at high zinc(II) methanesulfonate concentration of 1.5 mol dm^{-3} and at low methanesulfonic acid concentration of 1 mol dm^{-3} in the negative electrolyte.

In the presence and in the absence of electrolytic additives including: tetrabutylammonium hydroxide, potassium sodium tartarate and indium oxide, no dendrite formation was observed in the zinc electrodeposits at 50 mA cm^{-2} and at 60 ^{o}C over 4 hours. This suggested that electrodeposition of zinc in aqueous methanesulfonic acid is promising for zinc-based redox flow battery as dendritic growth has been a major problem in the zinc-halogen systems, resulting in short circuiting and hence a reduced life cycle. The low deposition overpotential on addition of 2×10^{-3} mol dm^{-3} potassium sodium tartarate and indium oxide produced irregular, rough layer-like and boulder-shaped granular microstructures, respectively, giving an appearance of a relatively rough surface. Among the three electrolytic additives tested, only indium oxide was considered suitable to be used in the redox flow battery as the energy efficiency of the zinc half-cell reaction improved significantly from 62 % in the absence of the additive to 73 %. Poor performance or an insignificant effect was observed with the other two electrolytic additives.

Since zinc is an active (anodic) material, zinc corrosion and cathodic evolution of hydrogen have a high tendency to take place at open circuit in acidic medium. Zinc

corrosion was characterized in a 100 cm^3 electrolyte containing 1 mol dm^{-3} methanesulfonic acid by measuring the zinc weight loss and hydrogen evolution at 22 ^oC for 10 hours. These conditions were similar to the operating conditions tested in the flow battery experiment. After 10 hours of immersion, the total zinc weight loss and hydrogen evolution were 2.4 g and 789 cm^3, respectively. The rate of zinc weight loss showed the same trend with that of the hydrogen evolution, as zinc corrosion rate increased initially and leveled off after the sixth hour. The variation of zinc corrosion rate against time was highly dependent on the surface condition. With an active layer of zinc oxide, zinc corrosion rate increased significantly and followed a decline once the proton concentration reached *c.a.* 0.5 mol dm^{-3} in the electrolyte. Zinc corrosion, measured in terms of weight loss and hydrogen evolution, increased significantly at lower zinc(II) ion concentration, higher methanesulfonic acid concentration and at elevated temperature.

In order to reduce the corrosion rate and maintain the discharge capacity for a period of time after battery charge, corrosion inhibitors, including cetyltrimethylammonium bromide (CTAB), butyltriphenyl phosphonium chloride, indium ions (In^{3+}) and lead ion (Pb^{2+}) were incorporated into the electrolyte. Due to the strong adsorption and the blocking effect of CTAB and butyltriphenyl phosphonium compounds on the zinc surface, zinc corrosion in 1 mol dm^{-3} methanesulfonic acid was inhibited effectively over the 10 hour immersion at 22 ^oC. With the addition of indium and lead ions, zinc corrosion was delayed for nearly one hour and approximately three hours, respectively, due to the formation of the less chemically active metallic layers reduced on the top of the corroding zinc surface. Despite this, zinc corrosion cannot be inhibited with those inorganic inhibitors in the long term as such metallic layers formed did not completely cover on the zinc surface. Once the bare zinc metal was in contact with the electrolyte, zinc corroded preferentially instead of

such metallic coatings through the pores and a fast corrosion resulted. The inhibitive efficiencies of lead and indium ions were less than 6.2 % after immersion for 10 hours.

The electrochemistry of the positive Ce(III)/Ce(IV) redox couple was also studied in methanesulfonic acid at a platinum electrode. The cyclic voltammetry experiments indicated that the diffusion coefficient of Ce(III) ions was 0.5 x 10^{-6} cm^2 s^{-1} and that the electrochemical kinetics for the oxidation of Ce(III) and the reduction of Ce(IV) was slow. Although a low concentration of cerium (III) methanesulfonate leads to a more reversible redox reaction, such a low concentration of Ce(III) ions would not be practical for a redox flow battery. The use of a low concentration of methanesulfonic acid also limits the solubility of Ce(IV) in the solution, hence the energy density available in a flow battery will be restricted. As a compromise and in order to maximize the solubility of both Ce(III) and Ce(IV) ions, a positive electrolyte composition of 0.8 mol dm^{-3} cerium (III) methanesulfonate in 4.0 mol dm^{-3} methanesulfonic acid was suggested for the redox flow battery application.

In an electrolyte containing a higher concentration of methanesulfonic acid and cerium(III) methanesulfonate, the ratio of cathodic to anodic peak current density was closer to one. By increasing the acid concentration from 2 to 5 mol dm^{-3}, the degree of oxygen evolution decreased by up to 50 %. The oxidation of Ce(III) and reduction of Ce(IV) were also investigated during a constant current batch electrolysis in a parallel plate zinc-cerium redox flow cell; with a 3-dimensional platinised titanium mesh electrode, the current efficiencies over 4.5 hour of the process Ce(III) to Ce(IV) and 3.3 hour electrolysis of the reverse reaction Ce(IV) to Ce(III) were 94.0 % and 97.6 %, respectively. With a

2-dimensional planar platinised titanium electrode, the redox reactions of Ce(III)/Ce(IV) were under mass-transport rate control, while reaction rates at the 3-dimensional mesh electrode appear to be charge-transferred controlled but became mass-transport controlled after 2.5 – 3 h of electrolysis when the concentrations of Ce(III) and Ce(IV) ions were lower.

Due to the evolution of hydrogen during the reduction of Ce(IV) using a 2-dimensional planar electrode, negative cell voltages were obtained which resulted in no energy released from the battery during discharge. The cell potential value when the cell was fitted with the 3-dimensional platinised titanium mesh electrode was positive (1.8 V) and provided 0.35 W h g^{-1} specific energy output during discharge at 50 mA cm^{-2}. Therefore, a 3-dimensional platinised titanium mesh positive electrode was found to be crucial to discharge a zinc-cerium redox flow battery at 50 mA cm^{-2} and 50 ^{o}C in the optimized positive electrolyte containing 0.8 mol dm^{-3} cerium (III) methanesulfonate in 4 mol dm^{-3} methanesulfonic acid.

Based on the optimum electrolyte compositions obtained in the half-cell studies of zinc and cerium reactions, the performance of a divided, parallel plate zinc-cerium redox flow battery was studied first with eight positive electrode materials. High surface area positive electrodes, such as carbon felt and 3-dimensional platinised titanium mesh electrodes, used to discharge the cell yield ≈ 70 % coulombic and ≈ 60 % voltage efficiencies at 50 mA cm^{-2}, giving better performance than the 2-dimensional electrodes. Most of the 2-dimensional materials and the reticulated vitreous carbon electrodes had a large cell voltage drop during discharge at increased current densities, the initial cell voltages were *c.a.* 2.0 V at 5 mA

cm^{-2} and dropped to values below 0 V at 50 mA cm^{-2}.

With a Sigratherm® carbon felt positive electrode, the change in cerium half-cell voltage between the charge and discharge cycle at 50 mA cm^{-2} was remarkably small, at just 0.07 V compared to 0.29 V observed in the 3-dimensional platinised titanium mesh electrode. This suggests that the cerium redox reaction at the Sigratherm® carbon felt electrode shows some degree of reversibility than at platinised titanium and could be a promising prospect for future use in this system. Despite this, a 3-dimensional platinized titanium mesh electrode was preferred as the positive electrode material in the divided battery due to the poor electrical conductivity and the poor adherence of the carbon adhesive, used to attach the carbon felts, after a few cycles.

The charge and discharge characteristics of divided redox flow battery were studied over a wide range of applied current densities, operating temperatures, mean linear electrolyte flow velocities, methanesulfonic acid concentration as well as zinc and cerium concentrations. The highest energy efficiency was obtained at 50 ^{o}C with a mean linear electrolyte flow velocity of 7.8 cm s^{-1}, while the optimum composition for the positive electrolyte was confirmed in the flow battery experiment as 0.8 mol dm^{-3} cerium methanesulfonate in 4.0 mol dm^{-3} methanesulfonic acid. In all cases, the positive cerium half-cell was the limiting reaction for battery discharge as the discharge reaction of zinc lasted longer than that of cerium reaction in the early cycles.

In all charge/discharge modes at different charging times, the zinc half-cell reaction was the limiting factor for life cycle at longer times. This was because the initial higher

acid concentration in the positive compartment and the formation of acid during charge. After prolonged charge/discharge cycling, negative electrolyte became more acidic and led to more difficult zinc electrodeposition. At a low state of charge, the number of possible cycles increased from 4 cycles in the 4 hour charge/discharge experiments to 57 cycles in the 15 minutes case.

In order to avoid the transfer of acid across the membrane, the possibility of using a common electrolyte for both negative and positive electrodes in an undivided system has been evaluated. With the addition of 0.2 mol dm^{-3} cerium(III) methanesulfonate, coulombic efficiency of the zinc half-cell reaction was found to decrease slightly. Also, higher Ce(IV) ion concentration can only be made soluble at concentrated methanesulfonic acid, in which hydrogen evolution would become significant at the negative electrode and could lead to a poor coulombic efficiency. Therefore, an electrolyte composition of 1.5 mol dm^{-3} zinc(II) methanesulfonate and 0.2 mol dm^{-3} cerium(III) methanesulfonate in 0.2 mol dm^{-3} methanesulfonic acid was tested in this preliminary study.

In the undivided flow battery, carbon polyvinyl-ester was used as the negative electrode as a substrate for zinc electrodeposition and dissolution to take place. The positive electrode was made up of three pieces of carbon felts compressed to the carbon polyvinyl ester substrate. Under room temperature, the battery was cycling at 20 mA cm^{-2} for 30 minutes. In the intial ten charge/discharge cycles, average coulombic and energy efficiencies were 90 % and 76 %, respectively. The change in cerium half-cell potential was also found to be small (c.a. < 50 mV) over a wide range of current densities (0 — 80 mA cm^{-2}) suggesting that cerium redox reaction was highly reversible at the high surface

area of carbon felt. Despite these, oxygen evolution became dominant at higher temperature and lead to poor conversion of Ce(IV) during charge. This was possibly due to the low concentration of cerium and acid, suggested by the voltammetric study in the cerium half-cell chapter.

Furthermore, the low cerium concentration (0.2 mol dm^{-3}) also limits the energy density to only *c.a.* 11 W h dm^{-3} compared to 20 — 35 W h dm^{-3} of an all vanadium system. Therefore, further investigation should focus on the use of other supporting electrolytes in order to allow the use of higher cerium concentration in this flow battery system. The self-discharge was also evaluated as both zinc and cerium species were mixed in a common electrolyte by monitoring the open-circuit potentials. The capacity was observed to last for more than 7 hours after being charged for 30 minutes.

In conclusion, the fundamental and operation of the zinc-cerium redox flow battery have been investigated. Half-cell studies and the characterization of a divided and an undivided systems have carried out. It has been demonstrated that a practical energy storage system can be applied using this chemistry. In term of system efficiencies, both divided and undivided zinc-cerium flow batteries had a comparable performance with the conventional systems. In order to facilitate zinc electrodeposition and prevent zinc corrosion, several electrolytic additives and corrosion inhibitors have been suggested. Further challenges and research directions are discussed in the following section.

10.2. Future work

In this work, the electrochemistry and operating parameters of a zinc-cerium redox flow battery have been investigated and optimized. Carbon felt material was found to be a

promising positive electrode material due to its lower material cost and higher reversibility of a cerium redox reaction compared to platinised titanium electrode. However, the use of this material has been limited by the poor electrical conductivity and the poor adhesives after a few charge/discharge cycles. Further research on improved mechanical design of a membrane electrode assembly and more advanced conducting adhesive in such acidic and oxidizing environment is needed.

An improved electrolyte composition is possible to further enhance the charge-discharge performance. For instance, ionic liquid can be used as background electrolyte to improve the conductivity and avoid evaporation of electrolyte at higher than room temperature. Electrolytic additives and catalysts can be incorporated into the electrolyte or doped into the electrode for both zinc and cerium reactions to increase the reaction rate, avoid side reactions, improve the reversibility and decrease the self-discharge. Life cycle of an undivided flow battery can be enhanced by defining the limiting factors and seeking solutions for further remedial treatment in large scale operation.

Energy capacity can be further increased by using higher cerium concentration in the common electrolyte. However, Ce(IV) ion can only be made soluble at high methanesulfonic acid concentration. In order to improve the solubility of Ce(IV) species, further investigations should focus on the ligand chemistry of cerium species in other solvents, such as trifluoromethanesulfonic acid, Lewis acid p-toulenesulfonic acid or the used of mixed acid electrolytes. For instance, previous literatures reported that more than 0.7 mol dm^{-3} Ce(III) and Ce(IV) ions can be made soluble at low concentration of methanesulfonic acid [1] and sulphuric acid [2],respectively. Hence, the mixed acid electrolyte systems needs to be

investigated further. On the other side, metallic substrates, such as cadmium [3] and copper, or other carbon composite materials [4], can be used as substrate to allow efficient zinc electrodeposition in an acidic environment. The ratio between the positive and negative electrode areas was also found to play an important role on the self discharge of the system, which needs further investigation. For the larger energy and power output, further investigation on the scale up of bipolar electrode stack and the dimensionless group used in mass transport, such as Sh, Re, Sc and Gr, is necessary.

10.3 References

1. R.P. Kreh, R.M. Spotnitz, J.T. Lundquist, J. Org. Chem. *54* (1989) 1526-1531.

2. A. Paulenova, S.E. Creager, J.D. Navratil, Y. Wei, J. Power Sources 109 (2002) 431-438.

3. L. Zhang, J. Cheng, Y.S. Yang, Y.H. Wen, X.D. Wang, G.P. Cao, J. Power Sources 179 (2008) 381-387.

4. G. Nikiforidis, L. Berlouis, D. Hall, D. Hodgson, J. Power Sources (2011) doi:10.1016/j.jpowsour.2011.01.036.

Electrochimica Acta 56 (2011) 6536–6546

Contents lists available at ScienceDirect

Electrochimica Acta

journal homepage: www.elsevier.com/locate/electacta

Zinc deposition and dissolution in methanesulfonic acid onto a carbon composite electrode as the negative electrode reactions in a hybrid redox flow battery

P.K. Leung, C. Ponce-de-León*, C.T.J. Low, F.C. Walsh

Electrochemical Engineering Laboratory, Energy Technology Research Group, University of Southampton, Highfield, Southampton, SO17 1BJ, United Kingdom

ARTICLE INFO

Article history:
Received 24 January 2011
Received in revised form 26 April 2011
Accepted 27 April 2011
Available online 6 May 2011

Keywords:
Dendrite
Electrodeposition
Flow battery
Methanesulfonic acid
Zinc

ABSTRACT

Electrodeposition and dissolution of zinc in methanesulfonic acid were studied as the negative electrode reactions in a hybrid redox flow battery. Cyclic voltammetry at a rotating disk electrode was used to characterize the electrochemistry and the effect of process conditions on the deposition and dissolution rate of zinc in aqueous methanesulfonic acid. At a sufficiently high current density, the deposition process became a mass transport controlled reaction. The diffusion coefficient of Zn^{2+} ions was 7.5×10^{-6} cm^2 s^{-1}. The performance of the zinc negative electrode in a parallel plate flow cell was also studied as a function of Zn^{2+} ion concentration, methanesulfonic acid concentration, current density, electrolyte flow rate, operating temperature and the addition of electrolytic additives, including potassium sodium tartarate, tetrabutylammonium hydroxide, and indium oxide. The current-, voltage- and energy efficiencies of the zinc-half cell reaction and the morphologies of the zinc deposits are also discussed. The energy efficiency improved from 62% in the absence of additives to 73% upon the addition of 2×10^{-3} mol dm^{-3} of indium oxide as a hydrogen suppressant. In aqueous methanesulfonic acid with or without additives, there was no significant dendrite formation after zinc electrodeposition for 4 h at 50 mA cm^{-2}.

1. Introduction

Power generation sources need to develop energy storage capabilities to be more efficient during off-peak hours [1]. Excess power generation and transmission are underused every year due to insufficient energy storage leading to problems, such as raised volatility, reduced reliability and energy wastage [1,2]. The increasing interest in renewables has drawn attention to the fact more reliable, affordable, flexible and safer energy storage systems are required.

Recently, redox flow batteries have emerged as possible systems for energy storage. Some advantages over conventional energy storage systems are that they can be installed anywhere, as standalone systems and no special terrain or climate is necessary. Compared to the conventional lead acid battery, redox flow batteries are less costly to maintain. The modular nature of the redox flow battery enhances its transportability and makes its construction and maintenance costs, lowest among other energy storage systems [3]. Since 1970, a number of redox flow batteries have been developed for applications in bulk energy storage, load-levelling, strategic power supplies and electric vehicles. Due to the electronegativity of zinc, its large negative potential in aqueous medium and its widespread availability, the zinc redox couple has been considered as the negative electroactive species in redox flow batteries.

The large negative potential of the zinc redox couple allows a high energy density when coupled with other electropositive redox couples, such as chlorine/chloride [4,5], bromine/bromide [6,7], ferrocyanide/ferricyanide (hexacyanoferrate II/III) [8], ceric/cerous [9] and oxygen/water [10]. The combination of zinc with these couples facilitates a high energy density. During the charge–discharge cycle of a redox flow battery, the electrodeposition of zinc:

$$\mathrm{Zn(II)} + 2\mathrm{e}^- \underset{\text{discharge}}{\overset{\text{charge}}{\rightleftharpoons}} \mathrm{Zn} \quad E^\circ = -0.76\,\mathrm{V}\,vs.\,\mathrm{SHE} \tag{1}$$

is the reaction at the negative electrode.

In the case of a zinc–cerium hybrid redox flow battery, the positive electrode reaction is [11]:

$$\mathrm{Ce(III)} - \mathrm{e}^- \underset{\text{discharge}}{\overset{\text{charge}}{\rightleftharpoons}} \mathrm{Ce(IV)} \quad E^\circ \approx +1.28 - 1.72\,\mathrm{V}\,vs.\,\mathrm{SHE} \tag{2}$$

The range of the cell potential difference for this pair of redox couples depends on the type of electrolyte used. According to Plurion Inc. (UK), the open-circuit cell voltage of a zinc–cerium flow battery can be up to 2.4 V [12]. Recent attention has focused on the application of aqueous methanesulfonic acid as an electrolyte

* Corresponding author. Tel.: +44 23 80598931; fax: +44 23 80597051.
E-mail address: capla@soton.ac.uk (C. Ponce-de-León).

0013-4686/$ – see front matter © 2011 Elsevier Ltd. All rights reserved.
doi:10.1016/j.electacta.2011.04.111

for redox flow batteries, as this electrolyte allows a high solubility for a wide range of metal ions, including the highly electropositive lead [13] and cerium ions [14]. Methanesulfonic acid has comparable conductivity and is generally less corrosive than other common electrolytes, such as sulfuric and hydrochloric acids [13].

Although zinc electrodeposition has been practised for a long time using acidic chloride [15–21] and sulfate [22–25] baths, there have been few studies of zinc electrodeposition from methanesulfonic acid electrolytes [26]. Recent patents have suggested that methanesulfonic acid can significantly decrease the dendritic growth [10,27], thus increasing the life cycle in a zinc-based flow battery. In contrast to the electroplating industry, where the majority of the substrates are metals, carbon-based materials are the commonest electrode materials used in redox flow batteries [28–30], as in many cases they are chemically inert and do not undergo dissolution and formation of oxides. In this work, the electrochemistry of zinc in methanesulfonic acid was studied via cyclic voltammetry at a glassy carbon rotating disk electrode. In order to optimize the conditions for a zinc-based redox flow battery, a range of electrodeposition and dissolution experiments have been carried out in a parallel plate flow-cell using different electrolyte compositions and operating parameters. A detailed discussion of zinc morphology and system efficiency is included in this study.

2. Experimental details

2.1. Chemicals

All chemicals used were analytical reagent grade from Alfa Aesar (UK) and Sigma Aldrich (Germany); the solutions were prepared with ultra-pure water (18 MΩ cm resistivity) from an Elga water purification system. The solutions were purged with a fast stream of dispersed nitrogen gas (The BOC Group, UK) for 10 min to avoid interference from the oxygen reduction reaction. Zinc(II) methanesulfonate solutions were produced by stirring zinc carbonate basic (Alfa Aesar, UK, 99 wt.%) using a PTFE-coated steel magnetic stirred bar (Fisherband, UK, 1 cm diameter, 4 cm length) in 70% methanesulfonic acid (Sigma Aldrich, Germany). The resulting zinc methanesulfonate solutions were colourless, clean solutions with no precipitate. All electrolytic additives were laboratory grade, supplied by Fluka (Austria) or Sigma Aldrich (Germany).

2.2. Cyclic voltammetry

Cyclic voltammetry was carried out in a divided, three-electrode glass cell. The electrolyte volume contained in the working electrode compartment was approximately 100 cm^3. The glass cell was equipped with a water jacket connected to a Grant LV FG water thermostat to control the electrolyte temperature in the range of 20–60 °C. The working electrode was a static glassy carbon disk electrode (area: 0.13 cm^2) while the counter electrode was a large area platinum mesh (projected area: 1 cm^2). The working and counter electrode compartments were separated by a Nafion® membrane (Dupont, NF115/H^+). The electrode potential was measured against a saturated silver/silver chloride electrode (ABB, Series 1400, 1.0 mol dm^{-3} KNO_3). For the cyclic voltammetry, the potential was linearly swept from −0.8 to −1.4 V *vs.* Ag|AgCl at a potential sweep rate in the range from 8 to 128 mV s^{-1}. Cyclic voltammograms were recorded over a wide range of electrolyte composition including 10–80 mmol dm^{-3} zinc methanesulfonate in 0.5 mol dm^{-3} sodium methanesulfonate solution adjusted to pH 0–4 with methanesulfonic acid. All electrochemical measurements were made with an EcoChemie Autolab (PGSTAT20) computer controlled potentiostat using the General Purpose, Electrochemical Software (GPES) Version 4.5.

2.3. Electrolysis in a flow cell

Electrodeposition and dissolution of Zn in methanesulfonic acid were carried out in a divided, parallel plate flow cell. A cation-conducting Nafion® membrane (DuPont, NF117/H^+) separated the two compartments. Carbon polyvinyl-ester composite (BMC 18649, Engtegris GmbH, Germany) was used for both the negative and the positive electrodes. Each electrode had an area of 4.5 cm × 2 cm (9 cm^2) with a gap of 2.0 cm between the electrode surface and the membrane. The volume of each electrolyte contained in separated tanks was 100 cm^3. Both positive and negative electrolytes were circulated at a mean linear flow velocity between 1.8 and 7.8 cm s^{-1} through the cell using a peristaltic pump (Masterflex® Model 7553079, Cole-Parmer) with high-pressure tubing (Masterflex® Norprene®, Cole-Parmer). The negative electrode compartment contained 0.5–2 mol dm^{-3} zinc methanesulfonate in 0.5–3 mol dm^{-3} methanesulfonic acid while the positive electrode compartment contained 1.0 mol dm^{-3} methanesulfonic acid. The temperature of both electrolytes was controlled at (293–343) ± 2 K by thermostat (Grant Model LV FG) and circulated water through jackets fitted to each electrolyte reservoir.

At the negative electrode, zinc was electrodeposited at current density in the range of 20–80 mA cm^{-2} for 4 h. The electrode was then left at open-circuit for 1 min followed by zinc dissolution using the same current density. The electrolysis during the oxidation stopped when the zinc half-cell voltage shifted towards more positive values than 0 V *vs.* Ag|AgCl to avoid the oxidation of the substrate material. The reference electrodes were saturated silver–silver chloride electrode, Ag|AgCl (ABB, Series 1400, 0.1 mol dm^{-3} KNO_3) placed at the entrance of the flow cell in each channel. The electrochemical measurements were made by BaSyTec (5 A/12 V, Germany) battery test system. The anode- and cathode-potentials together with the cell potential difference were continuously monitored throughout the experiment.

2.4. Electrodeposition and microscopy

Zinc electrodeposition in the presence and absence of additives was carried out in an electrolyte containing 1.5 mol dm^{-3} zinc methanesulfonate and 1 mol dm^{-3} methanesulfonic acid electrolyte (60 cm^3) in a 100 cm^3 glass beaker. The applied current density was 50 mA cm^{-2} for 4 h. Carbon polyvinyl-ester composite (Engtegris Inc., BMC 18649, Germany) electrodes of 8 cm × 1 cm dimensions and with an exposed electrode area of 4 cm × 1 cm were used as both cathode and anode. The electrodes faced each other when fitted into a nylon holder with an interelectrode gap of 1 cm. Before each experiment, the electrodes were polished using silicon carbide paper (grade P120), degreased with detergent then left in an ultrasonic bath for 10 min in deionized water. The electrode holder was immersed in a double walled water jacket container that allows water circulation from the bath thermostat to maintain the temperature of the solution constant, typically at 50 °C.

Throughout the experiment, the solution was stirred at 400 rpm using an IKa yellowline® magnetic stirrer. After the electrodeposition and before taking the microscopic images, the samples were rinsed with ultrapure water (Elga water purification system) for 10 s, air-dried and stored in a sample bag placed in a container with silica gel granules. The images of the zinc electrodeposits were taken with a JEOL scanning electron microscope (model JSM 6500 F) equipped with an energy-dispersive X-ray spectroscopic analyzer, which was used to estimate the elemental composition.

3. Results and discussion

3.1. Cyclic voltammetry

Fig. 1a shows the cyclic voltammogram of Zn(II) ions using a glassy carbon electrode at 20 mV s^{-1} potential sweep rate in an electrolyte containing 0.01 mol dm^{-3} zinc methanesulfonate and 0.5 mol dm^{-3} sodium methanesulfonate adjusted at pH 4 with methanesulfonic acid at 295 K. The potential was firstly swept from −0.8 V to −1.4 V *vs.* Ag|AgCl.

The voltammogram is similar to those reported in other acid media. The cathodic scan shows the potential at −1.15 V *vs.* Ag|AgCl, which is comparable to *ca.* −1.2 V *vs.* SCE reported in sulfate, chloride and acetate electrolytes [31]. The sharp increase in current reduction was due to the formation of fresh zinc nuclei, and the further increase of the available deposition area. The peak current density reached *ca.* 2.57 mA cm^{-2} at −1.22 V *vs.* Ag|AgCl due to the reaction of Zn(II) ions already on the electrode surface. After the peak, the current density decreased as no more Zn(II) ions were present at the surface and new Zn(II) species had diffused from the bulk of the electrolyte. Since the standard electrode potential of zinc deposition is more negative than hydrogen evolution, hydrogen gas could evolve by the cathodic reduction of hydrogen ions on the newly formed zinc nuclei. Although the cyclic voltammogram does not show the evolution of hydrogen gas, a fraction of the current is probably due to proton reduction. The scan was reversed at −1.4 V *vs.* Ag|AgCl in order to avoid hydrogen evolution at more negative potentials.

While sweeping the potential towards the positive direction, zinc ions were still being reduced until the crossover potential at −1.16 V *vs.* Ag|AgCl on the foot of the stripping peak. At −1.14 V *vs.* Ag|AgCl, solid zinc was no longer thermodynamically stable on the electrode surface and the metallic zinc deposited on the electrode oxidizes very quickly as the oxidation process was not diffusion controlled and a sharp high current peak was observed. The forward and reverse scans form a nucleation loop between −1.16 V and −1.18 V *vs.* Ag|AgCl. The slightly more negative potential during Zn(II) reduction observed during the forward scan shows that the deposition of zinc on the less-conductive glassy carbon substrate required slightly more energy than that on the freshly deposited zinc surface.

In this study, the overpotential for zinc electrodeposition was *ca.* −20 mV, as the nucleation potential on glassy carbon electrode is more negative than that on metallic electrode. For instance, Gomes and da Silva Pereira [32] reported that the nucleation potential of zinc electrodeposition was observed at *ca.* −0.8 V *vs.* SCE at a stainless steel electrode from the sulfate bath in the absence of an electrolytic additive. Such an overpotential was reported to have important implications for the morphology of the deposit and the current efficiency. Volmer and Weber [33] suggested that a larger overpotential could lead to faster nucleation rate and prevent further grain growth [33–37], which has been reviewed by Budevski et al. [38]. Finer grain size and sometimes more uniform deposits have been obtained at larger deposition overportentials, which was found to be largely dependent on anions molecules [31,39,40], electrolytic additives [36,41,42], temperature [31,43] and the influence of pH on the formation of zinc complexes [44,45]. As suggested by Morón et al. [46], the crystal size of zinc deposit was also influenced by the exchange current density. Due to the reduced exchange current density induced by the adsorption of electrolytic additives on the electrode surface, compact and reflective coatings have been obtained from an acid chloride bath.

In terms of electron transfer, the zinc deposition reaction in a methanesulfonate bath is considered to be a quasi-reversible reaction, as the separation of peak potentials was 160 mV. Literature reports show that the separation of peak potentials for the Zn(II)/Zn(0) reaction in chloride and sulfate electrolytes was *ca.* 100 mV and 150 mV, respectively, in an electrolyte containing 0.01 mol dm^{-3} Zn(II) ions and 0.5 mol dm^{-3} Na(I) ions. The results in this paper suggest that zinc electrodeposition from methanesulfonaic bath shows a similar electrochemical behaviour to that from a sulfate bath. Moreover, the ratio of anodic to cathodic charge was found to be consistent with the previous findings in sulfate bath. The charge ratio between the anodic and cathodic processes in methaneulfonate bath was 82% while the reported value in a sulfate bath was 81% [47]. This suggests that some of the charge during zinc electrodeposition was used for hydrogen evolution.

Plotting the logarithm of the current density *vs.* the potential range of zinc nucleation, a Tafel slope of -52 ± 2 mV $decade^{-1}$ was obtained which is almost the double the magnitude of the theoretical calculation of −30 mV $decade^{-1}$ for a two electron transfer reaction. The value agrees with other works reported in the literature: Ibrahim [43] reported that the Tafel slope was

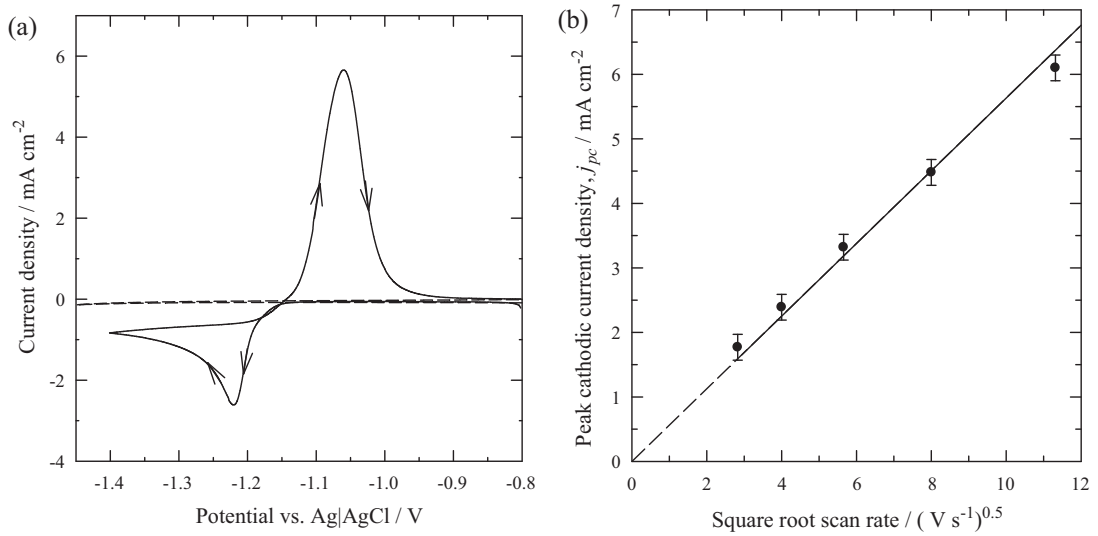

Fig. 1. Electrochemistry of zinc electrodeposition at a glassy carbon electrode in methanesulfonic acid. Electrolyte: 0.01 mol dm^{-3} $Zn(CH_3SO_3)_2$ in 0.5 mol dm^{-3} $NaCH_3SO_3$ adjusted at pH 4 with CH_3SO_3H. (a) Cyclic voltammogram, from −0.80 to −1.40 V *vs.* Ag|AgCl at 20 mV s^{-1} and 20 °C. (b) Randles-Sevcik plot, using potential sweep rates of 8, 16, 32, 64 and 128 mV s^{-1}.

56 mV s^{-1} at 0.09 mol dm^{-3} zinc in 0.2 mol dm^{-3} sodium sulfate. In the investigation of Guerra in zinc sulfate, the Tafel slope was *ca.* 60 mV $decade^{-1}$ in neutral pH solution and *ca.* −30 mV $decade^{-1}$ in highly acidic electrolyte. The smaller Tafel slope (high cathodic current density) was due to the surface condition, as the hydrogen adsorbed on the newly formed zinc nuclei reacted. This resulted in the combined cathodic reactions of hydrogen evolution and zinc deposition, leading to a sharp increase in current density [48].

Fig. 1b shows a plot of the cathodic peak current densities *vs.* the square root of the potential sweep rate. For a mass transport controlled reaction, a linear increase of the peak current density with the square root of the potential sweep rate can be predicted by the Randles-Sevcik equation:

$$j_p = 2.69 \times 10^5 z^{1.5} D^{0.5} \nu^{0.5} c \quad (3)$$

where j_p is the peak current density, c is the zinc ion concentration in the electrolyte, z is the number of electrons involved the electrode process, ν is the potential sweep rate and D is the diffusion coefficient of the zinc ions. From the Randles-Sevcik plot, the diffusion coefficient for zinc ions was found to be 7.2×10^{-6} cm^2 s^{-1}, while Meas et al. [49] reported a value of 7.27×10^{-6} cm^2 s^{-1} in hydrochloric acid. The value found here is comparable to previous estimations for the diffusion coefficient of zinc ions reported in the literature in other acid electrolytes: Yu et al. [31] calculated 2.1, 5.5 and 8.4×10^{-6} cm^2 s^{-1} in acetic, sulphuric and hydrochloric acids. The current used for zinc electrodeposition in methanesulfonic acid would be expected to be similar to that used in other common acids but the less-corrosive nature of methanesulfonic acid and its ability to dissolve high levels of metal ions makes it more attractive for energy storage applications.

3.2. Linear sweep voltammetry

3.2.1. Mass transport

As well as the charge-transfer process taking place on the electrode surface, mass transport of the Zn(II) ions towards the electrode contributes to the overall rate of the reaction. As the electrode potential becomes gradually more negative during the linear sweep voltammetry, the reduction of Zn(II) becomes dominated by the rate at which the ions reach the electrode surface. Fig. 2a shows a family of linear sweep voltammograms of Zn(II) reduction on a glassy carbon rotating disk electrode at various speeds: 400, 900, 1600, 2500 and 3600 rpm. The electrolyte composition was the same as that used in the experiments of Fig. 1a and b. In order to avoid excessive hydrogen evolution, the electrode potential was swept from −1.0 V to −2.0 V *vs.* Ag|AgCl at 20 mV s^{-1}. The reduction of zinc was observed at the same potential as in the cyclic voltammogtam, −1.2 V *vs.* Ag|AgCl, and well defined plateau of constant current density where observed at potentials more negative than −1.4 V *vs.* Ag|AgCl. The constant supply of the zinc ions to the electrode surface due to the rotation of the electrode at different rates helps to maintain the Zn(II) ion concentration at the surface. An increased rotation speed was found to shorten the plateau region, leading to earlier hydrogen evolution.

The limiting current density for each rotating speed was measured at the mid-point of the plateau at −1.7 V *vs.* Ag|AgCl. The supply rate of zinc ions to the cathode surface is necessary to equalize with the rate of charge transfer. This is especially important during the charge and discharge of a redox flow battery; if the applied current density during the charge or discharge cycles is too high compared to the limiting current density, hydrogen evolution might take place instead of zinc electrodeposition or dissolution. The evolution of hydrogen can also increase the electrolyte resistance and reduce the effective plating area, which can result in burnt deposit [50]. Under such conditions, the transport rate of zinc ion to the surface of the negative electrode needs to be increased. As shown in Fig. 2b, a linear relationship between the limiting current density with the square root of the rotation rate is observed and follows the Levich equation.

$$j_{lim} = 0.620 z F D^{2/3} \omega^{1/2} \nu^{1/6} c \quad (4)$$

where j_{lim} is the limiting current density (A cm^{-2}), F is Faraday's constant, ω is the rotation rate of the disk (rad s^{-1}) and ν is the kinematic viscosity of the electrolyte (cm^2 s^{-1}). The linear behaviour indicates that the reduction of Zn(II) ions is under complete mass transport control. By using the gradient of Fig. 2b, a diffusion coefficient for zinc ions of 7.8×10^{-6} cm^2 s^{-1} was estimated. This value is slightly larger than the one obtained from the Randles-Sevik equation as possibly both hydrogen adsorption and oxygen reduction reactions are more significant under the mass transport controlled regime and contribute to a higher degree to the observed limiting current than in the cyclic voltammetry experiment. In this study, the average diffusion coefficient of zinc ion obtained from the Levich and Randles-Sevik equations in 0.01 mol dm^{-3} zinc methanesulfonate and 0.5 mol dm^{-3} sodium methanesulfonate at pH 4 is 7.5×10^{-6} cm^2 s^{-1}.

In the electroplating industry, high speed metal deposition is usually required and increasing the mass transport is a common strategy to provide a high current density and a fast electrodeposition rate. In the literature, it has been reported that powdery and burnt deposits can be avoided by increasing the limiting current density via enhanced mass transport techniques [35,50]. Turbulent flow and a high rate of cathode movement are often used for industrial high speed zinc electrodeposition [51].

3.2.2. Zinc ion concentration

Fig. 2c shows the linear sweep voltammogram of zinc electrodeposition over a range of zinc concentrations of 10, 20, 40, 60 and 80×10^{-3} mol dm^{-3} at 600 rpm rotation speed in 0.5 mol dm^{-3} sodium methanesulfonate at pH 4 and 295 K. The electrode potential was swept from −1.0 to −2.0 V *vs.* Ag|AgCl at 20 mV s^{-1}. As the concentration of zinc ions increased, the nucleation potential shifted towards positive values and changed linearly with the logarithm of Zn(II) ion concentration by 58 ± 2 mV per 10-fold change in concentration. The magnitude of this potential shift is similar to that obtained in sulfate electrolytes reported in the literature [43].

Fig. 2d shows the limiting current densities for zinc deposition as a function of the concentration of the zinc ion. The limiting current density of zinc electrodeposition increased by *ca.* 10 mA cm^{-2} per every 10 mM zinc ion concentration. The linear plot confirms the fact that the system was under mass transport control according to the Levich equation. The potential window of the limiting current plateau decreases as the concentration of zinc increases suggesting that hydrogen evolution was more favourable as more zinc was deposited on the electrode surface.

3.2.3. Concentration of protons

Fig. 3a shows the linear sweep voltammogram of zinc electrodeposition over a range of pH from 0 to 4 at the rotation speed of 600 rpm. The electrolyte composition is the same as in Fig. 1. The electrode potential was swept from −1.0 to −2.0 V *vs.* Ag|AgCl at 20 mV s^{-1}. At higher pH values, the nucleation potentials were shifted towards more positive values, which is due to the higher conductivity of the electrolyte and to the increased concentrations of protons. Large limiting current plateaus were observed at pHs 4 and 3 than at lower pHs 0, 1 and 2.

At increased electrolyte acidity from pH 2 to 0, the stability of the zinc methanesulfonate complexes decreases and the reduction of protons occur on the newly formed zinc nuclei. This results in an undefined plateau at pH 0 and 1 and a slightly larger current density plateau at pH 2. At the lowest pH zinc electrodeposition competes with hydrogen evolution and the sharp increase in current density

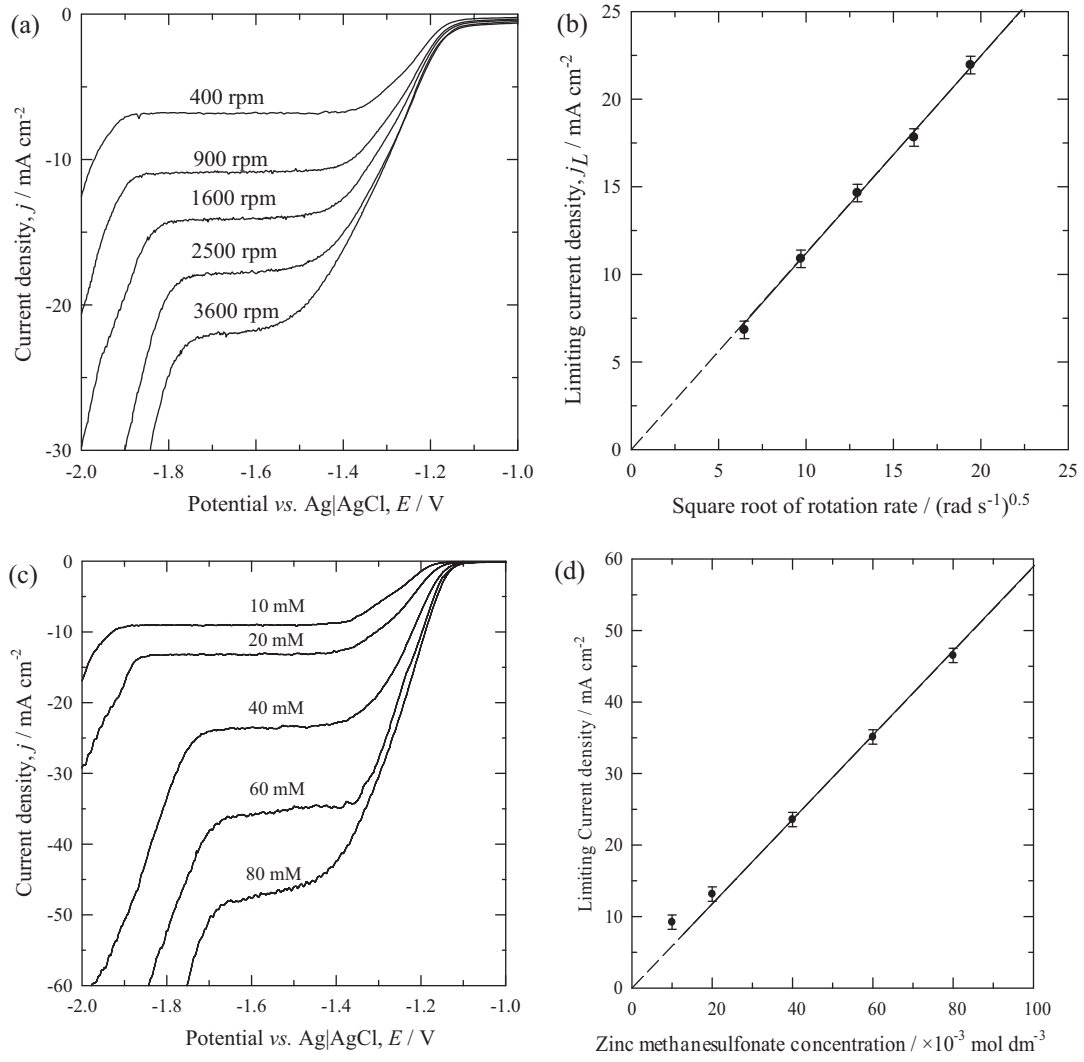

Fig. 2. Effect of rotation speed and zinc ion concentration on zinc electrodeposition in methanesulfonic acid at glassy carbon electrode (293 K). (a) The effect of rotation speed on the cyclic voltammogram, (b) Levich plot, (c) the effect of zinc ion concentrations on the cyclic voltammogram and (d) the plot of zinc ion concentrations against the limiting current densities. Electrolyte: as in Fig. 1. Rotation speeds were 400, 900, 1600, 2500 and 3600 rpm. Zinc concentrations: 10, 20, 40, 60 and 80×10^{-3} mol dm^{-3}. The electrode was swept from −1.0 to −2.0 V *vs.* Ag|AgCl scanning at 20 mV s^{-1} at 600 rpm and 20 °C.

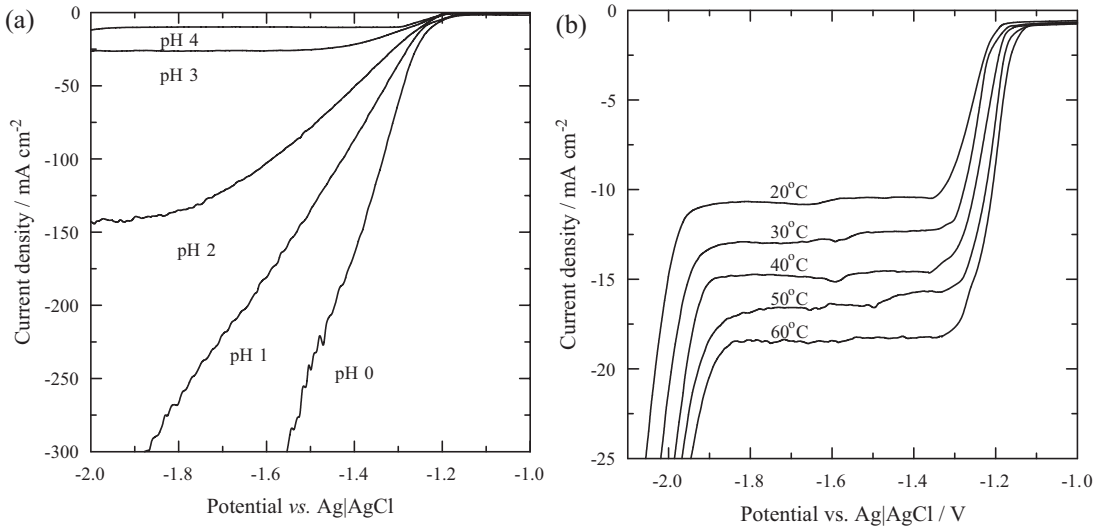

Fig. 3. Effect of electrolyte acidity and operating temperatures on zinc electrodeposition in methanesulfonic acid at glassy carbon electrode at 600 rpm. (a) Effect of electrolyte acidity on the cyclic voltammogram, (b) effect of electrolyte temperature on the cyclic voltammogram. Electrolyte: as in Figs. 1 and 2. Solution acidity was pH 4, 3, 2, 1 and 0. Electrolyte temperature: 20, 30, 40, 50 and 60 °C. The electrode was swept from −1.0 to −2.0 V *vs.* Ag|AgCl at 20 mV s^{-1} and 20 °C.

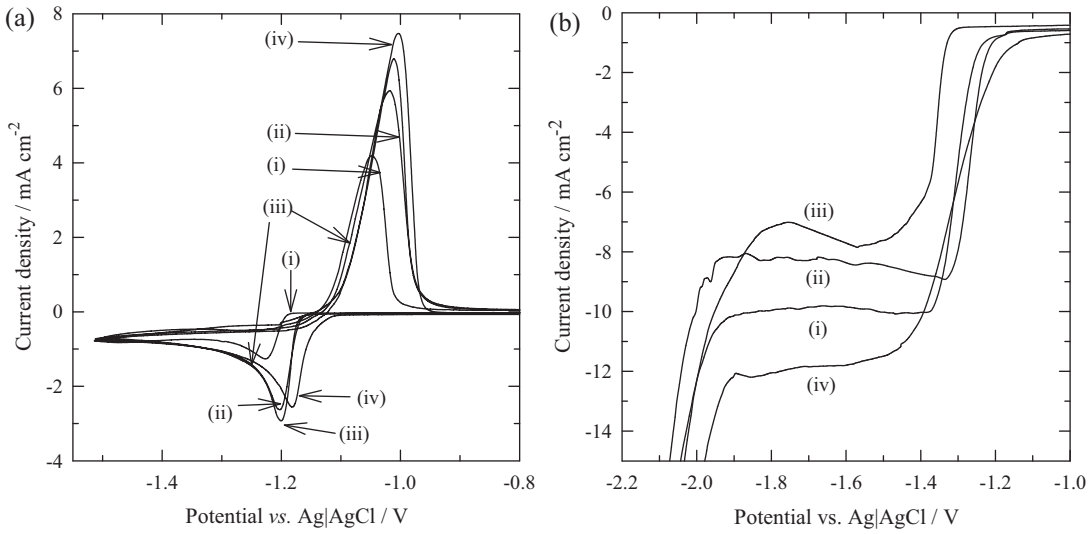

Fig. 4. Effect of electrolytic additive on cyclic voltammogram of zinc electrodeposition in methanesulfonic acid (a) at static electrolyte and (b) at 600 rpm. Electrolyte: as in Figs. 1–3. Electrolytic additives were at 2×10^{-3} mol dm^{-3}, (i) no additive, (ii) potassium sodium tartarate, (iii) tetrabutylammonium hydroxide and (iv) indium oxide.

was due to the excessive hydrogen evolution. The competition of the deposition of zinc and hydrogen evolution has been confirmed by the reaction model reported by Cachet and Wiart [52], which stated that the discharge of zinc ion is firstly inhibited by hydrogen adsorption followed by the hydrogen evolution on the surface of the zinc deposit. At such highly acidic media, the zinc ion concentration on the electrode surface is relatively low and hydrogen adsorption on the electrode is hence easy. In this case, the current is mainly used for hydrogen evolution and the current efficiency of zinc deposition decreases.

The suppression of the hydrogen evolution reaction is necessary to promote zinc electrodeposition. In the system used by Plurion Inc., indium has been suggested as an additive to increase the hydrogen overpotential giving a current efficiency almost 95% compared to 70–80% without the additive [9,53]. Other finding suggests that additives, such as Na-benzylnicotinate [54], polyethylene glycol (PEG) [22,54], cetyltrimethyl ammonium bromide (CTAB) [32], tetrabutylammonium bromide (TEBACl) [55], perfluorosurfactants [56], tartaric acid [57], succinic acid [57], thallium [9], indium [12], cellulose [58] are capable of suppressing the hydrogen evolution reaction. In the plating industry, buffer reagents, for example H_3BO_3, are often incorporated to stabilize the pH and avoid excessive hydrogen evolution [59].

3.2.4. Operating temperature

Fig. 3b shows the linear sweep voltammograms of zinc electrodeposition over a range of electrolyte temperatures from 20 to 60 °C on a glassy carbon rotating disk electrode at 600 rpm. The electrolyte composition range is the same as that in the experiments described in Figs. 1 and 2. Both, the nucleation potential of zinc ions and hydrogen evolution potential shifted towards more positive values as the temperatures increased. The change in electrode potential obeys the Nernst equation, as a lower driving force for zinc electrodeposition and hydrogen evolution reactions is required as a higher temperature.

The electrode potential for the deposition of Zn(II) shifted 60 mV from −1.19 V *vs.* Ag|AgCl at 20 °C to −1.13 V *vs.* Ag|AgCl at 60 °C. Similar findings were observed by Zhang et al. [60] who reported that the cathodic potential decreased by *ca.* 65 mV when the temperature increased from 30 °C to 45 °C during zinc deposition in a sulfate electrolyte with 1-butyl-3-methylimidazolium hydrogen sulfate as an electrolytic additive. Elevated temperature can hence reduce the polarization of zinc ions reduction effectively. Since diffusion coefficient is a function of temperature, the limiting current densities will increase; every 10 °C increase in the temperature of the electrolyte lead to an increase in current density of *ca.* 5 mA cm^{-2}. During the zinc dissolution process (not shown) the charge of the zinc stripping peak was higher at elevated temperature confirming that zinc electrodeposition has been facilitated.

3.3. Effect of electrolytic additives on the cyclic voltammetry

Electrolytic additives are often employed in the plating industry to obtain durable, uniform and more compact coatings as well as to decrease the rate of undesired reactions. Fig. 4a shows the cyclic voltammogram for zinc electrodeposition with the addition of three selected electrolytic additives: tetrabutylammonium hydroxide, potassium sodium tartarate and indium oxide at a glassy carbon static disk electrode. The concentration of the additives in all cases was 2×10^{-3} mol dm^{-3} in an electrolyte containing 0.01 mol dm^{-3} zinc methanesulfonate and 0.5 mol dm^{-3} sodium methanesulfonate adjusted to pH 4 with methanesulfonic acid at 295 K. The potential was firstly swept from −0.8 V to −1.5 V *vs.* Ag|AgCl then reversed. The reduction and oxidation processes can be seen as the charge and discharge cycles of a half-cell zinc battery, respectively. Larger anodic peaks were observed with the addition of the additives except with tetrabutylammonium hydroxide. The ratio between the anodic and cathodic (discharge/charge) processes (Table 1) was 67%, whereas when indium oxide and potassium sodium tartarate were used, the ratio was approximately 88%. The addition of these two additives represented an improvement compared to the experiment in the absence of additives (82.3%). Despite the presence of indium oxide, single cathodic and anodic peaks were observed.

Linear sweep voltammograms in the presence of the three electrolytic additives were also carried out on a rotating vitreous carbon electrode disc at 600 rpm. Well-defined limiting current densities plateaus were observed in all the experiments but each additive presented different limiting current density value, this could be due to the additive reacting or adsorbing on the newly formed zinc deposit on the carbon electrode surface, thus decreasing the above surface area. Nucleation potentials of zinc in the presence of indium oxide and potassium sodium tartrate shifted to more positive values as shown in Table 1. This can be beneficial for battery

Table 1
The electrochemical behaviour of the electrolytic additives: (i) no additive, (ii) potassium sodium tartarate, (iii) tetrabutylammonium hydroxide and (iv) indium oxide at static and rotating glassy carbon electrodes. The electrolyte compositions were the same as in Fig. 4 a and b.

Additive	Static electrode						Rotating electrode
	Nucleation potential *vs.* Ag/AgCl (V)	Cathodic peak		Anodic peak		Charge ratio (%)[a]	Limiting current density, j_{lim} for zinc deposition at 600 rpm/mA cm^{-2}
		Potential *vs.* Ag/AgCl (V)	Current density (mA cm^{-2})	Potential *vs.* Ag/AgCl (V)	Current density (mA cm^{-2})		
(i) No additive	−1.16	−1.19	−2.86	−1.03	5.8	82.3	−9.8
(ii) Potassium sodium tartarate	−1.15	−1.20	−2.60	−1.01	6.7	87.6	−8.3
(iii) Tetrabutylammonium hydroxide	−1.18	−1.22	−1.21	−1.05	4.2	66.6	−7.7
(iv) Indium oxide	−1.12	−1.18	−2.58	−1.01	7.5	87.7	−11.8

[a]This percentage was calculated from the electrical charge under the anodic and cathodic curves of the cyclic voltammogram.

efficiencies, as lower charge voltages can be expected due to the reduced overpotential and zinc electrodeposition taking place prior to hydrogen evolution. The charge efficiency slightly improved except when tetrabutylammonium hydroxide was used. Although larger overpotentials obtained with tetrabutylammonium hydroxide result in lower voltage efficiency, such overpotentials were reported to be useful for refining the grain size and hence brightening the electrodeposit by partly covering the electrode surface and blocking the growth of the zinc crystals [61].

3.4. Zinc half-cell efficiencies in a parallel plate flow cell

Aiming to achieve the optimum electrolyte compositions and operating conditions for a zinc-based redox flow battery, the electrodeposition and stripping of zinc were carried out over a wide range of concentrations, electrolyte flow rates, temperatures, applied current densities and electrolytic additives in a divided parallel flow cell. Unless indicated otherwise, the electrolyte composition was at 1.5 mol dm^{-3} zinc methanesulfonate in 1 mol dm^{-3} methanesulfonic acid in the negative compartment while the other compartment contained 1 mol dm^{-3} methanesulfonic acid. Electrodeposition of zinc on a carbon polyvinyl-ester composite substrate was carried out at 50 mA cm^{-2} and 50 °C for 4 h. Table 2 summarizes the estimated half-cell efficiencies in terms of voltage, charge and energy at different operating conditions.

3.4.1. Effect of operating parameters

Fig. 5a–c shows the effect of current density, temperature and electrolyte flow rate, respectively, on the charge–discharge curves of the zinc half cell reaction. In the absence of additives, the curves in Fig. 5a show that the largest energy efficiency was 70%, obtained at a low current density of 20 mA cm^{-2} (Table 2). This high efficiency was attributed to the reduced ohmnic drop and improved voltage efficiency as the self-discharge of zinc became more significant while discharging at low current density. At a higher applied current density, the charge efficiencies were found to be higher but overall efficiency decreased. Similar findings were also reported by Saba and Elsherief [62] over a range of sulfuric acid and Zn(II) ion concentrations.

Fig. 5b shows the electrode potential *vs.* time at different temperatures during reduction and oxidation of zinc. Higher energy efficiency was obtained at lower operating temperatures, despite the fact that the solution conductivity and the resulting voltage efficiency increased with temperature. The charge efficiency significantly decreases from 94% at 20 °C to 68% at 70 °C. This is because higher temperature can lead to stronger depolarizing effect on hydrogen evolution than zinc deposition [63]; therefore less zinc was deposited at such a high temperature. Fig. 5c shows that as the mean linear electrolyte flow velocity increased from 1.8 to 5.8 cm s^{-1}, an increase in charge efficiency was observed. This could be due to the fact that at a high mean linear flow velocity the diffusion layer brcomes thinner and facilitates the transport of zinc ions to the working electrode. Despite this, larger voltage drop was also observed at a higher mean linear flow velocity. Therefore, the increase of electrolyte velocity did not significantly improve the overall energy efficiency of the zinc half-cell reaction.

3.4.2. Effect of zinc ions and acid concentration

Electrolyte compositions, especially the concentration of acid, were found to be crucial for the flow cell performance. Energy efficiency was as high as 62% at 1 mol dm^{-3} methanesulfonic acid compared to 41% at 3 mol dm^{-3} methanesulfonic acid. Alfantazi and Dreisinger reported that electrical conductivity increase linearly with sulfuric acid concentration; therefore higher voltage efficiency was obtained [64]. Due to the more dominant hydrogen evolution reaction and faster corrosion rate at higher acid concentration, a

Table 2
Half-cell efficiencies of electrodeposition and stripping of Zn on a carbon polyvinyl-ester composite substrate from a methanesulfonic acid bath in a parallel plate flow cell. Unless indicated otherwise, the current density was 50 mA cm^{-2}, deposition time 4 h, temperature 50 °C, mean linear flow velocity 3.9 cm s^{-1}. The solution was 1.5 mol dm^{-3} $Zn(CH_3SO_3)_2$ and 1 mol dm^{-3} CH_3SO_3H.

Operating parameter	Zinc half cell overpotential $-\eta$ (V)	Zinc half-cell charge potential *vs.* Ag|AgCl (V)	Zinc half-cell discharge potential *vs.* Ag|AgCl (V)	Zinc half-cell efficiencies (%)		
				Voltage	Charge	Energy
Current density (mA cm^{-2})						
20	0.26	−1.17	−0.91	78	90	70
50	0.41	−1.28	−0.85	68	91	62
80	0.41	−1.30	−0.87	63	92	62
Temperature (°C)						
22	0.45	−1.32	−0.87	66	94	62
40	0.43	−1.31	−0.88	67	94	62
50	0.41	−1.28	−0.85	68	91	62
70	0.27	−1.19	−0.92	71	68	52
CH_3SO_3H concentration (mol dm^{-3})						
0.5	0.42	−1.26	−0.84	67	94	62
1	0.41	−1.28	−0.85	68	91	62
2	0.36	−1.24	−0.88	71	87	62
3	0.34	−1.24	−0.89	72	57	41
Zn^{2+} concentration (mol dm^{-3})						
0.5	0.33	−1.27	−0.94	74	78	58
1	0.34	−1.24	−0.91	74	83	62
1.5	0.41	−1.28	−0.85	68	91	62
2	0.38	−1.21	−0.83	69	92	64
Mean linear flow velocity (cm s^{-1})						
1.8	0.33	−1.24	−0.92	74	86	63
3.9	0.41	−1.28	−0.85	68	91	62
5.8	0.37	−1.25	−0.88	70	92	64
7.8	0.41	−1.27	−0.86	67	92	62
Additive ($\times$0.002 mol dm^{-3})						
No additive	0.41	−1.28	−0.85	68	91	62
Potassium sodium tartarate	0.35	−1.26	−0.91	72	86	62
Tetrabutylammonium hydroxide	0.44	−1.37	−0.93	68	39	26
Indium oxide	0.27	−1.21	−0.94	78	94	73

significant decrease in charge efficiency was observed. The increase in zinc ion concentration was found to facilitate the electrodeposition process indicated by the improvement of the charge efficiency but this does not improve the energy efficiency [64].

The lower charge cell voltages observed as the concentration of Zn(II) ions increases can be explained by the Nernst equation. Since the dissolution of zinc back to Zn(II) species becomes more difficult at higher Zn(II) ion concentration in the vicinity of the electrode surface, lower discharge voltages were obtained. Despite this, higher Zn(II) ion concentration can be advantageous for redox flow battery as it allows the battery to charge at high current densities without mass transport limitations. Such a high concentration ensures that enough Zn(II) ions exist at all state of charges. In addition, two moles of methanesulfonic acid are formed per mol of zinc methanesulfonate during the electrodeposition reaction as shown in Eq. (1) [65]. In order to minimize the hydrogen evolution and facilitate zinc electrodeposition, higher Zn(II) ion concentration is preferred in the negative electrolyte.

3.4.3. *Effect of electrolytic additives in the parallel flat plate flow cell*

Three electrolytic additives from different categories were tested at a concentration of 2×10^{-3} mol dm^{-3}. Both indium oxide [66] and potassium sodium tartarate [67] are inorganic additives, while tetrabutylammonium hydroxide is a surface active agent. In order to determine whether they are suitable additives for battery performance, charge–discharge experiments were carried out in the presence of these additives. The electrode potential during the charge/discharge cycle is shown in Fig. 5d. With the addition of indium oxide, the energy efficiency improved significantly from 62% without additive to 73% (Table 2). In this case, higher charge and voltage efficiencies were obtained. The high charge efficiency obtained could be attributed to the large hydrogen overpotential of indium as an additive also observed in the Plurion Inc.'s zinc–cerium system [12], hence larger current values can be used for zinc electrodeposition. As presented in the voltammetry study in Section 3.3, lower deposition overpotential was observed. Hence, an improved voltage efficiency was expected in this electrolysis study, which is consistent with the previous finding of Yang and Lin [66] in their alkaline zinc-air battery.

The other two additives did not have a significant improvement on the half-cell efficiencies probably due to their strong adsorption and inhibiting effect (levelling property). Ganne et al. reported that some electrolytic additives could slow down the charge transfer reactions, poisoning the active kink sites and increasing the deposition overpotential [37]. For instance, the charge and energy efficiencies in the presence of tetrabutylammonium hydroxide were only 39% and 26%, respectively (Table 2). As a result, only indium oxide was suitable to be used as an electrolytic additive in a zinc-based hybrid redox flow battery.

3.5. *Coating morphologies*

Fig. 6a–d shows the microstructures of the zinc electrodeposits using different additives at 2×10^{-3} mol dm^{-3}: (a) no additive, (b) potassium sodium tartarate, (c) tetrabutylammonium hydroxide and (d) indium oxide. In the absence of additive, hexagonal-like crystalline structure was aligned plate-by-plate parallel to the substrate (Fig. 6a). This morphology is typical of zinc deposition and has already been observed in the literature [64,68]. On the uppermost of such hexagonal plates, a relatively rough, irregular plate-like structure was observed because of the continued growth and the stacking of the hexagonal platelet on the top of one another during the prolonged deposition for 4 h.

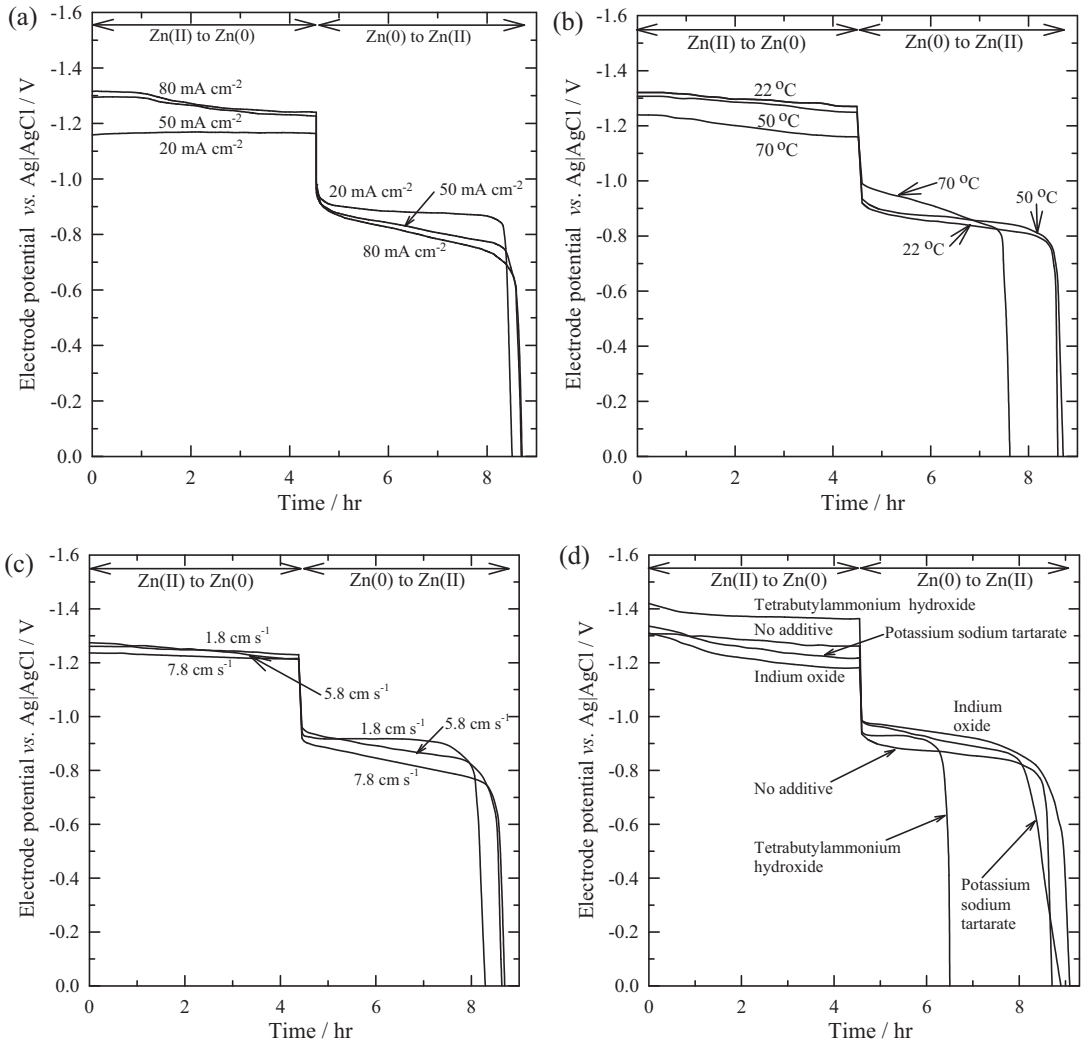

Fig. 5. The effect of current density, temperature, mean linear electrolyte flow rate and electrolytic additives of zinc half cell on a carbon polyl-ester composite substrate from a methanesulfonic acid bath in a parallel plate flow cell. Unless indicated, the current density was 50 mA cm^{-2}, deposition time 4 h, temperature 50 °C, mean linear flow velocity 3.9 cm s^{-1} and the solution was 1.5 mol dm^{-3} $Zn(CH_3SO_3)_2$ and 1 mol dm^{-3} CH_3SO_3H.

The mechanisms of such stacking behaviour from nucleation to growth have been discussed by a proposed model of Lee et al. [69] with schematic diagrams and microscope images in the medium of zincate.

In general, the microstructure of the zinc deposit without additive is quite smooth indicated by a shiny appearance without any nodule or dendrite. This finding is consistent with previous investigations that methanesulfonic acid can reduce the dendritic growth [10,27], which has been a major problem in the zinc-halogen redox flow batteries, leading to short circuit and hence reduced life cycle [70–73]. In a zinc–bromine system, zinc dendrite was observed at current density as low as 15 mA cm^{-2} [3]. Therefore, methanesulfonic acid is attractive for zinc-based redox flow battery, as it not only minimizes the dendritic growth but also maintain high charge efficiency (91%) as discussed in Section 3.4.

With the addition of potassium sodium tartrate, similar microstructure of the rough, irregular plate-like structure was observed as in the absence of additive (Fig. 6b). Comparing with the previous micrograph, the hexagonal platelets were more difficult to distinguish and were mostly covered by the irregular plate structures. This was due to the faster growth rate of the zinc platelets at the lower overpotential of potassium sodium tartarate as suggested in the voltammetric study of this work. In the presence of tetrabutylammonium hydroxide (Fig. 6c), the microstructure was very different and was formed by nano size needle-shaped structures. Similar morphology has been reported by Gomes and da Silva Pereira [68] in the presence of cetyl trimethyl ammonium bromide in the sulfate medium. The needle-shaped microstructure was due to the competition between nucleation and crystal growth by the strong blocking effect of the absorbed surfactant as discussed in Section 3.5. The strong blocking effect and the adsorption of tetrabutylammonium hydroxide has been examined by the low charge and voltage efficiencies in the deposition and stripping experiment in a parallel flow cell (Section 3.4.3).

Among the additives tested, indium oxide had the highest half-cell efficiencies and a significant effect on the cell voltage. Due to the low deposition overpotential, zinc deposited at a faster rate and boulder-like agglomerates were observed after the addition of indium oxide. The boulder structure as shown in Fig. 6d has been considered to be a precursor of dendrites but the latter will not necessarily develop [74]. In this work, relatively rough and nodular morphology was observed instead of dendrites. On the coating surface, a small amount of indium (0.55 wt.%) has been detected by the energy-dispersive spectroscopy. In all

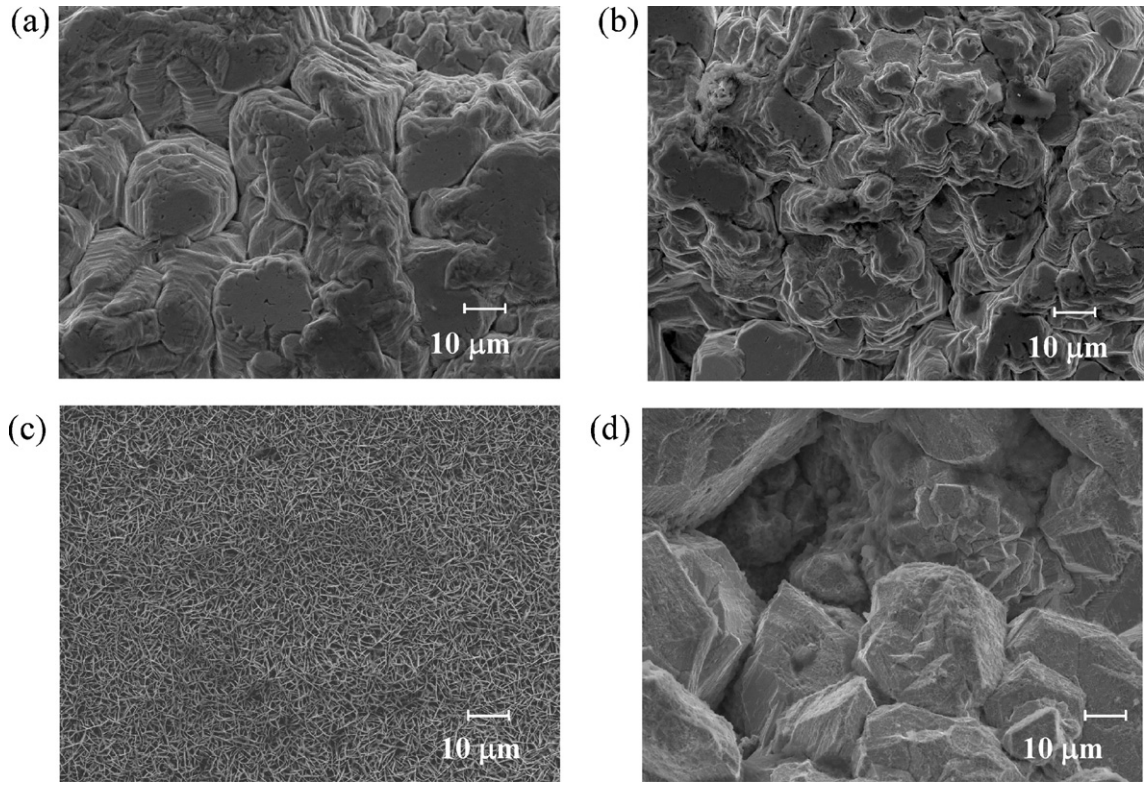

Fig. 6. The effect of electrolytic additives on microstructure of zinc electrodeposits obtained on a carbon polyvinyl-ester composite for a methanesulfonic acid bath in a beaker. Electrolytic additives 2×10^{-3} mol dm^{-3}, (i) no additive, (ii) potassium sodium tartarate, (iii) tetrabutylammonium hydroxide and (iv) indium oxide. Electrolyte compositions and operating conditions were as in Fig. 5 but stirring at 400 rpm.

electrodeposits, no dendrite has been observed after depositing for 4 h at 50 mA cm^{-2} in the absence or presence of the electrolytic additives.

4. Conclusions

Zinc electrodeposition from 0.01 mol dm^{-3} Zn(II) ions in methanesulfonic acid is a mass transport controlled process and with a zinc ion diffusion coefficient of 7.5×10^{-6} cm^2 s^{-1} obtained from the Randles-Sevick and Levich equations.

At a higher acid concentration, a significant decrease in charge efficiency was observed due to more dominant hydrogen evolution and faster corrosion rate. Although higher zinc ion concentration led to more difficult dissolution process, it is still advantageous for redox flow battery application as not only facilitates the deposition process, but also allows the battery to charge at a high current density without mass transport limitation and ensures enough Zn(II) ions at all state of charge. The optimum electrolyte compositions for flow battery application were suggested at high zinc(II) methanesulfonate concentration (1.5–2 mol dm^{-3}) and at low methanesulfonic acid concentration (i.e. 0.5 mol dm^{-3}).

In the presence and absence of the electrolytic additives tested, no dendrite was observed in all zinc electrodeposits at 50 mA cm^{-2} and 60 °C over 4 h. The low deposition overpotential observed with the addition of 2×10^{-3} mol dm^{-3} potassium sodium tartarate and indium oxide led to irregular, layer-like and granular microstructures, respectively. Among the three additives tested, only indium oxide was suitable for zinc-based redox flow battery as energy efficiency improved significantly from 62% in the absence of additives to 73% due to the improvement of both charge and voltage efficiencies in the presence of additives.

Acknowledgements

Financial support has been provided by the Research Institute for Industry (RIfI) at the University of Southampton. The authors are grateful to Dr. L. Berlouis, University of Strathclyde for helpful discussions. The authors particularly appreciate the training in electron microscopy provided by Miss Chao Ma and Dr Shuncai Wang. This work represents part of P.K. Leung's PhD research programme on the development of zinc-based flow batteries for energy storage and conversion technologies.

References

[1] N. Tokuda, T. Kanno, T. Hara, T. Shigematsu, Y. Tsutsui, A. Ikeuchi, T. Itou, T. Kumamoto, SEI Technol. Rev. 50 (1998) 88.
[2] J. Makansi, J. Abboud, Energy Storage Council White Paper, 2002.
[3] C. Ponce de León, A. Frías-Ferrer, J. González-García, D.A. Szánto, F.C. Walsh, J. Power Sources 160 (2006) 716.
[4] J. Jorné, J.T. Kim, D. Kralik, J. Appl. Electrochem. 9 (1979) 573.
[5] T.R. Crompton, Battery Reference Book, 3rd ed., Elsevier Science & Technology Books, Newnes, Oxford, England/Boston, 2000, Chapter 14.
[6] P.C. Butler, D.W. Miller, A.E. Verardo, 17th Intersociety Energy Conversion Engineering conference, Los Angeles, 1982.
[7] H.S. Lim, A.M. Lackner, R.C. Knechtli, J. Electrochem. Soc. 124 (1977) 1154.
[8] G.B. Adams, Electrically rechargeable battery, US Patent 4180623 (25/12/1979).
[9] R.L. Clarke, B.J. Dougherty, S. Harrison, P.J. Millington, S. Mohanta, Cerium Batteries, US Patent 2004/0202925 A1 (2004).
[10] R. Clarke, Zinc air battery with acid electrolyte, US Patent 7582385 B2 (01/09/2009).
[11] J. Bard, L.R. Faulkner, Electrochemical Methods – Fundamentals and Applications, 2nd ed., Wiley, 2001.
[12] Plurion Systems Inc., http://pluriionsystems.com/contact.html, 2011 (accessed on 26.04.11).
[13] M.D. Gernon, M. Wu, T. Buszta, P. Janney, Green Chem. 1 (1999) 127.
[14] R.P. Kreh, R.M. Spotnitz, J.T. Lundquist, J. Org. Chem. 54 (1989) 1526.
[15] J.Y. Lee, J.W. Kim, M.K. Lee, H.J. Shin, H.T. Kim, S.M. Parka, J. Electrochem. Soc. 151 (2004) C25.
[16] K. Saber, C.C. Koch, P.S. Fedkiw, J. Mater. Sci. Eng. A341 (2003) 174.

[17] M. Mouanga, L. Ricq, G. Douglade, J. Douglade, P. Berçot, J. Surf. Coat. Technol. 201 (2006) 762.
[18] J.X. Yu, Y.Y. Chen, H.X. Yang, Q.A. Huang, J. Electrochem. Soc. 146 (1999) 1789.
[19] G. Trejo, R. Ortega, Y. Meas, P. Ozil, E. Chaînet, B. Nguyen, J. Electrochem. Soc. 145 (1998) 4090.
[20] D.S. Baik, D.J. Fray, J. Appl. Electrochem. 31 (2001) 1141.
[21] M. Sanchez Cruz, F. Alonso, J.M. Palacios, J. Appl. Electrochem. 23 (1993) 364.
[22] M.C. Li, S.Z. Luo, Y.H. Qian, W.Q. Zhang, L.L. Jiang, J.I. Shen, J. Electrochem. Soc. 154 (2007) D567.
[23] M. Shanmugasigamani, J. Pushpavanam, Appl. Electrochem. 36 (2006) 315.
[24] M.C. Li, L.L. Jiang, W.Q. Zhang, Y.H. Qian, S.Z. Luo, J.N. Shen, J. Solid State Electrochem. 11 (2007) 549.
[25] C.K. Sarangi, B.C. Tripathy, I.N. Bhattacharya, T. Subbaiah, S.C. Das, B.K. Mishra, Miner. Eng. 22 (2009) 1266.
[26] G. Nikiforidis, L. Berlouis, D. Hall, D. Hodgson, J. Power Sources. Available online from 21 January 2011. doi:10.1016/j.jpowsour.2011.01.036.
[27] G. Brodt, J. Haas, W. Hesse, H.U. Jäqer, Method for electrolytic galvanizing using electrolytes containing alkane sulphonic acid, US Patent 2003/0141195 Al (31/07/2003).
[28] M. Skyllas-Kazacos, F. Grossmith, J. Electrochem. Soc. 134 (1987) 2950.
[29] H.T. Zhou, H.M. Zhang, P. Zhao, B.L. Yi, Electrochim. Acta 51 (2006) 6304.
[30] C.M. Hagg, M. Skyllas-Kazacos, J. Appl. Electrochem. 32 (2002) 1063.
[31] J.X. Yu, H.X. Yang, X.P. Ai, Y.Y. Chen, Russian J. Electrochem. 38 (2002) 321.
[32] A. Gomes, M.I. da Silva Pereira, Electrochim. Acta 52 (2006) 863.
[33] A.M. Volmer, Z. Weber, J. Phys. Chem. 119 (1926) 277.
[34] J.C. Ballesteros, P. Díaz-Arista, Y. Meas, R. Ortega, G. Trejo, Electrochim. Acta 52 (2007) 3686.
[35] F.C. Walsh, M.E. Herron, J. Phys. D: Appl. Phys. 24 (1991) 217.
[36] R.C. Kerby, H.E. Jackson, T.J. O'Keefe, Y.M. Wang, Metall. Mater. Trans. B 8 (1977) 661.
[37] F. Ganne, C. Cachet, G. Maurin, R. Wiart, E. Chauveau, J. Petitjean, J. Appl. Electrochem. 30 (2000) 665.
[38] E. Budevski, G. Staikov, W.J. Lorenz, Electrochim. Acta 45 (2000) 2559.
[39] B.Z. Jugović, T.L. Trišović, J.S. Stevanović, M.D. Maksimović, B.N. Grgur, Electrochim. Acta 51 (2006) 6268.
[40] J. McBreen, E. Gannon, J. Electrochem. Soc. 130 (1983) 1667.
[41] H. Fischer, Electrochim. Acta 2 (1960) 50.
[42] H. Fischer, Elektrolytische Absecheichung and Electrokrystallisation der Metallen Springer Berlin, 1954.
[43] M.A.M. Ibrahim, J. Chem. Technol. Biotechnol. 75 (2000) 745.
[44] A. Zirino, M.L. Healy, Limnol. Oceanogr. 15 (1970) 956.
[45] A.E. Dong, J. Appl. Spectrosc. 27 (1977) 124.
[46] L.E. Morón, Y. Meas, R. Ortega-Borges, J.J. Perez-Bueno, H. Ruiz, G. Trejo, Int. J. Electrochem. Sci. 4 (2009) 1735.
[47] J. Torrent-Burgués, E. Guaus, J. Portugaliae Electrochim. Acta 21 (2003) 179.
[48] E. Guerra, Evaluation of Zinc Electrodeposition Kinetics from Acidic Zinc Sulfate Solutions using a UPD Modified Platinum Substrate, University of British Columbia, 2003. https://circle.ubc.ca/handle/2429/16770 (accessed 26.04.11).
[49] G. Trejo, H. Ruiz, R. Ortega Borges, Y. Meas, J. Appl. Electrochem. 31 (2001) 685.
[50] K. Sato, K. Yamato, K. Iozumi, Trans. Iron Steel Inst. Jpn. 23 (1983) 946.
[51] L.J. Durney, W.H. Safranek, Electroplating engineering handbook, in: High Speed Electroplating, Common Technique for Sustaining High Current Density and a Fast Deposition Rate, Chapman & Hall, 1998, Chapter 39.
[52] C Cachet, R. Wiart, Electrochim. Acta 44 (1999) 4743.
[53] M. Yano, S. Fujitani, K. Nishio, Y. Akai, M. Kurimura, J. Power Sources 74 (1998) 129.
[54] L. Mirkova, G. Maurin, I. Krastev, C. Tsvetkova, J. Appl. Electrochem. 31 (2001) 647.
[55] B.C. Tripathy, S.C. Das, G.T. Hefter, P. Singh, J. Appl. Electrochem. 28 (1998) 915.
[56] J.L. Zhu, Y.H. Zhou, C.Q. Gao, J. Power Sources 72 (1998) 231.
[57] C.W. Lee, K. Sathiyanarayanan, S.W. Eom, H.S. Kim, M.S. Yun, J. Power Sources 159 (2006) 1474.
[58] C.W. Lee, K. Sathiyanarayanan, S.W. Eom, H.S. Kim, M.S. Yun, J. Power Sources 160 (2006) 161.
[59] Jr. Diaddario, L. Leonard, Method for improving the macro throwing power for chloride zinc electroplating baths, US Patent 6143160 (2000).
[60] Q.B. Zhang, Y.X. Hua, T.G. Dong, D.G. Zhou, J. Appl. Electrochem. 39 (2009) 1207.
[61] E.M. Hofer, H.E. Hintermann, J. Electrochem. Soc. (1963) 103.
[62] A.E. Saba, A.E. Elsherief, Hydrometallurgy 54 (2000) 91.
[63] F. Galvani, I.A. Carlos, J. Met. Finish 95 (1997) 70.
[64] A.M. Alfantazi, D.B. Dreisinger, J. Hydrometallurgy 69 (2003) 99.
[65] A. Hazza, D. Pletcher, R. Wills, Phys. Chem. Chem. Phys. 6 (2004) 1773.
[66] C.C. Yang, S.J. Lin, J. Power Sources 112 (2002) 497.
[67] C.C. Hu, C.Y. Chang, J. Mater. Chem. Phys. 86 (2004) 195.
[68] A. Gomes, M.I. da Silva Pereira, Electrochim. Acta 51 (2006) 1342.
[69] S.K. Lee, J.H. Lee, Y.H. Kim, J. Electronic Mater. 36 (2007) 1442.
[70] Y. Ando, T. Ochiai, Electrolyte for zinc–bromine storage batteries, US Patent 4510218 (04/09/1985).
[71] Y. Ando, Zinc dendrite inhibitor, US Patent 4479856 (1984).
[72] F.G. Will, Dendrite-inhibiting electrolytic solution and rechargeable aqueous zinc-halogen cell containing the solution, US Patent 4074028 (02/14/1978).
[73] R.A. Putt, M.J. Montgomery, Metal-halogen battery having reduced dendrite growth, US Patent 4218521 (08/19/1980).
[74] I.N. Justinijanović, J.N. Jovićević, A.R. Despić, J Appl. Electrochem. 3 (1973) 193.

Electrochimica Acta 56 (2011) 2145–2153

Contents lists available at ScienceDirect

Electrochimica Acta

journal homepage: www.elsevier.com/locate/electacta

Ce(III)/Ce(IV) in methanesulfonic acid as the positive half cell of a redox flow battery

P.K. Leung, C. Ponce de León*, C.T.J. Low, F.C. Walsh

Electrochemical Engineering Laboratory, Energy Technology Research Group, University of Southampton, Highfield, Southampton, Hampshire SO17 1BJ, United Kingdom

ARTICLE INFO

Article history:
Received 19 October 2010
Received in revised form 8 December 2010
Accepted 9 December 2010
Available online 16 December 2010

Keywords:
Cerium
Energy storage
Methanesulfonic acid
Redox flow battery

ABSTRACT

The characteristics of the Ce(III)/Ce(IV) redox couple in methanesulfonic acid were studied at a platinum disk electrode (0.125 cm^2) over a wide range of electrolyte compositions and temperatures: cerium (III) methanesulfonate (0.1–1.2 mol dm^{-3}), methanesulfonic acid (0.1–5.0 mol dm^{-3}) and electrolyte temperatures (295–333 K). The cyclic voltammetry experiments indicated that the diffusion coefficient of Ce(III) ions was 0.5×10^{-6} cm^2 s^{-1} and that the electrochemical kinetics for the oxidation of Ce(III) and the reduction of Ce(IV) was slow. The reversibility of the redox reaction depended on the electrolyte composition and improved at higher electrolyte temperatures. At higher methanesulfonic acid concentrations, the degree of oxygen evolution decreased by up to 50% when the acid concentration increased from 2 to 5 mol dm^{-3}. The oxidation of Ce(III) and reduction of Ce(IV) were also investigated during a constant current batch electrolysis in a parallel plate zinc–cerium flow cell with a 3-dimensional platinised titanium mesh electrode. The current efficiencies over 4.5 h of the process Ce(III) to Ce(IV) and 3.3 h electrolysis of the reverse reaction Ce(IV) to Ce(III) were 94.0 and 97.6%, respectively. With a 2-dimensional, planar platinised titanium electrode (9 cm^2 area), the redox reaction of the Ce(III)/Ce(IV) system was under mass-transport control, while the reaction on the 3-dimensional mesh electrode was initially under charge-transfer control but became mass-transport controlled after 2.5–3 h of electrolysis. The effect of the side reactions (hydrogen and oxygen evolution) on the current efficiencies and the conversion of Ce(III) and Ce(IV) are discussed.

1. Introduction

In recent years, increasing attention has been given to the development of sustainable utility-scale energy storage and conversion technologies. The redox flow battery can provide an efficient supply and management of electrical power. This technology has applications in bulk energy storage, load levelling, strategic power supplies and electric vehicles [1]. Several papers have focused on the application of methanesulfonic acid as an electrolyte for redox flow batteries [2–4] since many metal ions are readily soluble at high concentrations and are stable in this electrolyte [5]. Such conditions are attractive for a redox flow battery since they can result in a longer battery cycle life and greater energy storage capacity. The Ce(III)/Ce(IV) redox couple [6–8] has been considered as the positive electrode reaction in zinc–cerium [9–11] and vanadium–cerium flow batteries [12] since it offers a large positive potential which leads to a high potential difference for a charged battery. At the positive electrode, the standard electrode potential of the Ce(III)/Ce(IV) redox couple, reaction (1), lies between 1.28 V and 1.72 V *vs.* SHE depending on the supporting electrolytes [13]:

$$Ce(III) - e^- \leftrightarrows Ce(IV) \quad (1)$$

In the case of a zinc–cerium redox flow battery, the desired negative electrode reaction on charge would be:

$$Zn(II) + 2e^- Zn, \quad E^0 = -0.76\,V\ vs.\ SHE \quad (2)$$

In order to optimise the cerium half-cell as the positive electrode reaction in a redox flow battery, an improved understanding of the electrochemical kinetics of Ce(III)/Ce(IV) redox couple in methanesulfonic acid at different conditions is crucial. To date, only a limited number of investigations have been directed to the electrochemistry of cerium in methanesulfonic acid, the reduction of Ce(IV) and to the reversibility of the Ce(III)/Ce(IV) system. Earlier studies have been mainly focused on the oxidation of Ce(III) in sulfuric and nitric acid electrolytes. Previous studies of the oxidation of Ce(III) and reduction of Ce(IV) in methanesulfonic acid have typically used 0.01–0.1 mol dm^{-3} cerium (III) methanesulfonate [14–16]. Such a low concentration of the electroactive species is not

* Corresponding author at: Electrochemical Engineering Group, School of Engineering Sciences, University of Southampton, Highfield, Southampton, Hampshire SO17 1BJ, United Kingdom. Tel.: +44 (0)23 80598931; fax: +44 (0)23 80597051.
E-mail address: capla@soton.ac.uk (C. Ponce de León).

0013-4686/$ – see front matter © 2010 Elsevier Ltd. All rights reserved.
doi:10.1016/j.electacta.2010.12.038

practical in a redox flow battery since the amount of energy that can be made available depends on the concentration of the electroactive species. These investigations are useful to calculate the kinetic parameters of the Ce(III)/Ce(IV) redox couple but a cerium based flow battery requires a higher concentration of cerium (III) methanesulfonate, typically 0.5–2.0 mol dm^{-3} in a wide concentration range of methanesulfonic acid e.g. from 1.0 to 6.0 mol dm^{-3}. This is mainly due to changes in the electrolyte concentration during the charge–discharge cycles.

In this work, we report the electrochemistry of the Ce(III)/Ce(IV) redox couple in methanesulfonic acid over a range of electrolyte compositions typically found in a redox flow battery. The oxidation of Ce(III) and reduction of Ce(IV) are studied via cyclic voltammetry at a platinum disc electrode and at constant current electrolysis in a divided, two compartment parallel plate flow reactor. The reversibility of the Ce(III)/Ce(IV) redox couple as a function of cerium (III) methanesulfonate and methanesulfonic acid concentrations at various electrolyte temperatures is investigated. A suitable electrolyte composition for the positive electrode reaction in a redox flow battery using a cerium half-cell is suggested.

2. Experimental

2.1. Preparation of cerium (III) methanesulfonate solution

Cerium (III) methanesulfonate was prepared by mixing cerium (III) carbonate powder (Treibacher Industrie AG, Germany; 99 wt.%) with aqueous methanesulfonic acid (Sigma–Aldrich, U.K.; 70 vol.%) to produce concentrations in the range of 0.1–1.2 mol dm^{-3}. During the chemical reaction, the temperature was maintained at 80 °C and the solution was stirred via a magnetic stirrer at approximately 500 rpm using a polytetrafluoroethylene (PTFE) coated steel magnetic bar (Fisherband, U.K.; 1 cm diameter, 4 cm length). Cerium (III) carbonate from different suppliers was tested but only the one from the supplier mentioned above yielded a clear solution of cerium (III) methanesulfonate with no residual precipitated carbonate, after being stirred for 6 h. This preparation method is similar to those reported in the literature [5,17]. In these experiments, the clear solution was used.

2.2. Cyclic voltammetry

Cyclic voltammetry was carried out in a divided, three-electrode glass electrochemical cell between +0.5 V and +1.9 V *vs.* Ag|AgCl at a potential sweep rate in the range of 4–256 mV s^{-1}. The working electrodes were static platinum and glassy carbon disk electrodes (area 0.125 cm^2) (Metrohm) while the counter electrode was a platinum mesh (area 1 cm^2). Prior to each measurement, the working electrodes were manually polished using alumina powders (Leco) of 3 and 0.05 μm on a moist polishing cloth (Beuhler). The powder was then wiped with a clean piece of polishing cloth and rinsed with plenty of ultra-pure water (18 MΩ cm resistivity, Elga water purification system). The working and counter electrode compartments were separated by a Nafion® membrane (Dupont, NF115/H^+).

The electrode potentials were measured against a saturated silver-silver chloride reference electrode, Ag|AgCl (ABB, Series 1400). The volume of the working electrode compartment was approximately 160 cm^3 and the electrolyte temperature was in the range 273–343 ± 2 K maintained with a thermostatic water bath (Grant, LVF6). The cyclic voltammograms were recorded over for a wide range of electrolyte compositions including 0.05–1.2 mol dm^{-3} cerium (III) methanesulfonate in 0.1–5.0 mol dm^{-3} methanesulfonic acid. All electrochemical measurements were carried out using an EcoChemie Autolab (PGSTAT20) computer controlled potentiostat fitted with the General Purpose Electrochemical Software (GPES) Version 4.5.

2.3. Electrolysis in a flow cell

The electrochemical oxidation of Ce(III) and reduction of Ce(IV) were carried out in a divided, parallel plate flow cell. The cell consisted of a polyvinyl chloride (PVC) casing holding two acrylic flow channels of 8 mm thickness each, which contained the negative and positive electrodes, separated by a cation-conducting Nafion® membrane (DuPont, NF115/H^+). Rubber silicon gaskets of 1.5 mm thickness were used between the compartments and membrane. The overall dimensions of the cell were 10.2 cm × 4.7 cm × 4.5 cm. The positive electrodes were 2- and 3-dimensional platinised titanium: the exposed area of the 2-dimensional electrode was 9 cm^2 (4.5 cm × 2.0 cm) and 3.5 μm thickness with a platinum load of 7.0 mg cm^{-2} (Magneto GmbH, Netherlands). The 3-dimensional electrode was manufactured by spot-welding four pieces of platinised titanium mesh (7.0 mg cm^{-2}, 4.4 cm × 1.6 cm, Magneto GmbH, Netherlands) onto a planar platinised titanium plate (Magneto GmbH, Netherlands). The negative electrode material was a carbon polyvinyl-ester composite (BMC 18649, Engtegris GmbH, Germany) with an exposed area of 9 cm^2 (4.5 cm × 2.0 cm). The gap from the electrode surface to the membrane was 2 cm.

The volume of the positive electrolyte was 100 cm^3 and contained 0.8 mol dm^{-3} cerium (III) methanesulfonate in 4.0 mol dm^{-3} methanesulfonic acid while the negative electrolyte was also 100 cm^3 containing 1.5 mol dm^{-3} zinc methanesulfonate in 1.0 mol dm^{-3} methanesulfonic acid. Each electrolyte was circulated through the cell at a mean linear flow velocity of 3.9 cm s^{-1} from separated storage tanks using two peristaltic pumps (Cole-Parmer, Masterflex® model 7553079). The temperature of both electrolytes was controlled at 323 K by a water thermostat (Grant Model LV FG). The oxidation of Ce(III) was carried out at constant applied current densities of 20, 50 and 80 mA cm^{-2} for 4.5 h and the Ce(IV) ions were reduced at the same current densities of opposite sign until a sharp drop of output potential difference was observed during discharge. The current density reported in these experiments was calculated taking into account the geometrical area of the 2-dimensional negative electrode.

2.4. Determination of the concentration of Ce(IV)

The concentration of Ce(IV) in methanesulfonic acid was determined via a colorimetric redox titration method [18–20]. The steps followed were: (a) extraction of approximately 0.5 cm^3 of solution containing Ce(IV) from the electrolyte storage reservoir; (b) this volume was mixed with 9.5 cm^3 of 2.0 mol dm^{-3} methanesulfonic acid and few drops of ferroin (1,10-orthophenanthroline-ferrous sulphate complex, Fluka, Switzerland) indicator; (c) this solution was then titrated with of 0.01 mol dm^{-3} ammonium iron(II) and (d) the concentration of Ce(IV) was determined from the amount of Fe(II) required for the complete reduction of Ce(IV) to Ce(III), indicated when the solutions changed from blue to a red colour due to the colorimetric redox indicator.

3. Results and discussion

3.1. Substrate material

Fig. 1 shows the cyclic voltammetry of the Ce(III)/Ce(IV) redox couple recorded at platinum and glassy carbon disk electrodes in an electrolyte containing 0.8 mol dm^{-3} cerium (III) methanesulfonate and 4.0 mol dm^{-3} methanesulfonic acid at 295 ± 2 K at a potential sweep rate of 50 mV s^{-1}. The oxidation of Ce(III) started at approximately +1.2 V *vs.* Ag|AgCl on both electrodes and the anodic current rose steadily as the potential became more positive. A higher current density, c.a. 39 mA cm^{-2} was recorded on the

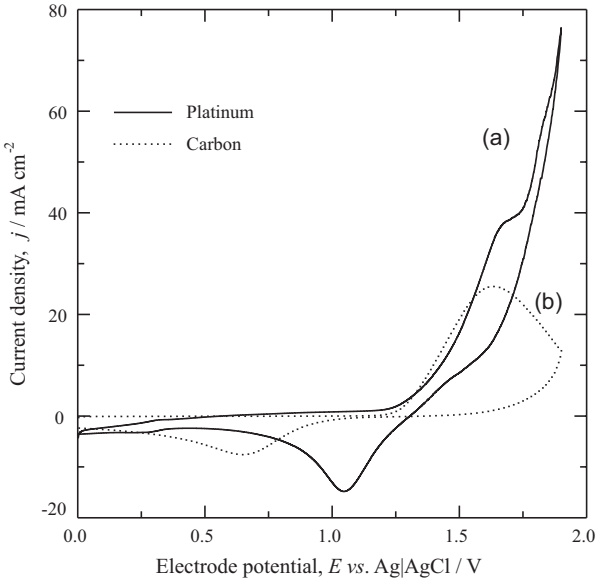

Fig. 1. Cyclic voltammograms for the Ce(III)/Ce(IV) redox couple in methanesulfonic acid at (a) platinum and (b) glassy carbon electrodes. Electrolyte: 0.8 mol dm^{-3} cerium (III) methanesulfonate in 4.0 mol dm^{-3} methanesulfonic acid at 295 K. The electrode potential was swept from 0 to +1.9 V *vs.* Ag|AgCl then from +1.9 to 0 V *vs.* Ag|AgCl at 50 mV s^{-1}.

platinum electrode compared with c.a. 25 mA cm^{-2} on the glassy carbon electrode at around 1.65 V *vs.* Ag|AgCl for both electrodes. At a more positive potential, the anodic current at the glassy carbon electrode decayed while at the platinum electrode continued to rise sharply due to the oxygen evolution reaction (and the formation of platinum oxides) [21,22]. The influence of oxygen evolution reaction does not seem to be significant on the glassy carbon electrode as the current during the oxidation of Ce(III) on this electrode did not increase at more positive potentials.

On the reverse scan, a more negative potential was required for the reduction of Ce(IV) on the glassy carbon than on the platinum electrode. A maximum cathodic peak current density of 15 mA cm^{-2} on platinum was observed at c.a. +1.05 V *vs.* Ag|AgCl while only 7.5 mA cm^{-2} at +0.65 V *vs.* Ag|AgCl at the glassy carbon electrode. The separation between the oxidation and reduction peaks on each electrode was approximately 0.7 V on platinum and 1.0 V on carbon. The anodic current was higher than the cathodic one and the ratio of cathodic to anodic peak current was approximately 0.4–0.6 on both electrodes. Platinum gives a more favourable electrochemical response than carbon for the oxidation of Ce(III) and reduction of Ce(IV) in methanesulfonic acid because the peak separation is smaller. Several features in the voltammogram are worth to mention: the separation of peak potentials is relatively high (several hundreds of millivolts) and the ratio of cathodic to anodic peak current is far below 1, the value expected for an ideally reversible system. The magnitude of oxygen evolution as a secondary reaction, especially on platinum electrode, also needs to be reduced in order to improve the current and conversion efficiencies. Since platinum gave a higher oxidation current and the separation between the oxidation and reduction peaks is smaller than using the glassy carbon electrode in the cyclic voltammograms, the following studies were carried out on a platinum electrode only.

3.2. Potential sweep rate

Fig. 2(a) shows the effect of the potential sweep rate on the cyclic voltammetry of the Ce(III)/Ce(IV) redox couple on a platinum electrode in an electrolyte containing 0.8 mol dm^{-3} cerium (III) methanesulfonate and 4.0 mol dm^{-3} methanesulfonic acid at 295 K. The peak current density of the oxidation and reduction processes increased linearly with the square root of the potential sweep rate. Fig. 2(b) shows the linear Randles–Sevćik relationship [13,23–25] indicating that the oxidation of Ce(III) and reduction of Ce(IV) in methanesulfonic acid were diffusion limited. Using the value of the slope from this plot during the oxidation process, the diffusion coefficient of Ce(III) ion in methanesulfonic acid was estimated to be 0.5×10^{-6} cm^2 s^{-1} at 295 K and increases to 1.52×10^{-6} cm^2 s^{-1} at 323 K. This value agrees with previous measurements of diffusion coefficients that where in the range of $0.27–0.72 \times 10^{-6}$ cm^2 s^{-1} [26], using a glassy carbon electrode in an electrolyte containing 0.034–0.152 mol dm^{-3} cerium (III) methanesulfonic in 1.0 and 4.0 mol dm^{-3} methanesulfonic acid at room temperature.

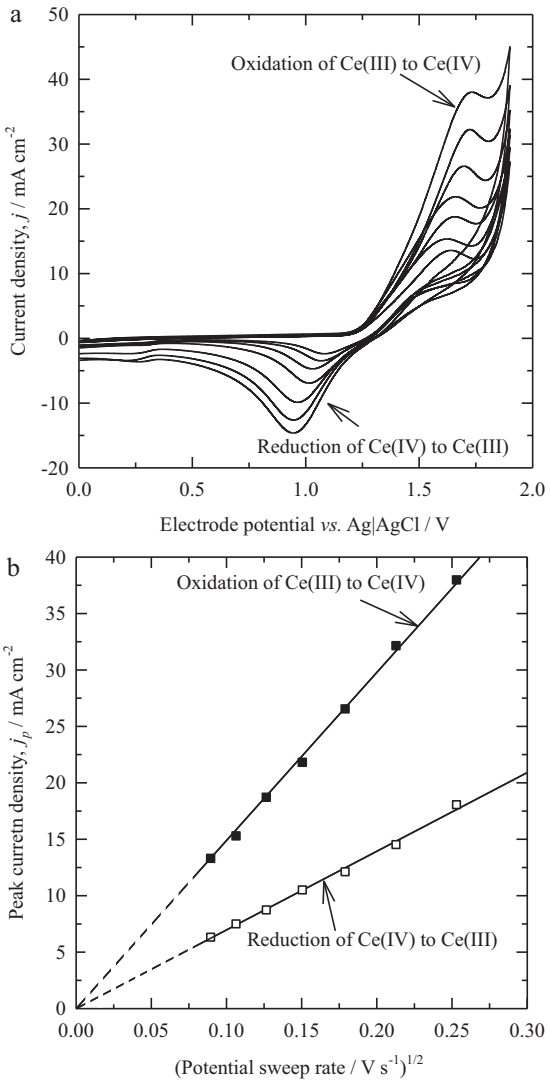

Fig. 2. The effect of potential sweep rate on the Ce(III)/Ce(IV) redox couple in methanesulfonic acid. (a) Cyclic voltammogram and (b) Randles–Sevćik plot. Electrolyte: as in Fig. 1. The potential sweep rates were 8, 11, 16, 22.6, 32, 45.3 and 64 mV s^{-1}. (■) Oxidation of Ce(III) and (□) reduction of Ce(IV).

The diffusion coefficient of Ce(III) ions in methanesulfonic acid was an order of magnitude smaller than those reported for many metal ions in aqueous electrolytes, which are typically $(4.0–6.0) \times 10^{-6}$ cm^2 s^{-1} [27,28] possibly due to the complexation with methanesulfonate ion [16]. Indeed, a lower diffusion coefficient value was found at increased methanesulfonic acid concentration, e.g. in an electrolyte containing 0.152 mol dm^{-3}

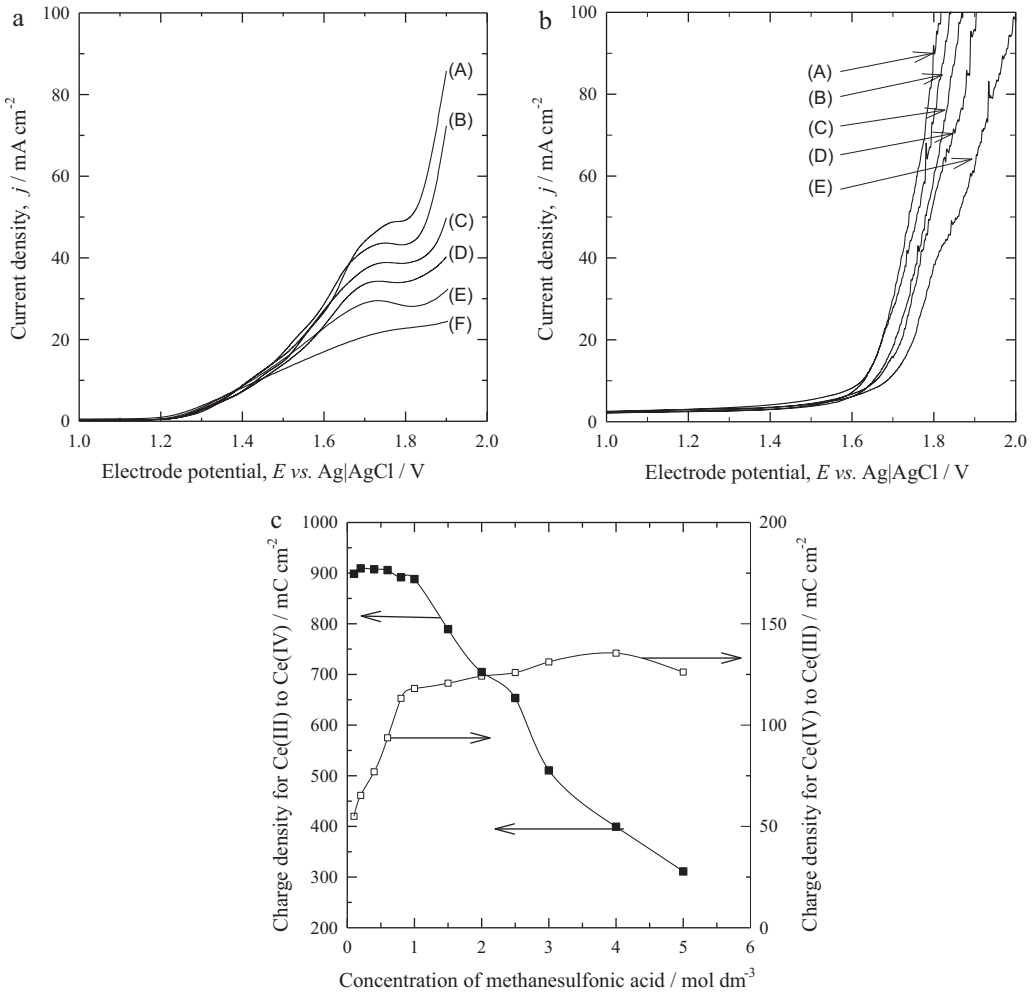

Fig. 3. The effect of methanesulfonic acid on (a) oxidation of Ce(III) to Ce(IV): (A) 2 mol dm^{-3}, (B) 2.5 mol dm^{-3}, (C) 3 mol dm^{-3}, (D) 4 mol dm^{-3}, (E) 4.5 mol dm^{-3} and (F) 5 mol dm^{-3} CH_3SO_3H, respectively, (b) oxygen evolution at platinum without Ce(III) ions: (A) 1 mol dm^{-3}, (B) 2 mol dm^{-3}, (C) 3 mol dm^{-3}, (D) 4 mol dm^{-3} and (E) 5 mol dm^{-3} CH_3SO_3H, respectively and (c) charge density for Ce(III)/Ce(IV) redox couple. Other electrolyte conditions were similar to those in Fig. 1. The charge density was calculated from the area under curve of the cyclic voltammograms between 0 and +1.9 V *vs.* Ag|AgCl at 50 mV s^{-1}. (■) Oxidation of Ce(III) and (□) reduction of Ce(IV).

cerium (III) methanesulfonate, the diffusion coefficient of Ce(III) was approximately 0.69×10^{-6} cm^2 s^{-1} in 1.0 mol dm^{-3} methanesulfonic acid but only 0.27×10^{-6} cm^2 s^{-1} in 4.0 mol dm^{-3} methanesulfonic acid [26].

For all potential sweep rates, the ratio of cathodic to anodic peak current was approximately 0.5. The charge density for the reduction of Ce(IV) was lower than the charge involved in the oxidation of the Ce(III) ion possibly due to the oxygen evolution secondary reaction during and after the oxidation of Ce(III) but no visible side reactions occurred during the reduction of Ce(IV). Earlier investigations also suggested that the larger anodic peak current could also be due to the contribution of the weak adsorption of Ce(III) ions on the electrode surface, which was demonstrated via cyclic voltammograms of the Ce(III)/Ce(IV) redox couple in sulfuric and methanesulfonic acids [16].

Recent studies have also shown that the cathodic and anodic peak currents can be brought closer via the complexation of Ce(III) and Ce(IV) ions with ligands such as ethylenediaminetetraacetic acid and diethylenetriaminepentaacetic acid [29,30]. Such strategy has been advantageous since the reversibility of the Ce(III)/Ce(IV) redox couple was significantly improved and higher charge densities were obtained [31]. The work also showed that the faster electrochemical kinetics in the presence of the ligands are due to a higher charge transfer coefficient and an increased rate constant for the Ce(III) ⇄ Ce(IV) redox reaction. The electron transfer rates were also found to be similar on the oxidation of Ce(III) and the reduction of Ce(IV), confirming that an improvement in the reversibility of these reactions using complexing ligands [31] can be achieved.

By increasing the potential sweep rate during the oxidation of Ce(III), the peak potential shifted to more positive values while for the reduction of Ce(IV) to more negative potentials. The separation of the peak potentials increased at higher potential sweep rates e.g. 560 mV at 8 mV s^{-1} compared to 790 mV at 64 mV s^{-1}. This finding suggests that the electrochemical kinetics of the Ce(III)/Ce(IV) redox couple is slow. Previous results reported similar observation in an electrolyte containing 0.034 mol dm^{-3} cerium (III) methanesulfonate in 4.0 mol dm^{-3} methanesulfonic acid at a glassy carbon electrode [14] e.g. the reduction peak shifted by approximately –100 mV as the potential sweep rate increased from 10 to 160 mV s^{-1}. Earlier investigations also showed a quasi-reversible behaviour of the Ce(III)/Ce(IV) redox couple in commodity electrolytes, such as sulfuric acid [6,32].

3.3. Concentration of methanesulfonic acid

Cyclic voltammograms of the Ce(III)/Ce(IV) redox couple were recorded at a platinum electrode in a wide range of methanesulfonic acid concentration from 0.1 to 5.0 mol dm^{-3}. Fig. 3(a) shows that the anodic current density for the oxidation of Ce(III) decreased as the concentration of methanesulfonic acid increased

when the electrolyte contained 0.8 mol dm^{-3} Ce(III) methanesulfonate. For example, the anodic peak current density was approximately 50 mA cm^{-2} in 2.0 mol dm^{-3} methanesulfonic acid but no oxidation peak was observed at 5.0 mol dm^{-3} acid concentration, although the current density reached 20 mA cm^{-2}. The change in the peak current density was due to the increase in the solution viscosity at high acid concentrations and high conductivity of the acid at low concentrations in aqueous electrolytes [6,33]. Other findings reported in the literature also showed similar observation: the anodic peak current was 3.6 mA cm^{-2} in 1.0 mol dm^{-3} methanesulfonic acid and decreased to 1.6 mA cm^{-2} in 6.0 mol dm^{-3} methanesulfonic acid in a solution where the starting electroactive species was Ce(IV) at 0.033 mol dm^{-3} concentration [16].

Further increase in the anodic current after the oxidation of Ce(III) was caused by oxygen evolution, which was found to be influenced by the methanesulfonic acid concentration. The linear sweep voltammograms in the absence of Ce(III) with different concentrations of the acid in Fig. 3(b) shows that oxygen evolution shifted to more positive potentials at a higher acid concentration. For example, at an electrode potential of approximately +1.8 V *vs.* Ag|AgCl, the anodic current density was around 80 mA cm^{-2} in 2.0 mol dm^{-3} methanesulfonic acid, but at the same potential the current density was only 40 mA cm^{-2} in 5.0 mol dm^{-3} methanesulfonic acid. Although a similar behaviour has been found in sulfuric acid, the cathodic current density in such media was smaller [34]. These findings suggest that the oxidation of Ce(III) is the dominant reaction at a higher concentration of methanesulfonic acid and is consistent with observations during the experiment where less oxygen bubbles appeared on the electrode surface during the oxidation of Ce(III) at high acid concentrations.

Fig. 3(c) shows the charge density involved in the oxidation and reduction of Ce(III) and Ce(IV) ions respectively, *vs.* the concentration of methanesulfonic acid. The charge density, calculated from the area under the curve of the cyclic voltammogram, during the oxidation of Ce(III) is constant up to 1 mol dm^{-3} of methanesulfonic acid and then decreases sharply as the acid concentration increases. This is consistent with the observations made on the cyclic voltammograms shown in Fig. 3(a and b). The charge density for the reduction of Ce(IV) increased significantly with the concentration of acid up to 1 mol dm^{-3}, after that the charge increase is slow and reaches a maximum at 4.0 mol dm^{-3} methanesulfonic acid. A further increase in the acid concentration led to a slight reduction in both charge and current density for the reduction of Ce(IV). This is attributed to an increase in solution viscosity [35] and the solubility limit of Ce(III) in 5.0 mol dm^{-3} methanesulfonic acid, which might have been exceeded. At such a high acid concentration, the solubility limit of Ce(III) was estimated to be approximately 0.7 mol dm^{-3} [15].

3.4. Concentration of cerium (III) methanesulfonate

Fig. 4(a) shows that the charge density for both the oxidation of Ce(III) and reduction of Ce(IV) increased when the Ce(III) methanesulfonate changed from 0.1 to 1.0 mol dm^{-3} in a solution containing 4.0 mol dm^{-3} methanesulfonic acid. A further increase in the concentration of cerium (III) methanesulfonate to 1.2 mol dm^{-3} led to a reduction in the charge density for both processes. This was due to the limited solubility of Ce(III) at such acid concentration as previous results showed that 1.0 mol dm^{-3} was the solubility limit for Ce(III) and Ce(IV) in 4.0 mol dm^{-3} methanesulfonic acid at room temperature [15,36]. This observation is also consistent with previous results where a high concentration of Ce(III) could only be achieved in a low concentration of methanesulfonic acid. The concentration of Ce(IV) however, could only be increased in higher methanesulfonic acid concentrations [15].

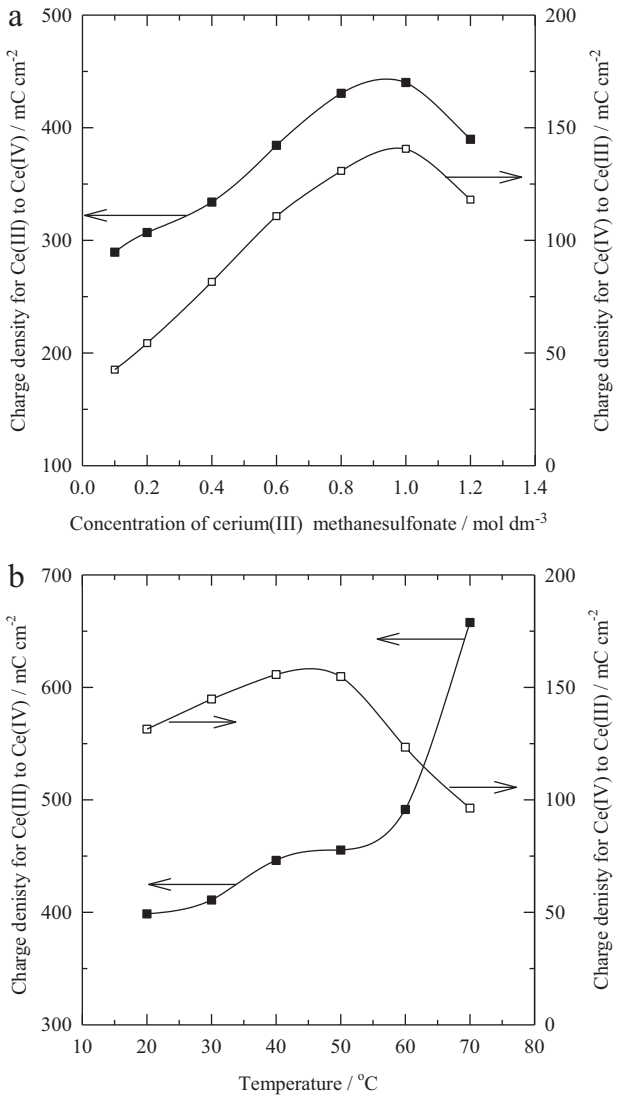

Fig. 4. The effect of operating parameters on the cyclic voltammograms of the Ce(III)/Ce(IV) redox couple in methanesulfonic acid: (a) concentration of Ce(III) in the electrolyte and (b) temperature of the electrolyte on the charge density for Ce(III)/Ce(IV) redox couple. Other electrolyte conditions: as in Fig. 1. The charge density was calculated from the area under the cyclic voltammograms between 0 and +1.9 V *vs.* Ag|AgCl at 50 mV s^{-1}. (■) Oxidation of Ce(III) and (□) reduction of Ce(IV).

Since the acidity of the electrolyte in the flow battery will change during charge–discharge cycles, the challenge is to use an appropriate concentration of methanesulfonic acid which provides sufficient solubility for both Ce(III) and Ce(IV) species. The results above show that a solution with higher concentration of Ce(III), e.g. 1.5–2.0 mol dm^{-3} could be prepared in a low acid concentration. However, the Ce(IV) solution obtained during or from a constant current electrolysis under this conditions was highly viscous and slurry [37]. A high concentration of Ce(IV) could be prepared if the concentration of acid is high but the solubility of Ce(III) became limited and the Ce(III)/Ce(IV) redox couple demonstrated poor reversibility. Therefore, a solution of 0.8 mol dm^{-3} cerium (III) methanesulfonate was prepared in 4.0 mol dm^{-3} methanesulfonic acid as a compromise in order to maximize the solubility of both Ce(III) and Ce(IV) ions.

Table 1
The effect of operational parameters on the separation of the peak potentials and the ratio of peak currents. Unless stated, the temperature of the electrolyte was 295 K and the electrolyte contained 0.8 mol dm^{-3} cerium (III) methanesulfonate in 4.0 mol dm^{-3} methanesulfonic acid. The data was estimated from cyclic voltammograms recorded in the potential range from 0 to +1.9 V *vs.* Ag|AgCl at a potential sweep rate of 50 mV s^{-1}.

Operational parameter	Separation of the peak potentials (mV)	Ratio of cathodic to anodic peak current
Potential sweep rate (mV s^{-1})		
8	558	0.51
16	557	0.54
32	736	0.50
64	788	0.51
Concentration of methanesulfonic acid (mol dm^{-3})		
1.0	654	0.42
2.0	710	0.43
4.0	738	0.53
5.0	965	0.65
Concentration of cerium (III) methanesulfonate (mol dm^{-3})		
0.1	591	0.32
0.4	632	0.49
0.8	707	0.53
1.0	857	0.53
Temperature of the electrolyte (K)		
295	738	0.53
303	659	0.54
313	631	0.56
323	619	0.65
333	660	0.62

3.5. Electrolyte temperature

Fig. 4(b) shows that the charge density during the oxidation of Ce(III) increases with temperature. The reduction of Ce(IV) also increased but reached a maximum at 323 K. The higher charge density for the oxidation of Ce(III) could be due to the simultaneous oxygen evolution reaction which is favourable at high temperatures. Cyclic voltammograms recorded for 0.01 mol dm^{-3} Ce(III) in 1.0 mol dm^{-3} sulfuric acid also showed an increase in the charge density at elevated electrolyte temperature, e.g. 333 K [6]. During the electrolysis of Ce(III) ions in an undivided and divided electrochemical cell using nitric acid electrolyte, the applied cell potential difference decreased slightly as the temperature increased due to improved reaction kinetics, increased electrolyte conductivity and reduced viscosity. The study also showed that the current efficiency of the electrolysis of Ce(III) to Ce(IV) improved from 77% at 313 K to 93% at 363 K in nitric acid medium [35].

Previous work also demonstrated that the conversion of Ce(III) to Ce(IV) was higher at high electrolyte temperature, e.g. conversion increased from 45% to 93% when the temperature raised from 313 K to 363 K in 1.0 mol dm^{-3} Ce(III) contained in 3.0 mol dm^{-3} nitric acid [35]. An increase in the diffusion coefficient of Ce(III) ions and the rate constant for Ce(III) oxidation have also been observed at high electrolyte temperature [34]. Literature studies confirm that an Arrhenius, semi-logarithmic plot of the diffusion coefficient against the inverse of the electrolyte temperature is a linear relationship for the Ce(III) $\rightleftarrows$ Ce(IV) redox reaction in nitric and sulphuric acid electrolytes [33].

3.6. Reversibility of the Ce(III)/Ce(IV) redox couple

A series of cyclic voltammograms were recorded at a platinum electrode in various electrolyte compositions and the reversibility of the Ce(III)/Ce(IV) redox couple was investigated in terms of the separation of peak potentials and the ratio of cathodic to anodic peak currents. Table 1 shows these estimated values. Since the separation of the peak potentials was more than 59 mV and the ratio of the peak currents was less than unity, the Ce(III)/Ce(IV) redox couple in methanesulfonic acid can be considered as a quasi-reversible system [13,23]. The increase in the separation of peak potentials at increasing potential sweep rate shows that the redox reaction involved a slow electrochemical kinetic. The separation of peak potentials decreased at lower concentrations of cerium (III) methanesulfonate and methanesulfonic acid as well as at higher electrolyte temperatures. The ratio of cathodic to anodic peak current density varied from 0.3 to 0.65 depending on the electrolyte composition. The ratio was closer to one in an electrolyte containing a higher concentration of methanesulfonic acid and cerium (III) methanesulfonate as well as at an elevated electrolyte temperature.

At higher concentrations of cerium (III) methanesulfonate and methanesulfonic acid, the separation of oxidation and reduction peak potentials increased due to an increase in the ohmic drop and changes in the solution viscosity and conductivity. The high concentration also deteriorated the reversibility of the Ce(III)/Ce(IV) redox couple. At such concentration, the oxidation potential remains fairly constant but the reduction potential became more negative leading to lower discharge cell potential difference of a cerium-based redox flow battery. Such observations agree with other studies, for example the separation of peak potentials increased from 140 mV to 240 mV when the acid concentration changed from 2 to 5 mol dm^{-3} in a solution containing 0.033 mol dm^{-3} of Ce(III) [16].

Although a low concentration of cerium (III) methanesulfonate leads to a more reversible redox reaction, such a low concentration of Ce(III) ions would not be practical for a flow battery. Besides, the use of a low concentration of methanesulfonic acid also limits the solubility of Ce(IV) in the solution, hence the energy density available in a flow battery will be restricted. As mentioned earlier, in this study, a solution of 0.8 mol dm^{-3} cerium (III) methanesulfonate in 4.0 mol dm^{-3} methanesulfonic acid was suggested for flow battery applications. The use of elevated electrolyte temperature could also provide a more reversible redox reaction but will be limited by the properties of the materials used to construct the cell.

3.7. Constant current electrolysis in a zinc–cerium redox flow battery

The electrochemical oxidation of Ce(III) followed by the reduction of Ce(IV) ions was investigated in an electrolyte containing 0.8 mol dm^{-3} Ce(III) methanesulfonate in 4.0 mol dm^{-3} methanesulfonic acid. The reaction on the negative electrode was the electrodeposition and stripping of zinc onto a carbon polyvinyl-ester composite using 1.5 mol dm^{-3} zinc (II) methanesulfonate in 1.0 mol dm^{-3} methanesulfonic acid electrolyte. Both electrolytes were contained in external tanks and were approximately 100 cm^3 volume, circulated through the cell at a mean linear flow rate of 3.9 cm s^{-1} at 323 K temperature. Fig. 5(a) shows the concentration of Ce(IV) as a function of the electrolysis time using two types of platinised titanium electrodes: a 2-dimensional planar electrode and a 3-dimensional mesh electrode described in the experimental section. During the first 4.5 h, a charge current density of 50 mA cm^{-2} was applied through the cell and it was found that the concentration of Ce(IV) ion was higher when the 3-dimensional mesh electrode was used instead of the 2-dimensional planar electrode. At the end of the first 4.5 h, a current density of 50 mA cm^{-2} of opposite sign was applied to discharge the flow battery, reducing Ce(IV) ions to Ce(III) ions. As shown in Fig. 5(a), the concentration of Ce(IV) ion appears to increase and decrease linearly when the 3-dimensional electrode was used but not linear behaviour was observed on the 2-dimensional electrode.

The logarithm of the normalised cerium (IV) concentration *vs.* the electrolysis time was plotted in Fig. 5(b). This graph shows that a linear behaviour was observed during the oxidation of Ce(III) and

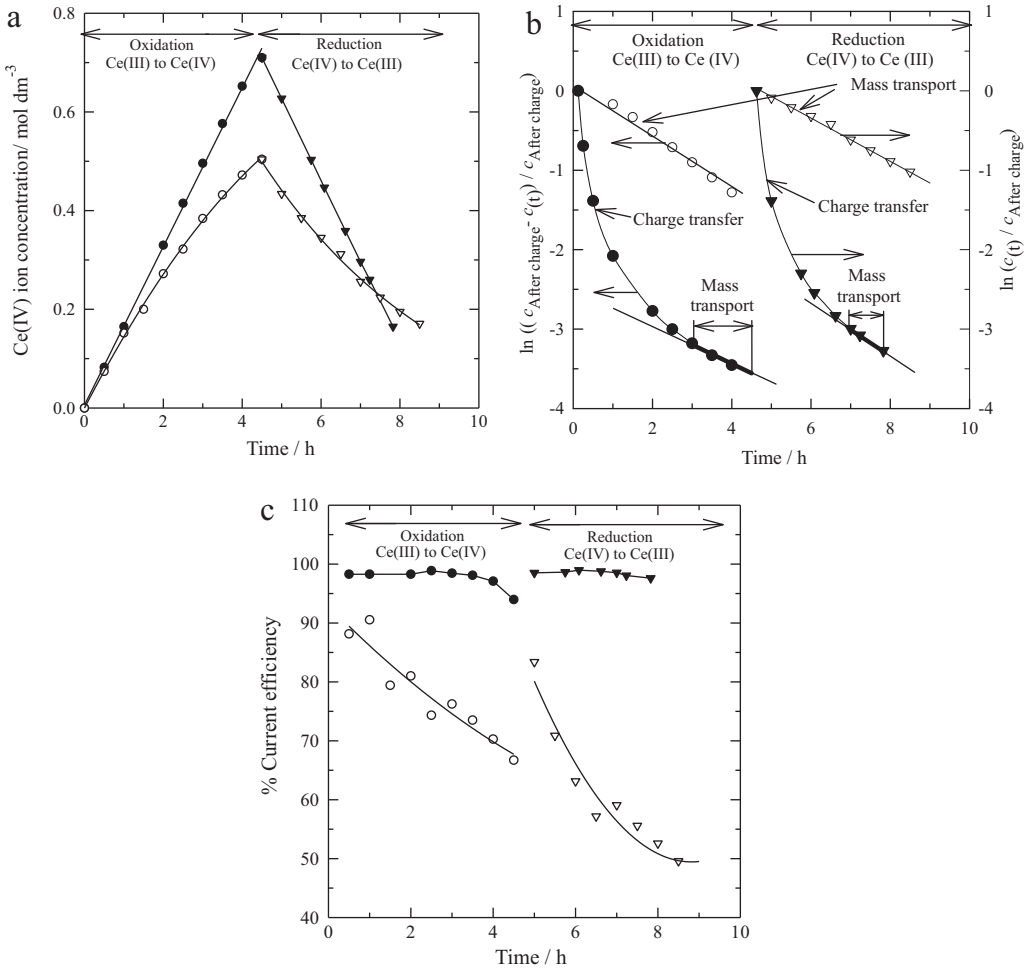

Fig. 5. Electrolysis at a constant current (approximately 50 mA cm^{-2}) of a solution containing 0.8 mol dm^{-3} cerium (III) methanesulfonate in 4.0 mol dm^{-3} methanesulfonic acid. Negative electrolyte was 1.5 mol dm^{-3} zinc methanesulfonate in 1.0 mol dm^{-3} methanesulfonic acid. Both electrolytes were circulated at 3.9 cm s^{-1} and at 323 ± 2 K. (a) Concentration of Ce(IV) *vs.* electrolysis time, (b) logarithmic plot of Ce(III) and Ce(IV) concentration *vs.* electrolysis time and (c) current efficiency. (○) Oxidation of Ce(III) using a 2-d planar electrode, (●) oxidation of Ce(III) using a 3-d mesh electrode, (▽) reduction of Ce(IV) using a 2-d planar electrode and (▼) reduction of Ce(IV) using a 3-d mesh electrode.

the reduction of Ce(IV) processes using a 2-dimensional planar electrode. This indicates that the increase and decrease in concentration of Ce(IV) ions on this electrode are mass transport controlled processes and follow a first order reaction kinetics on a continuous stirred tank batch model [38] given by the following equations:

During oxidation:

$$\ln\left(\frac{c_{\text{after charge}} - c_{(t)}}{c_{\text{after charge}}}\right) = -kt \tag{3}$$

During reduction:

$$\ln\left(\frac{c_{(t)}}{c_{\text{after charge}}}\right) = -kt \tag{4}$$

where $c_{\text{after charge}}$ is the concentration (mol m^{-3}) of Ce(IV) when the battery is charged, $c_{(t)}$ is the Ce(IV) concentration (mol m^{-3}) at the time t, k is the apparent first order rate constant (s^{-1}) and t is the time (s). This result is consistent with the previous findings in the cyclic voltammograms which showed that the oxidation of Ce(III) and reduction of Ce(IV) at a platinum rotating disk electrode were diffusion controlled reactions following the Randles–Sevćik equation. The apparent first order rate constant k, is equal to $k_m A/V$, where k_m is the mass transport coefficient (m s^{-1}), A is the electrode area (m^2) and V is the volume of electrolyte within the reactor (m^3).

Table 2 shows several reactor performances obtained at a constant current electrolysis during the oxidation of Ce(III) and reduction of Ce(IV) ions. The parameters were calculated based on a simplified bath reactor model [39], while the current efficiency (%) and the specific electrochemical energy consumption (W h g^{-1}) were calculated according to the Eqs. (5) and (6) below, respectively.

$$\text{Current efficiency, } \varphi = \frac{m_{\text{experimental}}}{m_{\text{theoetical}}} \times 100 \tag{5}$$

$$\text{Specific electrochemical energy consumption} = \frac{EIt}{m} \tag{6}$$

where $m_{\text{experimental}}$ is the amount of product determined experimentally during the electrolysis and $m_{\text{theoretical}}$ is the theoretical value calculated by Faraday's law. E is the cell potential difference (V), I is the applied current (A), t is the duration of the electrolysis (s) and m (g) is the mass of the reaction product.

In the case of the oxidation of Ce(III) and reduction of Ce(IV) on the 3-dimensional mesh electrode, the relationship between log $c_{(t)}/c_{(0)}$ and time was not linear as can be seen in Fig. 5(b). This indicates that the reaction on this electrode was possibly charge transfer controlled, when 50 mA cm^{-2} current density was applied during the first 3 h of electrolysis. After these 3 h, the concentrations of Ce(III) and Ce (IV) during charge and discharge respectively, are low and the processes appear to become mass transport controlled.

Table 2
Calculated parameters of the electrolysis of Ce(III) and Ce(IV) in methanesulfonic acid using a divided, parallel plate zinc–cerium flow cell. The positive electrolyte contained 0.8 mol dm^{-3} cerium (III) methanesulfonate in 4.0 mol dm^{-3} methanesulfonic acid. Negative electrolyte was 1.5 mol dm^{-3} zinc methanesulfonate in 1.0 mol dm^{-3} methanesulfonic acid. Both electrolytes were circulated at 3.9 cm s^{-1} and at 323 ± 2 K. The values were estimated using the assumption of a first order reaction in a constant volume stirred well mixed batch reactor.

Parameters	Electrode							
	Oxidation of Ce(III)				Reduction of Ce(IV)			
	2-d			3-d	2-d			3-d
Applied current density (mA cm^{-2})	20	50	80	50	20	50	80	50
Cell potential difference (V)	3.0	3.4	3.7	3.0	−0.5	−0.8	−0.9	1.8
First order rate constant (×10^{-5} s^{-1})	3.3	6.1	9.2	4.7 (mass-transport region)	2.1	5.0	7.7	5.6 (mass-transport region)
Mass transport coefficient (×10^{-6} s^{-1})	3.6	6.8	10.2	5.3 (mass-transport region)	2.4	5.6	8.5	6.2l (mass-transport region)
Change in concentration of Ce(IV) in the anolyte compartment at the end of the electrolysis (mol dm^{-3})	0.30	0.50	0.63	0.71	0.23 (4.0 h)	0.34 (4.0 h)	0.46 (4.0 h)	0.55 (3.3 h)
Specific electrochemical energy consumption (W h g^{-1})	0.58	0.98	1.36	0.61	0.11 (4.0 h)	0.30 (4.0 h)	0.40 (4.0 h)	−0.35 (3.3 h)
Overall % current efficiency	99.3	66.2	52.1	94.0	86.0	50.0	43.0	97.6

The parameters reported in Table 2 for this electrode were calculated using the linear region indicated as mass transport region in the Fig. 5(b). The apparent first-order rate constant for the reduction of Ce(IV) ion was lower than the apparent first-order rate constant for the oxidation of Ce(III) when the 2-dimensional electrode was used. The percentage of conversion and current efficiency for the reduction of Ce(IV) was lower than the oxidation of Ce(III), as shown in Table 2 and Fig. 5(c), on both electrodes. The lower current efficiency observed in the 2-dimensional electrode at high current densities could be due to the leakage of Ce(IV) ions towards the negative electrolyte compartment across the membrane and the secondary reactions such as oxygen evolution during oxidation of Ce(III) and hydrogen evolution during Ce(IV) reduction process. The ionic transport of Ce(IV) ions through the membrane was confirmed by a very slightly yellow colouration observed in the negative electrolyte compartment [40]. The low current efficiency for the reduction of Ce(IV) also suggests that the current density was too high and that large part of the current was used in the hydrogen evolution reaction, which was indicated by a negative cell potential difference value of the zinc–cerium redox flow battery during discharge, as shown in Table 2. Current efficiencies of the cerium redox reactions were high (>94%) when employing a 3-dimensional mesh electrode.

Current efficiency could be increased by enhancing the mass transport of cerium (III) ions. Previous investigations have shown that the oxidation of Ce(III) in nitric acid improved at a higher electrolyte flow rate in a divided flow cell [33]. For example, to achieve 0.84 mol dm^{-3} Ce(IV) using an applied constant cell potential difference of 2.5 V, approximately 2 h were required at an electrolyte flow rate of 50 cm^3 min^{-1} but only 1.5 h were required at 100 cm^3 min^{-1} to obtain the same concentration. This effect was also seen when the reaction was carried out in a beaker where the rate of Ce(III) oxidation increased with the stirring rate [41,42]. These findings agree with our experimental results to be published in a following paper, where the current efficiency of Ce(III) oxidation increased from 95.2% at 1.2 cm s^{-1} to 99.6% at 5.8 cm s^{-1} using a 3-dimensional platinised mesh electrode in a divided parallel plate flow reactor [43].

Table 2 shows that, both the apparent first order rate constant and the mass transport coefficient improved at increased current densities. At higher applied current densities, cerium (III) and cerium (IV) conversion improved but the current efficiency decreased. Since more oxygen evolved at increased current density during the oxidation of Ce(III), more specific electrochemical energy was consumed. The specific electrochemical energy consumption during the oxidation of Ce(III) was reported to be dependent on different electrode materials. For example, on a mixed RuO–IrO–TiO_2 electrode the specific electrochemical energy consumption was 0.9 W h g^{-1} but approximately 2.1 W h g^{-1} was required at a SnO_2/Ti electrode [26]. These values are higher than those obtained in this work on 2- and 3-dimensional platinised titanium (see Table 2). Due to the evolution of hydrogen during the Ce(IV) reduction using a 2-dimensional planar electrode, negative cell potential differences were obtained which resulted in no energy released from the battery during discharge; this is indicated by the positive value of the specific electrochemical energy consumption in Table 2. The cell potential value observed when the cell was fitted with the 3-dimensional platinised titanium mesh electrode was positive (1.8 V) and provided 0.35 W h g^{-1} specific energy output during discharge at 50 mA cm^{-2}, this is indicated by the minus sign in Table 2. Therefore, a 3-dimensional platinised titanium mesh positive electrode were found to be crucial to discharge a zinc–cerium redox flow battery at 50 mA cm^{-2} and 50 °C in the positive electrolyte containing 0.8 mol dm^{-3} cerium (III) methanesulfonate in 4 mol dm^{-3} methanesulfonic acid.

4. Conclusions

1. The Ce(III)/Ce(IV) redox couple in methanesulfonic acid is a quasi-reversible and diffusion limited redox reaction at a platinum disc electrode. The magnitude of reversibility was found to be strongly dependent on the concentration of cerium (III) methanesulfonate in 0.1–5.0 mol dm^{-3} methanesulfonic acid between 273 and 343 K. On a glassy carbon electrode the electrochemistry of the Ce(III) ⇆ Ce(IV) redox reaction was found to be less favourable than on a platinum electrode.
2. Cyclic voltammograms show that higher concentrations of cerium (III) and methanesulfonic acid lead to an increase in the cathodic-anodic peak current ratio but wider the peak separation. The reversibility of the Ce(III)/Ce(IV) redox reaction in methanesulfonic acid was found to be improved at elevated electrolyte temperature.
3. The acid strength needed to be sufficiently high to maintain solubility of Ce(IV), however, the solubility of Ce(III) decreased at higher acid concentrations. As a compromise to maximize the solubility of both ions, an electrolyte composition for the positive electrode reaction in a flow battery using cerium half-cell was suggested as: 0.8 mol dm^{-3} cerium (III) methanesulfonate in 4.0 mol dm^{-3} methanesulfonic acid at 343 K.
4. This quasi-reversible characteristics of the Ce(III)/Ce(IV) redox couple at current densities of 20–80 mA cm^{-2} during the charge–discharge cycles at a relatively high concentration of electroactive species, e.g. 0.5–1.0 mol dm^{-3} and its high cell potential difference, suggests that the couple could be used as

a high energy positive electrode reaction in a flow battery. The methanesulfonic acid concentration had a crucial influence on the efficiencies of the Ce(III)/Ce(IV) redox reaction.

5. With a 2-dimensional planar platinised titanium electrode, the redox reactions of Ce(III)/Ce(IV) were under mass-transport controlled regime, while reactions at the 3-dimensional mesh electrode appear to be charge-transferred controlled but became mass-transport controlled after 2.5–3 h of electrolysis when the concentrations of Ce(III) and Ce(IV) were lower.
6. At 50 mA cm^{-2}, hydrogen evolution takes place during the reduction of Ce(IV) at the 2 dimensional planar electrode, which resulted in a negative cell potential difference and no energy output released from the flow battery. Using a 3-dimensional platinised titanium mesh electrode instead to discharge the battery, the cell potential difference reached 1.8 V and the energy output was 0.35 W h g^{-1}.

Acknowledgements

Financial support has been provided by the Research Institute for Industry (RIfI) at the University of Southampton. The authors are grateful to Dr. L. Berlouis, University of Strathclyde for helpful discussions. This work represents part of the zinc-cerium P.K. Leung's PhD research programme on the development of zinc-based flow batteries for energy storage and conversion technology.

References

[1] C. Ponce de León, A. Frías-Ferrer, J. González-García, D.A. Szánto, F.C. Walsh, J. Power Sources 160 (2006) 716–732.
[2] D. Pletcher, H.T. Zhou, G. Kear, C.T.J. Low, F.C. Walsh, R.G.A. Wills, J. Power Sources 180 (2008) 630–634.
[3] D. Pletcher, H.T. Zhou, G. Kear, C.T.J. Low, F.C. Walsh, R.G.A. Wills, J. Power Sources 180 (2008) 621–629.
[4] J. Collins, G. Kear, X. Li, C.T.J. Low, D. Pletcher, R. Tangirala, D. Stratton-Campbell, F.C. Walsh, C. Zhang, J. Power Sources 195 (2010) 1731–1738.
[5] M.D. Gernon, M. Wu, T. Buszta, P. Janney, Green Chem. 1 (1999) 127–140.
[6] B. Fang, S. Iwasa, Y. Wei, T. Arai, M. Kumagai, Electrochim. Acta 47 (2002) 3971–3976.
[7] A. Paulenova, S.E. Creager, J.D. Navratil, Y. Wei, J. Power Sources 109 (2002) 431–438.
[8] P. Trinidad, C. Ponce de Leon, F.C. Walsh, J. Environ. Manage. 88 (2008) 1417–1425.
[9] R.L. Clarke, B. Dougherty, S. Harrison, J.P. Millington, S. Mohanta, WO03017408 (A1), Lanthanide Batteries (2003).
[10] Clarke, B. Dougherty, S. Harrison, J.P. Millington, S. Mohanta, US2008233484 (A1), Battery with Gelled Electrolyte (2008).
[11] R.L. Clarke, B. Dougherty, S. Harrison, J.P. Millington, S. Mohanta, US2004197649 (A1), Load leveling battery and methods therefore (2004).
[12] Y. Liu, X. Xia, H. Liu, J. Power Sources 130 (2004) 299–305.
[13] J. Bard, L.R. Faulkner, Electrochemical Methods—Fundamentals and Applications, 2nd ed., Wiley, 2001.
[14] V. Devadoss, M. Noel, K. Jayaraman, C. Ahmed Basha, J. Appl. Electrochem. 33 (2003) 319–323.
[15] R.P. Kreh, R.M. Spotnitz, J.T. Lundquist, J. Org. Chem. 54 (1989) 1526–1531.
[16] T. Vijayabarathi, D. Velayutham, M. Noel, J. Appl. Electrochem. 31 (2001) 979–986.
[17] R.M. Spotnitz, R.P. Kreh, J.T. Lundquist, P.J. Press, J. Appl. Electrochem. 20 (1990) 209–215.
[18] P. Patnaik, Dean's Analytical Chemistry Handbook, 2nd ed., McGraw-Hill, 2004.
[19] I.M. Kolthoff, E.B. Sandell, Texture of Quantitative Inorganic Analysis, 3rd ed. The Macmillan Company, 463–481.
[20] A.I. Vogel, Textbook of Quantitative Inorganic Analysis, 5th ed. Wiley, New York.
[21] E. Bishop, P. Cofré, J. Analyst. 106 (1981) 316–322.
[22] M. Breiter, P. Delahay, C.W. Tobias, Advances in Electrochemistry and Electrochemical Engineering vol. 1, Interscience, New York, 1961.
[23] D. Pletcher, A First Course in Electrode Processes, The Electrochemical Consultancy, Romsey, 1991.
[24] F.C. Walsh, A First Course in Electrochemical Engineering, Electrochemical Consultancy, Romsey (1993).
[25] C.M.A. Brett, M.O. Brett, Electrochemistry Principles, Methods and Applications, Oxford University Press, 1993.
[26] V. Devadoss, C.A. Basha, K. Jayaraman, J. Ind. Eng. Chem. Res. 47 (2008) 4607–4616.
[27] T.H. Randle, A.T. Kuhn, J. Chem. Soc., Faraday Trans. 1: Phys. Chem. Condensed Phases 79 (1983) 1741–1756.
[28] Y. Maeda, K. Sato, R. Ramaraj, T.N. Rao, D.A. Tryk, A. Fujishima, Electrochim. Acta 44 (1999) 3441–3449.
[29] A. Abbaspour, M.A. Mehrgardi, J. Talanta 67 (2005) 579–584.
[30] P. Glentworth, B. Wiseall, C.L. Wright, A.J. Mahmood, J. Inorg. Nucl. Chem. 30 (1968) 967–986.
[31] P. Modiba, A.M. Crouch, J. Appl. Electrochem. 38 (2008) 1293–1299.
[32] D. Pletcher, E.M. Valdes, Electrochim. Acta 33 (1988) 499–507.
[33] Y. Wei, B. Fang, T. Arai, M. Kumagai, J. Appl. Electrochem. 35 (2005) 561–566.
[34] K. Kramer, P.M. Robertson, N. Ibl, J. Appl. Electrochem. 10 (1980) 29–36.
[35] M. Matheswaran, S. Balaji, S.J. Chung, I.S. Moon, Bull. Korean Chem. Soc. 28 (2007) 1329–1334.
[36] T. Raju, C.A. Basha, J. Ind. Eng. Chem. Res. 47 (2008) 8947–8952.
[37] T. Raju, C.A. Basha, J. Portugaliae Electrochim. Acta 23 (2005) 367–378.
[38] P. Trinidad, F.C.I Walsh, Chem. E: Symp. Series 145 (1999) 281–290.
[39] P. Trinidad, F. Walsh, D. Gilroy, Int. J. Eng. Educ. 14 (1998) 431–441.
[40] S. Harrison, USP 5679235, Titanium and cerium containing acidic electrolyte (1997).
[41] T.A. Sedneva, J. Appl. Chem. 78 (2005) 907–911.
[42] T. Raju, C.A. Basha, Chem. Eng. J. 114 (2005) 55–65.
[43] P.K. Leung, C. Ponce-de-León, F.C. Walsh, J. Power Sources, (2010) submitted.

Journal of Power Sources 196 (2011) 5174–5185

Contents lists available at ScienceDirect

Journal of Power Sources

journal homepage: www.elsevier.com/locate/jpowsour

Characterization of a zinc–cerium flow battery

P.K. Leung, C. Ponce-de-León*, C.T.J. Low, A.A. Shah, F.C. Walsh

Electrochemical Engineering Laboratory, Energy Technology Research Group, University of Southampton, Highfield, Southampton, SO17 1BJ, United Kingdom

ARTICLE INFO

Article history:
Received 26 November 2010
Accepted 25 January 2011
Available online 2 February 2011

Keywords:
Cerium
Energy storage
Methanesulfonic acid
Redox flow battery
Zinc

ABSTRACT

The performance of a divided, parallel-plate zinc–cerium redox flow battery using methanesulfonic acid electrolytes was studied. Eight two and three-dimensional electrodes were tested under both constant current density and constant cell voltage discharge. Carbon felt and the three-dimensional platinised titanium mesh electrodes exhibited superior performance over the 2-dimensional electrodes. The charge and discharge characteristics of the redox flow battery were studied under different operating conditions and Zn/Ce reactant, as well as methansulfonic acid concentration. The cell performance improved at higher operating temperatures and faster electrolyte flow velocities. The number of possible cycles increased at reduced states of charge. During 15 min charge/discharge per cycle experiment, 57 cycles were obtained and the zinc reaction was found to be the limiting process during long term operation.

1. Introduction

Large and medium scale energy storage technologies can be combined with conventional power generation sources such as fossil fuels and hydro-electricity [1,2]. Insufficient energy storage capacity can lead to problems, such as raised volatility and an increased burden on electricity distribution systems [3]. Since the 1970s, a number of redox flow batteries (RFBs), such as the iron–chromium [4,5], all vanadium [6–10], zinc–bromine [11], polysulfide–bromine [12,13] and soluble lead acid cells [14] have been developed. A typical application of RFBs is load-leveling, which consists of storing energy during off-peak hours and releasing it when the demand rises [3,15]. RFB technology can also be used in combination with renewable power sources, such as photovoltaic cells [16–18] and wind turbines [17,18]. Due to the rapid growth of renewable energy and more advanced power generating sources, increasing attention has been given to the development of more advanced, reliable and safer redox flow batteries.

The first zinc–cerium system was developed by Plurion Inc. (UK) [19,20]. Other systems using these couples include the zinc–chlorine [26–28], zinc–bromine [11,29], zinc–ferricyanide [30], zinc–air [31], vanadium–cerium [32] and zinc–cerium [19,20] cells. Both zinc [21] and cerium [22] are advantageous materials for energy storage due to the relatively large differences between their standard electrode potentials in aqueous media. This results in a system with a high thermodynamic open-circuit cell voltage of *c.a.* 2.4 V, and a large maximum energy density. This large potential difference necessitates the correct selection of materials and suppression of secondary reactions such as the hydrogen and oxygen evolution. At the negative electrode, the main electrode reactions are the electrodeposition and dissolution of zinc on a planar carbon/polyvinyl-ester composite material [19,20]:

$$Zn(CH_3SO_3)_2 + 2H^+ + 2e^- \underset{\text{Discharge}}{\overset{\text{Charge}}{\rightleftarrows}} Zn + 2CH_3SO_3H \quad (E^0 = -0.76\,\text{V}\ vs.\ \text{SHE}) \tag{1}$$

while hydrogen evolution can also take place on this electrode:

$$2H^+ + 2e^- \overset{\text{Charge}}{\longrightarrow} H_2 \quad (E^0 = 0\,\text{V}\ vs.\ \text{SHE}) \tag{2}$$

At the positive electrode, the primary reaction is the oxidation process of Ce(III) and the reduction of Ce(IV) during charge and discharge, respectively. The positive standard electrode potential lies between 1.28 and 1.72 V *vs.* Ag|AgCl, depending on the background electrolyte [23].

$$2Ce(CH_3SO_3)_3 + 2CH_3SO_3H \underset{\text{Discharge}}{\overset{\text{Charge}}{\rightleftarrows}} 2Ce(CH_3SO_3) + 2H^+ + 2e^- \tag{3}$$

While oxygen evolution can also take place:

$$H_2O \overset{\text{Charge}}{\longrightarrow} \frac{1}{2}O_2 + 2H^+ + 2e^- \quad (E^0 = 1.23\ \text{V}\ vs.\ \text{SHE}) \tag{4}$$

* Corresponding author at: School of Engineering Sciences, University of Southampton, University Road, Southampton, SO17 1BJ, United Kingdom.
Tel.: +44 23 8059 8931; fax: +44 23 8059 7051.
E-mail address: capla@soton.ac.uk (C. Ponce-de-León).

0378-7753/$ – see front matter © 2011 Elsevier B.V. All rights reserved.
doi:10.1016/j.jpowsour.2011.01.095

The overall cell reaction of the zinc–cerium redox flow battery, taking the standard potential of reaction (3) as 1.44 *vs.* SHE, is:

$$2Ce(CH_3SO_3)_3 + Zn(CH_3SO_3)_2 \underset{\text{Discharge}}{\overset{\text{Charge}}{\rightleftarrows}} Zn + Ce(CH_3SO_3)_4 \quad (E_{cell} = 2.4\ V) \tag{5}$$

Methanesulfonic acid is used as a solvent for both zinc and cerium ions, since its conductivity is comparable to that of hydrochloric acid, while posing a lower risk of corrosion compared with other mineral acids, such as sulphuric acid and is highly stable [24]. Cerium in methanesulfonic acid has the advantage of easy preparation and high solubility. The solubility limits of Ce(III) and Ce(IV) ions in methanesulfonic acid can be as high as 1 mol dm^{-3}, compared to less than 0.5 mol dm^{-3} in sulphuric acid. The solubility of zinc is also high (2.16 mol dm^{-3}) in this acid [25].

Although previous work by Plurion Inc. has been described in several patents [19,20], information on the experimental conditions and discharge performance is limited. Moreover, few papers in the literature consider the use of zinc and cerium in aqueous methanesulfonic acid [25]. An improved understanding of the flow battery performance under various operating conditions and electrolyte compositions are crucial. In this work, a comprehensive investigation is carried out with regards to the optimal electrode materials and characterization of the zinc–cerium system.

2. Experimental details

2.1. Chemicals

Analytical grade Zn(II) carbonate basic (Alfa Aesar, U.K., 99 wt.%), hydrate Ce(III) carbonate (Treibacher Industrie AG., Germany, 99 wt.%), and reagent grade aqueous methanesulfonic acid (Sigma Aldrich, U.K., 70 vol.%) were used as received. All solutions were prepared with ultra-pure water (18 MΩ cm resistivity) from an Elga water purification system. Zinc(II) and cerium(III) methanesulfonates of 2 mol dm^{-3} were prepared by stirring 0.4 mol dm^{-3} zinc carbonate basic and 1 mol dm^{-3} cerium carbonate powders in 10 and 6 mol dm^{-3} aqueous methanesulfonic acid, respectively, using a PTFE-coated steel magnetic stirred bar (Fisherband, U.K., 1 cm diameter, 4 cm length). During the preparation of Ce(III) methanesulfonate, the temperature was maintained at 80 °C for 6 h using a hot-plate stirrer (Ika Yellowline®) [24,33,34]. The resulting Zn(II) and Ce(III) methanesulfonate solutions were colourless with no precipitate.

2.2. Cyclic voltammetry

A typical divided, three-electrode glass cell with approximately 160 cm^3 of electrolyte volume in the working electrode compartment separated from the counter electrode by a Nafion® membrane (Dupont, NF117/H^+, USA) was used. This glass cell was equipped with a water jacket connected to a water thermostat controller (Grant, Model LV FG., UK) to maintain the temperature in the range of 20–60 °C. For the half-cell reactions of Zn and Ce, the working electrodes (area: 0.13 cm^2) were glassy carbon and platinum disc, respectively. The counter electrode was a platinum mesh (area: 1 cm^2). The electrode potentials were measured against a saturated Ag|AgCl electrode (ABB, Series 1400, 0.1 mol dm^{-3} KNO_3). The electrochemical measurements were made using an EcoChemie Autolab (PGSTAT20, Netherlands) computer controlled potentiostat and General Purpose, Electrochemical Software (GPES) Version 4.5.

2.3. Flow battery experiment

The electrical and electrolytic circuits of the flow battery are shown in Fig. 1a. An expanded view of the flow cell (102 mm × 47 mm × 45 mm dimensions) is shown in Fig. 1b. The cell was manufactured with a polyvinyl chloride (PVC) casing, two acrylic (Perspex®) flow channels, four 1.5 mm thickness rubber silicon gaskets as well as the negative and positive electrodes, separated by a cation-conducting Nafion® membrane (DuPont, NF117/H^+, USA). The dimensions of each electrode were 70 mm × 50 mm and were fitted with a silicone rubber gasket to expose an active surface area of 9 cm^2 (45 mm × 20 mm) to the electrolyte. The membrane-electrode gap was 11 mm. The electrolytes (100 cm^3 each) were contained in separate tanks.

Carbon polyvinyl-ester composite (Engtegris Inc., BMC 18649, Germany) was used as the negative electrode and a range of positive electrode materials were tested. A detailed description of the positive electrode materials used in this work is given in Table 1. The platinised titanium mesh was manufactured by spot welding four pieces of platinised titanium mesh (44 mm × 16 mm × 2.5 mm each, 70 g Pt m^{-2} loading, Magneto GmbH, Netherlands) onto a planar platinised titanium plate (70 g Pt m^{-2} loading, Magneto GmbH, Netherlands). Other three-dimensional positive electrode materials such as reticulated vitreous carbon and carbon felt were heat-bonded to a graphite plate using a conductive carbon adhesive (Binder & Cotronics Corp., 931, USA). After compressing the electrode to the graphite plate overnight, the adhesive was cured at 130 °C for 4 h.

Unless otherwise stated, the positive electrolyte contained 0.8 mol dm^{-3} Ce(III) methanesulfonate in 4.0 mol dm^{-3} methanesulfonic acid, while the negative electrolyte compartment contained 1.5 mol dm^{-3} Zn(II) methanesulfonate in 1.0 mol dm^{-3} methanesulfonic acid. The electrolytes were maintained at 50 °C by a water thermostat (Grant, Model LV FG, UK) through water jackets fitted to the containers. Both positive and negative electrolytes were circulated through the cell at 3.9 cm s^{-1} using two peristaltic pumps (Cole-Parmer, Masterflex® Model 7553079) with high-pressure tubings (Masterflex® Norprene®, Cole-Parmer, 6 mm inner diameter). Saturated Ag|AgCl electrodes served as reference electrodes (ABB, Series 1400, 0.1 mol dm^{-3} KNO_3) placed in line at the entrance of each flow channel.

In a typical experiment, the battery was charged at 450 mA (50 mA cm^{-2} with respect to the two-dimensional electrode) for 4 h. The current density reported in this paper is always referred to the negative 2D electrode but due to the higher surface areas of the positive electrodes tested, the current density on these electrodes would be smaller. After charge, the cell was left at open-circuit potential for 1 min and discharged at the same current. Cut-off voltages were set at 3.4 V and 0.5 V during battery charge and discharge, respectively. All electrochemical measurements were made using a BaSyTec (5A/12V, Germany) battery test system. The anode, cathode and cell potentials were continuously monitored.

2.4. Determination of the Ce(IV) concentration

A 0.5 cm^3 aliquot of positive electrolyte solution was removed during the charge and discharge cycles at regular intervals of time. The concentration of Ce(IV) in methanesulfonic acid contained in this aliquot was determined by a titration method as outlined in previous studies [35–37]. The 0.5 cm^3 volume of unknown concentration of Ce(IV) was mixed with 9.5 cm^3 of 2.0 mol dm^{-3} methanesulfonic acid and ferroin (1,10 orthophenanthroline–ferrous sulphate complex, Fluka) as a colorimetric redox indicator. A freshly prepared solution of 0.01 mol dm^{-3} $NH_4Fe(II)$ was used to titrate the solution of unknown Ce(IV) ion concentration. The concentration of Ce(IV) was then determined from the

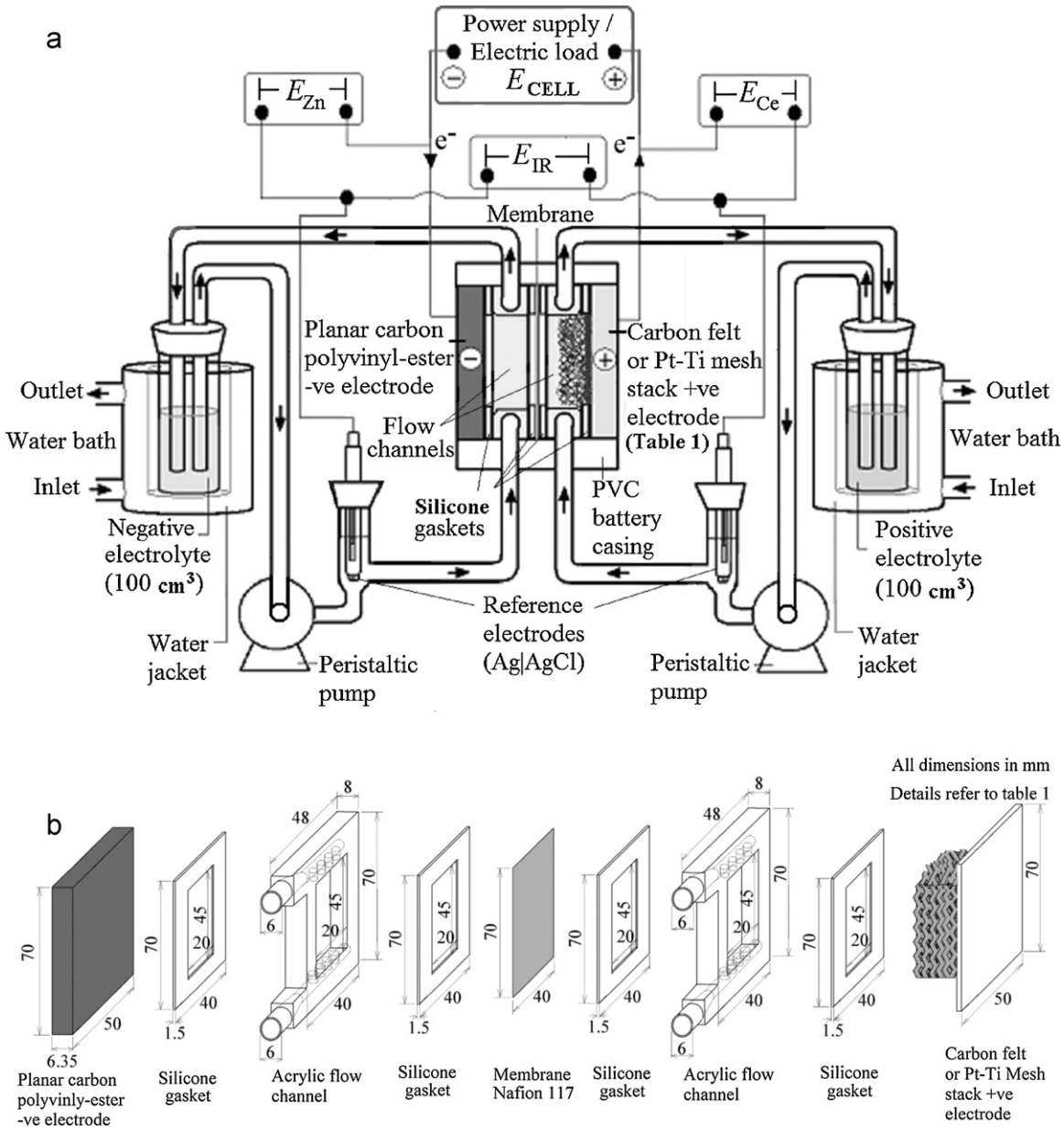

Fig. 1. Experimental arrangement and electrical circuit of a zinc cerium redox flow battery. (a) Overall set-up showing the points of measurement of the cell potential E_{cell}, the potential of the positive and negative electrodes, E_{Ce} and E_{Zn}, respectively and the ohmic voltage drop across the membrane E_{IR} and (b) expanded view of the components of a flow battery. The units are shown in mm.

amount of Fe(II) required to achieve complete reduction of Ce(IV) to Ce(III).

3. Results and discussions

3.1. Electrochemistry of zinc and cerium in methanesulfonic acid

Fig. 2 shows the combined cyclic voltammogram of the Zn and Ce half-cell reactions under static conditions at different temperatures. The voltammogram of Zn was carried out between −0.7 and −1.2 V *vs.* Ag|AgCl at 128 mV s^{-1} in the negative electrolyte containing 1.5 mol dm^{-3} Zn(II) methanesulfonate and 1 mol dm^{-3} methanesulfonic acid on a glassy carbon disc electrode (0.13 cm^2). The behaviour of the Ce half-cell reaction was recorded between +0.5 and +1.9 *vs.* Ag|AgCl at 128 mV s^{-1} in the positive electrolyte containing 0.8 mol dm^{-3} Ce(III) methanesulfonate and 4 mol dm^{-3} methanesulfonic acid using a platinum electrode (0.13 cm^2).

The cyclic voltammograms show that temperature has a much greater influence on the peak currents of the Zn reaction compared to those associated with the Ce reaction. The current density of Zn reduction increased tenfold when the temperature changed from 22 to 60 °C, whereas the oxidation current of Ce(III) was only doubled. It is also likely that hydrogen evolution (reaction (2)) contributed to the current for Zn electrodepositon, while oxygen evolution (reaction (4)) may have affected the current for Ce(III) oxidation. During charge, Zn(II) electrodeposition and Ce(III) oxidation take place at *c.a.*−1.08 V and +1.84 V *vs.* Ag|AgCl, respectively at 22 °C. During discharge, dissolution of Zn(0) occurs at −0.94 V *vs.* Ag|AgCl together with the reduction of Ce(IV) at +1.05 V *vs.* Ag|AgCl. A simple estimation of the charge and discharge cell voltages can be obtained by subtracting the Zn potential from the Ce potential. At 22 °C, the estimated values for charge and discharge would be 2.92 V and 1.99 V, respectively. An estimation of the charge and discharge cell voltages at 60 °C yields 2.81 V and 2.08 V, respectively.

Table 1
Positive electrode materials evaluated for the zinc–cerium redox flow battery.

Type	Electrode materials	Details	Specific surface area ($cm^2\ cm^{-3}$)	Total surface area (cm^2)	Observations		Ce(IV) after 4 h charge at 50 mA cm^{-2} ($mol^{-1}\ dm^{-3}$)
					Electrode	Electrolyte	
1	Platinised titanium (7 cm × 5 cm × 0.2 cm)	70 g Pt m^{-2} loading, 3. 5 μm thick, Magneto GmbH (Netherlands)	Nil (2D)	9	Stable, no observable change	Clear yellowish solution	0.456
2	Graphite (7 cm × 5 cm × 0.6 cm)	Grade S plate, Le Carbone Lorraine S.A. (France)	Nil (2D)	9	Graphite plate exfoliated, as particles came off after 10 min	Very dark solution with carbon particles	0.104
3	Carbon–polyvinylester (7 cm × 5 cm × 0.6 cm)	BMC 18649 Vinyl ester bipolar plate Entegris Inc. (Germany)	Nil (2D)	9	Carbon plate exfoliated, as particles came off after 10 min	Very dark solution with carbon particles	0.08
4	30 ppi reticulated vitreous carbon (4.5 cm × 2 cm × 2 cm)	Duocel®, ERG Material and Aerospace Corp. (USA)	19 [46]	342	Slightly expanded, and carbon particles came off after 2 h and 15 min	Dark solution with carbon particles	0.16
5	100 ppi reticulated vitreous carbon (4.5 cm × 2 cm × 2 cm)	Duocel®, ERG Material and Aerospace Corp. (USA)	65 [46]	1170	Slightly expanded, and carbon particles came off after 2 h and 15 min	Dark solution with carbon particles	0.128
6	Alfa Aesar carbon felt (4.5 cm × 2 cm × 0.8 cm)	Stock 42107, 99%, Alfa Aesar (UK)	452.3 [47]	3256	Became darker the appearance after the experiment	Clear orange solution with very few carbon particles	0.632
7	Sigratherm® carbon felt (4.5 cm × 2 cm × 0.8 cm)	GFA -05, SGL Group (Germany)	240–600 [48]	1728–4320	No observable change in appearance	Clear orange solution with very few carbon particles	0.656
8	4 Platinised titanium mesh (4.4 cm × 1.6 cm × 0.25 cm each) welded on a platinised titanium plate (7 cm ×5 cm × 0.2 cm)	70 g Pt m^{-2} loading, 3.5 μm thick, Magneto GmbH(Netherlands)	19.3	72.7	Stable, no observable change	Clear orange solution	0.652

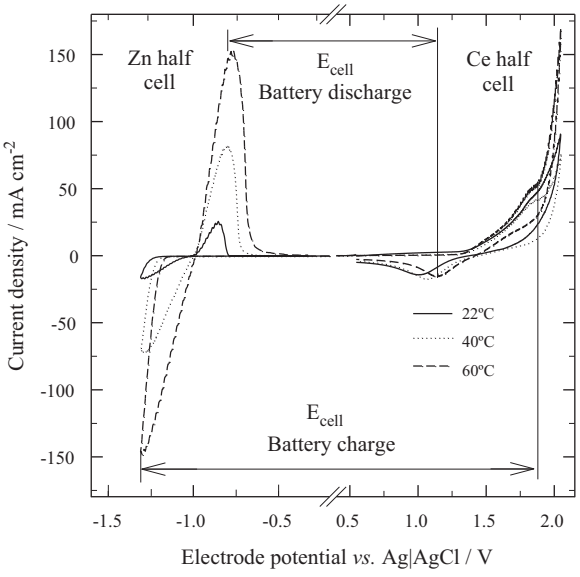

Fig. 2. A combined cyclic voltammetry of zinc half-cell at glassy carbon electrode and cerium half-cell reaction at platinum sweeping the potential linearly at 128 mV s^{-1} from +0.5 to +1.9 V *vs.* Ag|AgCl and −0.7 to −1.2 V *vs.* Ag|AgCl, respectively at electrolyte temperatures of 20, 40 and 60 °C. Negative electrolyte: 1.5 mol dm^{-3} zinc(II) methanesulfonate and 1 mol dm^{-3} methanesulfonic acid. Positive electrolyte: 0.8 mol dm^{-3} cerium(III) methanesulfonate and 4 mol dm^{-3} methanesulfonic acid.

These values do not include the ohmic losses across the electrolyte, electrodes and membrane. They do demonstrate, nevertheless, the increased voltage efficiency with higher temperature.

As the temperature was increased, the separation between the oxidation and reduction peaks of each redox couple decreased. For the Zn(0)/Zn(II) redox couple, the separation decreased by 30 mV and for the Ce(III)/Ce(IV) redox couple the separation decreased by 150 mV. At increased temperatures, the oxidation and reduction peak current density of both zinc and cerium reactions also increased. The cyclic voltammetry shows that the positive electrode reaction could limit the use of high currents. High surface area electrodes could be used to solve this problem. A range of two- and three-dimensional positive electrodes were, therefore, investigated, as detailed in the next section.

3.2. Selection of the positive electrode materials

A summary of the characteristics and behaviour of the eight positive electrode materials tested in a Zn/Ce redox flow battery (at 50 °C) is shown in Table 1. A carbon polyvinyl-ester composite was used as the negative electrode material. Both the positive and negative electrolyte compositions were the same as those used for the cyclic voltammetry described in Section 3.1 and were circulated through the respective half-cells with a mean linear flow velocity of 3.9 cm s^{-1}. The battery was first charged at 50 mA cm^{-2} for 4 h using different electrodes, after which the concentration of Ce(IV) was measured. These concentrations are shown in Table 1. The battery was then discharged at different

constant current densities in the range 5–50 mA cm^{-2} and different constant cell voltages in the range 2.2–1.0 V. In order to keep the Ce(IV) concentration approximately constant, each discharge current or voltage was applied for only 2 min, enough time to measure the cell voltage or current generated. The battery was recharged frequently to restore the concentration of Ce(IV) ions and maintain the same state of charge (SOC) for each experiment.

Table 1 shows that during charge at 50 mA cm^{-2}, the conversion of Ce(III) was highest when the two carbon felts and the three-dimensional platinised titanium mesh were used. Ce(IV) concentrations reached more than 0.60 mol dm^{-3} at current efficiencies of >90% using these electrodes. Platinum-based positive electrode materials were stable throughout the battery charge and discharge cycles [38]. The reticulated vitreous carbon, graphite and carbon polyvinyl-ester composite exhibited less stability and poorer performance as well as lower Ce(IV) conversion. These electrodes either exfoliated or expanded and carbon sludge appeared in the electrolytes during charge-discharge cycles. These observations and the changes in the electrolyte conditions are summarized for the eight positive electrodes tested in Table 1.

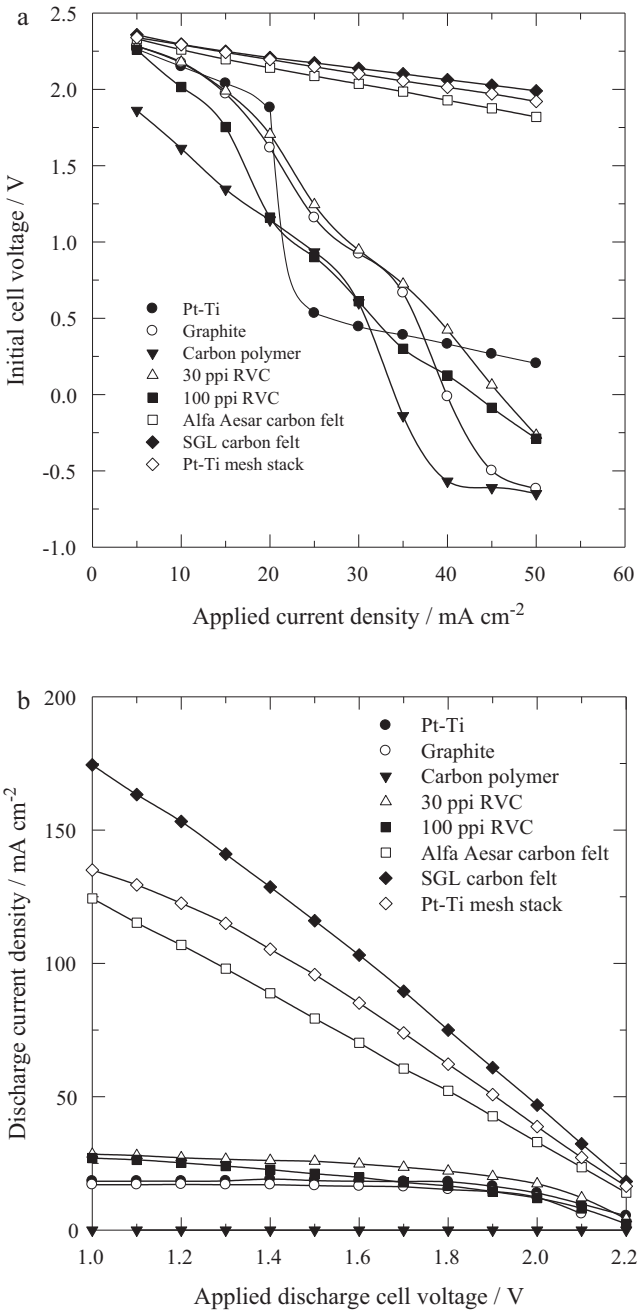

Fig. 3. Performance of 8 positive electrode materials in a zinc–cerium redox flow battery during the discharge cycle. (a) Constant current density. (b) Constant cell voltage; carbon–polyvinylester composite was used as a negative electrode material. Negative electrolyte was 100 cm^3 solution containing 1.5 mol dm^{-3} zinc(II) methanesulfonate in 1 mol dm^{-3} methanesulfonic acid. Positive electrolyte was 100 cm^3 solution containing 0.8 mol dm^{-3} cerium (III) methanesulfonate in 4 mol dm^{-3} methanesulfonic acid. Both negative and positive electrolytes were circulated at 3.9 cm s^{-1} by a peristaltic pump and maintained at 50 °C by a water bath. (●) 2-d Pt-Ti, (○) graphite, (▼) carbon polyvinyl-ester, (△) 30 ppi reticulated vitreous carbon, (■) 100 ppi reticulated vitreous carbon, (□) Alfa-Aesar carbon felt, (♦) SGL carbon felt and (◊) Pt–Ti mesh stack.

3.2.1. Constant current density and constant voltage discharge

The patented zinc–cerium system discharges at a constant cell voltage of 1.8 V [19,20], at which the current density undergoes an exponential decay. Despite a high initial current density, the full discharge of the battery requires a prolonged period of time [15]. In practice, constant current density discharge is preferred due to lower cost and a more steady power output. Fig. 3a shows the initial cell voltages of the eight positive electrode materials *vs.* a constant discharge current density (5–50 mA cm^{-2}). With all materials, the cell voltage decreased as the applied current density increased. This is attributed to the electrode overpotentials and ohmic drop across the electrodes, electrolytes and membrane. The majority of the two-dimensional materials and the reticulated vitreous carbon electrodes exhibited a large cell voltage drop during discharge at increased current densities.

The initial cell voltages using the carbon felts and the three-dimensional platinised titanium mesh were all above 1.8 V at current densities in the range 5–50 mA cm^{-2}, with less than a 0.55 V drop in the voltage. The high cell voltages were due to the high Ce(IV) concentration generated in the positive electrolyte (Table 1) and to the low local current density of the large surface area of the electrodes. In contrast, the two-dimensional platinised titanium electrode, the carbon polyvinylester and the reticulated vitreous carbon exhibited voltage drops of more than 1.5 V when the discharge current density increased from 20 to 25 mA cm^{-2}. This was possibly due to a low concentration of Ce(IV) near the electrode surface, which lead to an appreciable rate of hydrogen evolution. It is important to note that despite its high surface area, the performance of reticulated vitreous carbon electrodes is similar to that of the two-dimensional electrodes.

A similar picture emerged with a constant cell voltage discharge (1.0–2.2 V) after the 4 h charge at 50 mA cm^{-2} (Fig. 3b). The highest initial current densities were obtained with the two carbon felts and the platinised titanium mesh electrodes. The current densities associated with the two-dimensional electrodes and the reticulated vitreous carbon materials were appreciably lower. In the cases of the two carbon felts and the platinised titanium mesh electrode, the large current densities obtained at low discharge cell voltages were again due to hydrogen evolution. Discharging the zinc–cerium battery at such low voltages is not a practical approach (high rates of hydrogen evolution and lower efficiencies).

3.3. Charge/discharge performance of a zinc–cerium redox flow battery

Based on the above results, it was concluded that carbon felt and platinised titanium mesh are the optimum positive electrode materials. The charge–discharge performance of the redox flow battery was studied using Sigratherm® GFA-05 carbon felt and the pla-

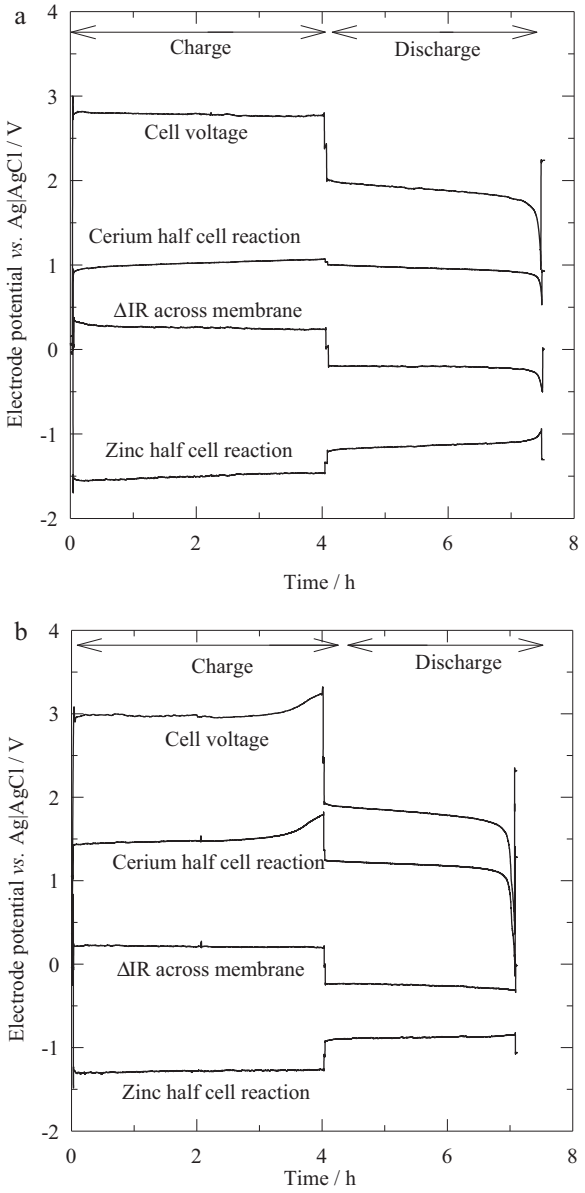

Fig. 4. Voltage *vs.* time characteristics of a zinc–cerium redox flow battery equipped with high surface areas of positive electrodes: (a) Sigratherm® carbon felt and (b) platinised titanium mesh electrodes. Electrolyte composition and operating conditions as in Fig. 3.

tinised titanium mesh as the positive electrodes, while the negative electrode consisted of a carbon polyvinyl-ester composite.

The cell voltage and electrode potentials using the GFA-05 felt and the platinised titanium mesh are shown in Fig. 4a and b, respectively. These figures also show the ohmic drops across the membrane and electrolyte during the 4 h charge/discharge cycle. The charge/discharge performance with the Sigratherm® carbon felt was superior. Using the platinised titanium mesh, the cell voltage began to rise after 3 h of charging, due to significant Ce(III) consumption and oxygen evolution in the positive electrode. With the Sigratherm® carbon felt, the coulombic efficiency was 92.4% and the energy efficiency at 50 mA cm^{-2} was 63%, which compares well with other systems such as the soluble lead acid flow battery (around 58% at 40–60 mA cm^{-2} [40]). The platinised titanium mesh yielded a coulombic efficiency of 71% and an energy efficiency of 43% at 50 mA cm^{-2}.

In the zinc–cerium battery fitted with a Sigratherm® carbon felt positive electrode, the change in the cerium half-cell potential between the charge and discharge cycle was only 0.07 V, compared to 0.29 V using the platinised titanium mesh electrode (Fig. 4a and b). This value of 0.29 V is smaller than the equivalent half-cell voltages in the zinc–chlorine [41] and zinc–bromine [39] systems. In addition to this advantage, carbon felt is less expensive than platinum and does not form an oxide layer during the oxidation of Ce(III) [42], i.e., the Ce redox reaction at the carbon felt electrode exhibits a greater degree of reversibility.

The carbon polyvinyl-ester composite negative electrode material in both systems (Fig. 4a and b) yielded a half-cell potential difference of 0.35 V between charge and discharge cycles. This value is larger than the equivalent values for the zinc–chloride [41] and zinc–bromide [39] systems, possibly due to the high stability of the Zn(II) methanesulfonate complexes. Additives, such as indium oxide [21], can be used to reduce the overpotentials in aqueous methanesulfonic acid. The reduction of Ce(IV) took slightly longer in the battery using the Sigratherm® carbon felt (see Fig. 4a and b). Fig. 4b also shows that zinc deposits remained on the mesh electrode at the end of the discharge cycles. In contrast, zinc electrodeposits were stripped away after discharging for 3.4 h, as indicated by the potential increase towards the end of the cycle in Fig. 4a. Both the zinc and cerium electrodes were completely utilized during battery discharge using the carbon felt. In the cell based on the platinised-titanium mesh electrode, the Ce half-cell reaction was the main limiting factor in the system. Despite the high efficiency of carbon felts as positive electrodes, poor conductivity and poor adherence of the carbon adhesive were observed after 2–3 charge/discharge cycles. Further developments on the construction of such electrodes and the connections in the highly acidic, oxidizing Ce(IV) methanesulfonate electrolyte are required.

3.4. Effect of flow conditions on battery discharge

In RFBs, mass-transport conditions play an important role in delivering a large power output. The effect of the mean linear flow velocity of the electrolyte on the battery performance was studied under constant current density and constant voltage discharge. The Sigratherm® carbon felt and platinised titanium mesh were again used as the positive electrodes, while the negative electrode was a carbon–polyvinylester composite. The battery was first charged at current density of 50 mA cm^{-2} (referred to the negative electrode area) for 4 h in order to achieve the same state of charge (SOC) before all tests. The battery was then discharged at a range of constant current densities (10–70 mA cm^{-2}) and cell voltages (1.0–2.2 V) under a wide range of mean linear electrolyte flow velocities (1.2–7.8 cm s^{-1}). In order to maintain the Ce(IV) concentration constant, each current and potential was applied for 2 min only and the battery was frequently charged between measurements to restore the Ce(IV) consumed and maintain the same state of charge SOC.

The effect of the flow velocity on the discharge current densities at constant cell voltage discharge, for both positive-electrode materials, is shown in Fig. 5. At a fixed cell voltage, the current density increased with increased flow velocity; the changes were more pronounced when the Sigratherm® carbon felt was used (Fig. 5a), for which the discharge current densities reached their maximum values at 3.9 cm s^{-1} for all cell voltages. In the cell using a platinised titanium mesh, the optimum flow velocity was also 3.9 cm s^{-1}, though the peak is less pronounced (Fig. 5b). As the velocity is increased, polarization losses would be expected to be lower at equivalent states of charge since the reactants would be distributed more evenly and the width of any Nernst diffusion layer decreased.

Fig. 5c and d show the effect of the mean linear flow velocity on the discharge voltage at a constant discharge current density. The maximum cell voltages using the Sigratherm® carbon felt were again found to occur at a velocity of 3.9 cm s^{-1}. In contrast, the

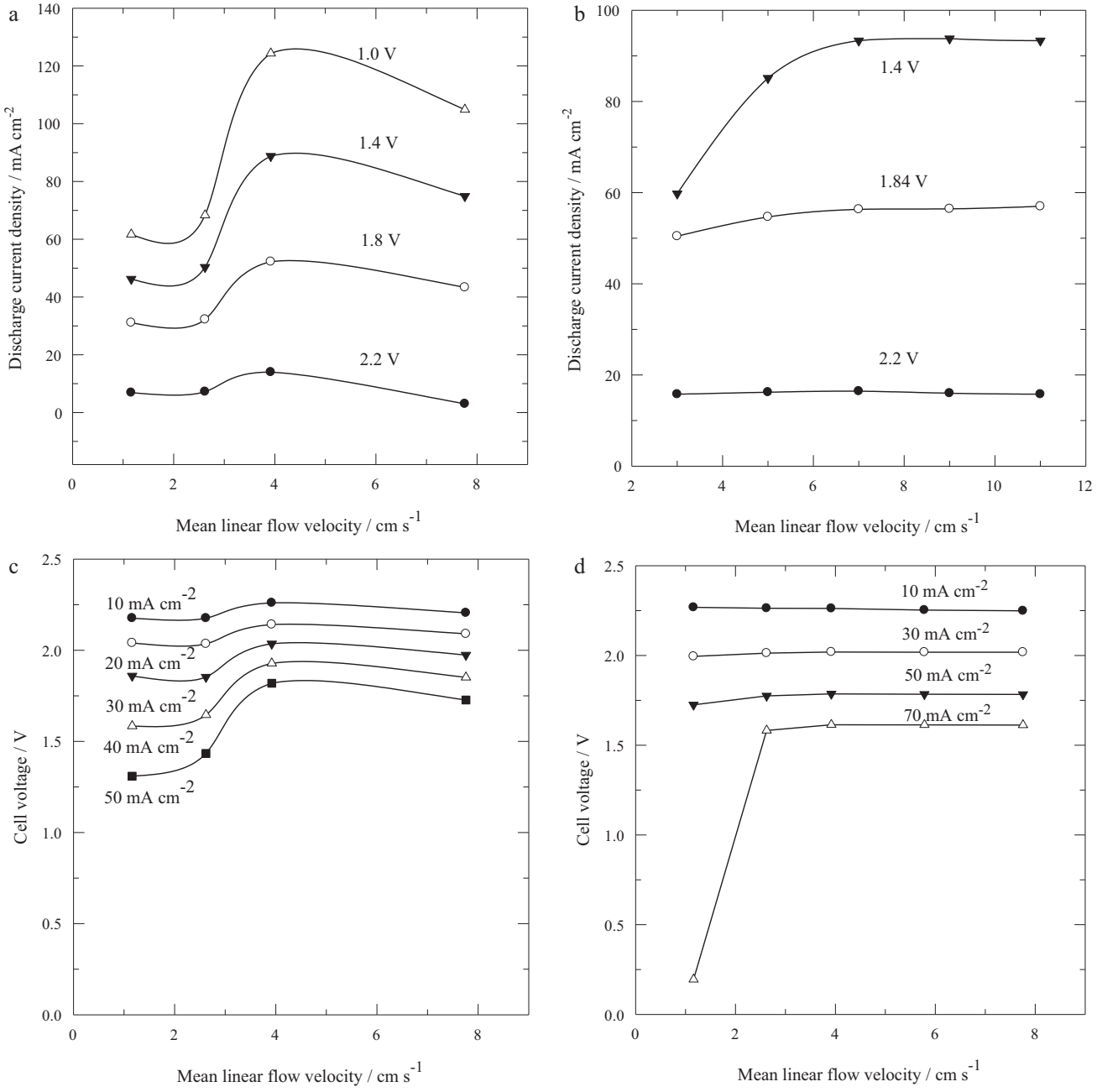

Fig. 5. Effect of flow condition on discharge performance of a zinc–cerium redox flow battery. (a) Constant voltage discharge at Sigratherm® carbon felt, (b) constant voltage discharge at platinised titanium mesh electrode, (c) constant current density discharge at Sigratherm® carbon felt and (d) constant current density discharge at platinised titanium mesh electrode. Electrolyte compositions and operating conditions were the same as in Fig. 3.

cell voltages obtained using the platinised titanium mesh remained almost constant over a wide range of flow velocities, except for a discharge current density of 70 mA cm^{-2}. At this value, high flow velocities (>2.62 cm s^{-1}) are required to offset the rapid Ce(IV) depletion.

3.5. Efficiencies of a zinc–cerium flow battery

In order to determine the optimum operating conditions and electrolyte compositions of a zinc–cerium flow battery, experiments were carried out over a broad range of operating conditions and electrolyte compositions. A platinised titanium mesh was used as the positive electrode. The flow battery was first charged for 4 h at a constant current and discharged at the same current until the cell voltage dropped below 0.5 V. Table 2 summarizes the charge–discharge voltages and the system efficiencies when the parameters were changed (discussed below). In all cases, the Ce half-cell was the limiting reaction for battery discharge since the redox reaction of Zn continued for longer than the cerium reaction, during both charge and discharge.

3.5.1. Operating parameters

Fig. 6a shows the charge–discharge performance at constant current density. A smaller cell voltage drop between the charge and discharge cycles was observed at low current densities, hence the voltage efficiency improved. At a higher current density, Ce(III) depletes more rapidly during charge at the positive electrode, leading to a higher potential and, therefore, an increased rate

Table 2
System efficiencies of a zinc–cerium redox flow battery at different operating compositions and electrolyte compositions. Unless specified, the operating conditions are the same as in Fig. 3.

Operating parameters	Average charge voltage (V)	Average discharge voltage (V)	[Ce(IV)] after charge (mol dm^{-3})	[Ce(IV)] after discharge (mol dm^{-3})	% Coulombic efficiency	% Voltage efficiency	% Energy efficiency
Current density (mA cm^{-2})							
20	2.67	1.98	0.264	0.098	63.1	74.2	46.8
50	2.98	1.79	0.652	0.184	71.4	60.1	42.9
80	3.33	1.57	0.728	0.271	43.6	47.1	20.5
Temperature (°C)							
25	3.30	1.55	0.600	0.288	47.6	47.0	22.4
40	3.13	1.61	0.616	0.218	60.7	51.4	31.2
50	2.98	1.79	0.652	0.184	71.4	60.1	42.9
60	2.86	1.82	0.672	0.260	62.8	63.6	39.9
Mean linear electrolyte flow velocity (cm s^{-1})							
1.16	3.15	1.61	0.640	0.396	37.3	51.1	19.1
1.79	3.02	1.74	0.616	0.280	51.4	57.6	29.6
3.92	2.98	1.79	0.652	0.184	71.4	60.1	42.9
5.78	2.93	1.74	0.669	0.201	71.4	59.4	42.4
[Ce(III)] (mol dm^{-3})							
0.4 (2.5 h electrolysis)	3.08	1.73	0.385	0166	56.0	56.2	31.5
0.8	2.98	1.79	0.652	0.184	71.4	60.1	42.9
1.0	3.01	1.72	0.632	0.237	60.3	57.1	34.5
1.2	3.04	1.65	0.628	0.293	51.1	54.3	27.7
[Zn(II)] (mol dm^{-3})							
0.5	2.99	1.80	0.652	0.204	68.4	60.2	41.2
1	2.98	1.77	0.652	0.179	72.2	59.4	42.9
1.5	2.98	1.79	0.652	0.184	71.4	60.1	42.9
2	3.13	1.51	0.652	0.201	69.0	48.2	33.3
[Methanesulfonic acid] in positive electrolyte (mol dm^{-3})							
2	3.01	No discharge (insoluble)	0.616	No discharge	Nil	Nil	Nil
3	3.01	1.74	0.608	0.307	45.9	57.8	26.6
4	2.98	1.79	0.652	0.185	71.4	60.1	42.9
5	3.00	1.68	0.656	0.291	55.7	56.0	31.2

of oxygen evolution. The low coulombic efficiencies observed at 20 and 80 mA cm^{-2} (Table 2) were due to a combination of limited mass transport of Ce(IV) ions and the secondary reactions. For instance, the Ce(IV) concentrations after discharge at 20 and 80 mA cm^{-2} were 0.098 and 0.271 mol dm^{-3}, respectively.

Fig. 6b shows the effect of flow velocity on the charge–discharge cycle. Higher coulombic and voltage efficiencies were obtained as the flow velocity increased up to 3.9 cm s^{-1}, indicating again the importance of reactant mass transport during discharge. Additionally, the improved supply of zinc and cerium ions towards the electrodes reduces the effects of side reactions. Further increases in mean linear electrolyte flow velocity above 3.9 cm s^{-1} did not yield any improvements since the reaction was no longer mass-transport controlled.

The effects of temperature on the charge–discharge performance are shown in Fig. 6c. Substantial improvements in both the charge and voltage efficiencies were obtained as the temperature increased from 25 to 50 °C. The coulombic efficiency increase was due to faster reaction kinetics, increased diffusion rates and a reduced viscosity. Higher voltage efficiencies were attributed to the increased electrolyte conductivity (decreased overpotentials) [32,43].

3.5.2. Electrolyte composition

The electrolyte compositions have a large influence on the charge/discharge performance of a zinc–cerium battery. The previous section demonstrated that the Ce half-cell reaction was the limiting factor at all operating conditions. Optimize the composition of the positive electrolyte is, therefore, crucial to the development of the system. Fig. 7a and b shows the cell voltage characteristics of the cell for different concentrations of Ce(III) and methanesulfonic acid in the positive electrolyte, respectively. In both figures, the cell voltage increases after 2 h of charging, with oxygen evolution becoming the main reaction when the concentration of Ce(III) ions gradually falls. The data in Table 2 shows that for Ce(III) ion concentrations higher than 0.8 mol dm^{-3}, the concentration of Ce(IV) generated at the end of the charge cycle drops, which is consistent with previous results using platinum as the positive electrode [43]. Increasing the Ce(III) concentration from 0.8 to 1.2 mol dm^{-3} decreased the voltage and coulombic efficiencies (Table 2) since the solutions became viscous and milky. This was mainly due to the low Ce(III) solubility in 4 mol dm^{-3} methanesulfonic acid. It has been reported that a high concentration of Ce(III) can only be obtained at low methanesulfonic acid concentrations [25]. In contrast, higher Ce(IV) concentrations are only soluble in concentrated methanesulfonic acid [25]. The solubility limit of both Ce(III) and Ce(IV) in 4.0 mol dm^{-3} methanesulfonic acid is *c.a.* 1.0 mol dm^{-3} at room temperature [25,44].

Increasing the methanesulfonic acid concentration up to 4 mol dm^{-3} in the positive electrolyte can increase both the voltage and coulombic efficiencies (Fig. 7b). For methanesulfonic acid concentrations of 2 and 3 mol dm^{-3}, the positive electrolyte was highly viscous after battery charge. This suggests that highly concentrated Ce(IV) solutions will be difficult to achieve in methanesulfonic acid concentrations lower than 4 mol dm^{-3}. The discharge behaviour using such electrolytes was unfavorable, resulting in poor coulombic efficiencies. No battery discharge was observed for the 2 mol dm^{-3} methanesulfonic acid solution. Taking into account the battery performance and the solubility of Ce(IV) ions in low concentrations of acid, the optimum positive electrolyte composition was determined to be 0.8 mol dm^{-3} Ce(III) methanesulfonate in 4 mol dm^{-3} methanesulfonic acid.

The solubility problem of Zn(II) methanesulfonate is less complicated. As summarized in Table 2, higher cell voltages during charge

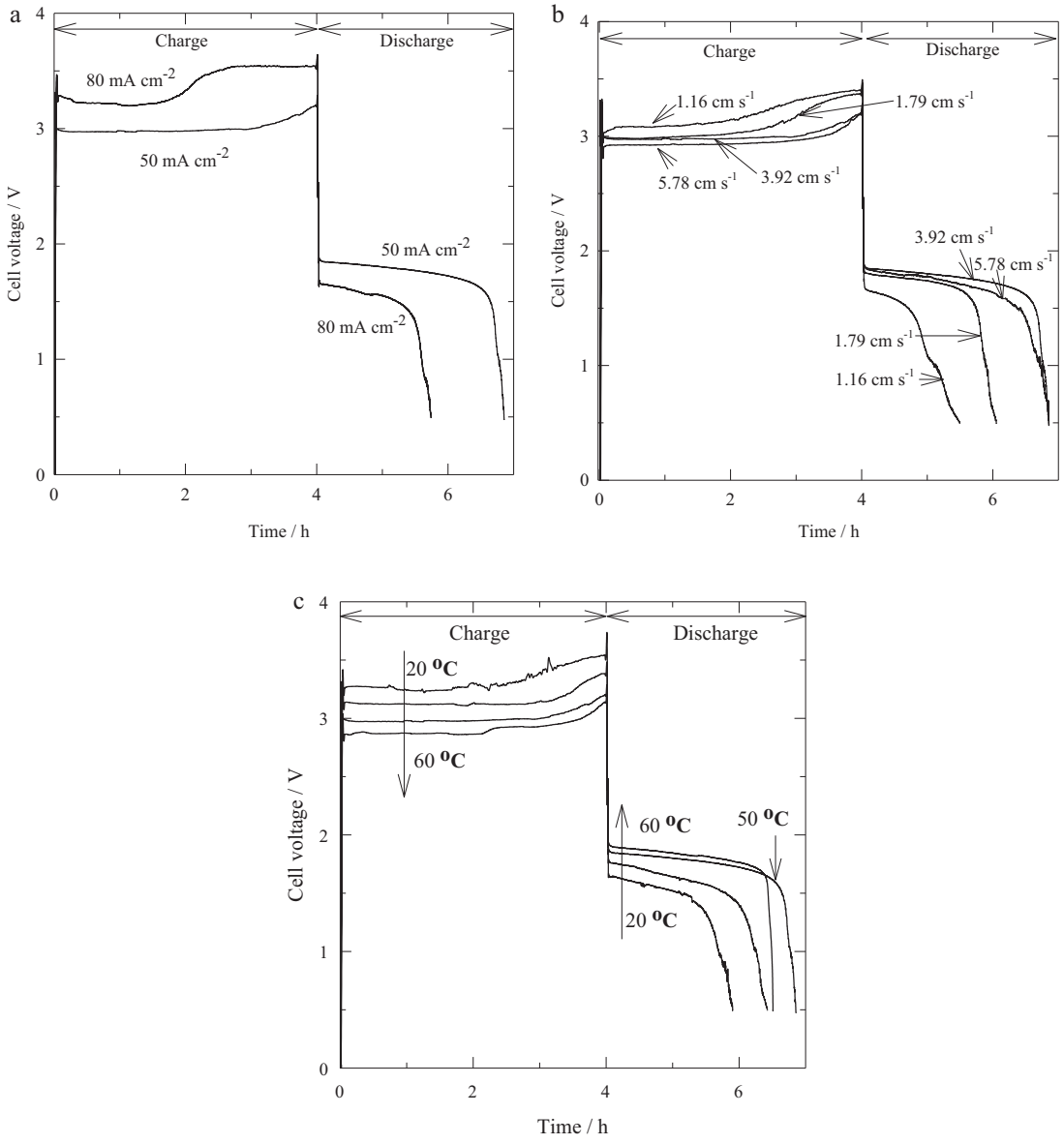

Fig. 6. Effect of operating conditions on the charge–discharge performance of a zinc–cerium redox flow battery: (a) current density, (b) mean linear electrolyte flow velocity and (c) temperature. Unless indicated, electrolyte compositions and operating conditions were the same as in Fig. 3.

and lower discharge cell voltages were observed at 2 mol dm^{-3} Zn(II), close to the solubility limit (2.16 mol dm^{-3}) in methanesulfonic acid [24]. For a Zn(II) methanesulfonate concentration in the range 0.5–1.5 mol dm^{-3}, no significant effect on either the coulombic or the voltage efficiency was observed. Higher Zn(II) ion concentrations, e.g. 1.5 mol dm^{-3}, can, on the other hand, be advantageous at high current densities in order to avoid mass transport limitation.

3.6. Life cycle

A number of charge–discharge experiments at the optimum operating conditions and electrolyte compositions (0.8 mol dm^{-3} Ce(III) methanesulfonate in 4.0 mol dm^{-3} methanesulfonic acid, 1.5 mol dm^{-3} Zn(II) methanesulfonate in 1.0 mol dm^{-3} methanesulfonic acid) were carried out on the zinc–cerium flow battery to investigate life cycle effects. The charge–discharge characteristics at different states of charge were recorded by charging at 50 mA cm^{-2} for different lengths of time: 15 min (Fig. 8a), 1 h, 2 h, and 4 h (Fig. 8b). In a further experiment, the battery was first charged at 50 mA cm^{-2} for 3 h following 15 min charge/discharge cycles for approximately 14 h (see Fig. 9). During charge and discharge, cut-off cell voltages were set at 3.4 V and 0.5 V, respectively. A platinised titanium mesh was used as the positive electrode, while the negative electrode was a carbon–polyvinylester composite.

The life cycle and system efficiencies of these experiments are summarized in Table 3. As shown in Fig. 8a and b, the maximum number of cycles that the battery was able to perform (before no discharge could be obtained) increased from 4 cycles in the 4 h charge/discharge experiments (Fig. 8b) to 57 cycles in the 15 min experiments (Fig. 8a). Column 5 in Table 3 shows that the average coulombic efficiency of the zinc–cerium battery was below 100% in all the experiments, indicating that the products formed during battery charge did not return completely to their initial states and, therefore, that a secondary reaction likely took place. At long charge times, the Ce(IV) product appeared to accumulate over time without being reduced completely during the discharge phases. This led to a depletion of Ce(III) at the beginning of successive charge phases as the cycle number increased. In all experiments, the life

Table 3
Life cycle of a zinc–cerium battery charging at 50 mA cm^{-2} for different lengths of time.

Charge/discharge cycle time	No. of cycle	Average charge voltage (V)	Average discharge voltage (V)	% Average coulombic efficiency	% Average voltage efficiency	% Average energy efficiency
0.25 h	57	3.06	1.41	84.9	46.2	39.2
1 h	19	3.00	1.75	81.5	58.3	47.5
2 h	7	2.95	1.77	69.4	60.0	41.3
4 h	4	2.96	1.86	68.3	62.8	42.8
First charged for 3 h and then 0.25 h charge/discharge	25	2.97	1.77	99.4	59.6	59.3

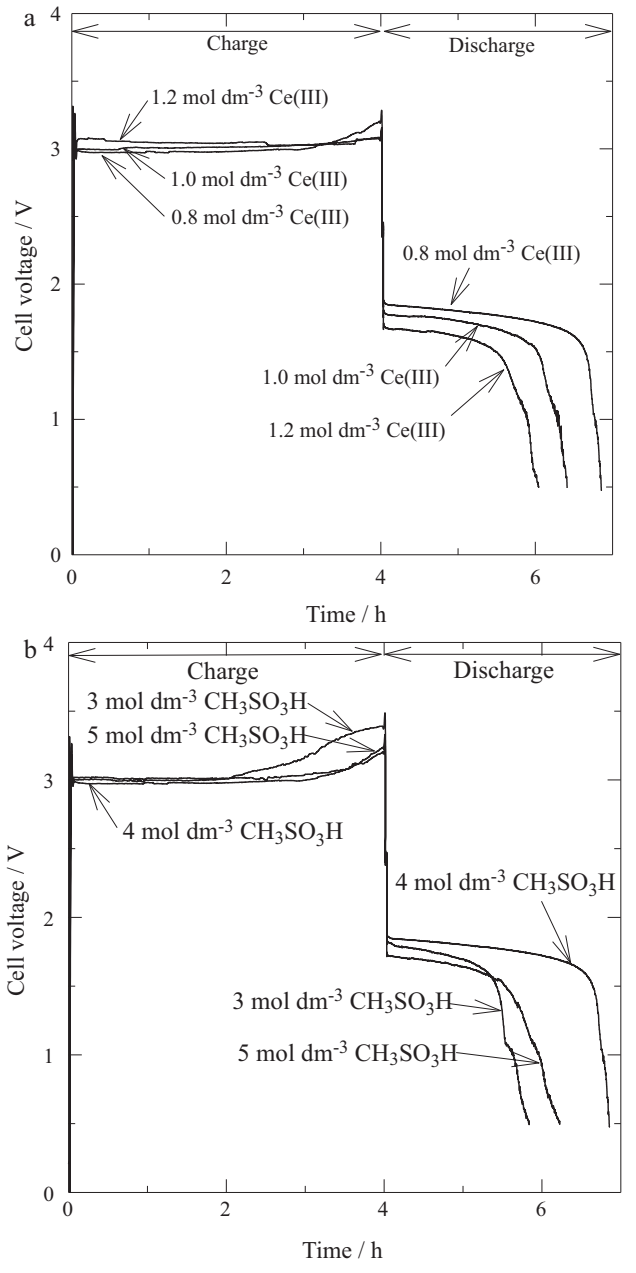

Fig. 7. Effect of electrolyte compositions on the charge–discharge performance of a zinc–cerium redox flow battery: (a) cerium (III) concentration and (b) methanesulfonic acid concentration in the positive electrolyte. Unless indicated, electrolyte compositions and operating conditions were the same as in Fig. 3.

of the battery was between 25 and 30 h, except in Fig. 9 where the cell was charged for 3 h before 15 min charge/discharge cycles.

Due to the initial higher acid concentration in the positive compartment and the formation of acid in the negative electrode during battery charge, reaction (1), the acidity of the negative electrolyte increased after prolonged charge/discharge cycling [45], which decreased the efficiency of zinc electrodeposition. For this reason, in all of the long life-cycle experiments, the zinc half-cell reaction was also a limiting factor. The acid concentration change and the diffusion of protons across the membrane were more significant towards the end of the 4 h charge/discharge cycle.

More cycles at longer charge–discharge times can be achieved by increasing the ratio of electrolyte volume to electrode area. As shown in Fig. 8a, the cell voltage during discharge dropped rapidly in the early cycles. The concentration of Ce(IV) ions generated was still too low for the battery to be able to discharge at 50 mA cm^{-2}. After a number of cycles, Ce(IV) ions accumulated and higher discharge cell voltages could be obtained. At later cycles, depletion of the Ce(III) led to a sharp increase in charge cell voltages.

In order to achieve long life cycles and a relatively high discharge cell voltage, the battery was first charged at 50 mA cm^{-2} for 3 h to obtain a high concentrations of Ce(IV). Following the 3 h charge, a charge/discharge cycle regime, each 15 min, was applied. This

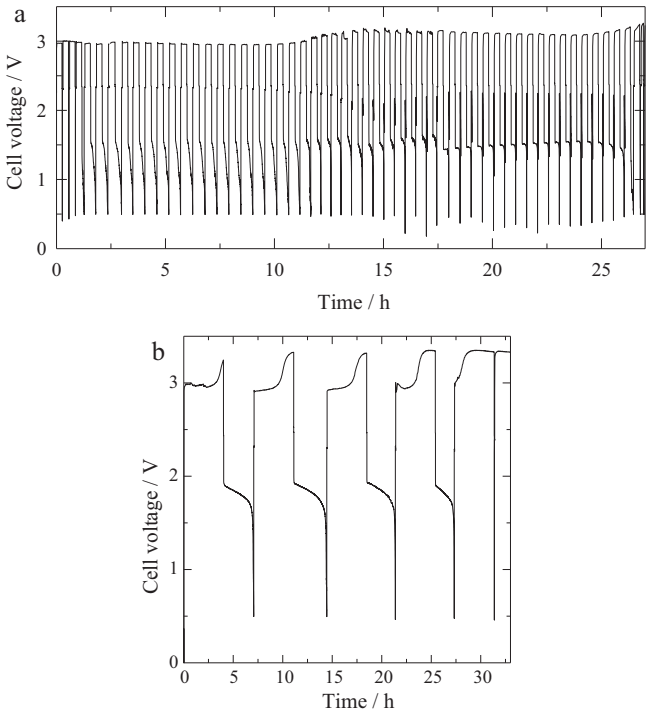

Fig. 8. Life cycle of a zinc–cerium battery charging at 50 mA cm^{-2} for different lengths of time: (a) 15 min and (b) 4 h. Electrolyte compositions and operating conditions were the same as in Fig. 3.

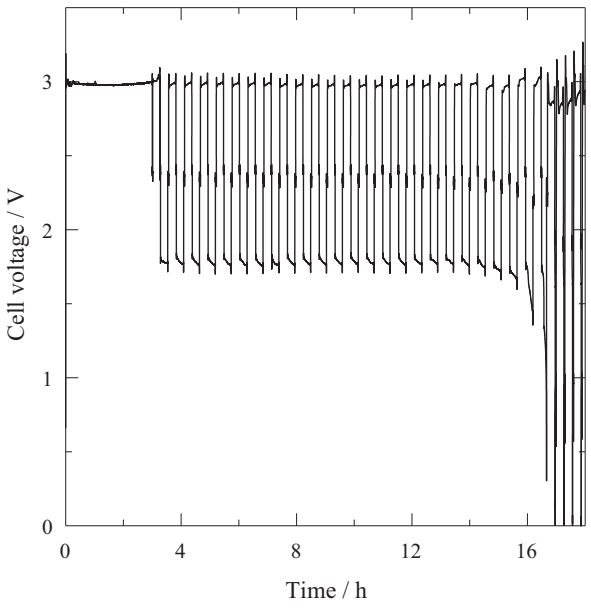

Fig. 9. Life cycle of a zinc–cerium battery charging at 50 mA cm^{-2} for 3 h followed by 15 min charge/discharge cycles. Electrolyte compositions and operating conditions were the same as in Fig. 3.

ensured a smaller change in the acid concentration and a slower depletion of Ce(III) ions. Fig. 9 shows that for this experiment, 25 cycles at an average discharge voltage of *c.a.* 1.77 V were obtained with average coulombic and energy efficiencies of 99.4% and 59.3%, respectively, higher than any of the other charge/discharge cycle regimes tested.

4. Conclusions

The performance of a zinc–cerium redox flow battery has been characterized through comprehensive investigations into the effects of operating conditions, materials and electrolyte compositions, as well as through life-cycle testing. The two-dimensional electrodes performed poorly. Carbon felt positive electrodes were capable of discharge at 50 mA cm^{-2} with high coulombic (>92%) and voltage (>68%) efficiencies. Due to the poor electrical conductivity and the poor adherence of the carbon adhesive (used to attach the carbon felts) after only a few cycles, a three-dimensional platinised titanium mesh electrode was found to be the optimal positive-electrode material.

The highest energy efficiency was obtained at 50 °C with a mean linear electrolyte flow velocity of 7.8 cm s^{-1}, while the optimum composition for the positive electrolyte was 0.8 mol dm^{-3} Ce(III) methanesulfonate in 4.0 mol dm^{-3} methanesulfonic acid. In most cases, flow velocities below 3.9 cm s^{-1} yielded a poor performance. Higher Ce(III) concentrations were not possible as a result of the low solubility in methanesulfonic acid. In all cases, the positive cerium half-cell was limiting for battery discharge due to inefficiencies in the discharge cerium reaction in the early cycles. In all charge/discharge modes at different times, the zinc half-cell reaction was the limiting factor for the life cycles. During the life cycles, the negative electrolyte acidity increased due to the migration of protons from the positive electrolyte and due to proton generation during zinc electrodeposition.

An improved electrolyte composition and alternative electrode materials could be used to enhance the performance of the zinc–cerium redox flow battery. For instance, the use of additives or ionic liquids to reduce secondary reactions such as hydrogen and oxygen, and the use of a catalyst incorporated into the electrode material to enhance the reaction rates. Further investigations into the acid concentrations in the negative and positive electrolytes and the use of bipolar electrodes in a stack, are necessary to scale-up the system and increase the power and energy outputs.

Acknowledgements

Financial support has been provided by the Research Institute for Industry (RIfI) at the University of Southampton. The authors are grateful to Dr. L. Berlouis, University of Strathclyde for helpful discussions and gratefully acknowledge the construction of the flow battery provided by the mechanical engineering workshop, University of Southampton. This work represents part of P.K. Leung's PhD research programme on the development of zinc-based flow batteries for energy storage and conversion technology.

References

[1] The Electricity Advisory Committee, Bottling Electricity: Storage as a Strategic Tool for Managing Variability and Capacity Concerns in the Modern grid - A report by The Electricity Advisory Committee, December 2008. http://www.oe.energy.gov/DocumentsandMedia/final-energy-storage_12-16-08.pdf Accessed on 25 November 2010.
[2] N. Tokuda, T. Kanno, T. Hara, T. Shigematsu, Y. Tsutsui, A. Ikeuchi, T. Itou, T. Kumamoto, SEI Tech. Rev. 50 (1998) 88–94.
[3] J. Makansi, J. Abboud, Energy Storage Council White Paper (2002).
[4] M. Yoshitake, M. Takabatake, O. Hamamoto, T. Hiramatu, S. Kondo, J. Proc. Electrochem. Soc. 266 (1988) 11–88.
[5] M. Shimizu, M.S. N. Mori, Japan Patent - 63128560, 01/07/1988, (1988).
[6] A. Pelligri, P.M. Spaziante, GB Patent 2030349, to Oronzio de Nori Impianti Elettrochimici S.p.A., (1978).
[7] M. Skyllas-Kazacos, M. Rychcik, P.G. Robins, A.G. Fane, M.A. Green, J. Electrochem. Soc. 133 (1986) 1057–1058.
[8] M. Rychcik, M. Skyllas-Kazacos, J. Power Sources 19 (1987) 45–54.
[9] M. Skyllas-Kazacos, F. Grossmith, J. Electrochem. Soc. 134 (1987) 2950–2953.
[10] M. Rychcik, M. Skyllas-Kazacos, J. Power Sources 22 (1988) 59–67.
[11] R.F. Koontz, R.D. Lucero, (2000), Handbook of batteries, vol. 39, 1–22.
[12] F.C. Walsh, J. Pure Appl. Chem. 73 (2001) 1819–1837.
[13] DTI, Regenesys Utility Scale Energy Storage, Project Summary, Pub URN 04/1048. http://www.dti.gov.uk/energy/renewables/publications/pubs_distributedgeneration.shtml Accessed on 25 November 2010.
[14] D. Pletcher, R. Wills, J. Power Sources 149 (2005) 96–102.
[15] C. Ponce de León, A. Frías-Ferrer, J. González-García, D.A. Szánto, F.C. Walsh, J. Power Sources 160 (2006) 716–732.
[16] I. Tsuda, K. Kurokawa, K. Nozaki, Conference Record of the Twenty Fourth IEEE Photovoltaic Specialists Conference – 1994, 1994 IEEE First World Conference, vol. 1, 1994, pp. 946–949.
[17] L. Joerissen, J. Garche, C. Fabjan, G. Tomazic, J. Power Sources 127 (2004) 98–104.
[18] K.L. Huang, X.G. Lia, S.Q. Liu, N. Tan, L.Q. Chen, Renewable Energy 33 (2008) 186–192.
[19] R.L. Clarke, B.J. Dougherty, S. Harrison, P.J. Millington, S. Mohanta, US 2004/0202925 A1, Cerium Batteries, (2004).
[20] R.L. Clarke, B.J. Dougherty, S. Harrison, J.P. Millington, S. Mohanta, US 2006/0063065 A1, Battery with bifunctional electrolyte, (2005).
[21] P.K. Leung, C. Ponce de León, C.T.J. Low, F.C. Walsh, submitted to Electrochim. Acta, January 2011.
[22] P.K. Leung, C. Ponce de León, C.T.J. Low, F.C. Walsh, Electrochim. Acta 56 (2011) 2145.
[23] J. Bard, L.R. Faulkner, Electrochemical Methods - Fundamentals and Applications, 2nd ed., Wiley, 2001.
[24] M.D. Gernon, M. Wu, T. Buszta, P. Janney, Green Chem. 1 (1999) 127–140.
[25] R.P. Kreh, R.M. Spotnitz, J.T. Lundquist, J. Org. Chem. 54 (1989) 1526–1531.
[26] T.R. Crompton, Elsevier Science & Technology Books, vol. 14, 3rd ed., Boston: Newnes, Oxford, England, 2000 (vol. Chapter 14).
[27] P.C. Symons, J Electrochem. Soc. International Conference on Electrolytes for Power Sources, Brighton, 1973.
[28] P.C. Butler, P.A. Eidler, P.G. Grimes, S.E. Klassen, R.C. Miles, Handbook of Batteries, vol. 39, 3rd ed., McGraw Hill, 2001.
[29] P.C. Butler, D.W. Miller, A.E. Verardo, 17th Intersoc. Energy Conversion Eng. Conf., Los Angeles (1982).
[30] L.W. Hruska, R.F. Savinell, J. Electrochem. Soc. 128 (1981) 18–25.
[31] Y.H. Wen, J. Cheng, S.Q. Ning, Y.S. Yang, J. Power Sources 188 (2009) 301–307.
[32] B. Fang, S. Iwasa, Y. Wei, T. Arai, M. Kumagai, Electrochim. Acta 47 (2002) 3971–3976.
[33] R.M. Spotnitz, R.P. Kreh, J.T. Lundquist, P.J. Press, J. Appl. Electrochem. 20 (1990) 209–215.
[34] L.B. Zinner, J. Ann. Assoc. Bras. Quim. 30 (1979) 27.
[35] P. Patnaik, Dean's Analytical Chemistry Handbook, 2nd ed., McGraw-Hill, 2004.
[36] I.M. Kolthoff, E.B. Sandell, Texture of Quantitative Inorganic Analysis, 3rd ed. The Macmillan Company, pp. 463–481.

[37] A.I. Vogel, Textbook of Quantitative Inorganic Analysis, 5th ed. Wiley, New York.
[38] V. Devadoss, C.A. Basha, K. Jayaraman, J. Ind. Eng. Chem. Res. 47 (2008) 4607–4616.
[39] H.S. Lim, A.M. Lackner, R.C. Knechtli, J. Electrochem. Soc. 124 (1977) 1154–1157.
[40] A. Pletcher, R. Wills, J. Power Sources 149 (2005) 96–102.
[41] J. Jorné, J.T. Kim, D. Kralik, J. Appl. Electrochem. 9 (1979) 573–579.
[42] Y. Liu, X. Xia, H. Liu, J. Power Sources 130 (2004) 299–305.
[43] T. Raju, C.A. Basha, Chem. Eng. J. 114 (2005) 55–65.
[44] T. Raju, C.A. Basha, J. Ind. Eng. Chem. Res. 47 (2008) 8947–8952.
[45] A. Hazza, D. Pletcher, R. Wills, J. Phys. Chem. Chem. Phys. 6 (2004) 1773–1778.
[46] J.M. Friedrich, C. Ponce-de-León, G.W. Reade, F.C. Walsh, J. Electroanal. Chem. 561 (2004) 203–217.
[47] A.P. Borole, C.Y. Hamilton, T.A. Vishnivetskaya, D. Leak, C. Andras, J. Morrell-Falvey, M. Keller, B. Davison, J. Power Sources 191 (2009) 520–527.
[48] J. Gonzaïlez-Garcıa, P. Bonete, E. Exposito, V. Montiel, A. Aldaz, R. Torregrosa-Macia, J. Mater. Chem. 9 (1999) 419–426.

Electrochemistry Communications 13 (2011) 770–773

Contents lists available at ScienceDirect

Electrochemistry Communications

journal homepage: www.elsevier.com/locate/elecom

An undivided zinc–cerium redox flow battery operating at room temperature (295 K)

P.K. Leung, C. Ponce de León *, F.C. Walsh

Electrochemical Engineering Laboratory, Energy Technology Research Group, University of Southampton, Highfield, Southampton, Hampshire SO17 1BJ, United Kingdom

ARTICLE INFO

Article history:
Received 19 March 2011
Received in revised form 12 April 2011
Accepted 12 April 2011
Available online 19 April 2011

Keywords:
Cerium
Flow battery
Undivided cell
Zinc

ABSTRACT

An undivided zinc–cerium hybrid redox flow battery is proposed. High discharge cell voltage of *c.a.* 2.1 V at 20 mA cm^{-2} and an average energy efficiency of 75% were obtained. The cerium half-cell reaction was highly reversible on a carbon felt electrode with less than a 15 mV change between charge and discharge cycles. The limiting factor for extended cycling was the zinc negative electrode, as residual zinc remained on the electrode after discharge. The battery self-discharge was evaluated by monitoring the open-circuit cell voltage, the capacity was found to last for approximately 7 h after being charged for 30 min.

1. Introduction

Redox flow batteries (RFB) are a relatively new technology used to store large quantities of energy more economically and efficiently [1]. Typical RBF such as all-vanadium, zinc–bromine and bromine–polysulfide require expensive ion-exchange membranes to divide the negative and positive electrolytes that have different chemical compositions. An undivided system would be desirable to reduce costs and simplify the cell design. Some efforts to achieve this aim have been reported; Hazza et al. [2] introduced an undivided lead acid RFB in 2004. This was followed by other systems such as zinc–nickel [3,4], copper–lead dioxide [5] and cadmium–chloranil [6]. These systems still have shortcomings such as the low operating cell voltages and limited storage capacity associated with the positive electrode materials [7].

The large cell voltage zinc–cerium RFB was recently developed by Plurion Inc. (UK) using a divided cell with a platinized titanium positive electrode at 60 °C [8–10]. This hybrid RFB is able to store energy in the zinc metal and in the soluble cerium species resulting in an open-circuit cell voltage of approximately 2.3 V, which is higher than other RFBs. Further characterizations of this system have been carried out using less expensive carbon felt as the positive electrode [11]. In this paper an alternative, undivided configuration using methanesulfonic acid (MSA) as supporting electrolyte is proposed [12,13]. At the negative electrode, the primary reactions are: [14,15]:

$$Zn(II) + 2e^- \underset{\text{Discharge}}{\overset{\text{Charge}}{\rightleftharpoons}} Zn \quad E^{\theta}_{-} = -0.76\text{V } \textit{vs.}\text{ SHE} \tag{1}$$

while at the positive electrode:

$$2\ Ce(III) - 2e^- \underset{\text{Discharge}}{\overset{\text{Charge}}{\rightleftharpoons}} 2\ Ce(IV) \tag{2}$$

The standard electrode potential of reaction (2) lies between 1.28 and 1.72 V *vs.* SHE depending on the supporting electrolyte [16]. The overall cell reaction is:

$$2\ Ce(III) + Zn(II) \underset{\text{Discharge}}{\overset{\text{Charge}}{\rightleftharpoons}} 2\ Ce(IV) + Zn \quad E_{cell} \approx +2.3\ \text{V} \tag{3}$$

The discharge cell voltage of the membraneless zinc–cerium RFB was *c.a.* 2.1 V at 20 mA cm^{-2} with an average energy efficiency of ≈75%.

2. Experimental details

2.1. Chemicals

All solutions were prepared with ultra-pure water (18 MΩ cm resistivity). Zn(II) and Ce(III) methanesulfonate at 2 mol dm^{-3} were prepared by stirring 0.4 mol dm^{-3} $[ZnCO_3]_2{\cdot}[Zn(OH)_2]_3$ (Alfa Aesar, U.K., 99 wt.%) and 1.0 mol dm^{-3} $Ce_2(CO_3)_3$ powders (Treibacher Industrie AG., Germany, 99 wt.%) in 4 and 6 mol dm^{-3} aqueous methanesulfonic acid (Lutropur®, BASF SE, Germany, 99 wt. %), respectively. A typical experiment contained 1.5 mol dm^{-3} zinc methanesulfonate and 0.2 mol dm^{-3} cerium (III) methanesulfonate in 0.5 mol dm^{-3} MSA in 100 cm^3 electrolyte.

* Corresponding author.
E-mail address: capla@soton.ac.uk (C. Ponce de León).

1388-2481/$ – see front matter © 2011 Elsevier B.V. All rights reserved.
doi:10.1016/j.elecom.2011.04.011

2.2. Flow battery experiments

Fig. 1a shows the electrical and electrolytic circuits of the undivided RFB. An expanded view of the flow cell is shown in Fig. 1b. Planar carbon polyvinyl–ester electrode (BMC 18649, Engtegris Inc., Germany) was used as the substrate for the zinc negative and cerium positive electrodes. The positive electrode also consisted of three pieces of carbon felt (Sigratherm® GFA-05, 4.5 cm × 2.0 cm × 0.5 cm, Germany) compressed onto the carbon substrate by a Perspex window to avoid contact with the zinc negative electrode. Silicone gaskets were used to form the negative electrolyte compartment and to prevent leakages. The inlet and outlet flow channels of the electrolyte were designed within the framework of the acrylic cell. The carbon polymer substrate of both electrodes, exposed to the electrolyte was 2 cm × 0.8 cm with a separation of 2 cm.

The electrolyte was recirculated through the cell at an average linear flow velocity of 3.9 cm s^{-1} with a peristaltic pump. The cell was charged and discharged at 20 mA cm^{-2} (32 mA) during 30 min at *c.a.* 22.5 °C while monitoring the electrode potentials with an Ag|AgCl (sat) reference electrode located near the inlet of the flow channel. All electrochemical measurements were made using a BaSyTec (Germany) battery test system (5 A/12 V).

3. Results and discussion

The cell voltage and the half-cell electrode potentials *vs.* time during the first ten charge–discharge cycles of the undivided RFB are shown in Fig. 2a. The open-circuit cell voltage was 2.34 V. In general, charge voltage was relatively flat at approximately 2.50 V. At the start of discharge cycle, the cell voltage decreased gradually from 2.1 V to 2.0 V followed by a sharp voltage drop at the end of the cycle when most of the zinc was stripped off from the negative electrode.

The cell voltage during discharge can be expressed as:

$$E_{CELL} = E_{Ce}^{o.c.} - E_{Zn}^{o.c.} - \Sigma IR - |\Sigma\eta| \quad (4)$$

Where $E_{Ce}^{o.c.}$ and $E_{Zn}^{o.c.}$ are the open-circuit potential of the half-cell reactions for cerium and zinc, respectively. The voltage drop due to the membrane was avoided (the typical resistance of Nafion® 1100 in a 1 mol dm^{-3} sulfuric acid is 0.13 Ω cm^2 [17]). The change in the half-

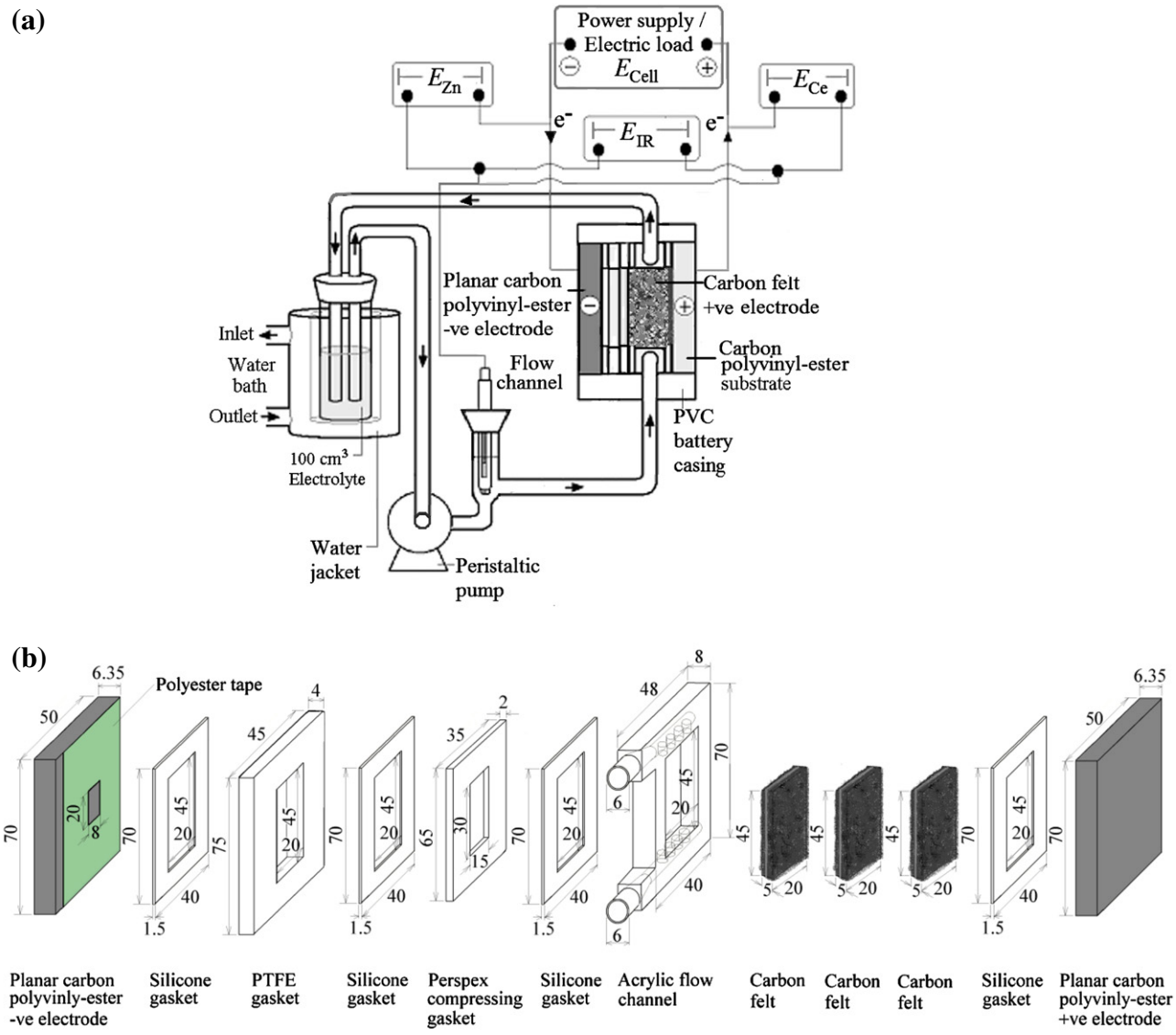

Fig. 1. Schematic diagram of the undivided zinc–cerium RFB. (a) overall experimental arrangement and electrical circuits, (b) the expanded view of the cell components. The units are shown in millimeter.

cell potentials of the zinc and cerium reactions during the charge–discharge cycles was approximately 430 mV and less than 15 mV, respectively. Therefore, the cell voltage change was mainly attributed to the polarization of the zinc negative electrode. The cut-off cell voltage was set at 0.8 V during discharge and at the end of each discharge cycle zinc was observed to be the limiting reaction. Fig. 2a shows some fluctuations of the zinc half-cell potential during the last discharge cycles possibly due to the residual zinc that remained on the substrate. This can be avoided by using electrolytic additives to extend the life cycle of the zinc half-cell reaction. During the discharge cycle of the redox reaction Ce(III)/Ce(IV), the electrode potential is stable but starts to fall slightly to negative values towards the end of the 8th cycle. However, the reaction appears to be highly reversible on this carbon felt but it has been found to be dependent on the type of carbon materials used [18–21]. Carbon felt material was found to be stable for the cerium reaction due to its very large surface area and hence relatively small local current density [11]. In this work, the coulombic efficiency and the change in cerium half-cell potential during the charge–discharge cycles are similar to those observed in the vanadium–cerium RFB in 1 mol dm^{-3} sulfuric acid reported by Fang et al. [19].

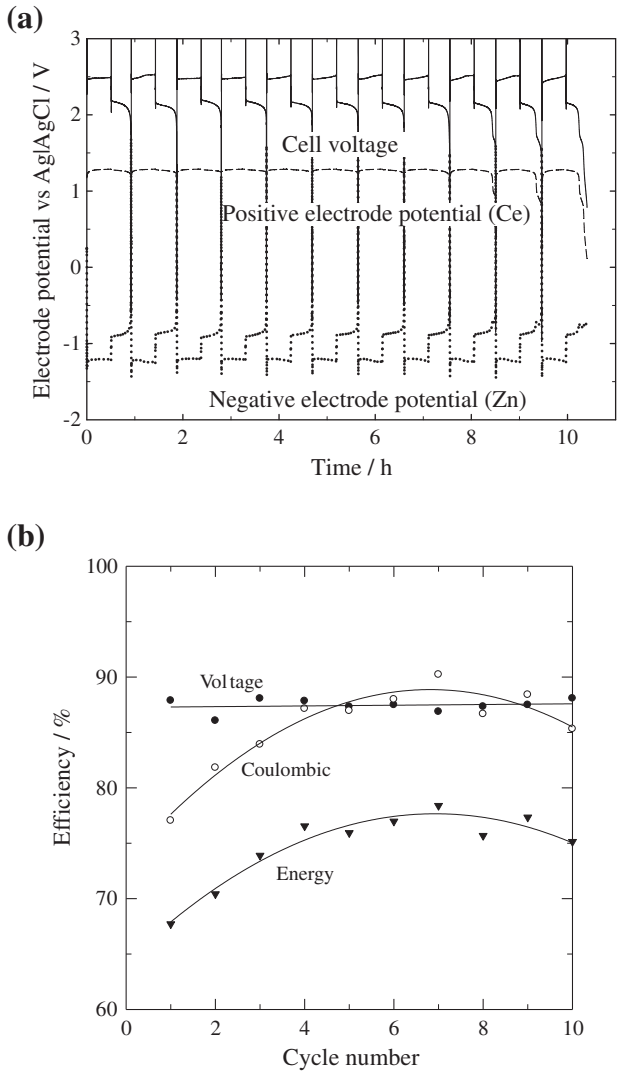

Fig. 2. Performance of an undivided zinc–cerium RFB during 10 charge–discharge cycles, (a) voltage *vs.* time, (b) efficiencies at 20 mA cm^{-2}, 22.5 °C and 3.9 cm s^{-1} electrolyte mean linear flow velocity.

The coulombic, voltage and energy efficiencies of the undivided zinc–cerium system during charge–discharge cycles are shown in Fig. 2b. The energy and coulombic voltage efficiencies varied between 68–76% and 76–90% respectively, both variables declined slightly after the 7th charge–discharge cycle while the voltage efficiency remained stable at 88%. Preliminary experiments carried out in a beaker containing a stirred electrolyte resulted in <40% coulombic efficiency which indicates the importance of using a flow cell design: the large surface area of the positive electrode allows the Ce(III)/Ce(IV) redox reaction to take place efficiently at low cerium concentration in the electrolyte, while the small area of the zinc negative electrode was used to minimize the area exposed to the electrolyte and to reduce the self-discharge effect. In order to avoid the depletion of cerium species within the carbon felt electrode (as in the case of the beaker cell), the electrolyte was circulated through the carbon felt within the acrylic flow channel as shown in Fig. 1a and b.

In this preliminary study of the undivided RFB, a low concentration of Ce(III) ions (0.2 mol dm^{-3}) was used and as a result the energy density was relatively low compared with the all-vanadium RFB, i.e. *c.a.* 11 *vs.* 20–35 W h dm^{-3} [22], respectively. A higher concentration of MSA would be needed to increase the concentration of Ce(IV) ions but this will lead to a poor coulombic efficiency of the zinc negative electrode due to the hydrogen evolution. Another possibility to increase the concentration of Ce(IV) is to use mixtures of H_2SO_4 with MSA as it has been reported that up to 0.7 mol dm^{-3} of Ce(IV) can be dissolved in low concentration of sulfuric acid [20]. As well as increasing the storage capacity of the battery, higher cerium concentration in the electrolyte can facilitate the mass transport of cerium ions towards the positive electrode. However, the high concentration of cerium ions may have an impact but not necessarily, on the self-discharge of zinc at the negative electrode. Therefore, further optimization of these parameters is important in further work.

Considering that an undivided system will be easily self-discharged at open-circuit due to the mixture of two reactive species the zinc and cerium half-cell potentials, together with the open-circuit cell voltage were monitored over a period of time. Fig. 3 shows these values during the self-discharge at 0.69 cm s^{-1} mean linear flow rate after the system was charged at 20 mA cm^{-2} during 30 min at 3.9 cm s^{-1}. The figure shows a slightly decrease of the zinc half-cell potential from −1.03 to −0.80 V *vs.* Ag|AgCl after 4 h followed by an exponential decrease starting before 7 h towards +0.20 V *vs.* Ag|AgCl. This sharp decline indicates that most of the zinc has been dissolved into the electrolyte. The open-circuit cell voltage follows similar trend changing

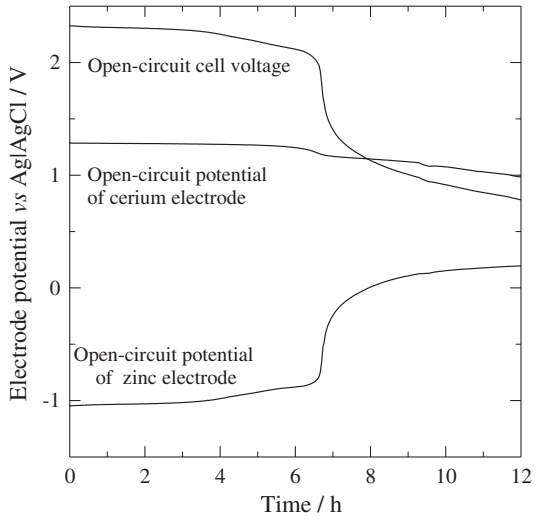

Fig. 3. Open-circuit potential *vs.* time of an undivided zinc–cerium RFB at electrolyte mean linear flow velocity of 0.64 cm s^{-1} after 20 mA cm^{-2} charge for 30 min.

from 2.4 V to 2.2 V within the first 5 to 6 h followed by a significant drop, starting before 7 h towards to 0.8 V at 12 h. The self-discharge rate was comparable to those of the conventional systems, such as all-vanadium RFB. For instance, the capacity of an all-vanadium RFB was reported to last for 11 h after being charged for 1.6 A h [23].

Self-discharge of all-vanadium RFB is mainly attributed to the crossover of vanadium ions across the membrane and bubbling nitrogen gas into the electrolyte is used to avoid oxidation. Ce(III) and Ce(IV) ions are less likely to be oxidized or reduced respectively, compared to their vanadium counterparts [19] due the large positive potential. While the battery is in operation the self-discharge of the zinc electrode is not a problem and in the short term, zinc corrosion can be effectively decreased with corrosion inhibitors [24]. If the battery needs to be discharged after being charged for a long period of time, the electrolyte can be pumped out from the cell to prevent self-discharge.

4. Conclusions

An undivided zinc–cerium RFB is proposed for the first time. This system features several advantages over the conventional zinc–cerium flow battery, such as the use of a single electrolyte, a simple cell design, the high open-circuit cell voltage (2.34 V) and the capability to operate at room temperature. At a current density of 20 mA cm^{-2}, average coulombic and energy efficiencies up to 90 and 76%, respectively, can be obtained. The change in cerium half-cell potential between charge and discharge cycles was less than 15 mV suggesting that cerium redox reactions were highly reversible at the carbon felt electrode. It was observed that the ratio between the positive and negative electrode areas played an important role for the self-discharge. The proposed membraneless zinc–cerium RFB seems to be a promising system for energy storage and requires further investigation.

Acknowledgements

The authors are grateful to Dr. J. Low for the provision of the original divided flow battery. The authors also gratefully acknowledge Dr. L. Berlouis (University of Strathclyde) for valuable discussions.

References

[1] C. Ponce de León, A. Frías-Ferrer, J. González-García, D.A. Szánto, F.C. Walsh, J. Power Sources 160 (2006) 716–732.
[2] A. Hazza, D. Pletcher, R. Wills, J. Phys. Chem. Chem. Phys. 6 (2004) 1773–1778.
[3] J. Cheng, L. Zhang, Y.S. Yang, Y.H. Wen, G.P. Cao, X.D. Wang, Electrochem. Comm. 9 (2007) 2639–2642.
[4] Y.H. Wen, J. Cheng, S.Q. Ning, Y.S. Yang, J. Power Sources 188 (2009) 301–307.
[5] J.Q. Pan, Y.Z. Sun, J. Cheng, Y.H. Wen, Y.S. Yang, P.Y. Wan, Electrochem. Comm. 10 (2008) 1226–1229.
[6] Y. Xu, Y.H. Wen, J. Cheng, G.P. Cao, Y.S. Yang, Electrochem. Comm. 11 (2009) 1422–1424.
[7] J. Pan, L. Ji, Y. Sun, P. Wan, J. Cheng, Y. Yang, M. Fan, Electrochem. Comm. 11 (2009) 2191–2194.
[8] R.L. Clarke, B.J. Dougherty, S. Harrison, P.J. Millington, S. Mohanta, US Patent 2004/0202925 A1, Cerium Batteries (2004).
[9] R.L. Clarke, B. Dougherty, S. Harrison, J.P. Millington, S. Mohanta, US Patent 20040197651, Lanthanide Batteries (2004).
[10] R.L. Clarke, B. Dougherty, S. Harrison, J.P. Millington, S. Mohanta, US Patent 2004197649 (A1), Load leveling battery methods therefore (2004).
[11] P.K. Leung, C. Ponce-de-Leon, C.T.J. Low, A.A. Shah, F.C. Walsh, J. Power Sources 196 (2011) 5174–5185.
[12] M.D. Gernon, M. Wu, T. Buszta, P. Janney, Green Chem. 1 (1999) 127–140.
[13] R.P. Kreh, R.M. Spotnitz, J.T. Lundquist, J. Org. Chem. 54 (1989) 1526–1531.
[14] P.K. Leung, C. Ponce de León, C.T.J. Low, F.C. Walsh, Electrochim. Acta (2011) Accepted.
[15] G. Nikiforidis, L. Berlouis, D. Hall, D. Hodgson, J. Power Sources (2011), doi:10.1016/j.jpowsour.2011.01.036.
[16] J. Bard, L.R. Faulkner, Electrochemical Methods—Fundamentals and Applications, 2nd ed, Wiley, 2001.
[17] S.M. Slade, T.R. Ralph, C. Ponce de León, S.A. Campbell, F.C. Walsh, Fuel Cell 10 (2010) 567–574.
[18] D. Pletcher, E. Valdes, Electrochim. Acta 33 (1988) 509–515.
[19] B. Fang, S. Iwasa, Y. Wei, T. Arai, M. Kumagai, Electrochim. Acta 47 (2002) 3971–3976.
[20] A. Paulenova, S.E. Creager, J.D. Navratil, Y. Wei, J. Power Sources 109 (2002) 431–438.
[21] P.K. Leung, C. Ponce-de-Leon, C.T.J. Low, F.C. Walsh, Electrochim. Acta 56 (2011) 2145–2153.
[22] M. Skyllas-Kazacos, J. Power Sources 124 (2003) 299–302.
[23] X.L. Luo, Z.Z. Lu, J.Y. Xi, Z.H. Wu, W.T. Zhu, L.Q. Chen, X.P. Qiu, J. Phys. Chem. B 109 (2005) 20310–20314.
[24] P.K. Leung, C. Ponce de León, F.C. Walsh, In preparation for corrosion science (2011).